# Plastic Instability and Failure of Sheet Metals Subjected to Complex Stress States

by

Jacqueline Noder

A thesis

presented to the University of Waterloo

in fulfillment of the

thesis requirement for the degree of

Doctor of Philosophy

in

Mechanical and Mechatronics Engineering

Waterloo, Ontario, Canada, 2022

## Examining Committee Membership

The following served on the Examining Committee for this thesis. The decision of the Examining Committee is by majority vote.

| | |
|---|---|
| External Examiner: | Chester van Tyne, Ph.D.<br>Professor Emeritus, Colorado School of Mines |
| Supervisor: | Clifford Butcher, Ph.D.<br>Assistant Professor, University of Waterloo |
| Internal Examiner: | Michael J. Worswick, Ph.D.<br>Professor, University of Waterloo |
| Internal Examiner: | Elliot Biro, Ph.D.<br>Assistant Professor, University of Waterloo |
| Internal-External Examiner: | Scott Walbridge, Ph.D.<br>Professor, University of Waterloo |

## Author's Declaration

This thesis consists of material all of which I authored or co-authored: see Statement of Contributions included in the thesis. This is a true copy of the thesis, including any required final revision, as accepted by my examiners.

I understand that my thesis may be made electronically available to the public.

## Statement of Contributions

The presented thesis comprises eight chapters. The introduction and literature review are presented in Chapters 1 and 2. Chapters 3-6 represent a concise overview of the research that has been published or prepared in manuscripts under review of which the candidate is the first author. The papers are attached to this thesis and can be found in appendices A-D. The thesis conclusions and recommendations for future work are presented in Chapters 7 and 8, respectively.

The following co-authors and colleagues have contributed to the current work:

**Professor Butcher** supervised this PhD thesis, provided guidelines and feedback on the research direction, and reviewed manuscripts.

**Jim Dykeman** of Honda Development & Manufacturing of America, Ohio, USA, provided scientific discussions on V-Bend testing.

**Jon Edward Gutierrez**, MASc Candidate, conducted and analyzed the Marciniak tests for the 3rd Gen 1180 V2 that were utilized in Chapter 6 to demonstrate applicability of the developed analytical-numerical framework to AHSS grades. The results are published as part of a larger experimental study in:

Noder, J., Gutierrez, J.E., Zhumagulov, A., Dykeman, J., Ezzat, H., Butcher, C., (2021b). A Comparative Evaluation of Third-Generation Advanced High-Strength Steels for Automotive Forming and Crash Applications, Materials, 14, 4970, https://doi.org/10.3390/ma14174970.

The balance of the work is my own.

## Abstract

The rapid development of new emerging classes of steels has outpaced the methodologies and modelling strategies to exploit the superior mechanical properties in the design stage of structural automotive lightweight components. The conventional in-plane forming limit curve, employed to assess part feasibility, fails to account for the delay in plastic instability due to bending and tool contact pressure and can lead to overly conservative product designs, especially in materials with low inherent formability. This research focuses on the characterization and methodology development to account for process and boundary conditions in acute localization in combined loading of sheet metals.

The ISO 12004-2 standard was followed for the baseline characterization of the stretching-dominated forming limits of the AA5182 and the DP980 AHSS. The non-linear strain path and higher limit strains in the Nakazima test, relative to the Marciniak test, are a natural consequence of the boundary conditions of the respective test method. A series of correction methods were applied to the Nakazima limit strains to linearize the strain path and to compensate for the triaxial stress state. The concept of phenomenological mapping under a constant in-plane stress ratio was shown to work reasonably well for the DP980 with its power law hardening characteristic but was problematic for the AA5182 with saturation-type hardening. Corrected limit strains for the AA5182 were sensitive to both the choice of the limit strain detection method and the hardening rate. Prediction of the *plane stress* forming limit curve (FLC) utilizing the phenomenological Modified Maximum Force Criterion (MMFC) correlated well with the Marciniak limit strains and the process-corrected Nakazima forming limits for the DP980. Key to avoiding artefacts associated with the shift of the $FLC_0$ is a constrained calibration of the constitutive model to reflect the plastic uniform elongation obtained in a tensile test.

The effect of a triaxial stress state on plastic instability was studied on a physical basis adopting the Hillier instability framework for the onset of instability. It was shown how commonly adopted instability criteria under plane stress loading are in fact special cases of the Hillier model under specific boundary conditions. Analytical solutions derived for triaxial loading revealed the explicit dependence of the boundary conditions upon plastic instability and highlighted the need to replace the traditional instability curve with a surface. Overall, a compressive normal stress caused an increase in limit strains for all studied boundary conditions. Highest formability gains were found for a contact pressure that proportionally evolves with the major in-plane stress. The formability increase in the presence of tool contact pressure between the phenomenological mapping criteria and the analytical solutions for plane strain tension only correlated for the proposed work-based mapping method and a hardening exponent of $n = 0.1$. An extension of the Hillier framework to diffuse localization was proposed in the Generalized Incremental Stability Criterion (GISC) that adopts the concept of neutral incremental stability to perform a quasi-stable transition

of the stress state to plane strain tension associated with the formation of an acute neck. It was revealed that the MMFC is in fact physically motivated and represents one special case of the GISC under approximately proportional loading or proportional stressing with a prescribed minor load.

The effect of out-of-plane loading with appreciable bending and tool contact pressure on the forming limits was characterized in an experimental test campaign comprising angular stretch-bend (ASB) tests and the VDA 238-100 tight radius V-Bend test. It was revealed that reliance upon the punch force for fracture detection in the V-Bend test may lead to inconclusive results since the punch force descends at large bend angles (>145°) as a consequence of the kinematic boundary conditions even in the absence of fracture. The proposed V-Bend stress metric mitigates inconclusive results by consideration of the geometric boundary conditions, punch force, and thinning of the cross-section. No new parameters were introduced such that the developed method is readily applicable to the VDA 238-100 test. A strain-rate based detection method was also considered as a local failure metric to detect lift-off of the specimen from the punch for both the 590R and the 270 Mild steel. Relative to the in-plane forming limit in Marciniak tests, forming limits for the 3rd Gen 1180 AHSS increased by a factor of approximately 2.6 in stretch-bending and by a factor of approximately five in tight-radius bending.

To account for the delay in plastic instability in the presence of through-thickness stress-strain gradients, a control algorithm was developed to resolve the evolution of the stress-strain state over the sheet cross-section. The effect of a superimposed contact pressure on the stress state in plane strain stretch-bending was derived on continuum level and shown to effectively shift the strain path from plane strain tension to positive minor strains for material layers within the cross-section. The convex layer remains in a state of plane strain tension. To capture the mechanics, plasticity-related equations were derived from general bending mechanics and coupled with the GISC framework. It was revealed that an incremental multi-layer modelling approach is required to properly capture non-monotonic straining of the lower cross-section when the sheet wraps around the punch. Application to the 3rd Gen 1180 AHSS demonstrated that the developed instability framework is able to capture the overall trend of the experimental limit strains.

A key outcome of this research is the understanding of the effect of a triaxial stress state and the importance of the boundary conditions on plastic instability. In particular, the analytical work to underline that the common assumption of a unique forming limit is fundamentally flawed and instead represents a forming limit surface are major accomplishments. Consideration of the combined effect of bending normal stresses and superimposed tool contact pressure in combined loading and implications upon acute necking limits constitute major novelties in sheet metal forming. The developed instability framework can be utilized by tool manufacturers to pursue a more aggressive product design as the part geometry can be tailored to the process window of the forming operation and costly tool re-cuts can be reduced.

## Acknowledgements

I would like to thank Prof. Butcher for giving me the opportunity to conduct research under his supervision. I sincerely appreciate your patience and enthusiasm as a teacher and researcher. I am particularly grateful for your empathy during the numerical development of the instability framework during the COVID-19 lockdown and our many math emails. You have shaped me to become the researcher I never envisioned I could be at the beginning of this journey.

I would like to thank Prof. Worswick for mentoring me from the very beginning of this journey, six years ago, when I came to Waterloo in 2015 with the intention to return "home" after my Master's degree. Thank you for your continuous faith in me and the many life lessons you provided me with. It was an honour to conduct and publish research with you.

Thank you to all the students, postdoctoral fellows, and research engineers/ associates in the Forming and Crash Lab. In particular, Dr. Imbert, thank you for your in-depth knowledge and advice – the lab without you would not be the same. Amir Zhumagulov, thank you for the many favors in the lab and your indestructible optimism, which made me smile in the moments I really needed it. Kenneth Cheong, thank you for being an amazing office mate and for the many V-Bend discussions. Advaith Narayanan, I am glad you joined us towards the end of my PhD. I am grateful for the many discussions and late night testing in the lab. Thank you, Dr. Joudaki, for your patience, the many math talks, and the UFC nights.

Edward Gutierrez, I cannot imagine what the AISI project would have been like without you. Your first term was challenging – for both of us – but you taught me how to be even more patient and that there is nothing that cannot be fixed with chocolate, ice cream, or fried chicken. I am incredibly grateful for meeting you on this long journey and will remember our late night and weekend shifts – Marciniak tests, your favourites. Timothy (Lei Wang) while being somewhat skeptical of trusting a first year student with my research, you proved me wrong. Your work attitude and enthusiasm are exceptional and it was a pleasure to work with you.

Eckhard Budziarek, I do not know what I would have done without you during the last six years. Your work in the lab has been priceless – as well as all the German dishes and snacks you have treated me with. Thank you for always being there. A special thanks to the lab technicians and technologists Andy Barber, Tom Gawel, and Richard Gordon as well as the EMS machine shop, in particular Rick Forgett, Mark Kuntz, Charlie Boyle, and Fred Bakker for all the rush machining orders and guidance. My sincere gratitude to the IT team, Mike Willson, Martha Morales, and William Penney for all the support and for recovering my

corrupted 6TB external hard drive. A special thanks also goes to the technologists in civil engineering, Richard Morrison and Douglas Hirst, for their support.

Thank you to those people who supported me during the ups and downs, my family and friends. Arshee, Kritika, Meghana, Nivedita and our newest addition, Ahana (Sabu) - I am incredibly blessed to have people like you in my life. Negar, I will always cherish our funny conversations and moments we had. I cannot thank you enough for truly believing in me and for being part of my life. Thank you Leah, Hossein, Yara, Malcolm, Melanie, Lisa, Aleena and Raphael – it is because of people like you that life is so much better.

Last but not least, I would like to acknowledge the financial support of the American Iron and Steel Institute and Honda Development & Manufacturing of America. In particular, I would like to thank Dr. Hesham Ezzat for his support and excellent project management as part of the B-Pillar research project, Mr. Jim Dykeman for the many discussions on V-Bend testing, Mr. Cameron O'Keeffe for assistance on the Honda cluster, and Mr. Neil Parker for sharing his vast knowledge of tool design and forming operations. I would like to thank the Deutscher Akademischer Austauschdienst (DAAD) for awarding me with the graduate scholarship for North America that led the way to my research at the University of Waterloo. Finally, I would like to express my gratitude to the University of Waterloo for awarding me with the International Doctoral award, one of five Ontario Graduate Scholarships available for international students in 2021/22, and the President Scholarship.

.

*Dedication:*

*To those who had faith in me*

# Table of Contents

## List of Figures

## List of Tables

## List of Abbreviations

AHSS .....Advanced high strength steel
AISI.....American Iron and Steel Institute
AKDQ.....Aluminum killed, drawing quality
ASB.....Angular stretch-bend tests
BH.....Bake-hardenable
BIW.....Body-in-white
BT .....Biaxial tension
CDR .....Critical distance rule
CGA .....Circle grid analysis
CMn .....Carbon Manganese
CP.....Complex phase steels
CSR.....Concave side rule
CxSR.....Convex side rule
DIC.....Digital Image Correlation technique
DP .....Dual-phase
FCC.....Face centered cubic
FE.....Finite-element
FLC .....Forming limit curve
$FLC_0$.....Plane strain point of the FLC
FLS.....Forming limit surface
Gen.....Generation
GFLC .....General Forming Limit Concept
GHG.....Greenhouse gas
GISC .....Generalized Incremental Stability Criterion
GV.....Generalized Voce
HDMA .....Honda Development & Manufacturing of America
HSLA .....High-strength low-alloy
iCSR.....Instantaneous concave side rule
IF .....Interstitial free
ISO .....International Organization for Standardization
LBF .....Linear best fit
MART.....Martensitic steel
MGV .....Modified Generalized Voce
MHS.....Modified Hockett-Sherby
MK .....Marciniak-Kuczynski
MMFC .....Modified Maximum Force Criterion
MPR.....Mid-plane rule
NLSP.....Non-linear strain path
ODE .....Ordinary differential equation
P .....Pressure
RD.....Rolling direction
PEPS .....Polar Effective Plastic Strain diagram

PHS .....Press-hardened steel
PST.....Plane strain tension
PLC .....Portevin-Le Chatelier
Q&P .....Quench and partitioning
RPP .....Rigid perfectly plastic
SFLC.....Stress-based forming limit curve
TBF .....Trip-assisted bainitic ferrite
TD .....Transverse direction
TRIP.....Transformation-induced plasticity
TWIP.....Twinning-induced plasticity
UE-p.....Plastic uniform elongation
UT .....Uniaxial tension
UTS.....Ultimate tensile strength
vM.....von Mises
VSGL .....Virtual Strain Gage Length
XSFLC.....Extended stress-based forming limit

## List of Symbols

$A_{ij}$ .....Contact areas (Hillier framework)
$a, b, c, d, f$ .....Calibration coefficients in the constitutive model
$C$ .....Ratio of equivalent plastic strain increment to the major strain increment
$\alpha$ .....Principal in-plane stress ratio
$\alpha_{VDA}$ .....VDA bend angle (V-Bend analysis)
$\alpha'$ .....Component stress ratio
$\alpha^{diff}$ .....Principal in-plane stress ratio at diffuse necking (linearized MMFC)
$\beta$ .....Ratio of the in-plane shear stress to the major stress
$\delta$ .....Kronecker delta
$d\gamma^p$ .....Plastic dimensionless shear deformation parameter
$dW^p$ .....Plastic work rate
$du_i$ .....Vector of applied displacement increments
$e_3$ .....Engineering thickness strain
$\tilde{\varepsilon}_{eq}^p$ .....Linearized equivalent plastic strain
$\varepsilon_{eq}^p$ .....Equivalent plastic strain
$\varepsilon_1, \varepsilon_2, \varepsilon_3$ .....Major, minor, through-thickness principal strain
$\tilde{\varepsilon}_1, \tilde{\varepsilon}_2$ .....Linearized major and minor strain
$\tilde{\varepsilon}_1^{MMFC}, \tilde{\varepsilon}_2^{MMFC}$ .....Linearized major and minor strains in the linearized MMFC
$\varepsilon_{el}^y$ .....Elastic strain at the onset of yielding of the neutral layer
$\varepsilon_1^b, d\varepsilon_1^b$ .....Major bending strain and increment
$\varepsilon_1^{mem}, d\varepsilon_1^{mem}$ .....Major membrane strain and increment
$\bar{\varepsilon}_1^{mem}$ .....Average major membrane strain of the cross-section
$E$ .....Young's modulus
$\eta$ .....Ratio of shear stress to tensile stress (utilized for shear conversion methodology)
$F$ .....Load (Hillier framework)
$F_x$ .....Horizontal punch force (V-Bend study)
$F_y$ .....Vertical (punch) force (V-Bend study)
$F_{res}$ .....Resultant force (V-Bend study)
$k$ .....Ratio of major stress to equivalent stress
$n, K, \varepsilon_0$ .....Calibration coefficients in the Swift hardening model
$h$ .....Hardening rate
$\kappa$ .....Sheet curvature
$\kappa_y$ .....Sheet curvature at the onset of yielding of the neutral layer
$\chi$ .....Principal resultant through-thickness stress ratio
$\chi_b$ .....Principal through-thickness stress ratio attributed to bending
$\chi_c$ .....Principal through-thickness stress ratio attributed to contact pressure
$\chi_{c,0}$ .....Prescribed principal through-thickness contact stress ratio on concave layer

$\chi_0$ .....Initial principal through-thickness stress ratio (Hillier framework)
$\tilde{\chi}, \hat{\chi}$ .....Evolving principal through-thickness stress ratio (Hillier framework)
$L_{m,x}$ .....Horizontal component of the moment arm (V-Bend analysis)
$L_0$ .....Half of the width of the roller gap including the roller radius
$\lambda$ .....Stretch-bend ratio
$M$ .....Bending moment
$N_i$ .....Normal vector
$\omega$ .....Principal through-thickness strain ratio
$r$ .....Radius arbitrary layer
$r_m$ .....Radius mid-plane layer
$r_{m,0}$ .....Radius initial mid-plane layer
$r_m^b$ .....Radius mid-plane layer in pure bending
$r_y,\ dr_y$ .....Radius convex layer and increment
$r_y^b,\ dr_y^b$ .....Radius convex layer in pure bending and increment
$r_i$ .....Radius concave layer
$r_u$ .....Radius unstretched layer
$r_n$ .....Radius neutral layer
$r_p$ .....Punch radius
$r_r$ .....Roller radius V-Bend set-up
$\rho,\ d\rho$ .....Principal in-plane strain ratio and increment
$\bar{\rho},\ d\bar{\rho}$ .....Average principal in-plane strain ratio of the cross-section and increment
$\rho^{\text{diff}}$ .....Principal in-plane strain ratio at diffuse necking (linearized MMFC)
$\Sigma$ .....Stress metric (V-Bend fracture detection method)
$\Sigma_{ij}$ .....Tractions (Hillier framework)
$s_{ij}$ .....Deviatoric stress components
$\sigma_{eq}$ .....Equivalent stress
$\bar{\sigma}$ .....Material flow stress
$\sigma_1, \sigma_2, \sigma_3$ .....Major, minor, through-thickness principal stress
$\sigma_{3,0}$ .....Compressive pre-stress (Hillier framework)
$\sigma_b$ .....Bending stress
$\sigma_{sb}$ .....Stretch-bending stress
$\sigma_c$ .....Contact pressure
$\sigma_y$ .....Yield stress
$t_0$ .....Nominal sheet thickness
$t$ .....Current sheet thickness
$t_{ref}$ .....Reference sheet thickness
$v$ .....Poisson's ratio
$w,\ dw$ .....Sheet width and increment
$\Delta w$ .....Change in the width of the entire cross-section

$w^p_{tensile}$ .....Plastic work per unit volume in tensile test

$w^p_{shear}$ .....Plastic work per unit volume in simple shear test

$x_n$ .....Variable to express location of current layer with respect to neutral layer

$\xi$ .....Dimensionless sheet thickness

$Y_1$, $Y_2$, $Y_3$, $Y_4$, $Y_5$ .....Parameters (analytical solutions for stretch-bend model, total strain formulation)

$z$ .....Critical subtangent (Hillier framework)

*"Without ambition one starts nothing. Without work one finishes nothing. The prize will not be sent to you. You have to win it."*

Ralph Waldo Emerson

# Synopsis of Thesis

## 1. Introduction

### 1.1 Motivation

Lightweighting has become a pressing topic in the automotive industry to meet legislative requirements to reduce greenhouse gas (GHG) emissions. Weight reduction in the body-in-white (BIW) has been identified as the key parameter with a predicted 29% BIW weight reduction adopting the 3-G approach of geometry, grade, and gauge optimization of advanced high strength steels (AHSS) (Zuldema, 2013). Selection of higher-strength steels can justify the adoption of a thinner sheet while maintaining or exceeding the mechanical strength for anti-intrusion of the passenger in a vehicle crash. Hot forming of press-hardened steels (PHS) can produce structural components of high strength and complex shape since forming occurs after solutionizing when the material is still soft followed by quenching. Despite its advantages, hot stamping processes can be more expensive due to relatively low cycle times and the infrastructure requirements compared to conventional cold stamping. Recent advances in cold forming have been focused on a new class of emerging steels, the 3rd Gen AHSS that feature high strength levels combined with superior ductility, which can form complex geometries in existing stamping lines (Billur and Altan, 2014c).

Nevertheless, an increase in material strength is usually accompanied with a reduction in the formability, which enforces constraints upon the product design (He *et al.*, 2013b). In the design of automotive lightweight components, the primary engineering tool to assess part feasibility has been the forming limit curve (FLC) based upon in-plane stretching. The International Organization for Standardization ISO 12004-2 (2008) outlines two test methodologies for experimental characterization of the forming limit strains, the Nakazima (Nakazima and Kikuma, 1967) and the Marciniak (1973) tests, schematically illustrated in **Figure 1a.** Despite the fundamental differences in the deformation mode – plane stress in-plane deformation in the Marciniak test and triaxial out-of-plane stretching in the Nakazima test – the FLC is commonly treated as a stationary metric to locally assess part feasibility. As depicted in **Figure 1b**, adoption of a global forming limit may not be representative of the local process conditions in a structural vehicle component with varying degrees of bending and stretching. The formability gain in the presence of bending and tool contact has been experimentally verified (Ghosh and Hecker, 1974; Till *et al.*, 2008; De Kruijf *et al.*, 2009; Kitting *et al.*, 2009; Barlo *et al.*, 2019) but cannot be exploited in the product design yet due to the lack of a framework to accurately account for the process conditions in the limit strain prediction. Selective efforts to model the delay in plastic instability due to the process conditions are limited owing to aggressive simplifications of the complexity attributed to bending mechanics and triaxial loading (De Kruijf *et al.*, 2009). Further complexity is added from the material side since bending locally induces

reverse loading effects (Crafoord 1970) that may alter the material response and manifest itself in the form of early re-yield (Bauschinger (1886) effect) and softening, summarized under kinematic hardening effects (Hasegawa and Yakou, 1975; Christodoulou *et al.*, 1986; Chung and Wagoner, 1986).

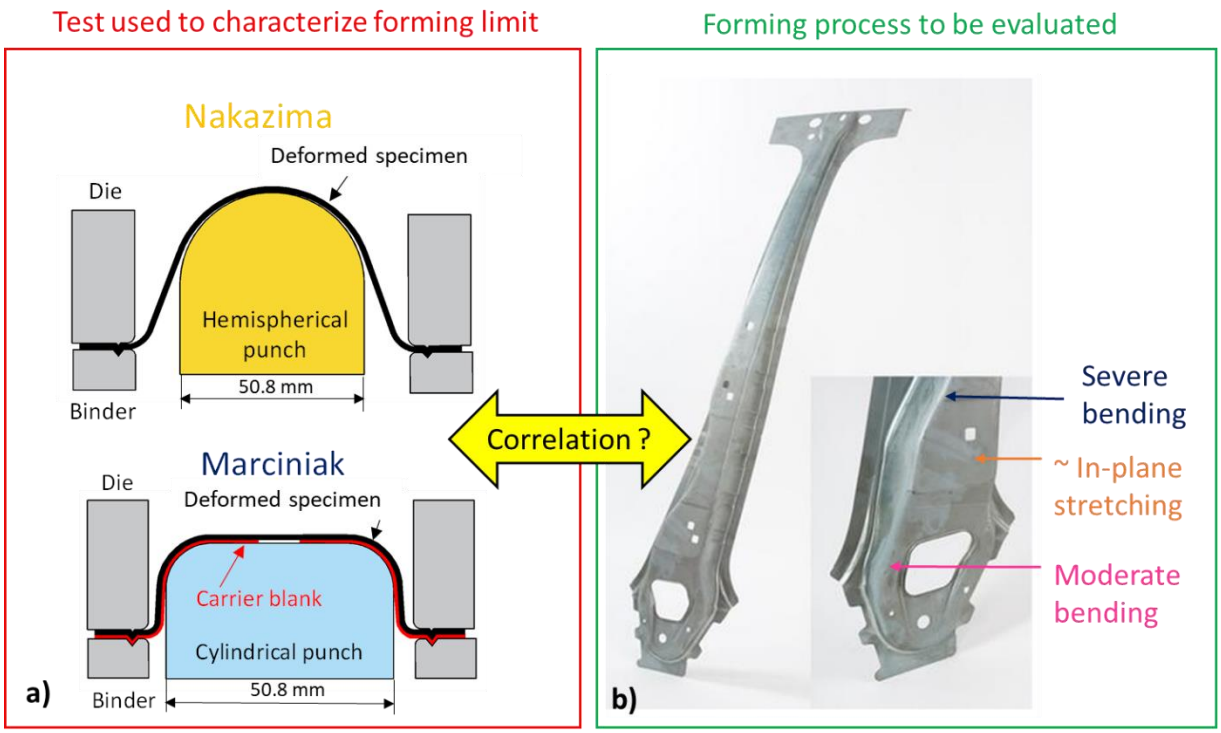


**Figure 1: Differences in boundary conditions between characterization tests utilized for the determination of the forming limits (ISO 12004-2, 2008) (a) and the local conditions of varying bend severity and stretching encountered in a forming process shown for a B-Pillar component (b) (adapted from Arcelor Mittal, 2020).**

The present thesis aims to address these gaps in the literature by developing a physically-motivated and mechanistic framework to analytically predict the instantaneous necking limits in sheet metal forming. An emphasis is placed upon resolving the through-thickness stress-strain gradients that arise due to combined loading of stretching with superimposed bending and tool contact pressure. Acute localization under a triaxial stress state is identified from a novel instability framework that considers the local conditions of the deformation process. In the scope of this thesis, a distinction is made between process conditions, which are concerned about the bend severity and tool contact, and the local boundary conditions attributed to how the loads and tractions are applied to deform the material, *e.g* a constant, proportional, or evolving contact pressure. The analytical framework will enable a rigorous evaluation of phenomenological techniques, which are currently employed to account for 3D stress states. The outcome of this research will provide an engineering tool for the local formability assessment in the design stage of automotive lightweight components.

## 1.2 Thesis Outline

A manuscript-based style has been adopted in this thesis. This entails a synopsis that contains a concise literature review to highlight current gaps upon which the objectives of the conducted research are based. Subsequent chapters entail a summary of the performed research, followed by the conclusion and recommendation. The conducted research to accomplish the immediate objectives outlined in Section 2.6.1 are presented in Chapter 3-6 and constitute distinct peer-reviewed articles, either published or under review. Details can be found in the appendices.

Appendix A: **Noder, J.,** Butcher, C., (2019a). A comparative investigation into the influence of the constitutive model on the prediction of in-plane formability for Nakazima and Marciniak tests, International Journal of Mechanical Sciences, 163, 105138, https://doi.org/10.1016/j.ijmecsci.2019.105138.

Appendix B: **Noder, J.,** Butcher, C. A General Instability Framework for Ductile Metals in Complex Stress States from Diffuse to Acute Localization, to be submitted, May 2022.

Appendix C: **Noder, J.,** Dykeman, J., Butcher, C., (2020a). New Methodologies for Fracture Detection of Automotive Steels in Tight Radius Bending: Application to the VDA 238-100 V-Bend Test, Experimental Mechanics, https://doi.org/10.1007/s11340-020-00597-2.

Appendix D: **Noder, J.,** Butcher, C. On the Influence of Tool Contact Pressure on Tensile Instabilities in Plane Strain Stretching and Bending of Sheet Metals, to be submitted, May 2022.

Additional publications stemming from this research, which are not the focus of the thesis but are referenced throughout, are:

Journal publications:

**Noder, J.**, Butcher, C. On the stress-state dependence of complex hardening behavior upon strain path reversal for a 3rd Gen AHSS, in preparation.

**Noder, J.**, Gutierrez, J.E., Zhumagulov, A., Dykeman, J., Ezzat, H., Butcher, C., (2021a). A Comparative Evaluation of Third-Generation Advanced High-Strength Steels for Automotive Forming and Crash Applications, Materials, 14, 4970, https://doi.org/10.3390/ma14174970.

**Noder, J.**, Gutierrez, J.E., Zhumagulov, A., Khameneh, F., Ezzat, H., Dykeman, J., Butcher, C., (2021b). Constitutive, Formability, and Fracture Characterization of 3rd Gen AHSS with an Ultimate Tensile Strength of 1180 MPa, SAE International Journal of Advances and Current Practices in Mobility, 3(3): 1395-1407, doi:10.4271/2021-01-0308.

Fast-Irvine, C., Abedini, A., **Noder, J.**, Butcher, C. (2021). An Experimental Methodology to Characterize the Plasticity of Sheet Metals from Uniaxial to Plane Strain Tension, Experimental Mechanics, https://doi.org/10.1007/s11340-021-00744-3.

**Noder, J.**, Abedini A., Butcher, C., (2020b). Evaluation of the VDA 238-100 Tight Radius Bend Test for Plane Strain Fracture Characterization of Automotive Sheet Metals, Experimental Mechanics, 60, 787-800, https://doi.org/10.1007/s11340-020-00597-2.

Gutierrez, E., **Noder, J.**, Butcher, C., (2020). Experimental Characterization and Deterministic Prediction of In-Plane Formability of 3rd Generation Advanced High Strength Steels, Metals, 10(7), 902, https://doi.org/10.3390/met10070902.

Abedini, A., **Noder, J.**, Kohar, C., Butcher, C., (2020). Accounting for Shear Anisotropy and Material Frame Rotation on the Constitutive Characterization of Automotive Alloys using Simple Shear Tests, International Journal of Mechanics of Materials, 103419, https://doi.org/10.1016/j.mechmat.2020.103419.

Rahmaan, T., **Noder, J.**, Abedini, A., Zhou, P., Butcher, C., Worswick, M.J., (2019). Anisotropic plasticity characterization of 6000- and 7000-series aluminum sheet alloys at various strain rates, International Journal of Impact Engineering, 103390, https://doi.org/10.1016/j.ijimpeng.2019.103390.

Conference paper and conference talks:

**Noder, J.**, Butcher, C., (2022). Novel instability framework to predict local formability in 3rd Gen AHSS B-Pillar technology demonstrator, Great Designs in Steel 2022, Michigan.

**Noder, J.**, Gutierrez, J.E., Zhumagulov, A., Khameneh, F., Dykeman, J., Ezzat, H., Butcher, C., (2021c). Constitutive, Formability, and Fracture Characterization of 3rd Gen AHSS with an Ultimate Tensile Strength of 1180 MPa, conference talk at SAE Conference 2021, virtual.

**Noder, J.**, Samadian, P., Dykeman, J., Abedini, A., Zhumagulov, A., Worswick, M.J., Butcher, C., (2021d). New Methods for Fracture Detection of Automotive Steels, ICTP Conference 2021, virtual, Forming the Future, The Minerals, Metals & Materials Series, https://doi.org/10.1007/978-3-030-75381-8_55.

**Noder, J.**, Butcher, C., (2021e). Fracture Detection in the VDA 238-100 Tight Radius Bend Test for Automotive Steels, Great Designs in Steel 2021, virtual.

Butcher, C., **Noder, J.,** Dykeman, J., Malcolm, S., Parker, N., Bowman, J., (2021). Virtual Design and Validation of 3rd Gen 980 and 1180 MPa B-Pillars, Great Designs in Steel 2021, virtual.

Gutierrez, J.E., **Noder, J.,** Parker, N., Bowman, J., Dykeman, J., Malcolm, S., Ezzat, H., Butcher, C., (2021). Formability Characterization of 3rd Generation Advanced High-Strength Steels and Application to Forming of a B-pillar, SAE Conference 2021, virtual, SAE Technical Paper 2021-01-0267, https://doi.org/10.4271/2021-01-0267.

Dykeman, J., **Noder, J.**, (2020). Local Formability and Fracture in Tight Radius Bending for Crash Applications, conference talk at the Fracture Symposium February 2019, Michigan.

Butcher, C., **Noder, J.**, Gutierrez, E., Ezzat, H., Dykeman, J., Bowman, J., (2020). Constitutive, Formability and Fracture for 3rd Gen AHSS with Application to a B-Pillar, conference talk at the Fracture Symposium February 2020, Michigan.

**Noder, J.**, Butcher, C., (2019b). New Methodologies for Fracture Detection in the 238-100 Tight Radius Bend Test, conference talk at NADDRG November 2019, Michigan.

**Noder, J.**, Butcher, C., (2019c). Prediction of In-Plane Formability and Process Corrections of AA5182 and DP980 in Nakazima and Marciniak Tests, conference talk at NADDRG April 2019, Michigan.

The research presented in this thesis is part of a larger research collaboration between the University of Waterloo, the Automotive Program of the American Iron and Steel Institute (AISI) and their member companies, and Honda Development & Manufacturing of America (HDMA). The overall aim of the project

was to characterize the mechanical properties of different 3rd Gen AHSS and develop methodologies to leverage the properties of 3rd Gen steels in the design of structural automotive components. The project scope comprised material characterization on coupon-level (*e.g.* quasi-static and dynamic constitutive response, kinematic hardening effects, formability and fracture limits, tribological behavior), the design and forming trials of a technology demonstrator representative of a full-size B-Pillar for a mid-size SUV, and dynamic impact testing to assess crashworthiness. The research as part of this thesis is focused upon the methodology development and contains some of the experimental characterization conducted on coupon level. It is noted that all studied 3rd Gen AHSS grades and the DP980 AHSS were provided by member companies of AISI under the condition that no microstructural investigations be conducted. This condition is because the AISI Automotive Program represents a consortium of steel suppliers working together in a non-competitive manner to conduct joint research. As a result, the details on the steel composition and microstructure are kept blind. All steels are commercially available.

# 2. Literature Review

This chapter provides a brief introduction to Advanced High-Strength Steels (AHSS) (Section 2.1), followed by a review on the state-of-the-art in formability characterization and prediction under in-plane stretching (Section 2.2) and combined loading of stretching with superimposed bending (Section 2.3). Fracture under plane strain tension, which represents the limiting deformation mode for sheet metals, is discussed in Section 2.4. A concise summary and current gaps in literature are presented in Section 2.5. The chapter closes with an overview of the research scope with details on the research objectives and tasks (Section 2.6).

## 2.1 Advanced High-Strength Steels

The design of lightweight automotive components has been spurred by the development of AHSS. The conventional high-strength low-alloy steels (HSLA), utilized for energy-absorbing structural components, have largely been replaced with higher strength AHSS. The first generation of AHSS, denoted as 1st Gen AHSS, consists of a martensitic microstructure with one to two additional phases for enhanced formability and strength for application to sill, A- and B-Pillar reinforcements. As demonstrated in **Figure 2a**, higher-strength steel grades such as press hardenable steels (PHS) for anti-intrusion components exhibit only a narrow forming window and require heat assistance in the form of hot stamping to form complex geometries (Billur and Altan, 2014a). This limitation was addressed in the second generation (2nd Gen AHSS) that provides substantial strength and formability gains from adopting an austenitic microstructure. However, the high degree of alloying elements required to obtain the microstructures and induce twinning-induced plasticity (TWIP) effects led to high costs and welding issues that ultimately hindered their adoption (Billur and Altan, 2014b). The development of the 3rd Generation of AHSS (3rd Gen AHSS) represents as a trade-off between the first and second class of AHSS. The chemistry and thermomechanical processing produces microstructures containing martensite, ferrite, and retained austenite. During plastic deformation, the metastable retained austenite undergoes a stress-state dependent phase transformation to martensite, providing additional hardening and delaying instability (Speer *et al*., 2003). As depicted in **Figure 2b**, the total elongation of the higher strength 3rd Gen 980 steel is comparable to the 590R AHSS while the 3rd Gen 1180 AHSS exhibits comparable or superior ductility to the conventional DP980. The two most common classes of 3rd Gen steels are quench- and partitioned (Q&P) steels and trip-assisted bainitic ferrite (TBF) steels. An overview of the microstructure and processing routes can be found in Nanda *et al.* (2019). As discussed in Noder *et al.* (2021a), the stress-state dependent fracture performance between two 3rd Gen 1180 MPa steels, designated as 3rd Gen 1180 V1 and V2, may vary considerably with different hardening characteristics as shown in **Figure 2b**.

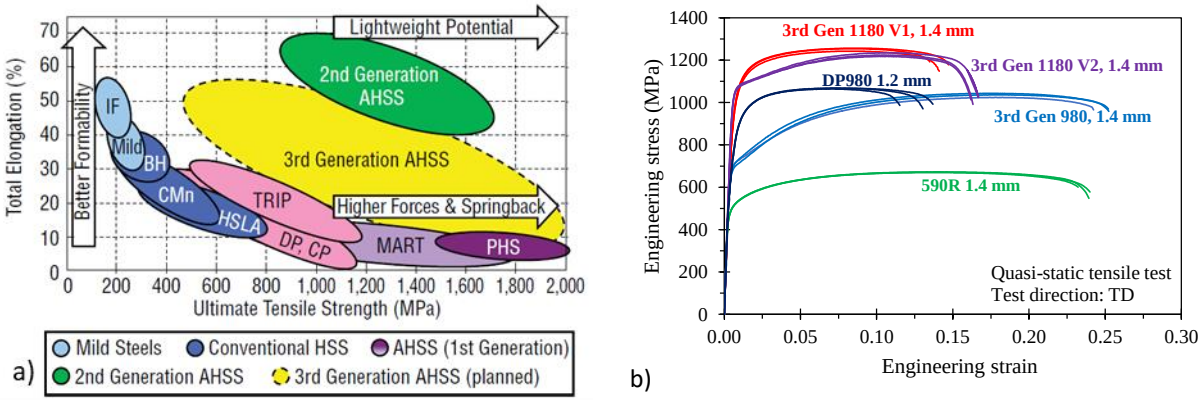


**Figure 2: Overview of the strength and ductility of different steel grades (Billur and Altan, 2014a) (IF = Interstitial free, BH = Bake-hardenable, CMn = Carbon Manganese, HSLA = High-strength low-alloy, TRIP = Transformation-induced plasticity, CP = Complex phase, DP = Dual-phase, MART = Martensitic, PHS = Press hardenable steels) (a) and performance comparison of selective 3rd Gen steels to conventional steels (Noder *et al.*, 2021a) (b).**

## 2.2 In-plane Formability: Characterization and Prediction

The classical tensile test remains one of the most important tests for material characterization of sheet metals but is limited to in-plane stretching and provides only limited correlation to the deformation modes found in forming and impact tests of structural components. As depicted in **Figure 3a,** a uniaxial tension test comprises two distinct stages of uniform stretching up to the strain level corresponding to the ultimate tensile strength (UTS) when a diffuse neck has formed. The width ($w$) of the instability zone initially corresponds to approximately twice the sheet thickness and collapses into a single plane when an acute neck has evolved (Maricniak *et al.*, 2002). The transition from a diffuse to an acute neck is reflected in the non-linearity of the strain path from uniaxial tension to a state of plane strain tension (zero minor strain increment) in **Figure 3b**. It is accompanied by a gradual transition to a triaxial stress state shortly after which fracture occurs. In the scope of this thesis, material instability is referred to as plastic instability that may either involve the formation of an acute or a diffuse neck. The ability of a material to deform homogeneously until the onset of tensile instability is defined as global formability whereas local formability is concerned with the fracture limits. Both formability metrics need to be considered in forming operations that often involve significant through-thickness strain gradients such as in bending-dominated forming operations when fracture may occur without a preceding neck (Schaeffler, 2017). It is important to emphasize that good global formability does not automatically infer good local formability and *vice versa* (Hance, 2016).

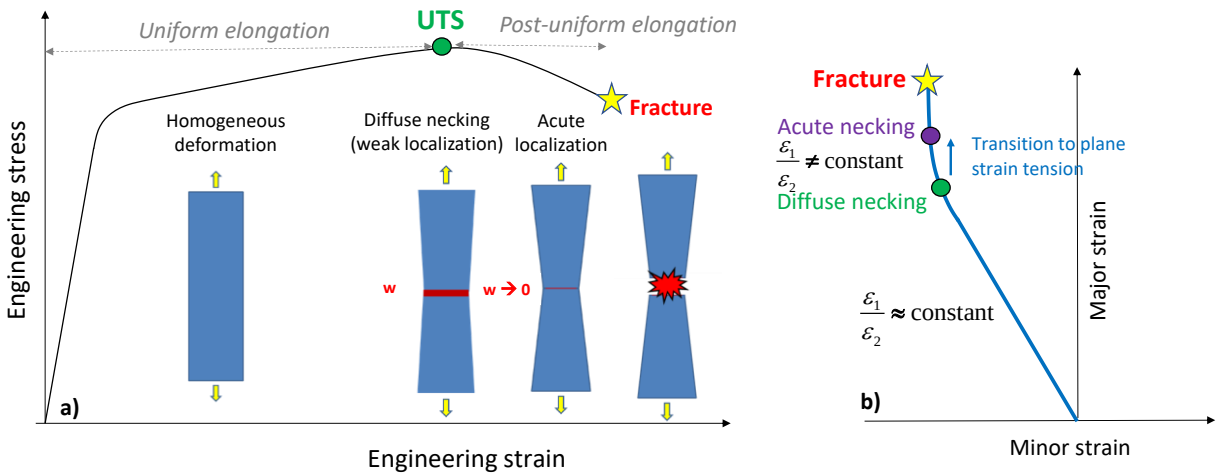


**Figure 3: Schematic of a stress-strain response obtained in a standard tensile test (a) and the transition of the strain path from uniaxial tension to a state of plane strain tension when an acute neck has formed (b).**

When discussing formability in the sheet metal forming literature, the term *proportional loading* is commonly used to refer to proportionality between the strain increment and stress state. A distinction is required in the present thesis to clarify that *proportional loading* corresponds to applying the forces proportionally according to load-control as in a hydraulic test frame. The surface tractions or stresses are not proportional as the geometry evolves with deformation. *Proportional stressing* refers to adjusting the applied force increments to compensate for the geometric change in a stress-control configuration. In analytical models of plastic deformation, proportional stressing is often obtained under strain-controlled boundary conditions, which simplifies the integration of the constitutive models.

### 2.2.1 Experimental Forming Limit Curve

The experimental characterization of the global forming limits dates back to the 1960s when Keeler and Backhofen (1963) and Goodwin (1968) performed stretch tests of various specimen widths using circle grid analysis (CGA). Necking limits were retrieved from post-test measurements of the deformed grid pattern, which had been etched onto the material prior to testing. The measured in-plane strain in the two principal directions was summarized in a major *versus* minor strain diagram ranging from uniaxial tension to equi-biaxial stretching that represents the traditional FLC depicted in **Figure 4a**. The part can successfully be formed if the strain remains below the FLC. In general, failure with respect to the FLC refers to the development of an acute neck and is not a fracture limit (Hendrick, 2017). The left side of the FLC is referred to as the "draw side" (owing to the negative minor strain that occurs in drawing operations) and loading conditions with a positive minor strain occur on the "stretch side". The $FLC_0$, represented by the global minima of the FLC, is the most critical loading condition since the material experiences a state of plane strain tension when the sheet thins by the same amount it is stretched in the primary loading direction. The diffuse and acute necking limits in plane strain are identical for a rate-independent material.

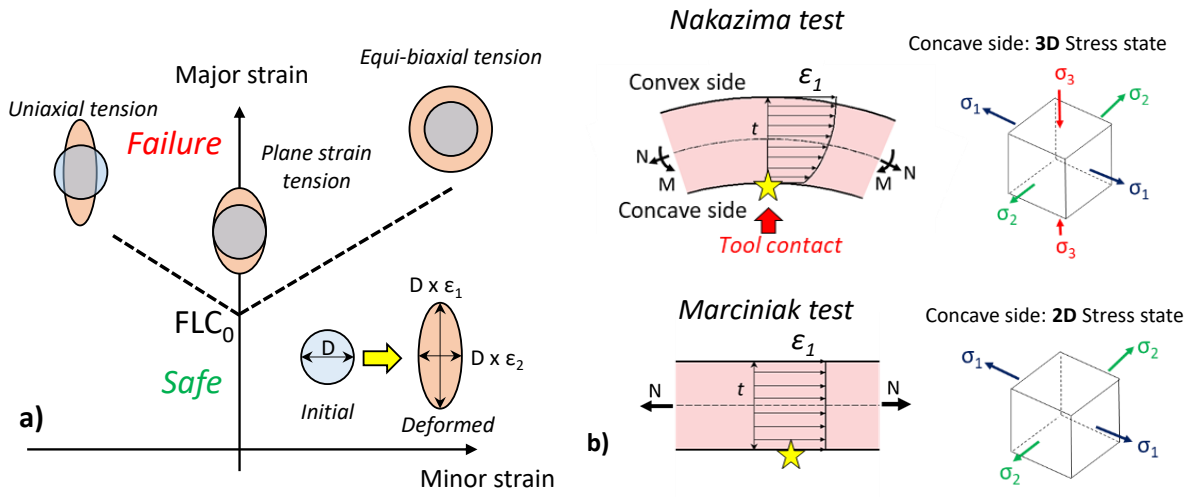


**Figure 4: Schematic of the forming limit curve for in-plane stretching (a) and resulting boundary condition of the sheet concave (inner) layer depending on the test method utilized to experimentally characterize the forming limit.**

The two fundamental test methodologies to characterize the forming limits are the Nakazima (Nakazima and Kikuma, 1967) and the Marciniak (1973) tests, schematically illustrated in **Figure 1a.** The punch geometry and resulting boundary condition represent a marked difference between the two test techniques. As a consequence of the hemispherical punch geometry in the Nakazima test, the strain history is non-linear and the material is stretched out-of-plane and induces a biaxial strain before transitioning to the target strain path. Punch contact causes a through-thickness stress gradient with a 3D (triaxial) stress state on the inner (concave) side, which transitions to a 2D (plane) stress state on the outer (convex) material surface, as illustrated in **Figure 4b**. Second-order effects are strain gradients due to curvature effects and through-thickness shear stresses caused by friction between the punch and the sheet specimen (Min *et al.*, 2016). Marciniak tests avoid these complications by using a cylindrical punch in addition to a carrier blank to approximately achieve in-plane deformation under a plane stress state. Marciniak tests are challenging from an experimental perspective since the strain path and fracture location can be sensitive to the carrier blank material, thickness, and hole size. Despite the apparent differences in the boundary conditions of the two test methodologies, the ISO 12004-2 (2008) standard treats both tests interchangeably for sheet thicknesses up to 4 mm, even though limit strains were reported to be different.

Ghosh and Hecker (1974) performed punch stretch tests for aluminum-killed steel, 70:30 brass, and cold-rolled aluminum and consistently reported higher limit strains, obtained from CGA, for out-of-plane deformation relative to in-plane stretching. More recent studies by Min *et al.* (2016) and Butcher *et al.* (2021) adopted 3D digital image correlation (DIC) and confirmed that differences in limit strains between the Nakazima and Marciniak tests are not caused by measurement uncertainties surrounding the use of

CGA. The use of DIC in Nakazima tests enables the local strain history to be measured revealing the non-linear strain path (Chen and Fang, 2018). Implications of the path-dependence of the strain-based FLC, depicted in **Figure 5a**, have been reported by many scholars (Hillier, 1966; Ishigaki, 1977; Kleemola and Pelkkikangas, 1977; Arrieux *et al.*, 1982; Graf and Hosford, 1993; Graf and Hosford, 1994; Stoughton, 2000). Effects of pre-strain on the subsequent forming limit are strongly dependent upon the type and amount of pre-strain and the stress state of the strain path (Graf and Hosford, 1993).

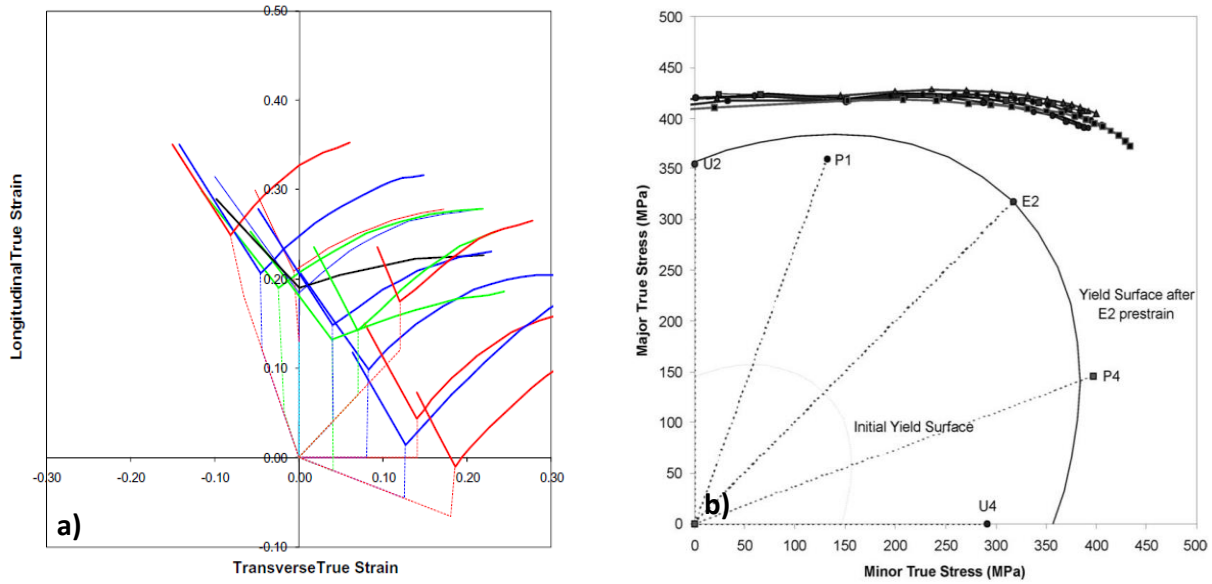


**Figure 5: Effect of path-dependence of the strain-based FLC for the 2008 T4 aluminum alloy (a) and transformation to the stress-based FLC that is approximately path-independent for isotropic hardening (Stoughton and Zhu, 2004) (b). The experimental campaign on the 2008 T4 aluminum alloy was conducted by Graf and Hosford (1993) who pre-strained the material under different loading conditions prior to performing forming limit tests.**

To remedy the shortcomings of strain-based FLCs, Hillier (1966) first proposed the concept of a stress-based forming limit curve (SFLC) that was later confirmed by Kleemola and Pelkkigangas (1977) and Arrieux *et al.* (1982). The advantage of a stress-based metric is that it is an instantaneous value unlike the total strain that accumulates differently based upon the strain path. The stress represents the current force with respect to the current area and thus provides a clear measurement of the material state. Stress-based representations are often described as path-independent and its unique dependence upon the stress state as shown in **Figure 5b**. The pre-strained forming limit curves in strain-space (**Figure 5a**) collapse to a single line (band) in stress space. While the approximate path-independence of SFLC has been theoretically verified (Zhao *et al.*, 1996; Stoughton, 2000), more recent experimental studies of Yoshida and Kuwabara (2007) revealed that the plane stress SFLC is only strictly path-independent for isotropic hardening. Despite its significant advantage over the strain-based FLC, the SFLC has received only limited acceptance since it requires the *a priori* calibration of a plasticity model and features poor resolution in differentiating stress limits at larger strains when the hardening rate becomes lower (Stoughton and Yoon, 2012). To remedy

these shortcomings, representation of the forming limit through the work-conjugate equivalent plastic strain was proposed by Müscheborn and Sonne (1975). Stoughton and Yoon (2012) proposed the Polar Effective Plastic Strain (PEPS) diagram using the equivalent plastic strain and an angle that tracks the direction of the plastic flow. An alternative approach to the SFLC was proposed by Volk *et al.* (2012) as the General Forming Limit Concept (GFLC) based on metamodeling and the transformation of a four-node element. Since the model calibration requires comprehensive experimental testing, Volk *et al.* (2012) justified the efforts through a potential applicability to various material thicknesses within the same material class but requires further validation.

### 2.2.2 Limit Strain Detection Methods

The widespread adoption of DIC has spurred the development of new limit strain detection methods. Recalling from **Figure 3**, necking is a gradual process making identification of the acute neck challenging. The various limit strain detection methods can be organized into three groups: (i) spatial methods concerned about the neck location and the strain distribution, (ii) time-dependent methods that monitor the evolution of the instability, often in terms of the strain rate, and (iii) combined tempo-spatial techniques. The ISO 12004-2 standard is a spatial method based upon the work of Bragard *et al.* (1972) who used CGA and fitting of quadratic functions to reconstruct the strain distribution from the fractured samples. As schematically illustrated in **Figure 6a** for the use of DIC, an inverse parabola is fitted through the strain distribution extracted from a line perpendicular to the crack, one image prior to fracture. The forming limit strain is identified from the corresponding maxima of the parabola. DiCecco *et al.* (2016) highlighted complications with the ISO 12004-2 method for asymmetric strain distributions that can lead to a malformed parabola and underestimate limit strains as shown in **Figure 6a** for an AA6013-T6 aluminum alloy tested at 250°C. Volk and Hora (2011) proposed a time-dependent technique, termed Linear Best Fit (LBF) method that tracks the thinning strain rate evolution inside the neck as depicted in **Figure 6b**. Necking is identified from the intersection of two line fits through the stable and unstable thinning strain rate inside the instability band. The fitting window for the line fits is arbitrarily selected to start from a specific image until the least square differences are met. The method of Merklein *et al.* (2010) performed regression analysis on major strain rate to identify the limit strain. Huang *et al.* (2008) and Situ *et al.* (2006, 2011) proposed using the evolution of the second time derivative of the major strain but was reported by Martinez-Donaire *et al.* (2014) to overestimate the forming limits. Motivated by the experimental observation of a sudden local change in the curvature, which will eventually evolve to an acute neck, spatio-temporal models have been proposed (Wang *et al.*, 2014; DiCecco *et al.*, 2016; Min *et al.*, 2017a,b).

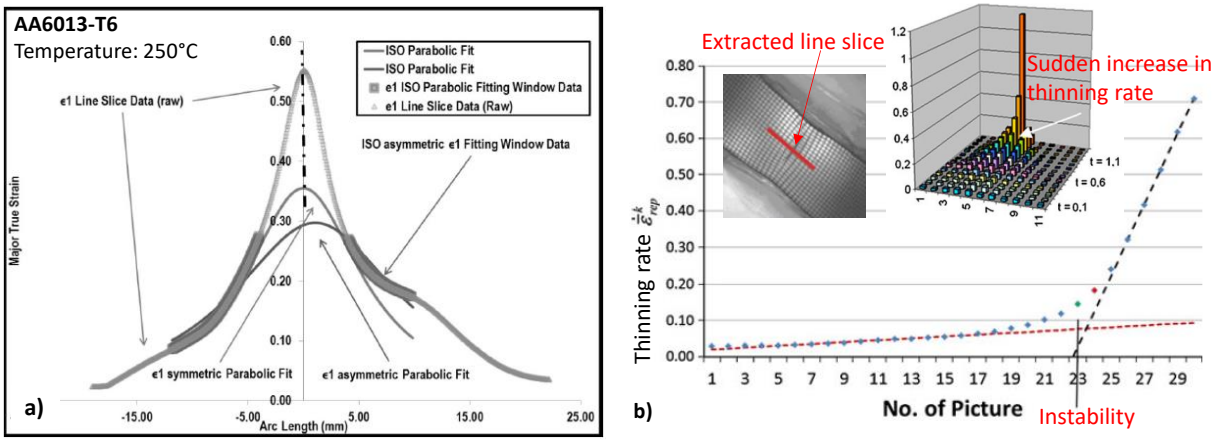


**Figure 6: Inverse parabola fit in the ISO 12004-2 method for identification of the forming limit strain (DiCecco *et al.*, 2016) (a) and identification of plastic instability using the LBF Method of Volk and Hora (2011) (b).**

### 2.2.3 Analytical FLC Models for In Plane-Plane Stress Loading

The experimental characterization of formability is costly and time-consuming particularly if alternative process parameters such as temperature, strain-rates, and strain paths are explored. Analytical models become necessary to predict formability in other process conditions and are reviewed for continuum-based approaches. There exists a wealth of literature on analytical models, however, the majority of them are strictly limited to in-plane stretching under a plane stress state that are only consistent with Marciniak limit strains. Historically, the plane-stress models have been compared and calibrated using Nakazima test data (Hora *et al.*, 2013; Pham *et al.*, 2018; Wang *et al.*, 2020). The use of Nakazima limit strains can provide apparent disagreement with the model predictions and introduce calibration biases into models as shown by Butcher *et al.* (2021).

Considère (1885) identified the onset of diffuse necking in a tensile test based upon the maximum load when the rate of the material hardening can no longer balance the thinning rate of the sheet cross-section as illustrated in **Figure 7a**. Dorn and Thomsen (1947) applied this criterion to stress states beyond uniaxial tension while Swift (1952) extended the maximum load theory to biaxial loading conditions in proportional stressing. Hill (1952) recognized the limited applicability of the diffuse necking models for practical forming applications, which are usually compromised by acute necking. Hill (1952) postulated that localization in uniaxial stretching would occur in the so-called “zero extension” direction in the plane of the sheet where a plane strain condition exists. Bressan and Williams (1983) extended the model of Hill (1952) for biaxial stretching when the zero extension direction exists in the through-thickness direction but not within the sheet plane.

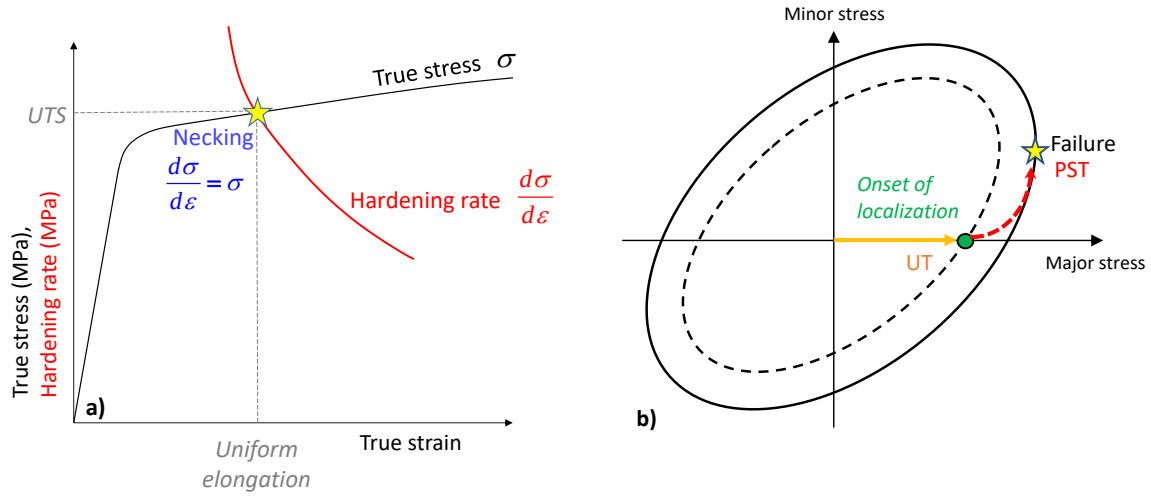


**Figure 7: Schematic to illustrate identification of diffuse necking in uniaxial tension following the Considère Criterion (a) and illustration of acute necking in the MMFC of Hora *et al.* (2013) (b). An incremental transition of the strain and stress state from uniaxial tension (UT) to plane strain tension (PST) delays localization.**

The pioneering work of Marciniak and Kuczynski (1967), hereinafter referred to as MK model, and further developed by Hutchinson and Neale (1977a, b) is most commonly utilized to predict formability. Localization occurs in a narrow band triggered by a thickness inhomogeneity, denoted as thickness imperfection factor. An acute neck has formed when the strain rate within the localization band relative to the homogeneous material has reached a threshold factor of usually ten (He *et al.*, 2013a). The major drawback of the MK model is the sensitivity of predicted forming limits upon the thickness imperfection factor (Tadros and Mellor, 1978; Shi and Gerdeen, 1991; Ratchev *et al.*, 1994; Zhang *et al.*, 2014; Lang *et al.*, 2015), which is utilized as a calibration parameter to make the FLC correlate with the experiments. The experimental study of Azrin and Backofen (1970) revealed that there appears to be little physical evidence in the form of surface imperfections to justify the magnitude of the reported imperfection factor in the MK model. Further complications may arise by the strong dependence upon a strain-rate dependent constitutive model to generate realistic limit strains on the draw side (Hutchinson and Neale, 1977b). In addition, the yield surface shape between plane strain and equi-biaxial tension was shown to markedly influence the shape of the predicted FLC (Lian *et al.*, 1989).

A more applied approach was proposed by Hora *et al.* (2013) in the Modified Maximum Force Criterion (MMFC). The MMFC also identifies localization from the transition of the strain path to plane strain tension analogous to the MK framework but does not enforce geometric boundary constraints in the form of a localization band. Diffuse necking is determined from the maximum load criterion of Dorn and Thomsen (1947) followed by an incremental transformation of the strain path and stress state inside the neck to a state of plane strain tension when an acute neck has formed (shown in **Figure 7b**). The rate of change of the strain path towards the maxima of the yield function (plane strain tension) effectively acts as a source

of secondary hardening to compensate for unstable material hardening to maintain stability. The faster the hardening rate of the material decreases after the peak load, the faster the transition to plane strain tension and acute necking. In contrast to the MK model, the MMFC is entirely mechanistic and only requires the hardening model and yield function. Despite the more rigorous treatment of localization within the MK model, it has been demonstrated that the MMFC provides predictions of similar accuracy for AISI 439, DC05 (Manopulo *et al.*, 2015) and AA6016 (Shen *et al.*, 2018) or superior accuracy for AHSS (Butcher *et al.*, 2021; Gutierrez *et al.*, 2020). The primary limitation of the MMFC lies in its restriction to plane stress and principal loading such that it neglects contact pressure effects and cannot distinguish between tensile and shear loading.

## 2.3 Out-of-Plane Formability: Characterization and Prediction

For stretching-dominated forming operations with deformation primarily limited to in-plane stretching, the FLC provides a reasonable estimate for the material necking limit (Stoughton and Yoon, 2011; Gutierrez *et al.*, 2021). Application of the same FLC to a forming operation with combined loading of stretching with superimposed bending leads to overly conservative forming predictions, which enforces unnecessary constraints upon the product design. The margin of error is particularly small for AHSS with limited formability windows and a large safety margin may lead to the component not appearing feasible (Geoffroy *et al.*, 2007; Till *et al.*, 2008; Atzema *et al.*, 2010; Gutierrez *et al.*, 2021). As noted by Stoughton and Yoon (2011) and Allwood and Shouler (2009), the material forming limit is an instantaneous metric governed by the process conditions. The following discussion focuses on experimental methodologies and analytical models to identify the material limit under combined loading conditions of stretching with superimposed bending.

### 2.3.1 Stretch-bend Experiments

Angular stretch-bend (ASB) tests, as depicted in **Figure 8**, are conducted to characterize the limit strains at higher bend severities and a varying degree of superimposed stretching. The hemispherical punch in the Nakazima test is replaced with a cylindrical single-curvature punch with smaller radii and the die set opening is rectangular instead of circular. The material is constrained from draw-in while the clearance (size of die opening) and choice of punch radii are varied to achieve different bend severities and contact pressure. The latter two process effects are intertwined such that a smaller bend severity (ratio of punch radius to sheet thickness denoted as $r/t$) infers a smaller contact area and thus leads to an increase in the contact pressure. It is noted that the geometric bend severity cannot differentiate between the relative amounts of stretching and bending.

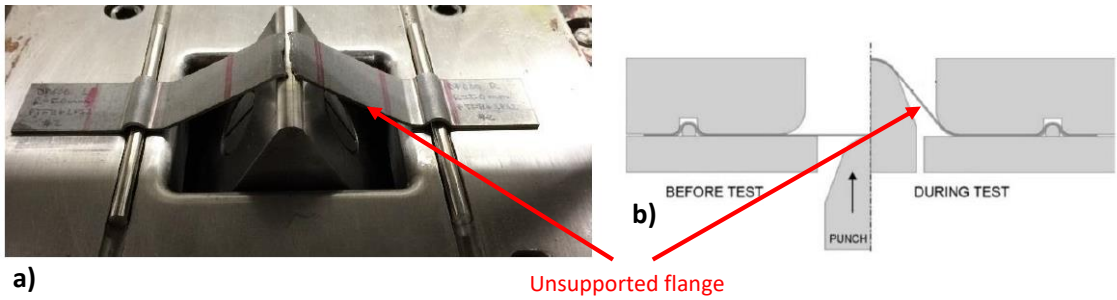


**Figure 8: Stretch-bend set-up (a) and schematic (b) adapted from Neuhauser *et al.* (2016). Depending upon the bend severity and sample geometry, premature failure can occur on the unsupported flange where deformation is approximately in-plane stretching.**

Motivated by the findings of Ghosh and Hecker (1974), who measured higher limit strains for out-of-plane than for in-plane deformation, Charpentier (1975) performed a comprehensive study utilizing five different punch geometries ranging from cylindrical with a flat tip to hemispherical and elliptical. For hot rolled AKDQ steel, the forming limit strains increased with increasing punch curvature. Demeri (1981) experimentally studied the effect of the sheet thickness on the limit strains for AK steel, DP80 steel, and HSLA-F50 steel and found that the forming limit increased as a function of the sheet thickness for stretching-dominated deformation but decreased for bending-dominated scenarios. Zadpoor *et al.* (2011) came to a similar conclusion in pure bending of 2024-T3 and 7075-T6 aluminum alloys and explained the phenomenon through lower bending normal stresses, reduced through-thickness strain gradients, and larger frictional forces for thicker sheet gauges. Interestingly, the failure strains for pure plane strain bending were found to be higher than the limit strains in uniaxial tension indicating suppression of necking. Cheong (2018) performed a comprehensive ASB study on DP980 and AA5182 with punch radii of 0.4 to15 mm. Material indentation was reported for punch radii smaller than 2 mm – a common complication encountered for sharp punch radii as reported by Kitting *et al.* (2009). A further complication arises from an intertwined effect of an increase in bend severity with a simultaneous shift in the strain path as reported by Kitting *et al.* (2010) and Cheong (2018).

In ASB tests, the strain distribution is always parabolic due to the shape of the punch. Consequently, the ISO 12004-2 method is not applicable as its inverse parabolic behavior was developed based upon in-plane stretching when deformation is uniform prior to localization (Centeno *et al.*, 2014; Lopez and van den Boogard, 2011). Instead, temporal methods have widely been adopted in literature for tests with through-thickness stress gradients (Neuhauser *et al.*, 2018; Cheong, 2018; Martínez-Donaire *et al.*, 2014). The limit strains under combined loading can be experimentally identified on the convex surface but the deformation history of the underlying material, the amount of stretch-bending, and the contact pressure evolution that give rise to the neck formation remain unclear. The challenge is how to generalize the results to the myriad of possible stretch-bend scenarios in a forming operation.

### 2.3.2 Instability Modes

The wealth of literature on the experimental characterization of formability provides valuable insight into the effect of bending but there is a paucity of research on the physics to predict the limit strains in practical applications. To understand localization in the presence of a through-thickness stress gradient, it is convenient to discretize the sheet thickness into infinitesimal layers. For in-plane stretching (see **Figure 9a**), *e.g.* in Marciniak tests, all layers are stretched uniformly and will reach the necking instability at the same point in time. In the case of combined loading with mild bending (see **Figure 9b**), *e.g.* in Nakazima tests, bending strains are superimposed to the in-plane membrane strains due to stretching and the strain evolution on the concave side is delayed. For combined loading with appreciable bending, as depicted in **Figure 9c**, the induced compressive bending strains can no longer be balanced by the tensile membrane stains. As a result, a severe strain gradient manifests through the sheet thickness with compression on the concave side and tension on the convex side (Morales-Palma *et al.*, 2013; Tharrett and Stoughton, 2003). From a theoretical perspective, the formation of a neck appears unlikely if the bending strains are larger than the membrane strains since the resultant strain path on the concave layer remains compressive (Tharrett and Stoughton, 2003). Fracture without necking is most likely in this scenario such that the limit strains are the fracture strains.

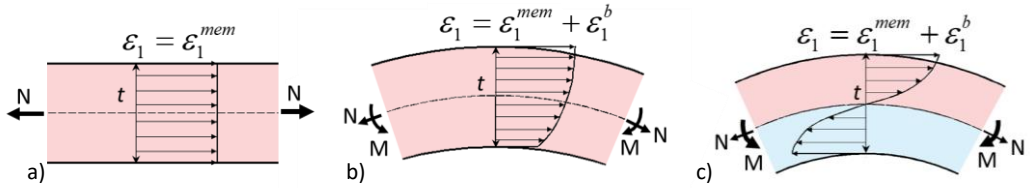


**Figure 9: Through-thickness strain distribution for (a) in-plane stretching, (b) stretching with mild bending superimposed, and (c) appreciable bending with mild stretching.**

The so-called Mid-Plane Rule (MPR) represents the conventional practice to account for the through-thickness strain gradient. In pure bending, the strain at the mid-thickness, which approximately corresponds to the neutral layer, is neglected. Thus, in theory, the strain history on the mid-plane in stretch-bending represents in-plane stretching. Tharrett and Stoughton (2003) argued that the MPR is overly conservative and postulated the Concave-Side Rule (CSR) advocating that necking only occurs if all material layers exceed the limit strain for in-plane deformation. Since tensile strain accumulation is delayed on the concave layer, the formation of an acute neck on the convex layer is essentially governed by the strain path on the concave layer. The CSR provides a simple and intuitive way to interpret formability but there remains debate within the literature on the universality of the CSR to arbitrary bend severities (Kitting *et al*., 2009; Vallellano *et al*., 2010; Neuhauser *et al.*, 2016). Instead of relying on a single layer, Vallellano *et al.* (2010)

and Morales-Palma *et al.* (2013, 2017) introduced the concept of the critical distance rule (CDR). Damage accumulation is considered over a specified material volume or critical distance, approximated from the alloy grain size (Morales-Palma *et al.*, 2013) or calibrated to formability data (Morales-Palma *et al.*, 2017). The models of Morales-Palma *et al.* (2013, 2017) identified necking from a combination of the CSR and CDR whereas abrupt fracture without a preceding neck was governed by the damage evolution on the convex surface, summarized in the convex side rule (CxSR). The predictive capability of their analytical model was limited to bend severities smaller than four times the sheet thickness since through-thickness normal stresses were not accounted for (Morales-Palma *et al.*, 2013). These limitations were partly addressed in a more recent publication of Morales-Palma *et al*. (2017) by consideration of bending normal stresses whereas tool contact stresses were still neglected. Although the CDR is attractive, it currently represents a material-specific calibration parameter that must be identified *a priori*. As with the MK model, its formability predictions hinge upon first calibrating the model to formability data.

### 2.3.3 Mechanics of Stretch-bending

The through-thickness stress-strain distribution must be considered in the modelling strategy to predict the instantaneous forming limit in general loading conditions. The mechanics of pure plane strain bending are well-established in the literature and first reviewed followed by modelling strategies to superimpose stretching.

The mechanics of bending (Hill, 1950) are described in **Figure 10** where the sheet cross-section is defined by the convex, $r_y$, and concave layer radius, $r_i$, respectively. The radius of the mid-layer, $r_m$, is located at half the sheet thickness and evolves with deformation. Initially, the radius of the sheet mid-layer, $r_{m,0}$, coincides with the radius of the neutral layer, $r_n$, defined as the layer with a vanishing major strain increment. The unstretched layer, $r_u$, is the layer whose length change is zero as the tensile and compressive strains balance. The neutral layer divides the sheet cross-section into distinct regions of the material layers that are elongated in tension (Zones I and Zone III) and the layers that thicken in compression (Zone II). With continued bending, the cross-section thins and the neutral layer shifts towards the concave side creating a load reversal as compressive layers become loaded in tension between the initial mid-layer radius, $r_{m,0}$, and the neutral layer (Zone III). As a consequence, complex kinematic hardening effects can be triggered and affect the overall response of the cross-section (Crafoord, 1970; Tan *et al.*, 1995; Zang, 2014). Accounting for these effects adds considerable complexity since the loading history of each layer of the cross-section has to be traced out separately in a multi-layer framework.

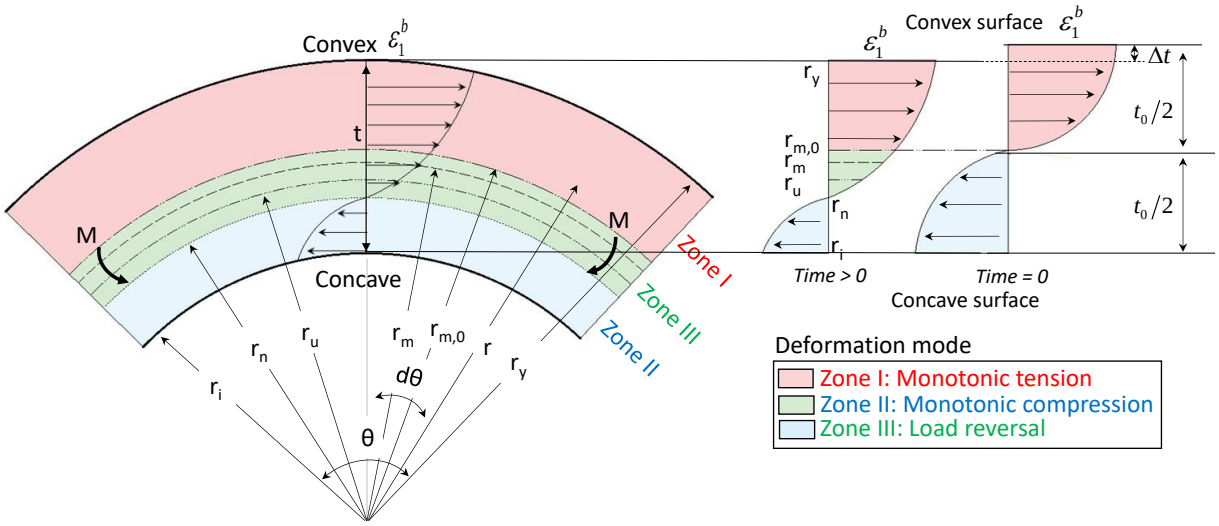


**Figure 10: Schematic of adopted terminology in bending mechanics and the evolution of the through-thickness distribution of the major strain during pure bending in the absence of tool contact pressure.**

The traditional theory of bending mechanics, pioneered by Ludwik (1903) was further developed by Wollter (1950), Lubahn and Sachs (1950), Hill (1950), and Proksa (1958, 1959) to account for sheet thinning, the shift in the neutral layer, and normal (radial) stresses. The foundational assumptions of pure bending and plane stress on the concave layer greatly limits their practical application since the process conditions of superimposed bending to stretching and tool contact pressure are not considered. In particular, the convenient total strain formulation is deeply problematic since accurate description of the complex hardening behavior requires an incremental approach. Kinematic hardening effects are either neglected or aggressively simplified (Crafoord, 1970; Dadras and Majlessi, 1982; Tan *et al.*, 1995). Engineering bending models have been preferred for industrial application due to their flexibility and simplicity (He *et al.*, 2013c) but introduce many simplifications such as setting the neutral layer equal to the sheet mid-plane, assuming a constant sheet thickness, and neglecting normal stresses. These approximations are only reasonable for pure bending (no tool contact) with bend severities of approximately $r_m / t > 10$ (Yu and Zhang, 1996). It is important to note that pure bending in plane stress does not arise in metal forming operations. Bending is caused by tool contact or in loading scenarios akin to three or four-point bending as in the V-Bend test. Pure bending in plane stress can only be obtained in laboratory tests with specialized fixtures to apply a bending moment to the sample ends during air-bending (Crafoord, 1970; Govindasamy, 2015).

Superposition of membrane stretching to bending adds another layer of complexity to the mechanics since the amount of stretching and bending governs the nature of the stress state (tensile or compressive) and the severity of the gradient that manifests over the cross-section. If deformation involves sufficient stretching (**Figure 11a**), the entire cross-section is under a tensile stress state and tensile instabilities may develop. Mathematically, the unstretched and neutral layer are located outside of the sheet thickness (layer

radii are smaller than the radius of the concave layer). In contrast, if bending is dominating and stretching is rather mild (**Figure 11b**), the lower part of the cross-section remains in a compressive stress state and necking is suppressed. In practice, the deformation mode is often a combination of both such that bending is dominating until the sheet has mostly wrapped around the punch when the deformation mode transitions to primarily stretching with mild bending. Thus, the neutral and unstretched layer may be located within or outside of the sheet cross-section.

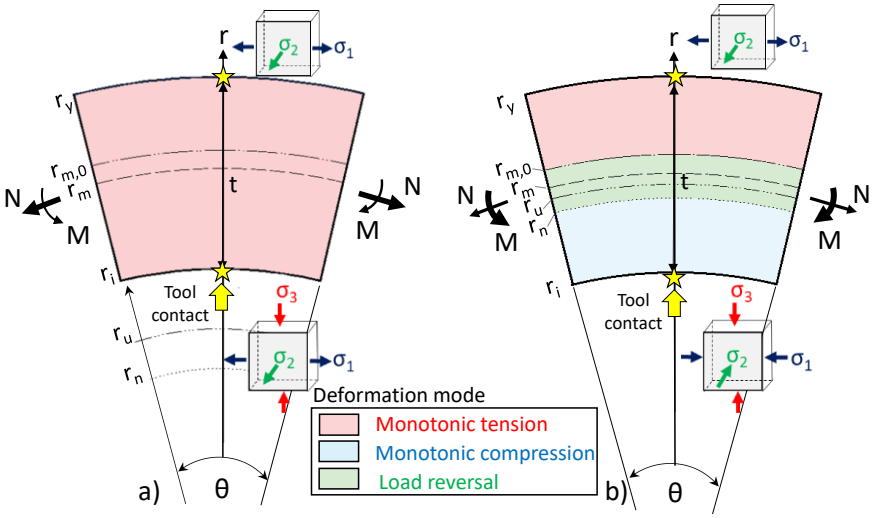


**Figure 11: Schematic of the cross-section and adopted terminology in combined loading considering severe stretching with mild bending (a) and mild stretching with severe bending (b).**

The transition of the deformation mode from bending to stretching essentially introduces non-monotonic straining (reversal from compression to tension) for material layers located in the lower half of the cross-section, requiring an incremental solution method. To avoid these complications, the mechanics of stretch-bending are commonly simplified to bi-linear loading in the two-stage model. The deformation history is decoupled into two distinct stages of (i) pure bending with a constant sheet thickness and a stationary neutral layer, followed by (ii) stretching with a constant curvature of the concave layer and sheet thinning (Vallellano *et al.*, 2010; Morales *et al.*, 2013; He *et al.*, 2013a,b). The simplicity of the approach is attractive but the study of De Kruijf *et al.* (2009) highlighted that de-coupling of simultaneous stretch-bending into two sequential stages fundamentally affects the predicted material response. Finite-element (FE) simulations revealed that pre-stretching prior to bending resulted in the absence of necking as the inner layer would always be in compression. Pre-bending prior to stretching resulted in premature necking since the material hardening capability was mostly exhausted during the bending stage leading to a low work-hardening rate during stretching and the onset of necking. Thus, for accurate prediction of the material under combined loading, it is paramount that stretching and bending effects be considered simultaneously.

### 2.3.4 Contact Pressure Models

In the presence of tool contact, the normal (through-thickness) stress distribution in bending is superimposed with an additional normal stress component. Contact pressure effects are commonly neglected within the literature by restricting the analysis to moderate bend severities (Xia and Zeng, 2008; Vallellano *et al.*, 2010; He *et al.*, 2013a,b; Morales-Palma *et al.*, 2013, 2017). In MK-based models it is common practice to assume a constant pressure (Nurcheshmeh and Green, 2012; Assempour *et al.*, 2010; Zhang *et al.*, 2014), which is seldom encountered in metal forming. Allwood and Shouler (2009) estimated the contact pressure utilizing the measured punch force and an approximated contact area whereas He *et al.* (2013c) and Stoughton and Yoon (2011) relied upon FE analysis.

The studies of Min *et al.* (2016), Ma *et al.* (2016, 2018), and Wang *et al.* (2019) adopted force equilibrium over the sheet cross-section to approximate the contact pressure utilizing the *average* major in-plane stress in a so-called homogenized model. Evolving normal stresses due to bending were neglected. Depending upon the assumption of the through-thickness evolution of the contact pressure, the magnitude of the contact pressure can drastically vary. For a linear distribution (Wang *et al.*, 2019; Ma *et al.*, 2018) the contact pressure increased by a factor of two compared to the method of Min *et al.* (2016) and Ma *et al.* (2016) who neglected the through-thickness distribution. Presently, there has been no rigorous validation of the above models for the contact pressure magnitude and its through-thickness distribution such that the applicability to a forming operation remains uncertain. In a recent publication of Meya *et al.* (2019) who introduced the concept of radial stress superposed bending (bending with forces applied on the convex and concave specimen side), the contact pressure was approximated from the elastic theory of Hertz (1881) with a quadratic distribution. Normal bending stresses, sheet thinning, and reverse loading effects were neglected in the simplified bending mechanics model. Compared to the FE solution, the simplified analytical model showed some deviations in the presence of tool contact and for higher punch forces. While these studies have provided limited validation of the contact pressure in sheet metal forming, the question of how to incorporate the contact pressure in a stretch-bend model that accounts for evolving normal stresses, the shift in the neutral layer, and thinning of the cross-section remains an open question.

### 2.3.5 Instability under a Triaxial Stress State

Accounting for tool contact pressure is imperative in the accurate description of the stretch-bending process but introduces a triaxial stress state on the concave layer that inhibits the use of the plane stress instability models discussed in Section 2.2.3. In the literature, phenomenological approaches based upon assumed mapping criteria between plane stress and triaxial stress states are employed (Smith *et al.*, 2003; Matin and Smith, 2005; Simha *et al.*, 2007, 2008; Min *et al.*, 2016). Analytical solutions for triaxial stress

states have been overlooked, likely due to the focus upon the acute necking limits in contrast to the onset of instability – diffuse necking for tensile stress states – where solutions can be obtained (Hillier, 1963).

The fundamental assumption in phenomenological mapping approaches rests upon the plane stress FLC being a universal material property that can describe tensile instability in general triaxial stress states. It is an attractive concept to formability engineers since the plane stress FLC is typically available while the triaxial formability limits are absent. In mapping-based models, the in-plane stresses and strains in triaxial loading are related to the plane stress limit strains. The limit strains can be mapped between stress states by assuming either a constant in-plane principal stress ratio ($\alpha = \sigma_2 / \sigma_1$) as proposed by Smith *et al.*, (2003) or constant in-plane principal strain ratio ($\rho = d\varepsilon_2 / d\varepsilon_1$) by Matin and Smith (2005). As depicted in **Figure 12a**, the stress-based mapping of Smith *et al.* (2003) predicted formability gains on the order of 500% for a hardening exponent of 0.2 and a through-thickness stress ratio ($\chi = \sigma_3 / \sigma_1$) of -0.45 that were later invalidated in double-sided high-pressure hydraulic bulge tests by Matin and Smith (2005). The strain-based mapping of Matin and Smith (2005) in **Figure 12b** only correlated with experimental formability gains when adjusting the material hardening response and contact pressure. The concept of mapping under a constant stress ratio was later adopted by Simha *et al.* (2007, 2008) in the extended stress-based FLC (XSFLC) for straight tube hydroforming and stretch flange forming, and by Min *et al.* (2016) in the process corrections of Nakazima tests. Min *et al.* (2016) provided a three-step procedure to correct for non-linear strain path, curvature, and pressure effects in Nakazima dome tests with two different punch sizes ($r_p$ = 50.8 mm and $r_p$ = 25 mm). Contrary to the findings of Smith *et al.* (2003), the corrected limit strains of the Nakazima test were in good agreement with Marciniak tests for in-plane stretching of an MP980 steel. Chen and Fang (2018) adopted the same methodology for Nakazima tests and reported satisfactory results for AA6014-T4. The difference between the strongly diverging formability gains in the study of Min *et al.* (2016) and Smith *et al.* (2003) might be attributed to the magnitude of the contact pressure. Smith *et al.* (2003) invalidated his model when considering experimentally-measured contact pressure values whereas Min *et al.* (2016) relied upon the homogenized modelling approach (Section 2.3.4), which is yet to be validated. The uncertainty surrounding the phenomenological mapping will be critically evaluated as part of this research from an experimental perspective by assessing the sensitivity of the hardening rate and limit strain detection method in Chapter 3 and under physical considerations in Chapter 4.

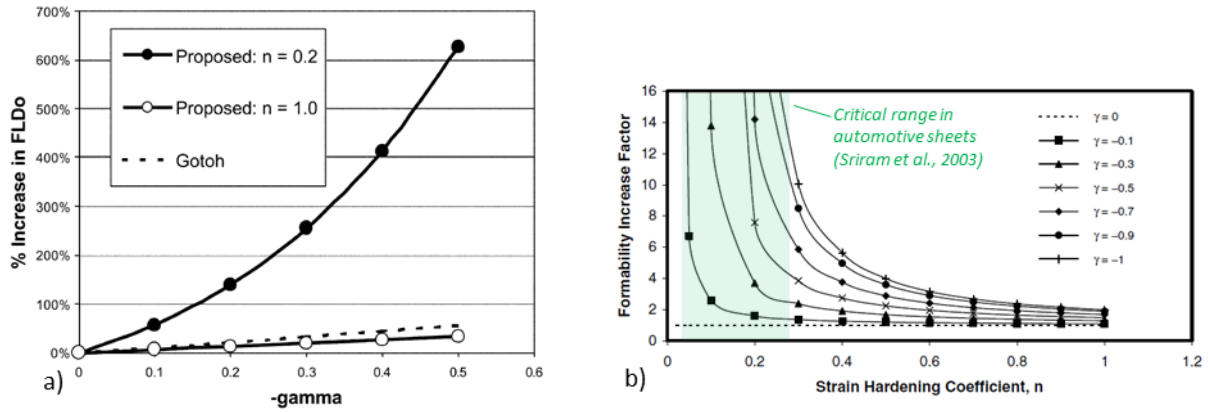


**Figure 12: Predicted formability gain adopting in the constant stress mapping methods of Smith *et al.* (2003) (a) and Matin and Smith (2003) (b).**

The analytical prediction of the acute necking limits in triaxial loading has predominantly focused upon the in-plane MK model with a superimposed contact pressure. In general, additional equilibrium and compatibility equations are required to account for a triaxial stress state. The imperfection is described in terms of a homogenous stress-strain distribution through the sheet thickness and along the groove width that makes it challenging to properly resolve stress-strain gradients as a consequence of bending and tool contact (He *et al.*, 2013c). Instead, the average through-thickness pressure is prescribed and the sheet thickness is treated as a single layer (Wang et al., 2019; Assempour *et al.*, 2010). The effect of the boundary condition of how the contact pressure is applied is not trivial and has been overlooked in the literature. The majority of the 3D MK models employ a *constant magnitude of the contact pressure* (Assempour *et al.*, 2010, Hashemi and Abrinia, 2014; Erfanian and Hashemi, 2018; Nurcheshmeh and Green, 2012; Zhang *et al.*, 2014; Lang *et al.*, 2015) where reported formability gains are relatively minor. For an AA6111-T43 and a ratio of the normal stress with respect to the material yield stress ($\sigma_3 / \sigma_y$) of -0.45, Zhang *et al.* (2014) predicted an approximately constant formability gain of the FLC across all stress states. The $FLC_0$ was shifted by about 17% from approximately 0.23 for plane stress to 0.27 in the presence of contact pressure. Much larger formability gains were predicted when the *contact stress evolves proportionally with the major in-plane stress*, reflected in a constant through-thickness stress ratio (Allwood and Shouler, 2009; Mirfalah-Nasiri *et al.*, 2016). For a 1050 aluminum and a constant component through-thickness stress ratio ($\sigma_{33} / \sigma_{11}$) of -0.5, Allwood and Shouler (2009) predicted an increase in the $FLC_0$ by about 58% from a major strain of 0.19 to 0.3 with the highest formability gains for biaxial strain paths. Mirfalah-Nasiri *et al.* (2016) reported a 35% increase in the plane strain limit strain for AA3104-H19 adopting a constant through-thickness stress ratio of -0.45. Ma *et al.* (2016) considered an *evolving through-thickness stress ratio* where the contact pressure was computed from the homogenized approach of the preceding section while neglecting the through-thickness distribution. The effect of an increase in the sheet thickness with a constant

punch radius of 25 mm revealed negligible formability gains for the draw side of the FLC with strongly magnified effects for biaxial strain paths.

The generalized instability framework of Hillier (1963) has been mostly overlooked in the literature despite its fundamental insight into material instability and the formulated dependence upon the boundary conditions of how the tractions are applied. Plastic instability is derived from the condition of a vanishing second order plastic work rate. Instability is expressed in terms of a critical subtangent, derived from applied loads, tractions, and the change in the contact area that intersects the material hardening curve. The advantage of the Hillier (1963) model lies in its generalized framework that admits arbitrary loading and boundary conditions such as combined tension and shear, triaxial stress states, and proportional loading *versus* proportional stressing. The stabilizing role of shear on localization was shown by Hillier (1963, 1964) and recently used by Butcher and Abedini (2019a) to explain the failure behavior of tension-torsion tests compared to tensile-based tests with the same stress triaxiality. Hillier (1964) also demonstrated how the seemingly conflicting instability solutions of Hill (1950), Mellor (1962), and Pugh (1964) for applied pressure in a tensile test represent special cases of the general framework and are a consequence of the adopted boundary conditions. The primary limitation of the general Hillier framework is its restriction to the onset of instability that is too conservative in a forming process for which acute localization is of primary concern.

## 2.4 Plane Strain Fracture Characterization

As discussed in Section 2.3.2, the presence of a severe through-thickness stress-strain gradient may lead to suppression of tensile instabilities with abrupt fracture. Since plane strain loading represents the global minimum of the FLC and the terminal strain path when an acute neck has formed (Hora *et al.*, 2013), fracture without necking under plane strain tension warrants consideration.

Plane strain notch tests have found widespread acceptance for fracture characterization of plane strain tension (Wagoner, 1980; Vegter and van den Boogaard, 2006; Tian *et al.*, 2017) but come at the cost of a stress-strain gradient along the gauge width and through the thickness as illustrated in **Figure 13a**. The formation of an acute neck causes fracture initiation at the specimen center (through-thickness in the mid-plane) where strains cannot be measured using DIC. Therefore, inverse FE analysis is required to extract the local non-proportional stress-strain history of the center element where fracture is initiated (Mohr and Henn, 2007). Nevertheless, the adoption of FE bears its own risks surrounding model uncertainties caused by the selected plasticity model, element formulation, and mesh discretization (Dunand and Mohr, 2010).

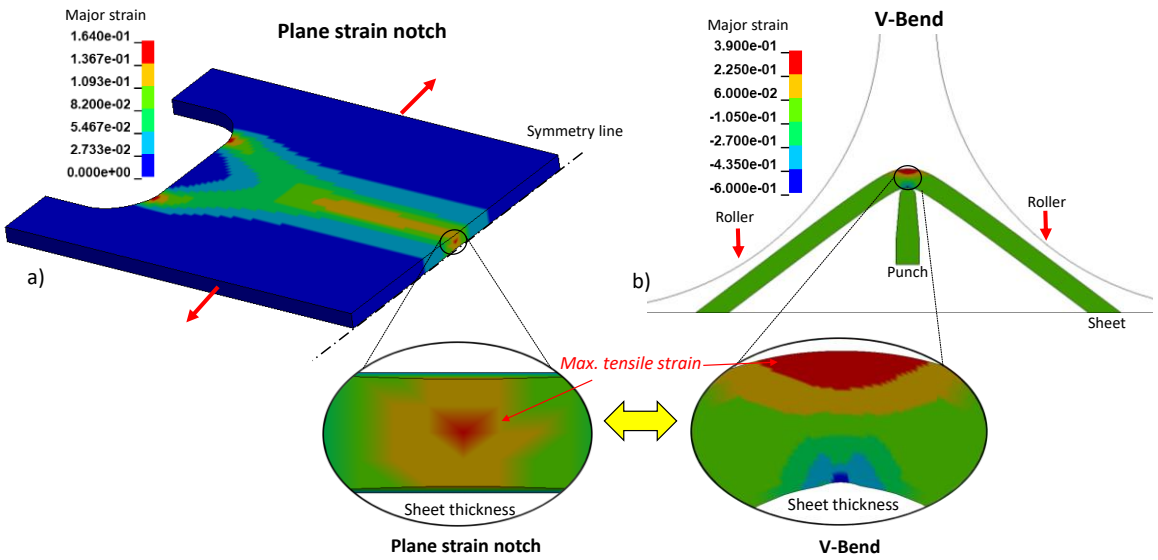


**Figure 13: Non-uniform strain distribution along the gauge length and through the thickness of the plane strain notch specimen (a) contrasted with the major strain distribution in the V-Bend test (b). Note that the FE simulation in (a) was provided by Fast-Irvine (2021).**

These complications can be avoided in the VDA 238-100 (2013, 2017) tight radius bend test, hereinafter referred to as V-Bend test, that represents a severe stretch-bend condition with plane strain bending as the primary deformation mode. A square specimen with a minimum width of approximately 20 times the sheet thickness is bent between two rollers with a gap of approximately twice the sheet thickness and a sharp knife of 0.2 mm or 0.4 mm tip radius depending on the material type. The primary advantage of the V-Bend over notch test lies in the suppression of necking owing to the severe through-thickness stress-strain gradient. As depicted in **Figure 13b**, fracture will occur on the convex surface where the tensile strains are highest and can be directly measured with the aid of DIC (Cheong *et al.*, 2018). For materials of homogeneous microstructure, fracture in the V-Bend test represents the true plane strain fracture strain unlike for steels with severe centerline segregation of martensite. In this case, martensite approximately coincides with the neutral layer during bending and is therefore not activated in contrast to in-plane loading where martensite centerline segregation was found to be detrimental for fracture (Bertolo *et al.*, 2022).

Following the VDA 238-100 specification, fracture is solely identified upon a load threshold of the punch force and the punch displacement is utilized to compute the bend angle, which is the reported metric for alloy comparison. The design of an inverted V-Bend frame equipped with a DIC system proposed independently by Roth *et al.* (2016) and Cheong *et al.* (2017) allows direct measurement of the plane strain failure strain and eliminates the dependence of the sheet thickness upon the reported bend angle. Complications may arise if the material plane strain fracture strain cannot be reached with the 0.2 mm radius punch and the material performs a full bend in the absence of fracture, termed “false positive”, as reported for the DP600 by Cheong (2018) and Larour *et al.* (2013). Different approaches have been

established to overcome the uncertainties surrounding the fracture detection in the VDA 238-100 tight radius bend test. The most recent version of the VDA 238-100 (2017) specification suggests to first pre-strain the material to 10% true strain using strips of 70 mm in width and 160 mm free clamping prior to extraction of V-Bend specimens. It was shown by Noder *et al.* (2020b) that this methodology results in a non-linear strain path; the effect upon the bend angle and failure strain was strongly dependent on the type of material, *e.g.* steel, aluminum, or magnesium alloy. Instead, Grolleau *et al.* (2019) proposed a novel stretch-bend set-up with a dihedral punch to promote fracture by superimposing tensile stretching. The test methodology of Grolleau *et al.* (2019), strictly speaking, represents combined loading and may impair the linearity of the strain path. In light of the excellent plane strain conditions in the V-Bend test, alternative approaches have focused on enhanced fracture detection methods. Boul *et al.* (2007) and Labudde and Bleck (2011) explored the use of acoustic sensors for fracture detection but highlighted potential complications arising from background noise. Troive (2017) proposed adoption of the bending moment of the cross-section to detect material failure. The strain, stress, and bending moment over the cross-section were computed from analytical approximations. Failure was determined from a change in the plastic bending moment relative to the elastic moment for a high-strength hot rolled steel with low ductility. Although promising, due to limited validation, the applicability of the methodology of Troive (2017) to high-hardening materials with superior ductility remains uncertain.

## 2.5 Summary and Current Deficits in the Literature

With advancements in material development, the need for instability models that account for the instantaneous nature of the forming limit under combined loading and tool contact pressure has become prominent. The conventional strain- or stress-based FLC developed for plane stress in-plane stretching performs too conservatively in the presence of strain gradients and appreciable contact pressure. This is particularly problematic for high strength steels and aluminum alloys with limited forming windows. The continued use of the in-plane FLC to evaluate forming operations can be attributed to the complexity of accounting for bending mechanics with superimposed tensile stretching. Knowledge of the through-thickness stress gradient, the complex hardening behavior within layers that undergo reverse loading, and identification of the critical number of material layers to reach instability are challenging to distill into a practical framework. Formability models that account for combined stretching and bending within the literature have been limited to moderate bend severities of $r_m / t > 10$ as a consequence of aggressive model simplifications and omission of evolving normal stresses caused by bending and tool contact. As a result, research on analytical models for approximation of the contact pressure and identification of instability under triaxial stress states are scarce. Selective approaches have focused on phenomenological mapping techniques between 2D and 3D stress states but can potentially lead to non-physical formability gains.

Alternative approaches were limited to the in-plane MK framework that typically requires an *a priori* FLC for identification of the imperfection factor. The through-thickness stress-strain gradients cannot be readily resolved due to the physical basis of the MK model upon localization of an imperfection in a wide strip of homogeneous stress-strain distribution. The Hillier framework provides a physically-consistent methodology for the general loading conditions but has received little attention due to its focus upon diffuse necking. Models must be able to account for the suppression of necking based upon the severity of the through-thickness gradient when fracture on the convex surface governs the forming process. Accurate knowledge of the plane strain fracture limit is critical. The inverted VDA238-100 tight radius V-Bend test is promising for fracture characterization but relies upon an arbitrary load threshold as a fracture criterion that can lead to significant under-reporting of the failure strains. The VDA load threshold fails to recognize that the load will drop even without fracture.

## 2.6 Research Scope

### 2.6.1 Objectives

The overall goal of this research is to enhance the current understanding and modelling of formability and fracture of automotive sheet metals with an emphasis upon 3rd Gen AHSS. This research will contribute to the adoption of AHSS in the design of automotive lightweight components for superior fuel efficiency and passenger safety. The outcome of this work will provide an instability framework for adoption in the product design stage to predict and assess instantaneous forming limits accounting for both the process and local boundary conditions in combined loading under complex stress states. AHSS are the primary material class considered although other materials such as aluminum alloys and mild steel will be considered for selective cases to demonstrate applicability of the developed methodologies. The thesis has been structured around four objectives:

(1) Characterization of the material forming limit for stretching-dominated loading conditions and development of a methodology for the prediction of the plane stress FLC.

(2) Development of a general instability framework to predict the effect of a triaxial stress state on plastic instability during in-plane loading.

(3) Development of a fracture detection methodology in the VDA 238-100 tight radius bend test to characterize the fracture limit under plane strain tension, in the absence of necking.

(4) Characterization of the necking limits in bending-dominated loading conditions and extension of the developed instability framework of objective (2) to account for evolving through-thickness stress-strain gradients due to bending and tool contact pressure.

### 2.6.2 Tasks

The preceding objectives are supported by the tasks discussed in the following section. The contribution of each task in the developed instability framework is visualized in **Figure 14**.

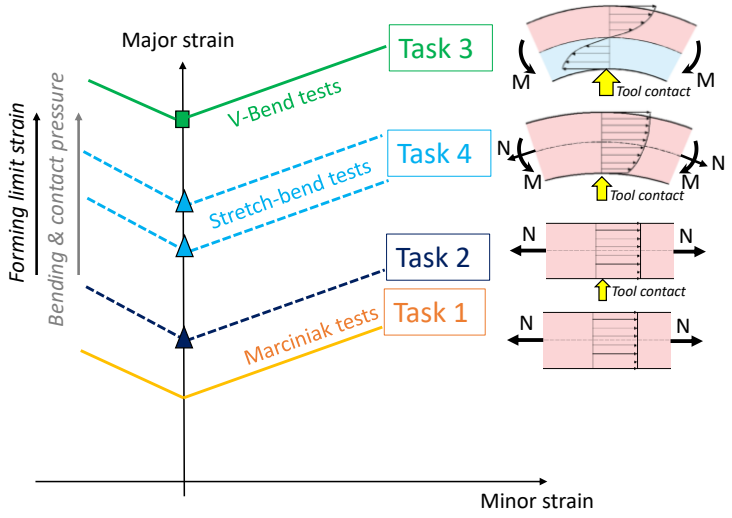


**Figure 14: Overview of tasks to attain the defined objectives.**

#### Task 1: Instability during In-plane Loading

For the characterization of the in-plane forming limits, the standard procedure outlined in the ISO 12004-2 standard is followed in Nakazima and Marciniak tests. The sensitivity of the limit strain detection method is studied using the method outlined in the ISO 12004-2 standard in addition to a refined version of the LBF Method of Volk and Hora (2011) to eliminate subjectivity in the identification of the fitting window for the stable strain rate. Applicability of the stress-based phenomenological mapping criterion (Smith *et al.*, 2003), which showed promising results for the MP980 steel in Min *et al.* (2016), is critically assessed for potential artefacts arising from the limit strain detection method, hardening rate, and calibration technique of the constitutive model. For analytical FLC prediction, the plane stress MMFC of Hora *et al.* (2013) is selected since it is entirely mechanistic and was shown to generate results of accuracy level comparable or superior to the MK model for AHSS (Gutierrez *et al.*, 2020; Butcher *et al.*, 2021). The outcome of Task 1 represents the lower bound of the instability framework in **Figure 14** to mechanistically predict in-plane formability.

#### Task 2: Instability under Triaxial Stress States

The physically motivated instability framework of Hillier (1963) is selected to establish a fundamental understanding of the effect of a compressive normal stress and the local boundary conditions upon plastic instability. Closed-form solutions are derived for different boundary conditions of the contact pressure, *e.g.*

constant, proportional, or evolving, and contrasted with the phenomenological mapping criterion adopted in Task 1 to critically assess their validity. An extension of the Hillier framework to acute localization is derived from physical considerations of the localization process in a tensile test and contrasted with the boundary conditions of the phenomenological plane stress MMFC (Hora *et al.*, 2013). The outcome of Task 2 provides an instability framework to predict acute localization under a triaxial stress state while accounting for the local boundary conditions of the deformation process.

**Task 3: Fracture in the Absence of Necking**

The limiting case of suppression of necking, *e.g.* in a forming operation with appreciable bending, the VDA 238-100 tight radius bend test is selected. Proportional straining and fracture initiation under plane stress makes the V-Bend test suitable for fracture characterization under plane strain tension but fracture detection based upon the punch force evolution is replaced with a more accurate failure criterion. The validity of the load drop methodology in the V-Bend tests is critically evaluated for AHSS of different ductility levels. The fundamentals of bending mechanics are employed to develop a stress-based fracture detection method that accounts for thinning and sample dimensions of the material cross-section, which have been neglected in the literature. The local instability of the material is studied utilizing surface strains measured from stereoscopic DIC that are then compared to the stress-based detection method. The outcome of Task 3 represents the upper limit of the instability framework in **Figure 14** to provide a robust fracture detection methodology for identification of the plane stress fracture limit in plane strain tension.

**Task 4: Instability in Combined Triaxial Loading**

The instability framework developed in Task 2 requires an extension for application to combined loading to obtain the stress history at each material layer to evaluate instability. The CSR is used as the governing metric of instability that requires all layers to reach their instability limit before a through-thickness neck can develop. The effect of a superimposed contact pressure upon the stress state in plane strain stretch-bending is derived on continuum level. The fundamentals of general bending mechanics are employed to derive plasticity-related equations in stretch-bending. An emphasis is placed upon developing a modelling strategy that accommodates compressive stressing of the lower part of the cross-section to mimic wrapping of the sheet around the punch at the beginning of the forming process. The analytical-numerical stretch-bend model is then coupled with the triaxial instability framework of Task 2 and the fracture limit identified in Task 3 to predict the instantaneous forming limit under combined triaxial loading. To demonstrate applicability to automotive lightweighting, angular stretch-bend tests are conducted and utilized along with the stretching-dominated conditions of Task 1 to assess the predictive capability of the developed framework.

# 3. Characterization and Prediction of In-plane Forming Limits (Task 1)

This chapter focuses on the state-of-the art formability characterization to determine the stretching-dominated forming limits. Owing to the large punch radius in the Nakazima test ($r_p$ = 50.8 mm), bending effects are mild and the deformation is approximated to in-plane loading (Chen and Fang, 2018). Nakazima limit strains are corrected for process effects (non-linear strain path and triaxial stress state), consistent with the physical framework of in plane-plane stress loading of the MMFC of Hora *et al.* (2013). The phenomenological stress-mapping criterion of Smith *et al.* (2003) is employed to correct for contact pressure effects by reverse mapping from 3D to 2D stress space. The reason for the reported controversy (Matin and Smith, 2005; Allwood and Shouler, 2009; Min *et al.*, 2016; Chen and Fang, 2018) surrounding the applicability of the phenomenological mapping criterion has been unclear and is assessed in this study. From an experimental perspective, Nakazima tests are preferred and reverse mapping to correct for the 3D stress state would provide a means to utilize the corrected limit strains for validation of common instability models. In addition, if a robust application window for the mapping criterion can be established, the phenomenological instability condition may be extendable to account for combined loading effects. To this end, parametric studies of the hardening rate, limit strain detection method, and calibration of the constitutive model on the FLC are conducted. In addition to the ISO 12004-2 standard, a refined version of the LBF necking detection method of Volk and Hora (2011) is implemented for user-independent identification of necking limits with applicability to stretch-bend and V-Bend tests in Chapter 5. The calibration of the constitutive model plays a central role in both the pressure corrections and the FLC prediction in the MMFC of Hora *et al.* (2013). Different strategies considering a constrained calibration and adoption of a plastic-work based shear conversion technique (Rahmann *et al.*, 2017) to obtain the hardening rate to large strains (in excess of diffuse necking in tensile tests) are explored. Special attention is devoted to assessing the artefacts of a shift in the predicted $FLC_0$ with selection of the constitutive model (Hora *et al.*, 2013; Pham *et al.*, 2018).

The published manuscript can be found in Appendix A in:

**Noder, J.**. Butcher, C., (2019a). A comparative investigation into the influence of the constitutive model on the prediction of in-plane formability for Nakazima and Marciniak tests, International Journal of Mechanical Sciences, 163, 105138, https://doi.org/10.1016/j.ijmecsci.2019.105138.

## 3.1 Material Selection and Calibration of the Constitutive Model

For this study, DP980 steel with its power-law hardening behavior was selected in addition to an AA5182-O aluminum alloy with its saturation-type hardening behavior. The different hardening behaviors will be shown to have a significant influence on the contact pressure corrections and limit strain predictions. The mechanical properties and sheet thicknesses are recorded in **Table 1**.

**Table 1: Tensile mechanical properties of the studied alloys. The total elongation is based on a virtual extensometer length of 50 mm and that the Lankford parameter (R-value) was fitted over a plastic strain range of 0.01-0.05 and 0.05-0.15 for the DP980 and the AA5182, respectively.**

| | Yield Stress (0.2% offset) (MPa) | Ultimate Tensile Stress (MPa) | Uniform Elongation UE (%) | Total Elongation TE (%) | R-value |
|---|---|---|---|---|---|
| **DP980, 1.2 mm, TD** | 735 (±2) | 1065 (±3) | 7.8 (±0.2) | 13.7 (±0.5) | 0.95 (±0.01) |
| **AA5182, 1.55 mm, RD** | 146 (±2) | 302 (±4) | 20.6 (±0.2) | 25.7 (±0.5) | 0.60 (±0.04) |

Central to the phenomenological process corrections and analytical FLC prediction is the material constitutive response to strain levels associated with the equi-biaxial limit strains. As hydraulic bulge test data were not available, four different calibration methodologies were considered to obtain the hardening response to strain levels beyond the uniform elongation using tensile and shear tests. The shear and tensile test geometries are shown in **Figure 15a,b**. A refined methodology of the shear conversion technique of Rahmaan *et al.* (2017) was adopted to convert the shear stress-strain response into an equivalent measure based upon the integrated plastic work

$$w^p_{tensile} = \int \sigma_1 d\varepsilon_1, \quad w^p_{shear} = \int \sigma_{12} d\gamma^p, \quad \sigma_{eq} = \frac{\tau}{\eta}, \quad \varepsilon^p_{eq} = \int \frac{dw^p_{shear}}{\sigma_{eq}} = 2\left(\frac{\sigma_{12}}{\sigma_{eq}}\right)\sinh(\varepsilon_1) \qquad \text{(1a-d)}$$

where $d\gamma^p$ is the plastic dimensionless shear deformation parameter and $d\varepsilon_1$ the major plastic strain increment. The ratio of the shear-to-tensile stress, $\eta$, is identified at the plastic work corresponding to diffuse necking in the tensile test. Adoption of the incremental plastic work balance then allows computation of the equivalent plastic strain, $\varepsilon^p_{eq}$.

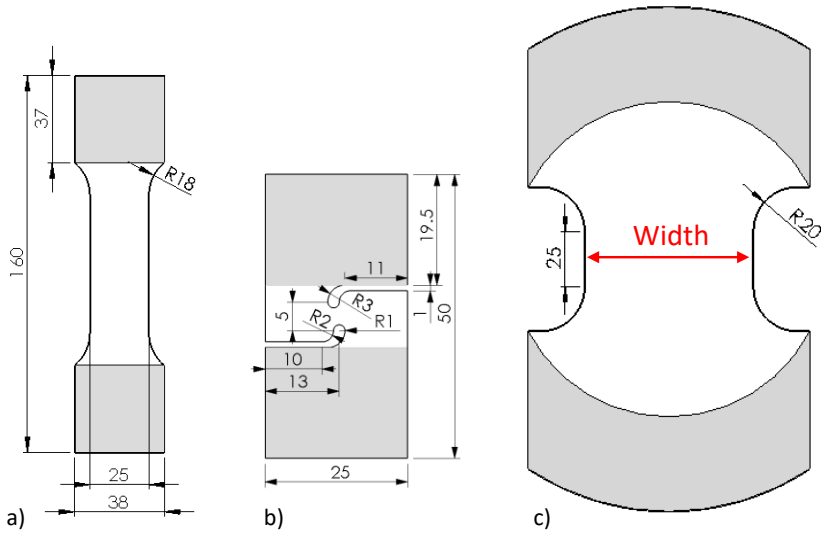


**Figure 15: Geometries of test coupons utilized to study the constitutive behavior in tensile tests (a), simple shear tests using the geometry of Peirs *et al.* (2012) (b), and the formability tests (c). Note that the shaded area reflects the clamping area. Units are in mm.**

Central to the hardening model calibration procedure is the Considère constraint that represents the plastic true strain, $\varepsilon_1^{UE-p}$, when diffuse necking occurs in the tensile test and can be computed from the engineering strain at uniform elongation, $UE$, the corresponding stress level, $\sigma_{UTS}$, and the Young's modulus, $E$

$$\varepsilon_1^{UE-p} = \ln\left(1+UE(\%)/100\right) - \frac{\sigma_{UTS}\left(1+UE(\%)/100\right)}{E} \tag{2}$$

Four scenarios were considered for calibration of the phenomenological constitutive model:

(i) Tensile data without enforcing the Considère constraint

(ii) Tensile data enforcing the Considère constraint

(iii) Converted tensile-shear approach while enforcing the Considère constraint

(iv) Calibration of an alternative hardening model under the conditions in case (iii)

The four hardening models considered are defined as

Hollomon (1945) $$\bar{\sigma} = a\left(\varepsilon_{eq}^{p}\right)^{b} \tag{3}$$

Hockett-Sherby (1975) $$\bar{\sigma} = a-(a-b)\exp\left[-c\left(\varepsilon_{eq}^{p}\right)^{d}\right] \tag{4}$$

Modified Hockett-Sherby (MHS) $$\bar{\sigma} = a-(a-b)\exp\left[-c\left(\varepsilon_{eq}^{p}\right)^{d}\right] + f\sqrt{\varepsilon_{eq}^{p}} \tag{5}$$

Modified Generalized Voce (MGV) $$\bar{\sigma} = a+\left(b+c\sqrt{\varepsilon_{eq}^{p}}\right)-\left[1-\exp\left(-d\,\varepsilon_{eq}^{p}\right)\right] \tag{6}$$

where the calibration coefficients $a$ - $f$ are specific to the model and are summarized in **Table 2**.

**Table 2: Summary of calibration coefficients of the constitutive models for the selected calibration scenarios.**

| | | | Calibration coefficients | | | | | |
|---|---|---|---|---|---|---|---|---|
| **Material** | **Hardening model** | **Scenario** | ***a*** | ***b*** | ***c*** | ***d*** | ***f*** | **UE-p** |
| DP980 | MHS | (i) | 1149.09 MPa | 505.66 MPa | 19.06 | 0.59 | 0.000 MPa | 0.046 |
| | | (ii) | 987.73 MPa | 576.61 MPa | 105.76 | 0.88 | 600.58 MPa | 0.069 |
| | | (iii) | 1092.54 MPa | 615.99 MPa | 11.54 | 0.50 | 333.25 MPa | 0.069 |
| | Hollomon | (iv) | 1387.51 MPa | 0.069 | x | x | x | 0.069 |
| AA5182 | MGV | (i) | 143.28 MPa | 128.62 MPa | 235.10 MPa | 17.77 | x | 0.201 |
| | | (ii) | 141.14 MPa | 252.22 MPa | 0.00 MPa | 11.39 | x | 0.182 |
| | | (iii) | 134.73 MPa | 182.76 MPa | 144.09 MPa | 16.25 | x | 0.182 |
| | HS | (iv) | 138.69 MPa | 412.51 MPa | 8.24 | 0.96 | x | 0.182 |

As depicted in **Figure 16** for the DP980 and **Figure 17** for the AA5182, the conventional unconstrained calibration – case (i) – inadvertently shifts the equivalent plastic strain when diffuse necking in a tensile test occurs from 0.069 to 0.046 for the DP980 and from 0.182 to 0.201 for the AA5182. Enforcing the

plastic uniform elongation (UE-p) provides some improvement but fails to capture the post-uniform hardening rate. For the DP980, calibration of the constitutive model is straightforward and mostly independent of the choice of the hardening model when the experimental hardening rate up to strain levels beyond diffuse necking in addition to the UE-p are considered. In contrast, the calibrated hardening rate still varies with the choice of constitutive model for the AA5182 even with the constrained calibration. The latter is shown to have implications on the process correction and the analytical FLC prediction.

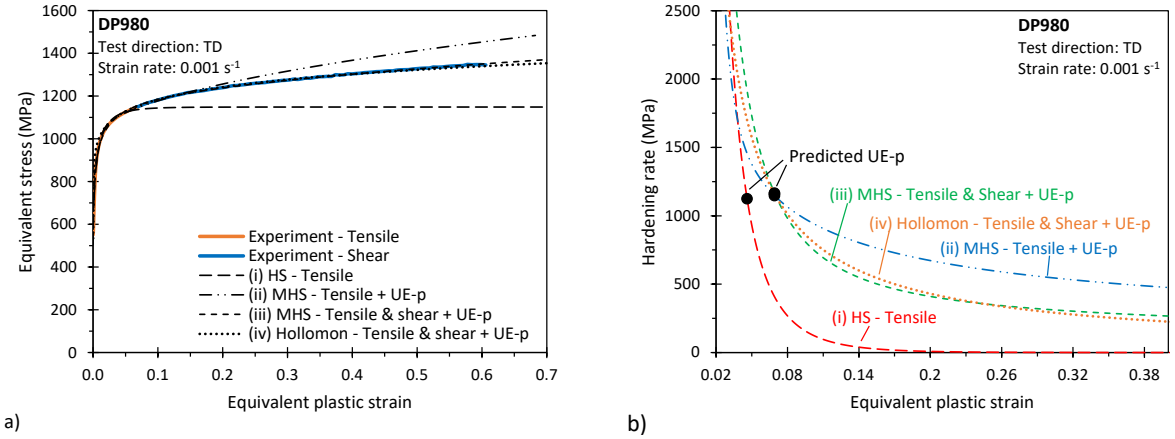


**Figure 16: Calibrated constitutive model considering different calibration techniques (a) and predicted hardening rate (b) for the DP980. Note that calibration of the MHS model reduced to the original HS model when only using tensile data.**

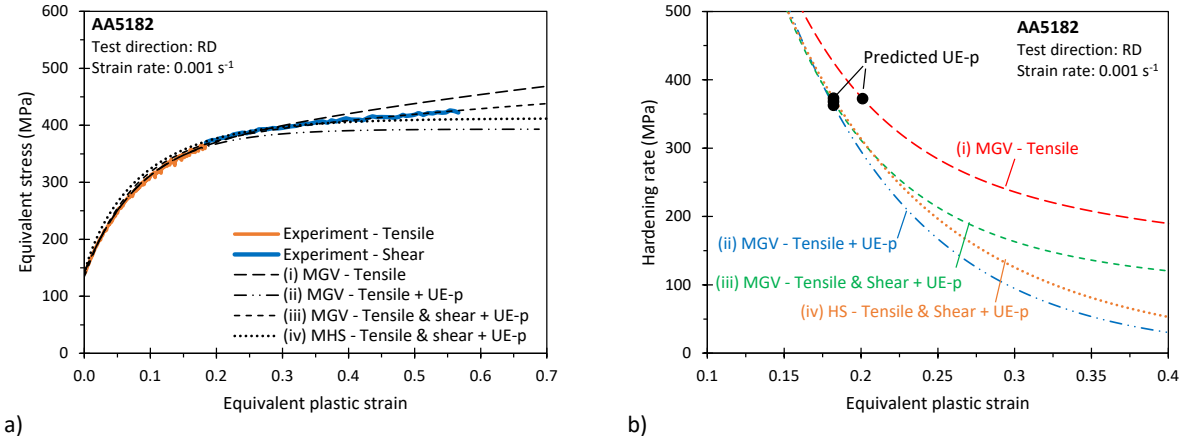


**Figure 17: Calibrated constitutive model considering different calibration techniques (a) and predicted hardening rate (b) for the AA5182.**

## 3.2 Characterization of Acute Necking Limits in Nakazima and Marciniak Tests

Two limit strain detection methods were considered to identify the formation of an acute neck in the Nakazima and Marciniak tests. The methodology documented in the ISO 12004-2 standard served as baseline to which a refined version of the time-dependent LBF model (Volk and Hora, 2011) was compared. The arbitrary selection of the fitting window of the stable thinning rate was replaced with a more physical method. The sheet in the Nakazima test is initially bent as it conforms to the punch curvature that results in

a sudden increase in the thinning strain rate at the beginning of the test, as depicted in **Figure 18**, and needs to be excluded from the fitting window.

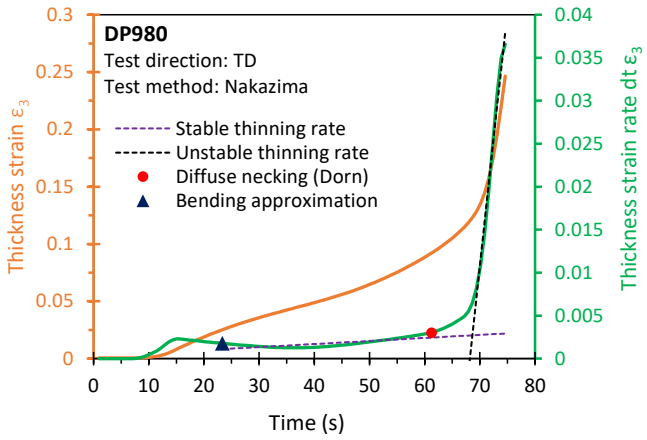


**Figure 18: Schematic of the Modified Linear Best Fit (Mod. LBF) Method to identify localization in formability tests, representatively shown for loading under uniaxial tension of the DP980 AHSS.**

The beginning of the fitting window is determined from large bending theory (see Appendix E1) to obtain an analytical approximation of the thickness strain for plane strain bending ( $\rho = 0$)

$$\varepsilon_{3,\rho=0} = -\ln\left(1+\frac{t}{r_p}\right), \qquad \varepsilon_3 = \varepsilon_{3,\rho=0}(1+\rho)\left(\frac{t}{t_{ref}}\right), \qquad \rho = \frac{d\varepsilon_2}{d\varepsilon_1} = \frac{N_2}{N_1}, \qquad N_i = \frac{\partial \sigma_{eq}}{\partial \sigma_i} \tag{7a-d}$$

where $\rho$ refers to the principal in-plane strain ratio and $N_i$ to the normal vectors of the yield surface, which defines the directions of plastic flow. Since Eq. (7a) is limited to plane strain loading, an extension to arbitrary loading was proposed in Eq. (7b) by adoption of a phenomenological scale factor where $r_p$ refers to the punch radius, $t$ to the nominal sheet thickness and $t_{ref}$ to an arbitrary reference sheet thickness of 1 mm. The principal in-plane strain ratio is approximated from ten data points in the middle of the test. The cut-off strain rate for identification of the stable thinning rate is determined from the Dorn criterion (Dorn and Thomsen, 1947) for diffuse necking when the hardening rate reaches a critical value

$$\frac{d\bar{\sigma}}{d\varepsilon_{eq}^{p}} \leq \frac{\bar{\sigma}}{k(\alpha)(1+\alpha\rho)}, \qquad k = \frac{\sigma_1}{\sigma_{eq}}, \qquad \alpha = \frac{\sigma_2}{\sigma_1} \tag{8a-c}$$

where $k$ represents the ratio of the major stress to the equivalent stress and $\alpha$ the principal in-plane stress ratio. It is noted that simple approximations of the plasticity model, *e.g.* adoption of the isotropic von Mises plasticity model can be selected to help with the identification of the fitting windows for homogeneous deformation.

Nakazima and Marciniak tests were performed according to the ISO 12004-2 standard. Schematics of the tool dimensions are provided in **Figure 20a,b**. Eight different strain paths were studied in the Nakazima tests and five and six different loading conditions were explored in the Marciniak tests for the DP980 and the AA5182, respectively. The dogbone specimen in **Figure 15c** was adopted and the width was varied from 25.4 mm to 203.2 mm to obtain different strain paths. A carrier blank – washer with center hole – was adopted in the Marciniak tests to inhibit fracture along the punch radius and promote uniform stretching of the sheet metal. The formability study was conducted under quasi-static conditions by selecting a punch velocity of 0.25 mm/s. To promote fracture at the dome apex, a combination of multiple Teflon sheets and Vaseline was employed. Full-field stereoscopic strain measurements were obtained using DIC with a virtual strain gage length (VSGL) of approximately 0.5 mm (image resolution of 0.0892 pixel/mm x strain filter of 5 x step size of 1 pixel).

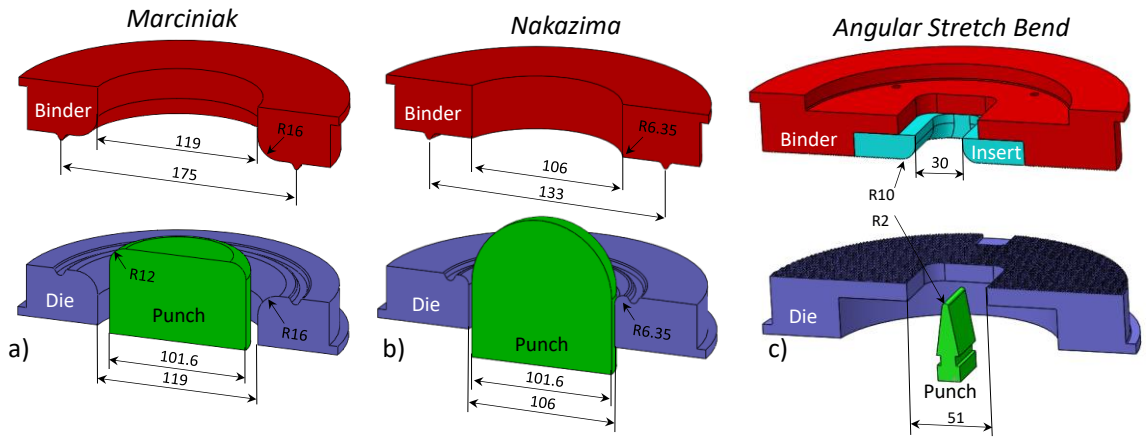


**Figure 19: Geometric dimensions of die sets utilized in the formability tests. All units are in mm.**

The strain paths in **Figure 20** and **Figure 21** were extracted from a 0.5 mm radius inspector tool and for analysis of the limit strains, five line slices perpendicular to the crack location were extracted following the ISO 12004-2 standard. Note that unless otherwise mentioned, a single layer of shims with a height of 1.4 mm were utilized for biaxial strain paths to reduce lockbead penetration and prevent material fracture along the lockbead. For the DP980, both limit strain detection methods are in good agreement on the draw side of the FLC and around plane strain tension whereas larger limit strains were identified by the ISO 12004-2 method on the stretch side, particularly for biaxial stretching. Greater deviations are apparent for the AA5182 where the presence of PLC effect (Portevin and Le Chatelier, 1923) impaired the inverse parabola fit in the ISO 12004-2 method. Overall, the strain path in the Nakazima test is non-linear compared to the Marciniak tests, which is a direct consequence of the boundary conditions in the specific test method. The initial equi-biaixal pre-strain as a consequence of the punch geometry in the Nakazima test and the resulting

shift in the $FLC_0$ is manifested in the experimental data of both the AA5182 and the DP980 and was corrected for in the next section, Section 3.3.

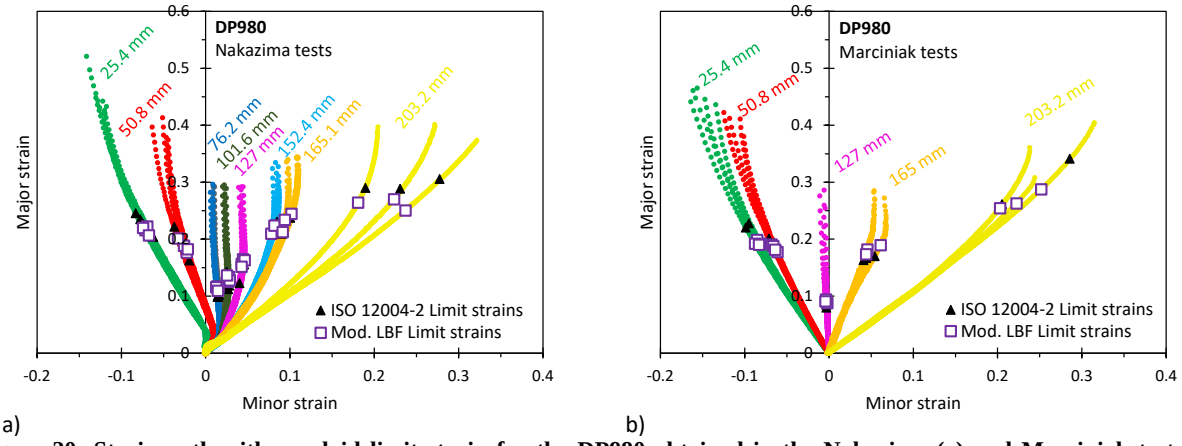


**Figure 20: Strain path with overlaid limit strain for the DP980 obtained in the Nakazima (a) and Marciniak tests (b) considering different limit strain detection methods. Note that the number above the strain path corresponds to the width of the dogbone specimen.**

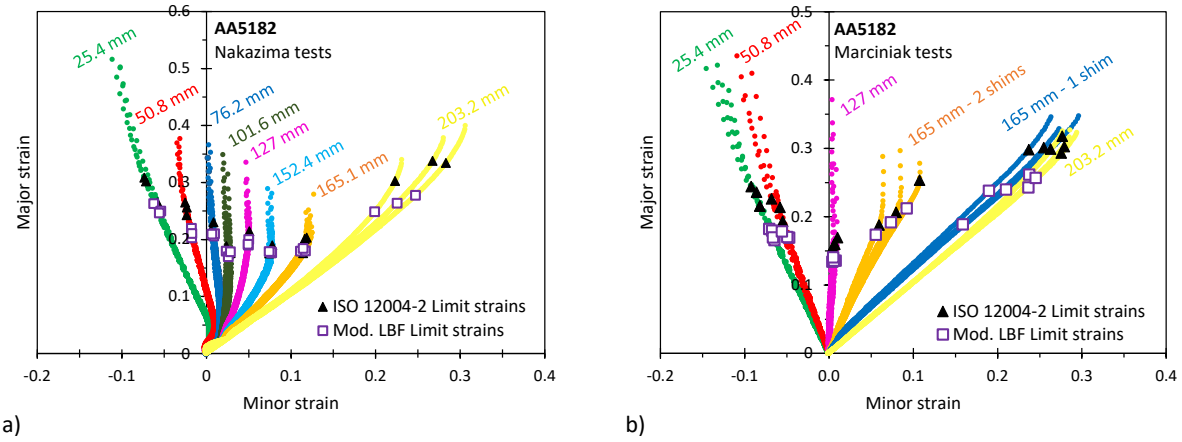


**Figure 21: Strain path with overlaid limit strain for the AA5182 obtained in the Nakazima (a) and Marciniak tests (b) considering different limit strain detection methods. Note that the number above the strain path corresponds to the width of the dogbone specimen.**

## 3.3 Effect of Constitutive Model on Process Corrections

Analytical formability models based upon plane stress are only in agreement with the boundary conditions in Marciniak tests. Thus, the process corrections outlined in Min *et al.* (2016) were employed to correct the limit strains in the Nakazima tests for non-linear strain path and contact pressure effects. The material was idealized as rigid-plastic such that elastic strains were neglected and the DIC strain history at the necking location was utilized. Owing to the large Nakazima punch radius and the studied sheet thicknesses of 1.2 and 1.55 mm, bending effects were neglected. Similarly, crowning in the Marciniak tests was not considered. The concave sheet surface, which is in contact with the hemispherical Nakazima punch, was considered as the critical layer since it exhibits the highest necking limit due to a compressive contact

stress that delays plastic instability. A triaxial stress state prevails on the concave layer while plane stress is maintained on the convex specimen side where DIC strains were measured. Min *et al.* (2016) proposed a novel methodology that can adopt a plane stress yield function for the inner layer of the material, which is in a 3D stress state, by defining an effective plane stress state. This method was employed in the published manuscript but for coherence with the overall structure of this thesis, the equations are expressed in the general form.

The equivalent plastic strain was integrated using the incremental plastic work balance and volume constancy

$$\varepsilon_{eq}^{p} = \int d\varepsilon_{eq}^{p} = \frac{\sigma_i : \varepsilon_i}{\bar{\sigma}} = \int k(\alpha, \chi)\left[1 + \alpha\rho - (1+\rho)\chi\right] d\varepsilon_1, \qquad \chi = \frac{\sigma_3}{\sigma_1} \tag{9a,b}$$

where the strain ratio $\rho$ is readily obtained from the measured DIC strains and $\alpha$ and $k$ are defined in Eq. (8b,c), respectively. The through-thickness stress ratio is defined through $\chi$, for which Min *et al.* (2016) provided an analytical solution

$$\chi = -\frac{t}{r_{\mathrm{p},1}}\left(1 + \frac{t}{2r_{\mathrm{p},2}}\right) - \frac{t}{r_{\mathrm{p},2}}\left(1 + \frac{t}{2r_{\mathrm{p},1}}\right)\alpha, \qquad t = t_0 \exp\left[-(1+\rho)\varepsilon_1\right] \tag{10a,b}$$

where the variables $r_{\mathrm{p},1}$ and $r_{\mathrm{p},2}$ correspond to the punch radii of the major and minor curvature and were set to 50.8 mm for the Nakazima punch. It is noted that the expression in Eq. (10a) has not been validated in FE analysis and was derived from a simplified analysis of force equilibrium using the average in-plane stress over the cross-section and neglecting the through-thickness distribution of the contact pressure. Sheet thinning is computed in Eq. (10b) adopting volume conservation of a rectangular element. The linearized principal in-plane strains, $\tilde{\varepsilon}_i$, are then readily obtained using the integrated equivalent plastic strain in Eq. (9a) and the experimental in-plane strain ratio at necking such that

$$\tilde{\varepsilon}_1 = \frac{\varepsilon_{eq}^{p}}{k(\alpha, \chi)\left[1 + \alpha\rho - (1+\rho)\chi\right]}, \qquad \tilde{\varepsilon}_2 = \rho\tilde{\varepsilon}_1 \tag{11a,b}$$

As depicted in **Figure 22a** for the DP980 and in **Figure 23a** for the AA5182, the non-linear strain path corrections are minor for the Marciniak limit strains since the biaxial wrapping of the sheet around the hemispherical punch in the Nakazima test is avoided. In contrast, the linearized limit strains of the Nakazima tests depicted in **Figure 22b** for the DP980 and in **Figure 23b** for the AA5182 are shifted up and to the left by about 0.01 to 0.02 major strain. Larger corrections are noted for the limit strains identified

with the ISO 12004-2 method on the stretch side of the FLC for which selective limit strains are shifted towards plane strain suggesting that the limit strains for these cases are likely too high. The instantaneous strain path at the necking limit rapidly converges towards plane strain tension and the non-linear strain path correction markedly reduces the minor strain as a result.

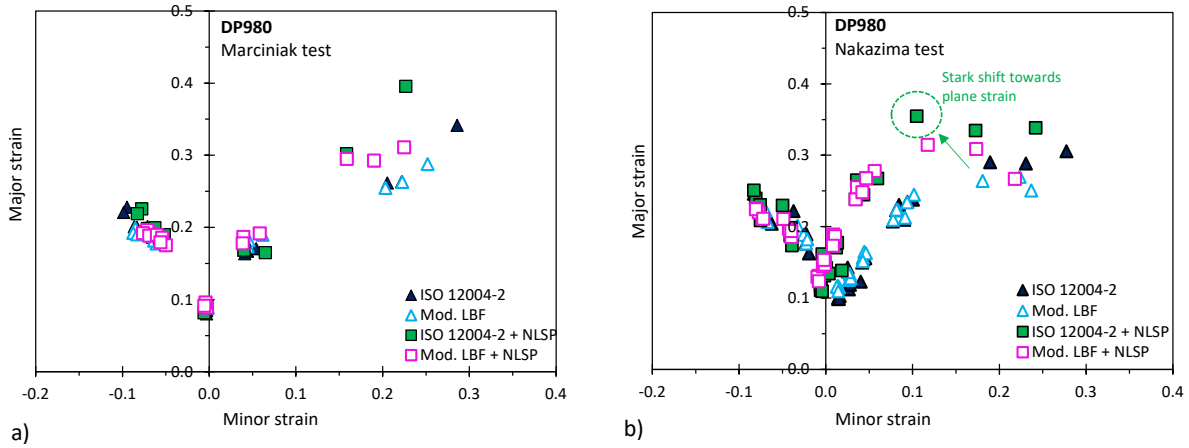


**Figure 22: Correction of the Marciniak (a) and Nakazima (b) limit strains of the DP980 AHSS for non-linear strain path (NLSP) effects considering the ISO 12004-2 and the Mod. LBF limit strain detection method.**

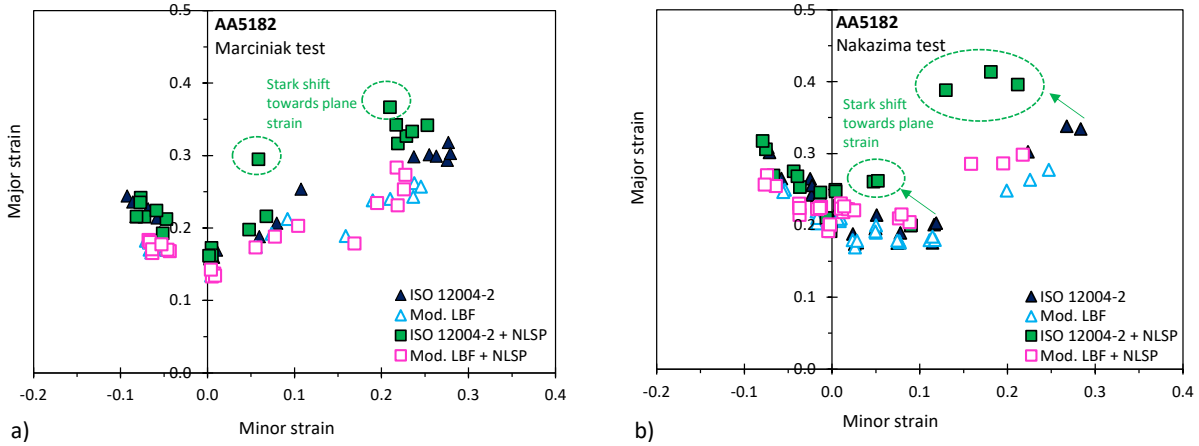


**Figure 23: Correction of the Marciniak (a) and Nakazima (b) limit strains of the AA5182 for non-linear strain path (NLSP) effects considering the ISO 12004-2 and the Mod. LBF limit strain detection method.**

Next, the limit strains in the Nakazima tests were corrected for a compressive through-thickness stress to enable comparison to Marciniak limit strains. The pressure corrections adopted by Min *et al.* (2016) are equivalent to the phenomenological mapping criterion of Smith *et al.* (2003) with the inherent assumption that plastic instability is independent of the stress state. The limit strains obtained under a triaxial stress state were mapped into plane stress space by keeping the principal in-plane stress ratio and the principal major stress constant. Thus, the equivalent stress under plane stress loading, $\sigma_{eq}^{2D}(\alpha)$, is readily computed and the equivalent strain, $\varepsilon_{eq}^{p,2D}$, is obtained by inversion of the hardening model

$$\bar{\sigma}\left(\varepsilon_{eq}^{p,2D}\right)=\frac{\sigma_1}{k^{2D}}=\bar{\sigma}\left(\varepsilon_{eq}^{p,3D}\right)\frac{k^{3D}}{k^{2D}},\qquad \varepsilon_1^{2D}=\frac{\varepsilon_{eq}^{p,2D}}{k^{2D}\left(1+\alpha\rho^{2D}\right)},\qquad \varepsilon_2^{2D}=\rho^{2D}\tilde{\varepsilon}_1^{2D} \tag{12a-c}$$

where the strain components are obtained from the flow rule and the incremental plastic work balance. The equivalent stress in Eq. (12a) is computed from the von Mises yield function for the DP980 and the Hosford yield function for face centered cubic (FCC) materials for the AA5182. The choice of yield function was shown to play a secondary role in the study of Min *et al.* (2016). The effect of the contact pressure correction on the Nakazima limit strains is visualized in **Figure 24**.

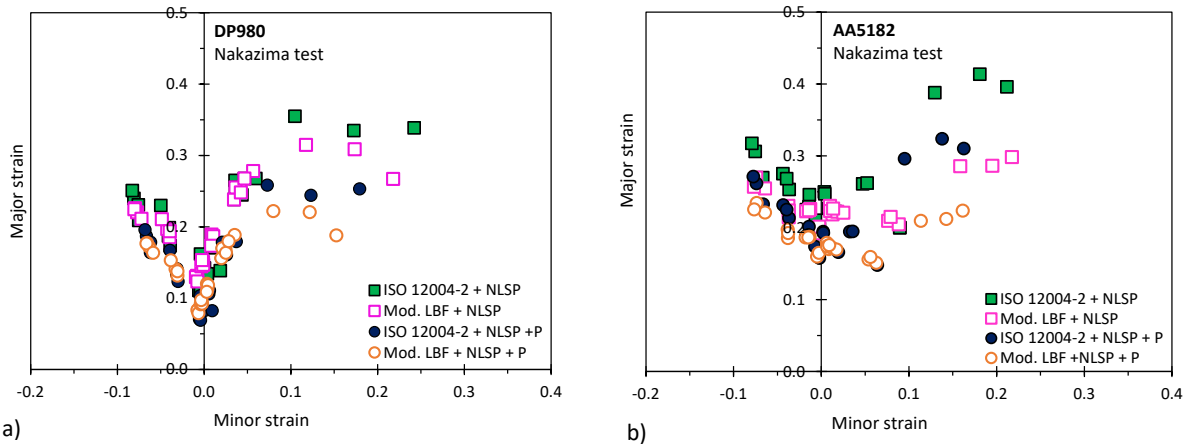


**Figure 24: Correction of the non-linear strain path (NLSP) corrected Nakazima limit strains for pressure (P) effects for the DP980 (a) and the AA5182 (b). The MHS and the MGV model both calibrated to experimental strain levels beyond 0.5 equivalent strain were adopted for the DP980 and the AA5182, respectively.**

Overall, removing the pressure effect reduces the forming limits and shifts them towards the draw side. This result is expected given that tool contact pressure delays the onset of instability. The pressure correction had the largest influence in biaxial loading; the major strains were reduced by 0.03-0.06 on the draw side *versus* a reduction of 0.05-0.09 on the stretch side of the FLC. The reasoning for increased pressure corrections for biaxial loading lies in the higher equivalent strains, which is attributed to the reduced hardening capacity of the material. The AA5182 with its saturation-type hardening behavior has a low hardening rate at strain levels associated with the observed biaxial limit strains such that the stress-based mapping procedure predicts a larger influence of the contact pressure.

To better highlight the explicit dependence of the stress-based mapping criterion on the material hardening rate, Eq. (12a) was inverted for a power law hardening model (see Appendix E2) to arrive at the ratio of the major principal strains between proportional plane stress and triaxial stressing

$$\frac{\varepsilon_1^{2D}}{\varepsilon_1^{3D}} = \frac{\left[1+\alpha\rho^{3D}-(1+\rho^{3D})\chi\right]}{\left[1+\alpha\rho^{2D}\right]}\left(\frac{k^{3D}}{k^{2D}}\right)^{\frac{1+n}{n}} \tag{13}$$

where superscripts 2D and 3D refer to the quantities in the respective stress state. Particularly for a rigid perfectly plastic material (hardening exponent $n = 0$), an infinitesimally non-zero contact stress predicts an infinite increase in formability. As a result, the projected limit strain corrections, or formability gains between 2D and 3D stress states, can be extremely sensitive to the hardening rate with stark changes in the limit strains at large contact pressures or for low hardening as visualized in **Figure 25**. The DP980 is less sensitive to the selected hardening model when calibrated to strain levels representative of biaxial limit strains in addition to enforcing the UE-p constraint. Similar trends apply to the AA5182 alloy but deviations are more pronounced for biaxial loading even though the constitutive models were calibrated to 0.5 equivalent plastic strain and reflect the plastic uniform elongation. The importance of the hardening model and its correct calibration is exacerbated for the DP980 AHSS. Adoption of the MHS model, which simplified to the HS model when only using tensile data, erroneously predicts saturation of the hardening capacity after the uniform elongation as shown in **Figure 16b**. This leads to a stark overcorrection of the contact pressure on the experimental limit strains.

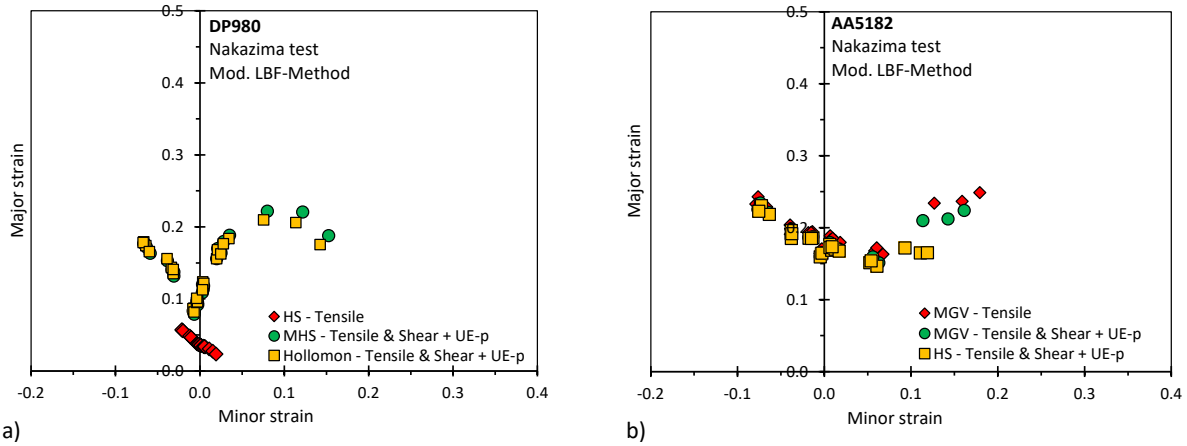


**Figure 25: Influence of the choice of constitutive model and calibration technique on the phenomenological mapping criterion to correct the Nakazima limit strains of the DP980 (a) and AA5182 (b) for contact pressure (P) effects.**

## 3.4 Prediction of the Plane-Stress FLC

The MMFC of Hora *et al.* (2013) determines stable deformation from the following condition

$$\frac{\partial\sigma_1}{\partial\varepsilon_1}+\frac{\partial\sigma_1}{\partial\rho}>\sigma_1, \qquad d\rho=\left(\sigma_1-\frac{\partial\sigma_1}{\partial\varepsilon_1}\right)d\varepsilon_1\left(\frac{\partial\sigma_1}{\partial\rho}\right)^{-1} \tag{14a,b}$$

where $d\rho$ represents the increment in the principal in-plane strain ratio during acute localization until a state of plane strain tension is reached. The functional form of $d\rho$ in the model of Hora *et al.* (2013) is phenomenologically derived from the experimental observation of an approximately constant load in a tensile test even for deformation beyond diffuse necking. This assumption is revisited in Chapter 4 from a physical consideration and shown to be one of two possible scenarios for a quasi-stable localization process.

In analogy to the process corrections, the sensitivity of the calibration technique of the constitutive model was also studied for the limit strain predictions using the MMFC. The yield function – von Mises and Hosford FCC for the DP980 and AA5182, respectively – was maintained constant. As depicted in **Figure 26**, the conventional calibration technique without enforcing the plastic uniform elongation resulted in an inadvertent shift of the plane strain limit strain by approximately 0.03 and 0.02 for the DP980 and the AA5182, respectively. Since limit strains in the MMFC are based upon the maximum load in plane strain loading, diffuse and acute necking limits are identical for a strain-rate independent material. As a result, enforcing the UE-p constraint in the calibration of the constitutive model mitigates artefacts in the predicted $FLC_0$ as demonstrated for the calibration scenarios (ii)-(iv). The DP980 is less sensitive to the choice of the constitutive model as long as it is calibrated to strain levels beyond diffuse necking, *e.g.* by consideration of shear or bulge data, and the plastic uniform elongation is enforced. In contrast to the DP980, limit strain predictions on the stretch side of the FLC for the AA5182 strongly vary with the selected hardening model even when calibrated to experimental strain data beyond 0.5 equivalent plastic strain.

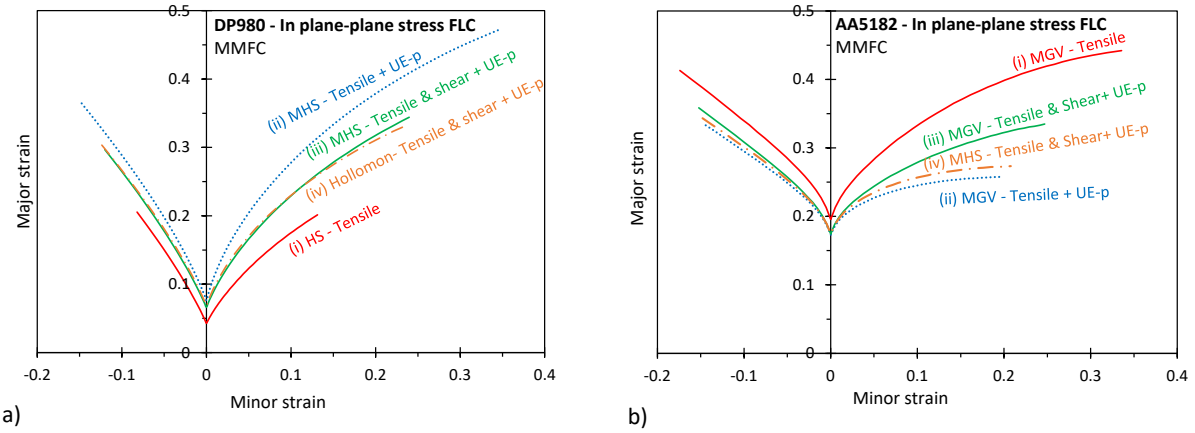


**Figure 26: Effect of the choice of constitutive model and calibration technique on the predicted in plane-plane stress limit strains using the MMFC of Hora *et al.* (2013) for the DP980 AHSS (a) and the AA5182 alloy (b).**

In agreement with the physical framework of the MMFC, the process-corrected Nakazima and Marciniak limit strains are adopted to assess correlations in **Figure 27**. It is emphasized that wrong conclusions may be drawn by comparing the predictions of analytical models or by calibration of the formability models to implicitly account for the process effects in the Nakazima FLC. Model predictions

for the DP980 are in excellent agreement with the corrected limit strains for in-plane deformation. In contrast, limit strain predictions for the studied AA5182 overestimate the experimental limit strains for in-plane stretching and the Marciniak FLC is still lower than the corrected Nakazima limit strains. Relative to the DP980, the AA5182 was shown to be more sensitive to the selection of the constitutive model in addition to complications surrounding the presence of PLC effects, which promoted asymmetric strain distribution and complicated identification of the limit strain. In addition, the negative strain rate sensitivity of the AA5182, as reported by Rahmaan *et al.* (2015), may lead to an acceleration of the localization process that was not considered in the MMFC implementation. Thus, limit strain predictions for the AA5182 should be considered as an upper limit since it is based upon localization when the strain path has reached plane strain tension. The MMFC predictions are in better agreement with the limit strains obtained from the ISO 12004-2 method, particularly around plane strain tension (major principal strain of 0.16 *versus* predicted 0.17).

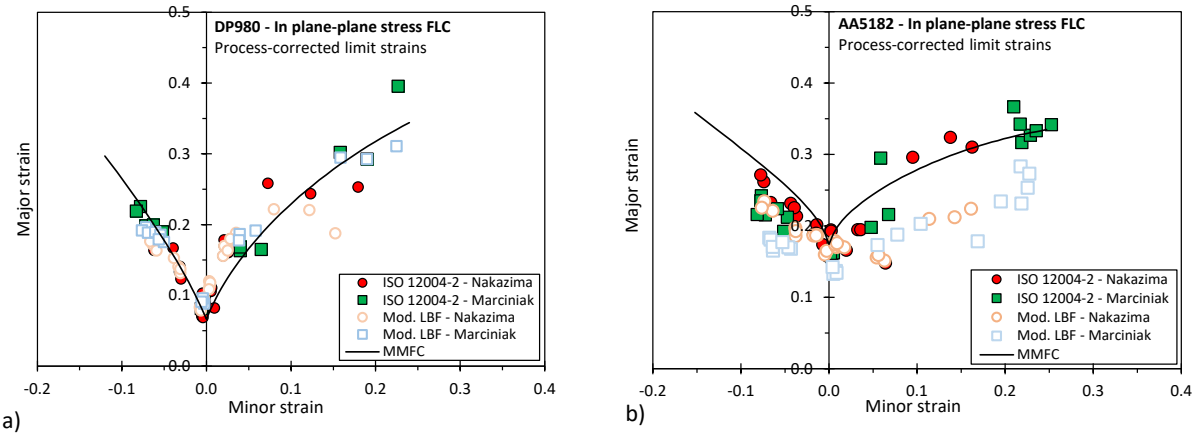


**Figure 27: Comparison of the analytical FLC prediction using the MMFC of Hora *et al.* (2013) with the process-corrected limit strains for the DP980 (a) and the AA5182 (a).**

## 3.5 Application of the MMFC to a Broader Class of Automotive Steels

The applicability of the MMFC (Hora *et al.*, 2013) to other classes of AHSS was critically assessed by consideration of the steel grades summarized in **Table 3**. It is noted that the experimental data for the MP980 was retrieved from the study of Min *et al.* (2016) that considered two different punch sizes ($r_p$ of Nakazima I: 25.4 mm and Nakazima II: 50.8 mm). The 3rd Gen 980 and 3rd Gen 1180 V1 were characterized in Gutierrez *et al.* (2020) and the 3rd Gen 1180 V2 in Noder *et al.* (2021b) employing the same experimental procedures and techniques as discussed in this chapter.

**Table 3: Tensile mechanical properties of AHSS grades obtained from the literature. Note that the MP980 was retrieved from the study of Min *et al.* (2016) and the 3rd Gen 980 and 1180 V1 in Gutierrez *et al.* (2020). Note that RD and TD refer to the sheet rolling and transverse direction, respectively.**

| | Yield Stress (0.2% offset) (MPa) | Ultimate Tensile Stress (MPa) | Uniform Elongation UE (%) | Total Elongation TE (%) | R-value |
|---|---|---|---|---|---|
| **MP980, 1.2 mm, RD** | NA | NA | NA | NA | 0.84 |
| **3rd Gen 980, 1.4 mm, TD** | 681 (±2) | 1034 (±10) | 18 (±0.5) | 24.9 (±0.6) | 0.90 (±0.00) |
| **3rd Gen 1180 V1, 1.4 mm, TD** | 950 (±12) | 1251 (±8) | 8.4 (±0.2) | 14.1 (±0.6) | 0.90 (±0.01) |
| **3rd Gen 1180 V2, 1.4 mm, TD** | 1043 (±4) | 1225 (±8) | 10.7 (±0.4) | 16.4 (±0.3) | 0.89 (±0.00) |

For consistency with the experimental limit strains, which were corrected for non-linear strain path effects, the predicted forming limits were corrected using a linearized MMFC (Gutierrez *et al.*, 2020). The equivalent plastic strain is integrated using the incremental plastic work balance in Eq. (9a) for plane stress loading ( $\chi$ = 0) and the in-plane strain and stress ratio at diffuse necking, $\rho^{diff}$ and $\alpha^{diff}$, are employed to linearize the principal in-plane strains

$$\tilde{\varepsilon}_1^{MMFC} = \frac{\varepsilon_{eq}^{p}}{k\left(\alpha^{diff}\right)\left(1+\alpha^{diff}\rho^{diff}\right)}, \qquad \tilde{\varepsilon}_2^{MMFC} = \rho^{diff}\tilde{\varepsilon}_1^{MMFC} \tag{15a,b}$$

**Figure 28** demonstrates the capability of the MMFC framework to accurately predict the in-plane forming limits for conventional AHSS and the new class of 3rd Gen AHSS. It is noted that the predicted $FLC_0$ is in good agreement with the experiments for all tested steel grades and is a direct consequence of the plastic uniform elongation enforced in the calibration of the constitutive model. The Marciniak limit strains for the MP980 appear somewhat higher around plane strain tension that may be a result of the curvature-based detection method. Strain-rate sensitivity can delay the formation of a neck to higher strains before an appreciable change in the curvature can be detected whereas the theoretical $FLC_0$ is for the onset of diffuse necking under quasi-static conditions. Overall, the difference in the MMFC variants is largest on the stretch side of the FLC where non-linear strain path effects are most prominent. The MMFC of Hora *et al.* (2013) can be seen as an upper limit whereas the linearized variant better captures the overall trend of the in-plane formability. Overall, the global formability of the studied 3rd Gen 1180 AHSS steel grades is similar and only marginally better than a DP1180 steel (Noder *et al.*, 2021b) whereas the local formability in Chapter 5 will be shown to vary significantly. In contrast, the superior performance of the studied 3rd Gen 980 AHSS relative to the DP980 and the MP980 steels exemplifies the potential of 3rd Gen steels for automotive lightweight applications.

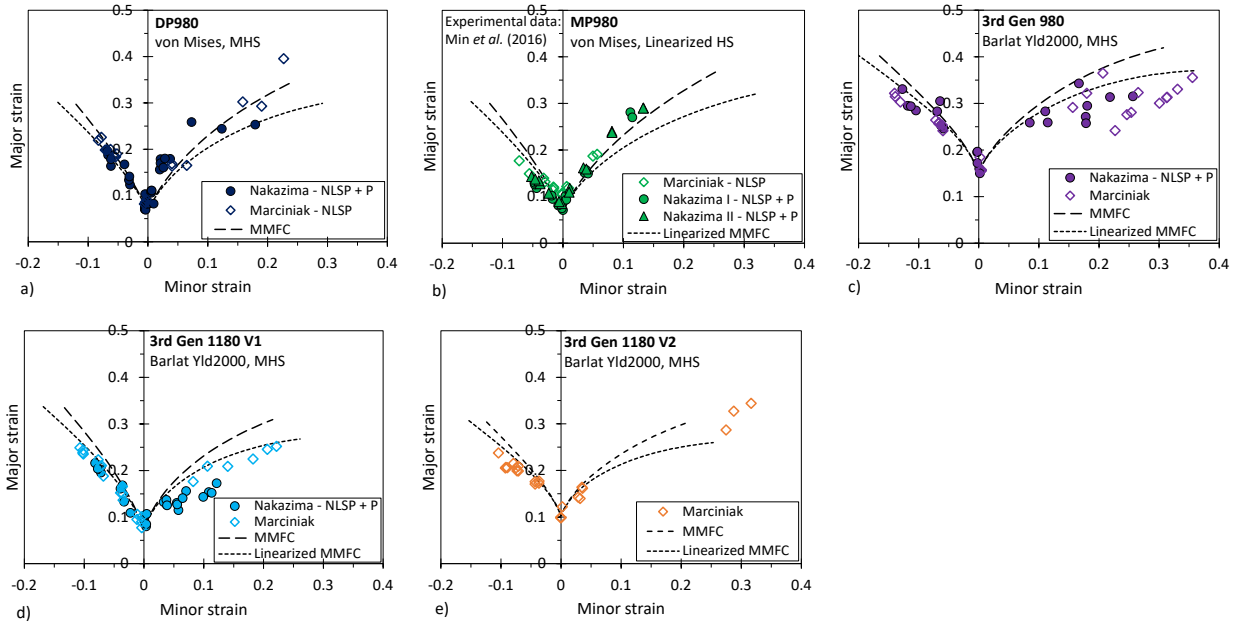


**Figure 28: Comparison of analytical forming limit predictions using the MMFC of Hora *et al.* (2013) and the linearized MMFC of Gutierrez *et al.* (2020) to experimental limit strains in process-corrected Nakazima and Marciniak tests for the DP980 (a), MP980 (b), 3rd Gen 980 (c), 3rd Gen 1180 V1 (d), and the 3rd Gen 1180 V2 (e).**

## 3.6 Discussion of In-Plane Formability

This study provided a robust and mechanistic framework to predict the in plane-plane stress forming limit curve for AHSS. The shortcomings of a drifting $FLC_0$ in the MMFC of Hora *et al.* (2013) was mitigated by adoption of a constrained calibration of the constitutive model to enforce the plastic uniform elongation identified in the tensile test. Thus, the introduction of additional material constants upon calibration of the MMFC, as proposed by Paraianu *et al.* (2010), was not required in the present study. In a rate-sensitive material, the Considère criterion would be enforced using the strain rates consistent with the formability tests. Accurate calibration of the constitutive model at strain levels associated with biaxial limit strains is crucial for the accurate prediction of the limit strains. In stark contrast to the DP980, the AA5182 with its saturation-type hardening behavior was very sensitive to the choice of the hardening model even when utilizing a constrained calibration and hardening data available to strain levels beyond diffuse necking in a tensile test.

From an academic perspective, Marciniak limit strains are preferred since they are consistent with the physical framework of plane stress loading, inherent to the vast majority of instability models in the literature. The strain path in Marciniak tests is approximately linear such that the value added by the non-linear strain path analysis and error associated with the choice of a yield function and constitutive model to integrate the equivalent plastic strain does not appear to be warranted. The Marciniak limit strains can be used directly. By contrast, non-linear strain path and pressure effects in the Nakazima tests cannot be

neglected. Erroneous conclusions may be drawn when the formability predictions are compared against an uncorrected Nakazima FLC. Unfortunately, correcting the Nakazima limit strains for process effects by linearization of the strain path and constant stress mapping were found to be very sensitive to the limit strain detection method and the material hardening rate. Selective limit strains identified from the ISO 12004-2 method experienced a stark shift towards plane strain tension suggesting that the limit strains were likely too high. A refined version of the LBF Method of Volk and Hora (2011) was employed as an alternative detection method. The fitting window for the stable strain rate was determined from physical considerations and is readily amenable to angular stretch-bend and V-Bend tests in Chapter 5. Limit strains of the two detection methods were in close agreement for the DP980 whereas larger deviations were found for the AA5182 due to challenges with multiple necking zones, asymmetric strain distribution, and PLC effect. The stress-based mapping to account for the contact pressure was found to be problematic for materials that exhibit a saturation-type hardening behavior similar to a perfectly plastic material for which an infinite formability gain is predicted for infinitesimally small non-zero contact pressures.

# 4. Prediction of In-Plane Forming Limits under 3D Stress States (Task 2)

The MMFC of Hora *et al.* (2013) and the linearized variant of Gutierrez *et al.* (2020) demonstrated excellent predictive capability for AHSS but the limitation to plane stress loading is problematic since tool contact pressure is neglected. In addition, the diffuse localization process to form an acute neck was proposed from experimental observations rather than physical considerations. Similarly, the phenomenological stress-mapping was found to be potentially problematic given its predictions for low-hardening materials. It remains uncertain whether the stress-mapping has any physical underpinning due to the lack of an analytical framework to compare against. To these ends, the effect of a compressive tool contact stress on plastic instability was studied on a physical basis adopting the Hillier (1963) general instability framework. First, the derivation of the Hillier (1963) framework is reviewed as part of this study to assess the underlying assumption of commonly adopted 2D instability models of Considère (1885), Swift (1952), Dorn (Dorn and Thomsen, 1947), and Zener-Holllomon (1944). To provide insight into the seemingly contradictive formability gains reported for the 3D MK framework between a constant contact pressure (Assempour *et al.*, 2010, Zhang *et al.*, 2014; Lang *et al.*, 2015) and a proportionally evolving normal pressure (Allwood and Shouler, 2009; Mirfalah-Nasiri *et al.*, 2016), closed-form solutions for the respective boundary conditions are derived from the Hillier framework. These closed-form solutions also serve to critically assess the validity of the predicted formability gains in the plane strain limit strain utilizing the phenomenological mapping criteria. The methods of Smith *et al. (*2003) and Matin and Smith (2005) only remove the effect of the stress incurred due to contact pressure whereas removing the plastic work appears more physically-motivated and is explored as part of this study.

The restriction of the Hillier (1963) framework to the onset of instability has hindered its adoption as the limit strains at the end of the diffuse necking, when an acute neck has formed, are relevant for industrial forming operation. The mechanics of the diffuse localization process in terms of a quasi-stable transition of the stress state under a vanishing second order plastic work rate can be derived from Hillier stability and assessed by careful analysis of the diffuse necking process in tensile tests of AHSS. In fact, it is shown that the MMFC (Hora *et al.*, 2013) is physically motivated and only one special case of the general framework proposed in this research. Application to formability tests and forming operations requires identification of the local boundary conditions of the deformation history. To this end, formability predictions under different boundary conditions are contrasted with the Marciniak and (uncorrected) Nakazima limit strains for the DP980 of Chapter 3.

The prepared manuscript can be found in Appendix B in:

**Noder, J.,** Butcher, C. A General Instability Framework for Ductile Metals in Complex Stress States from Diffuse to Acute Localization, to be submitted, May 2022.

## 4.1 Fundamentals

Hillier (1963) derived the onset of plastic instability for a rigid-plastic material that adheres to associated plasticity from a bifurcation in the stress path that he later derived from an energy consideration (1974). Instability occurs when the second order plastic work rate is exactly zero

$$dW^p \equiv \int_V \left( d\sigma_i d\varepsilon_i \right) dV = \int_A \left( dF_i du_i \right) dA = 0 \quad \text{where } du_i \geq 0 \tag{16}$$

where $du_i$ corresponds to the vector of applied displacement increments and $dF_i$ to the load increments. It is noted that Eq. (16) is equivalent to the condition of neutral incremental stability in Drucker's postulate (1951) and Hill's incremental stability for a rigid-plastic material (1950). Hillier adopted plastic work equivalence to express $d\sigma_{ij} d\varepsilon_{ij} = d\sigma_{eq} d\varepsilon_{eq}^p$ and re-casted the instability condition of Eq. (16) in terms of instantaneous tangents to the generalized equivalent stress and a critical subtangent, $z$

$$\frac{1}{\bar{\sigma}} \frac{d\bar{\sigma}}{d\varepsilon_{eq}^p} = \frac{1}{z} = \frac{N_{\delta j}}{\sigma_{eq}} \left( \frac{1}{A_\delta} \frac{\partial F_{\delta j}}{\partial \varepsilon_{ml}} \frac{d\varepsilon_{ml}}{d\varepsilon_{eq}^p} + \sigma_{\delta j} \delta_{\delta\beta} N_{\delta\beta} \right), \qquad N_{\delta j} = \frac{\partial \sigma_{eq}}{\partial \sigma_{\delta j}} \tag{17a,b}$$

which is governed by the plasticity model and the applied boundary conditions. For triaxial loading, Eq. (17a) is compactly written as

$$\frac{1}{\bar{\sigma}} \frac{d\bar{\sigma}}{d\varepsilon_{eq}^p} = \frac{1}{z} = \frac{1}{\sigma_{eq}} \sum_{\delta=1}^{3} \sum_{j=1}^{3} N_\delta \left( \frac{1}{A_\delta} \frac{\partial F_\delta}{\partial \varepsilon_j} \frac{d\varepsilon_j}{d\varepsilon_{eq}^p} + \sigma_\delta N_\delta \right) \tag{18}$$

where tensor summation rules are suspended for Greek suffixes. The variable $\bar{\sigma}$ corresponds to the material flow stress, $\sigma_{eq}$ to the equivalent stress, $A_\delta$ to the area upon which the loads, $F_\delta$, are applied and $N_\delta$ to the normal vector. The term on the left-hand side of Eq. (18) represents the equivalent material response in terms of the equivalent stress and hardening rate caused by the applied tractions and change in the area on the right-hand side. Deformation becomes unstable when the critical subtangent, visualized in **Figure 29**, intersects the material hardening curve. The larger the value of the critical subtangent, the higher is the strain for diffuse necking.

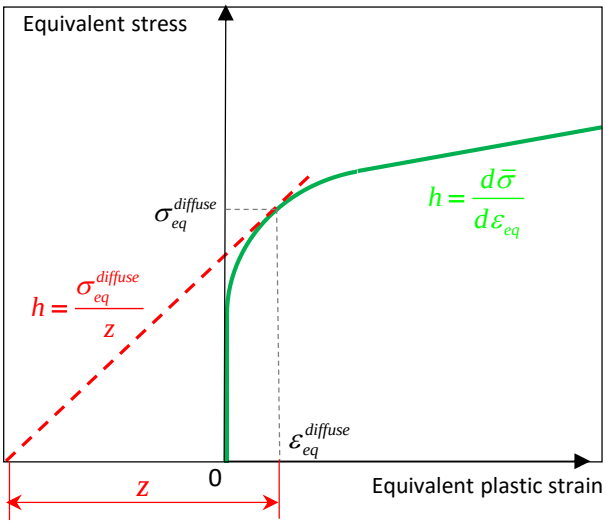


**Figure 29: Schematic illustration of instability at the intersection of the critical subtangent with the material hardening curve.**

The onset of instability is governed by the material response to the load rates. Hillier (1963) postulated that instability occurs when all applied load rates reach a maximum simultaneously or when one or more loads attain a maximum while the other(s) are constant or non-existent. The assumption of vanishing load rates for instability to occur is not required but convenient for analytical modelling since knowledge of the load rates is seldom known *a priori* unless in simple loading cases such as uniaxial stretching. In the scope of this study, the assumption of vanishing load rates is employed and further discussed in Section 4.4.

## 4.2 Effect of Boundary Condition on Diffuse Necking

To establish an understanding for how plastic instability is affected by the local boundary conditions of the deformation process, analytical solutions were derived from the general Hillier (1963) framework considering different loading scenarios. The von Mises (vM) yield function was selected to enable compact closed-form solutions. The flow stress and hardening rate are described through the Swift hardening model

$$\bar{\sigma} = K\left(\varepsilon_0 + \varepsilon_{eq}^p\right)^n, \qquad h = \frac{d\bar{\sigma}}{d\varepsilon_{eq}^p} = \frac{n\bar{\sigma}}{\left(\varepsilon_{eq}^p + \varepsilon_0\right)} \tag{19a,b}$$

with $K$ = 500 MPa, $\varepsilon_0$ = 0.002, and $n$ = 0.1

### 4.2.1 Instability under Plane Stress Loading

First, commonly adopted plane stress instability criteria were derived. Prior to Swift (1952), Dorn and Thomsen (1947) applied the Considère (1885) solution for uniaxial tension to arbitrary stress states. Instability occurs when the principal hardening rate is equal to the major principal stress

$$\frac{d\sigma_1}{d\varepsilon_1} = \sigma_1, \qquad \frac{1}{\bar{\sigma}}\frac{d\bar{\sigma}}{d\varepsilon_{eq}^p} = \frac{1}{z^{Dorn}} = N_1 \tag{20a,b}$$

which is re-casted into the critical subtangent of Hillier in Eq. (20b). Assuming plane stress *proportional loading*, the critical subtangent in Eq. (18) reduces to

$$\frac{1}{z^{\text{P. Load}}} = k(\tilde{\alpha})N_1\left(N_1 + \tilde{\alpha}N_2\right) = N_1(\tilde{\alpha}), \qquad \tilde{\alpha} = \frac{\sigma_2}{\sigma_1} \neq \text{constant} \tag{21a,b}$$

where $\tilde{\alpha}$ evolves with deformation to maintain proportionality of the loads. Details on the derivation are provided in Appendix E3. Although Eq. (21a) appears identical to the Dorn solution in Eq. (20b), it differs by the in-plane stress ratio that is taken as constant in Dorn but evolves in proportional loading. The Dorn model can be viewed as corresponding to approximately proportional loading conditions if the strain levels are sufficiently small to neglect geometric changes. To derive the Dorn solution under *proportional stressing* when the major load reaches a maximum, the critical subtangent is

$$\frac{1}{z^{\text{P. Stress}}} = \frac{1}{\sigma_{eq}}\left[\sigma_1(N_1)^2 + N_2\left(\frac{1}{A_2}\frac{\partial F_2}{\partial \varepsilon_m}\frac{d\varepsilon_m}{d\varepsilon_{eq}^p} + \alpha\sigma_1 N_2\right)\right] \tag{22}$$

where a non-zero load rate of the following form must exist to obtain neutral stability

$$\frac{1}{A_2}\frac{\partial F_2}{\partial \varepsilon_m}\frac{d\varepsilon_m}{d\varepsilon_{eq}^p} = \frac{\sigma_{eq}N_1\left(1-kN_1\right)}{N_2} - \alpha k\sigma_{eq}N_2 \tag{23}$$

which has a strong coupling with the stress ratio. Although the load rate in Eq. (23) is mathematically admissible, it appears unrealistic for such a specific load path to occur in formability characterization tests such as Nakazima or Marciniak tests. The Dorn solution based upon the extension of the Considère model appears to have a tenuous physical foundation for proportional stressing but can be viewed as a first-order estimate for proportional loading.

The instability model of Swift (1952) follows from Eq. (22) by assuming a vanishing minor load rate, $\partial F / \partial \varepsilon_{eq}^p = 0$, that further simplifies to the Considère (1885) criterion for a vanishing in-plane stress ratio ($\alpha = 0$). Additional conditions were explored by superimposing in-plane shear stresses that can be seen as an extension of the Swift (1952) model to shear loading in Eq. (27a,b). The Zener-Hollomon (1944) criterion follows for the limiting case of pure shear loading ($\sigma_{11} = -\sigma_{22}$) or simples shear ($\sigma_{12} \gg \sigma_{11}$) in Eq. (28a,b) where the critical subtangent vanishes and instability in shear can only occur when the material

hardening rate becomes negative. Equations for the critical subtangent and closed-form solutions for von Mises plasticity are summarized in **Table 4** and visualized in **Figure 30**. Even under plane stress conditions, instability in proportional stressing creates not a single curve but a surface based upon the composition of the stress state. A superimposed shear delays localization as discussed in Butcher and Abedini (2019a) in the context of tension-torsion tests. The typical S-shaped curve of the Swift model (1952) only correlates with the instability model of Dorn and Thomsen (1947) for strain paths of uniaxial tension (UT), plane strain tension (PST), and biaxial tension (BT).

**Table 4: Summary of critical subtangent derived for the respective instability criterion for plane stress loading.**

| Instability criteria | Critical subtangent and corresponding von Mises (vM) form | Eq. |
|---|---|---|
| Dorn and Thomsen (1947) | $\frac{1}{z}=N_1, \quad \frac{1}{z_{vM}}=\frac{1}{2}\frac{(2-\alpha)}{\left(1-\alpha+\alpha^2\right)^{\frac{1}{2}}}$ | (24a,b) |
| Considère (1885) | $\frac{1}{z}=1, \quad \frac{1}{z_{vM}}=1$ | (25a,b) |
| Swift (1952) | $\frac{1}{z}=k\left[(N_1)^2+\alpha\left(N_2\right)^2\right], \quad \frac{1}{z_{vM}}=\frac{1}{4}\frac{\left(4\alpha^3-3\alpha^2-3\alpha+4\right)}{\left(1-\alpha+\alpha^2\right)^{\frac{3}{2}}}$ | (26a,b) |
| Swift + Shear | $\frac{1}{z}=\frac{\sigma_{11}}{\sigma_{eq}}\left[\left(N_{11}\right)^2+\beta N_{12}\left(N_{11}+N_{22}\right)+\alpha'\left(N_{22}\right)^2\right]$ <br> $\frac{1}{z_{vM}}=\frac{1}{4}\frac{\left(4\alpha'^3-3\alpha'^2+3\alpha'\beta^2-3\alpha'+3\beta^2+4\right)}{\left(1-\alpha'+\alpha'^2+3\beta^2\right)^{\frac{3}{2}}}, \ \beta=\frac{\sigma_{12}}{\sigma_{11}}, \ \ \alpha'=\frac{\sigma_{22}}{\sigma_{11}}$ | (27a,b) |
| Zener-Hollomon (1944) | $\frac{1}{z}=0, \quad \frac{1}{z_{vM}}=0$ | (28a,b) |

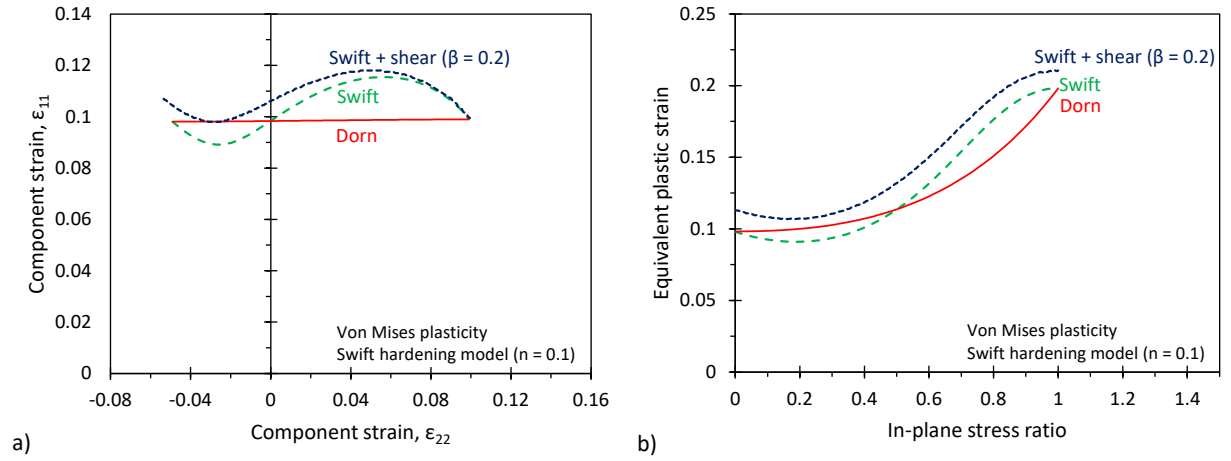


**Figure 30: Comparison of predicted diffuse necking limits considering different instability criteria under plane stress loading in component strain space (a) and equivalent strain space (b).**

### 4.2.2 Instability under Principal Triaxial Loading

Tool contact during forming produces compressive through-thickness normal and shear stresses. Since shear stresses were reported to be an order of magnitude lower than the normal pressure due to lubrication (Bettaieb and Abed-Meraim, 2017), the effect of shear stresses upon plastic stability in the presence of contact pressure was not considered in this study. To assess the effect of the boundary conditions upon a compressive normal stress, the following three loading scenarios were considered and are visualized in **Figure 31**. The critical subtangent is presented in general form and simplified to von Mises plasticity.

Case #1: Proportional triaxial stressing (*P. Stress*)

The material is *proportionally stressed* in- and out-of-plane and can be seen as an extension of the Swift (1952) instability model from 2D to 3D loading. The applied *loads* are *controlled independently* to maintain the target in-plane, $\alpha$ , and through-thickness stress ratio, $\chi$ .This loading scenario can be envisioned as an upgraded version of the servo-controlled biaxial tensile frame in the study of Kuwabara *et al.* (1998). In addition to the in-plane actuators, which are PID (proportional-integral-derivative) stress-controlled, a third actuator employs out-of-plane loading. The critical subtangent is

$$\frac{1}{z} = k\left(N_1\right)^2\left(1+\alpha\rho^2+\chi\omega^2\right), \qquad \omega = \frac{N_3}{N_1}$$

P. Stress (3D Swift)

$$\frac{1}{z_{vM}} = \frac{1}{4}\frac{\left(4\chi^3-3\alpha\chi^2-3\chi^2-3\alpha^2\chi+6\alpha\chi-3\chi+4\alpha^3-3\alpha^2-3\alpha+4\right)}{\left(1-\alpha+\alpha^2-\chi+\chi^2-\alpha\chi\right)^{\frac{3}{2}}} \tag{29a-c}$$

where $k$, $\alpha$, and $\chi$ are defined in Eq. (8b), (8c) and (9b), respectively and $\omega$ corresponds to the principal through-thickness strain ratio.

Case #2: Non-proportional triaxial stressing with a constant normal load (*NP., $F_3$ const.*)

In analogy to Case #1, the *in-plane loads* are controlled *independently* to maintain proportional in-plane stressing whereas a *constant normal load* ($dF_3 = 0$), in the form of a dead weight, is applied in the sheet normal direction. This is akin to a forming operation involving biaxial in-plane stretching under a constant binder load. During deformation, the contact area increases and since the normal load is assumed to be constant, the contact pressure decreases and introduces a non-linear strain path. The critical subtangent is

NP., $F_3$ const.

$$\frac{1}{z} = k\left(N_1\right)^2\left(1+\alpha\rho^2+\tilde{\chi}\omega^2\right), \qquad \tilde{\chi} = \frac{\sigma_{3,0}\exp\left(\varepsilon_3\right)}{\sigma_1}, \qquad \sigma_{3,0} = \chi_0\sigma_y$$

$$\frac{1}{z_{\mathrm{vM}}} = \frac{1}{4}\frac{\left(4\tilde{\chi}^3-3\alpha\tilde{\chi}^2-3\tilde{\chi}^2-3\alpha^2\tilde{\chi}+6\alpha\tilde{\chi}-3\tilde{\chi}+4\alpha^3-3\alpha^2-3\alpha+4\right)}{\left(1-\alpha+\alpha^2-\tilde{\chi}+\tilde{\chi}^2-\alpha\tilde{\chi}\right)^{\frac{3}{2}}} \tag{30a-d}$$

where the evolving through-thickness stress ratio, $\tilde{\chi}$, is expressed in terms of the initial compressive pre-stress, $\sigma_{3,0}$, defined with respect to the material yield stress, $\sigma_y$, an initial through-thickness stress ratio, $\chi_0$, and the instantaneous contact area obtained from volume conservation.

Case #3: Non-Proportional triaxial stressing with a constant normal pressure (*NP., $P_3$ const.)*

The boundary conditions for the in-plane loads are identical to the preceding cases but the normal load is adjusted to maintain a *constant magnitude of the normal pressure*, as common in the MK analysis (Assempour *et al.*, 2010, Hashemi and Abrinia, 2014; Erfanian and Hashemi, 2018; Nurcheshmeh and Green, 2012; Zhang *et al.*, 2014; Lang *et al.*, 2015). These boundary conditions are equivalent to a forming operation of equi-biaxial stretching in the sheet plane with an adjustable binder load. For a strain-hardening material the contact stress ratio decreases as the major stress increases. The critical subtangent is

NP., $P_3$ const.

$$\frac{1}{z} = k\left(N_1\right)^2\left(1+\alpha\rho^2\right), \qquad \hat{\chi} = \frac{\sigma_{3,0}}{\sigma_1},$$

$$\frac{1}{z_{\mathrm{vM}}} = \frac{1}{4}\frac{\left(\alpha\hat{\chi}^2+\hat{\chi}^2-4\alpha^2\hat{\chi}+4\alpha\hat{\chi}-4\hat{\chi}+4\alpha^3-3\alpha^2-3\alpha+4\right)}{\left(1-\alpha+\alpha^2-\hat{\chi}+\hat{\chi}^2-\alpha\hat{\chi}\right)^{\frac{3}{2}}} \tag{31a-c}$$

where the evolving through-thickness stress ratio, $\hat{\chi}$, is computed from the initial contact pressure and the current major stress.

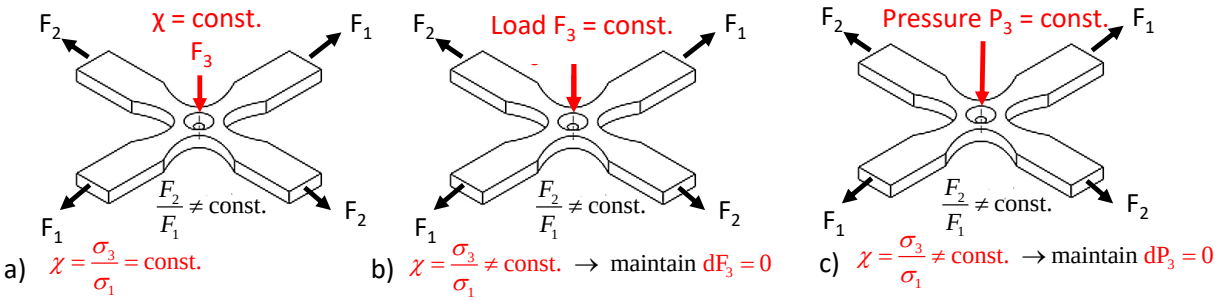


**Figure 31: Schematic of prescribed boundary conditions for the studied loading scenarios of proportional stressing (a) and non-proportional stressing with a constant binder load (b) or a constant contact pressure (c). Note that the schematic of the cruciform specimen is retrieved from Montalvão and Wren (2017).**

The effect of an initial through-thickness stress ratio of $\chi_0$ = -0.2 and the applied boundary conditions upon plastic instability are evaluated for the discussed loading scenarios in **Figure 32**.

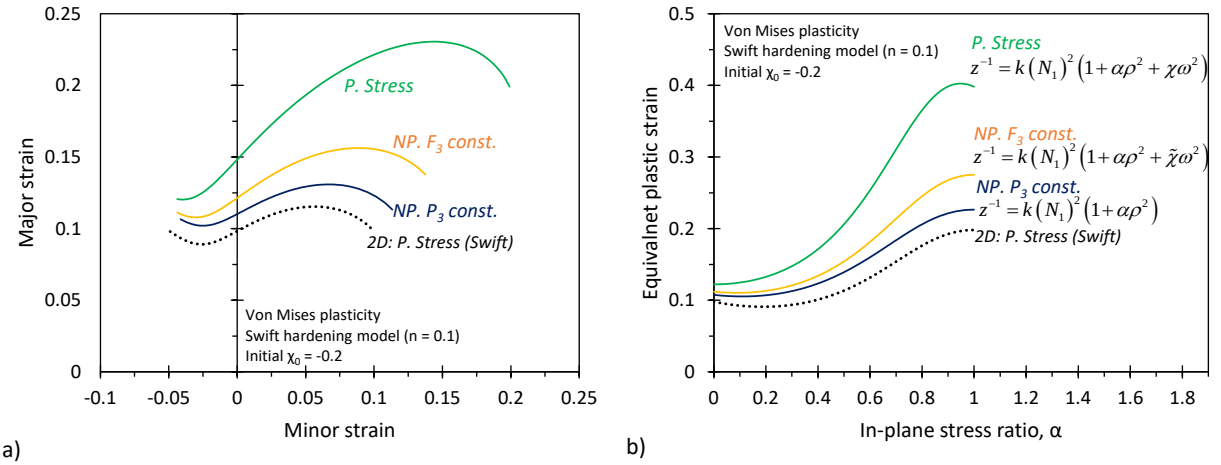


**Figure 32: Effect of compressive normal stress and applied boundary conditions upon diffuse necking in triaxial loading relative to a plane stress state shown for component strains (a) and equivalent plastic strain (b). Note that P. refers to proportional and NP. to non-proportional stressing. The normal load and normal pressure are abbreviated with $F_3$ and $P_3$, respectively.**

Relative to plane stress loading, the presence of a normal pressure leads to a delay in diffuse necking for all considered scenarios whereas the magnitude of the formability gain is governed by the boundary condition of how the out-of-plane pressure is applied. The largest formability gains are predicted when the contact pressure evolves proportionally with the major in-plane stress (proportional stressing) in which the increase in the limit strains is magnified for biaxial strain paths. Instead, if the compressive normal load is maintained constant, the instability curve is still increased relative to plane stress loading but the formability gains are lower than for proportional stressing. The decrease in the through-thickness stress ratio from an initial value of -0.2 to an average final value of -0.11 to maintain a constant normal load accelerates the

process to reach instability. For a constant contact pressure, the principal through-thickness stress ratio also decreases (from -0.2 to an average value of -0.13) but the contact pressure provides less stabilization since it is only embedded as a secondary effect *via* the constitutive model (compare Eq. (29a), (30a) *versus* Eq. (31a)). The shift in the instability strains manifest as an approximately constant offset across stress states and confirms the findings reported for the MK framework that commonly adopt a constant contact pressure (Abrinia, 2014; Erfanian and Hashemi, 2018; Nurcheshmeh and Green, 2012; Zhang *et al.*, 2014; Lang *et al.*, 2015). An advantage of the present work is that unlike the numerical MK framework, closed form analytical solutions for the influence of the boundary condition can be obtained using the Hillier framework.

The conventional representation of the instability limits in the form of a curve should be replaced with instability surfaces. The choice of surface depends upon the instantaneous boundary conditions and composition of the stress state as shown in **Figure 33**. Even in plane stress, the influence of the superimposed shear stress delays the onset of instability that is excluded in the current literature, which is focused on the major and minor stress in the absence of shear. The Hillier framework can readily be used to consider out-of-plane shear and other combined loading scenarios.

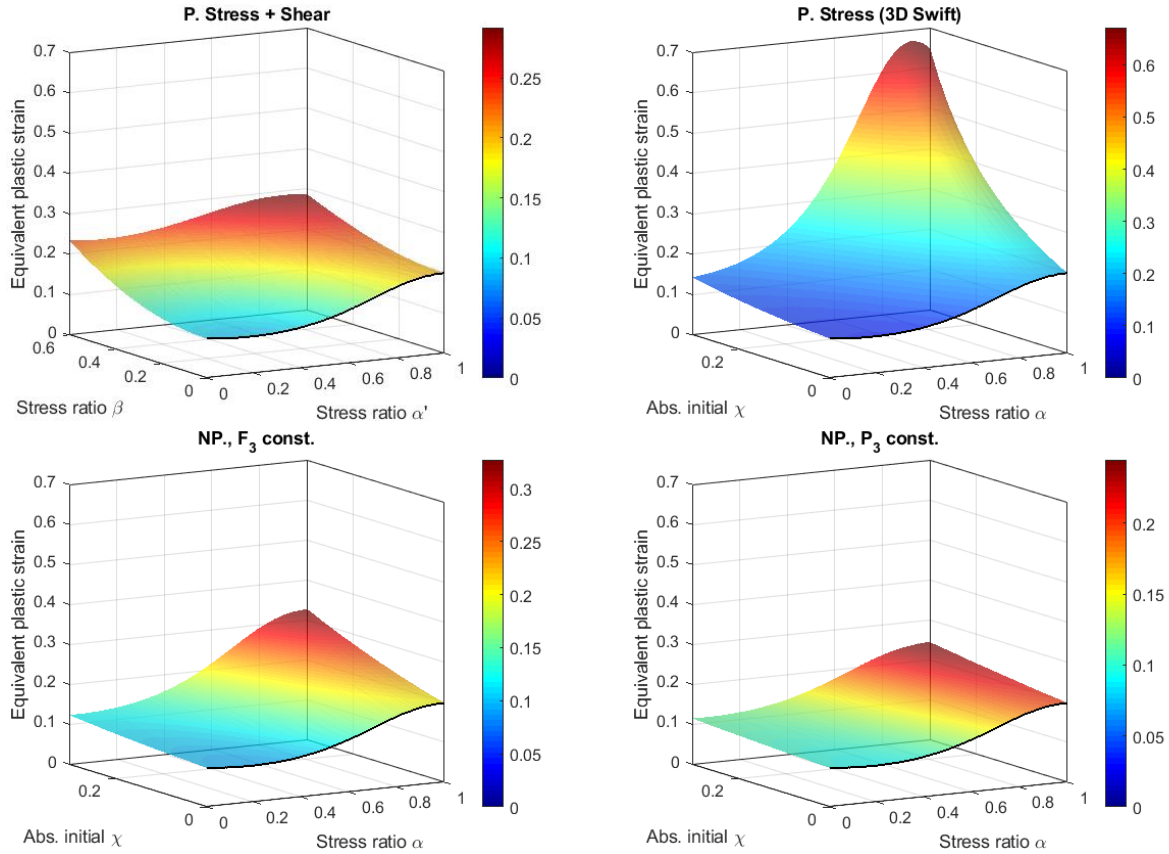


**Figure 33: Surfaces that demonstrate the instantaneous nature of plastic instability considering the effect of shear and a through-thickness normal pressure for proportional triaxial stressing (P. Stress) and non-proportional stressing assuming a constant normal load (NP, $F_3$ const.) or normal pressure (NP., $P_3$ const.).**

## 4.3 Evaluation of Mapping Criteria for Influence of Contact Pressure on Instability

The analytical solutions derived in the preceding section were utilized to evaluate the validity of phenomenological mapping criteria. To enable a discussion of formability in terms of the acute limit strains, only plane strain loading was considered since the diffuse and acute necking strains are identical for a strain-rate independent material. Loading of a wide plate in the principal 1-3 plane is assumed such that one load is applied in the primary loading direction to stretch the material in-plane and a second load acts normal to the sheet thickness to mimic tool contact. In the absence of the normal load – in the 2D stress space – the wide sheet is under plane strain tension due to in-plane stretching in the principal 1-direction. Both load rates are assumed to vanish at the instant of instability. The formability gain in the $FLC_0$ in the phenomenological mapping criteria is obtained by mapping from 2D to 3D stress space. It is emphasized that plane strain tension under a triaxial stress state is preserved as a natural consequence of mapping under a constant in-plane strain ratio, since similar to the stress-controlled implementation of the analytical solutions, the in-plane stress-ratio evolves with $\chi$. In contrast, mapping under a constant in-plane stress ratio inevitably induces a shift of the strain path to positive minor strains since the constant in-plane stress ratio does not reflect the constant strain path of plane strain tension as visualized in **Figure 34**. While it is true that an imposed contact pressure will induce a measure of biaxial straining for a pressure independent material, the applied stress state in the problem has been designed to produce plane strain. Thus, the predicted biaxial shift of the limit strains is erroneous as it violates the strain path imposed by discarding the through-thickness stress.

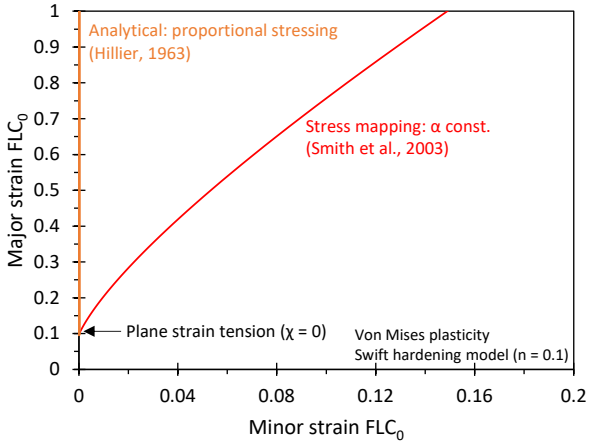


**Figure 34: Shift of the plane strain limit strain ($FLC_0$) to positive minor strains for increasing through-thickness stress ratios considering mapping under a constant principal in-plane stress ratio and the restored linear strain path when using the analytical Hillier solution for proportional stressing.**

Variables related to the stress state in this section are highlighted with a 2D or 3D superscript to clarify whether they depend upon the plane stress or triaxial stress state, respectively. Analytical solutions for the critical subtangent and the formability increase in plane strain loading are summarized in **Table 5**. Equivalent solutions to Eq. (34b) for the formability gain in non-proportional stressing with a constant contact pressure have been derived by Gotoh *et al.* (1995) using an extension of the Swift (1952) analysis by means of virtual work. Bettaieb and Abed-Meraim (2017) arrived at the same solution by conducting a bifurcation analysis of the acoustic tensor. Interestingly, for the analytical solutions, the formability gains relative to plane stress loading are only dependent upon the applied principal through-thickness stress ratio and not the material constitutive behavior. Thus, the plane strain formability increase for an alloy with a low or high hardening rate will be identical, which is in strong contrast to the stress-based phenomenological mapping criteria summarized in **Table 6**.

**Table 5: Summary of critical subtangent and projected formability gain in $FLC_0$ with respect to plane stress loading for von Mises plasticity and the Swift hardening model.**

| Boundary condition | Critical subtangent (von Mises plasticity) | Formability gain | Eq. |
|---|---|---|---|
| P. Stress | $\frac{1}{z_{vM}}=\frac{\sqrt{3}\left(\chi+1\right)}{2\left\|\chi-1\right\|},\ \left\|\chi-1\right\|\neq 0,\ \ \chi=\frac{\sigma_2}{\sigma_1}$ | $\left(\frac{\varepsilon_1^{3D}+\varepsilon_0}{\varepsilon_1^{2D}+\varepsilon_0}\right)=\frac{\left\|\chi-1\right\|}{\chi+1}$ | (32a,b) |
| NP., $F_3$ const. | $\frac{1}{z_{vM}}=\frac{\sqrt{3}\left(\tilde{\chi}+1\right)}{2\left\|\tilde{\chi}-1\right\|},\ \left\|\tilde{\chi}-1\right\|\neq 0,\ \ \tilde{\chi}=\frac{\sigma_{3,0}\exp\left(\varepsilon_3\right)}{\sigma_1}$ | $\left(\frac{\varepsilon_1^{3D}+\varepsilon_0}{\varepsilon_1^{2D}+\varepsilon_0}\right)=\frac{\left\|\tilde{\chi}-1\right\|}{\tilde{\chi}+1}$ | (33a,b) |
| NP., $P_3$ const. | $\frac{1}{z_{vM}}=\frac{\sqrt{3}}{2\left\|\hat{\chi}-1\right\|},\ \left\|\hat{\chi}-1\right\|\neq 0,\ \ \hat{\chi}=\frac{\sigma_{3,0}}{\sigma_1},\ \sigma_{3,0}=\chi_0\sigma_y$ | $\left(\frac{\varepsilon_1^{3D}+\varepsilon_0}{\varepsilon_1^{2D}+\varepsilon_0}\right)=\left\|\hat{\chi}-1\right\|$ | (34a,b) |

**Table 6: Summary of formability gain in $FLC_0$ with respect to plane stress loading in the phenomenological mapping criteria for von Mises plasticity and the Swift hardening model.**

| Type of mapping | Constant ratio | Formability gain | Eq. |
|---|---|---|---|
| Stress-based | $\alpha^{2D}=\alpha^{3D}$ | $\left(\frac{\varepsilon_1^{3D}+\varepsilon_0}{\varepsilon_1^{2D}+\varepsilon_0}\right)=\left(1-2\chi+\frac{4}{3}\chi^2\right)^{\frac{n+1}{2n}}\left(\frac{2\chi-3}{6\chi-3-4\chi^2}\right)$ | (35) |
| | $\rho^{2D}=\rho^{3D}$ | $\left(\frac{\varepsilon_1^{3D}+\varepsilon_0}{\varepsilon_1^{2D}+\varepsilon_0}\right)=\left(1-\chi\right)^{\frac{1}{n}}$ | (36) |
| Work-based | $\alpha^{2D}=\alpha^{3D}$ | $\left(\frac{\varepsilon_1^{3D}+\varepsilon_0}{\varepsilon_1^{2D}+\varepsilon_0}\right)=\left(\frac{6\chi-3-4\chi^2}{3\chi-3}\right)^{\frac{1}{n+1}}\left(1-2\chi+\frac{4}{3}\chi^2\right)^{\frac{1}{2}}\left(\frac{2\chi-3}{6\chi-3-4\chi^2}\right)$ | (37) |
| | $\rho^{2D}=\rho^{3D}$ | $\left(\frac{\varepsilon_1^{3D}+\varepsilon_0}{\varepsilon_1^{2D}+\varepsilon_0}\right)=\left(1-\chi\right)^{\frac{1}{n+1}}$ | (38) |

Mapping of the plane stress limit strains into triaxial stress space under the assumption of a *constant principal in-plane stress ratio* and a *constant major principal stress* by Smith *et al.* (2003) was adopted in Section 3.3 and is summarized in Eq. (35). The alternative approach of maintaining a *constant in-plane strain ratio* and a *constant major stress* (Matin and Smith, 2005) was studied in Eq. (36) but suffers from the same limitation due to the explicit dependence of the formability gain upon the hardening rate. Instead of constant stress mapping, an alternative mapping method based upon removing the plastic work incurred due to tool contact was derived as part of this research. The plastic work per unit volume is computed from the linearized equivalent plastic strain, $\tilde{\varepsilon}_{eq}^{p}$,

$$w^{p} = \sigma_{eq}\tilde{\varepsilon}_{eq}^{p} = \sigma_{1}\tilde{\varepsilon}_{1}\left[1+\alpha\rho-\chi\left(1+\rho\right)\right], \qquad \frac{\tilde{\varepsilon}_{1}^{3D}}{\tilde{\varepsilon}_{eq}^{p,3D}} = \frac{1}{k^{3D}\left[1+\alpha\rho-\chi\left(1+\rho\right)\right]} \tag{39a,b}$$

where $\tilde{\varepsilon}_{1}$ corresponds to the linearized major strain assuming proportional coaxial straining (directions of the principal strains during deformation remain aligned with the principal stress direction). Eq. (39a) can be re-arranged to express the ratio of the linearized major strain with respect to the linearized equivalent plastic strain in triaxial loading in Eq. (39b). Adopting Eq. (39a), the plastic work in plane stress, $w^{p,2D}$, is expressed by removing the accumulated work due to tool contact, $\Delta w^{p}$

$$w^{p,2D} = \sigma_{eq}^{2D}\tilde{\varepsilon}_{eq}^{p,2D} = w^{p,3D} - \Delta w^{p} = \sigma_{eq}^{3D}k^{3D}\tilde{\varepsilon}_{1}^{3D}\left(1+\alpha^{3D}\rho^{3D}\right) \tag{40}$$

Adopting Eq. (40), (39b) and integration of the equivalent plastic strain utilizing the Swift hardening model in Eq. (19a) yields

$$\tilde{\varepsilon}_{eq}^{p} = \frac{w^{p}}{\sigma_{eq}} = \frac{1}{\bar{\sigma}}\int_{0}^{\varepsilon_{eq}^{p}}\bar{\sigma}\,d\varepsilon_{eq}^{p} = \frac{\left(\varepsilon_{eq}^{p}+\varepsilon_{0}\right)}{n+1}, \qquad \left(\frac{\varepsilon_{eq}^{p,3D}+\varepsilon_{0}}{\varepsilon_{eq}^{p,2D}+\varepsilon_{0}}\right) = \left[\frac{1+\alpha^{3D}\rho^{3D}-\chi\left(1+\rho^{3D}\right)}{1+\alpha^{3D}\rho^{3D}}\right]^{\frac{1}{n+1}} \tag{41a,b}$$

Since the in-plane strain and stress ratios are only known for plane stress loading, an assumption is to be made upon the functional form in triaxial space. The formability gains for assuming a constant in-plane stress ratio or in-plane strain ratio are provided in **Table 7** in Eq. (37) and Eq. (38), respectively.

The predicted gains in the $FLC_0$ of the mapping methods were compared against the analytical solutions in **Figure 35**. Interestingly, correlation is only found between the work-based mapping methods and the analytical solution for a constant contact pressure for a hardening exponent of $n = 0.1$. Stress mapping under a constant in-plane strain or stress ratio predicted stark formability gains that were very sensitive to the contact stress ratio and may become non-physical at high contact stresses as noted in the study of Matin

and Smith (2005) in double-sided bulge tests. There is no analytical evidence that such marked formability gains are physical; the analytical solution for a proportionally evolving contact stress in fact reveals strong formability gains but which are an order of magnitude smaller. For moderate contact stress ratios of up to $\chi_0$ = -0.25, work mapping under a constant in-plane stress produces reasonable formability gains for loading conditions with a constant contact pressure. However, this agreement is coincidental and does not hold for other hardening exponents. It is emphasized that the mapping methods remain phenomenological in nature and the underlying assumption of a unique in-plane forming limit has been invalidated in the Hillier framework.

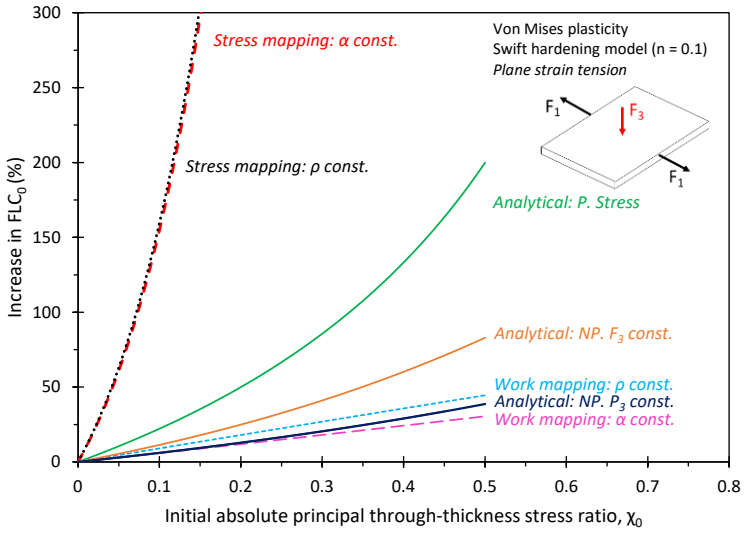


**Figure 35: Comparison of predicted formability gain between the phenomenological mapping criteria and the analytical solution for plane strain tension. Note that for the analytical solutions of loading under a constant contact pressure or load, an incremental procedure was adopted to compute the evolving through-thickness stress ratio.**

## 4.4 Generalized Incremental Stability Criterion (GISC)

The Hillier (1963) solution is only valid until the onset of instability. Additional information is required to specify the type of localization and its evolution. An extension to model the diffuse necking process was obtained by extending the analysis of Hillier to maintain neutral incremental stability.

The concept of neutral incremental stability was evaluated by analyzing the diffuse necking process in uniaxial tension. The onset of diffuse necking corresponds to the peak force and a vanishing load rate, $dF = 0$, satisfying the Considère criterion and Eq. (16) for the onset of Hillier instability. The force or engineering stress then remains approximately constant, $dF \sim 0$, during diffuse necking until an acute neck forms. Critically, no discontinuity of the stress is observed at the onset of diffuse necking, supporting Hillier's idealization of a quasi-stable bifurcation of the stress state. The onset of instability and transition from homogeneous to localized deformation occurs when the material hardening rate is exhausted and can

no longer balance the increase in stress due to the reduction in area of the cross-section. Deformation will otherwise become unstable as the second order plastic work rate is negative $dW^p = d\sigma_i d\varepsilon_i < 0$. To regain incremental stability, the second order plastic work rate must be positive or zero. The strain path and stress state undergo a continuous transition towards plane strain, the extrema of the yield function, as an effective source of secondary hardening (refer to **Figure 7b**). This causes the formation of a localization band in which the strain rate also increases and provides additional hardening for stability in a positive rate-sensitive material. The strain rate increases inside the band while unloading occurs outside such that $du = 0$ at the boundary and $dW^p = 0$, independent of the load rate. Either condition is sufficient to achieve $dW^p = 0$. The argument of localization occurring under neutral incremental stability is supported by the evolution of the load and the major strain along the gauge region in quasi-static tensile tests of 590R and 3rd Gen 1180 steel from Noder *et al.* (2021a) in **Figure 36**.

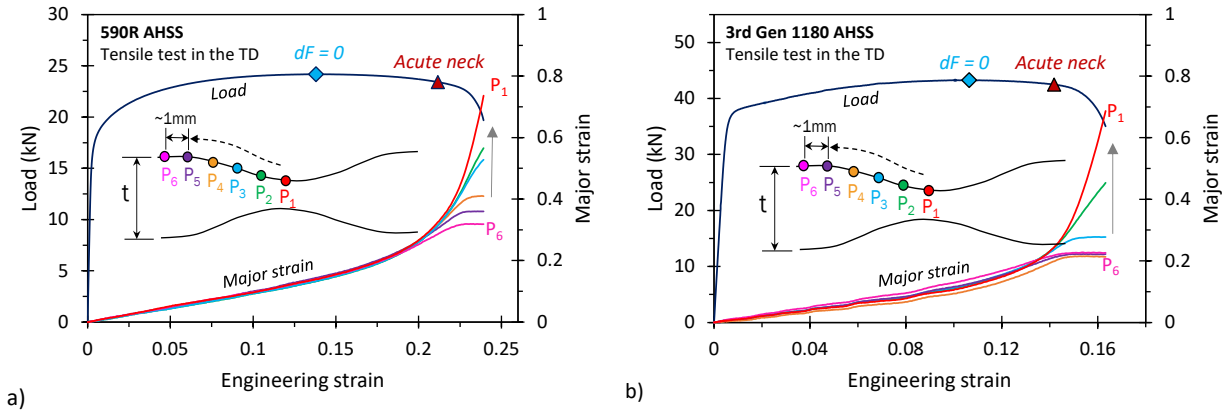


**Figure 36: Evolution of the load and the major principal strain along the localization band of a quasi-static tensile test for the 590R AHSS (a) and the 3rd Gen 1180 AHSS (b). Note that acute necking limits were obtained from the Mod. LBF-Method of Noder and Butcher (2019a).**

The major strain was extracted in equally-spaced increments of approximately 1 mm. For the 590R, the peak load is reached at an engineering strain of about 0.14 and remains approximately constant until $e_1 = 0.21$ when an acute neck has formed, shortly after which the strain increment at the boundary of the neck remains constant. The same behavior is observed in the 3rd Gen 1180 steel. The assumption of acute localization occurring under neutral incremental stability, whether due to vanishing load rates or a vanishing strain rate at the boundary of the band, or a combination of both factors at different times in the process, appears to be a realistic continuum description of the process. Similar observations of localization in tensile-dominated modes were made by Hora *et al.* (2013) to justify the assumption of a constant maximum force in the MMFC model but not in the broader context of incremental stability.

The instability criterion for localization was derived from the following two assumptions:

(i) The second order plastic work rate is zero to represent neutral incremental stability for an instantaneously stable transition between the stable and unstable stress state.

(ii) Localization is defined in terms of a transition of the strain and stress path to plane strain tension while the rate of change is governed by the major principal stress increment to maintain neutral incremental stability.

The required increment in the principal stress to satisfy neutral incremental stability is derived from the second order plastic work rate and conveniently expressed in terms of the critical subtangent of the Hillier framework for $d\varepsilon_{eq} > 0$

$$d\sigma_1 = \frac{k}{N_1}\left(\frac{\sigma_{eq}}{z} - h\right)d\varepsilon_1 \tag{42}$$

Before diffuse necking, the critical stress increment is negative analogous to a positive second order plastic work rate, which then becomes exactly zero when instability occurs. To maintain neutral incremental stability, the minimum increment in the second order plastic work rate is provided by a change in the strain path $d\rho$

$$d\sigma_1 = \frac{\partial\sigma_1}{\partial\rho}d\rho, \qquad d\rho = k\left(\frac{\sigma_{eq}}{z} - h\right)d\varepsilon_{eq}\left(\frac{\partial\sigma_1}{\partial\rho}\right)^{-1} \tag{43a,b}$$

to form the *Generalized Incremental Stability Criterion (GISC)*

$$\frac{\partial\sigma_1}{\partial\varepsilon_1} + \frac{\partial\sigma_1}{\partial\rho} \geq \frac{1}{z}\left(\frac{k}{N_1}\sigma_{eq}\right) \tag{44}$$

Since the equivalent plastic strain increment in Eq. (43b) evolves with the change in the strain path, an incremental implementation was employed. Details on the code implementation are provided in Appendix E4.

It is instructive to now assess the underlying assumption of the MMFC of Hora *et al.* (2013). Diffuse necking is determined from the Dorn (Dorn and Thomsen, 1947) model, which corresponds to $z^{-1} = N_1$. Substitution into the GISC reduces the term on the right-hand side of Eq. (44) to the major stress that is equivalent to the MMFC (Hora *et al.*, 2013) in Eq. (14a). Thus, the MMFC in fact is physically motivated and the localization process satisfies neutral incremental stability. The MMFC emerges as a special case of the GISC under plane stress proportional stressing with a specific minor load rate (see Eq. (23)). Instead, if

the minor load rate is assumed to vanish, plane stress proportional stressing is restored in the GISC that is equivalent to replacing the Dorn model in the MMFC with the Swift (1952) instability condition. Implications of the specific minor load in the Dorn model upon acute localization are visualized in **Figure 37a**. Necking limits are similar on the draw side but differ somewhat for biaxial strain paths. Referring to Eq. (24a) and (26a), the critical subtangent of the Dorn model is identical to the Swift model for UT, PST, and BT (see **Figure 30a**). However, for proportional stressing, the magnitude of the critical subtangent is decreased for strain paths in between UT to PST and increased between PST and BT that leads to an accelerated necking process for the draw side and a delay in plastic instability on the stretch side of the FLC (see **Figure 37b**).

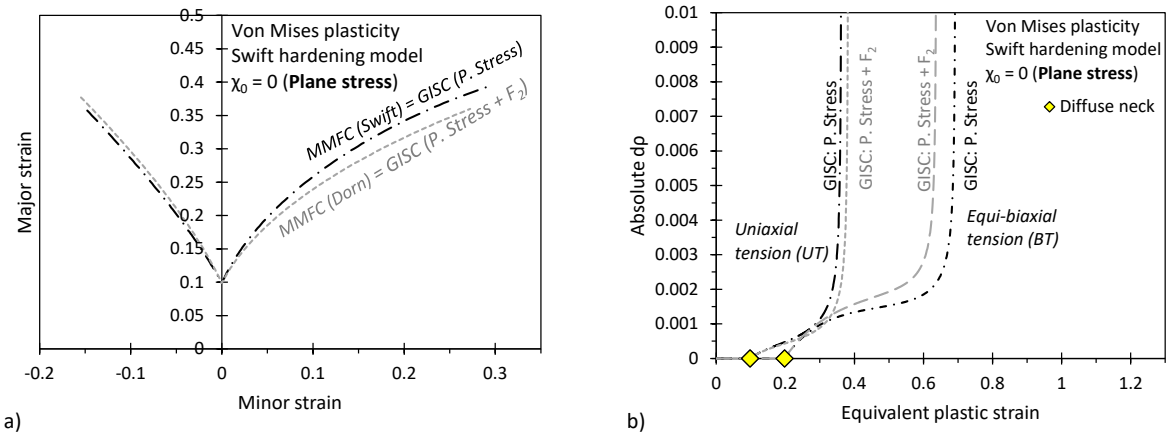


**Figure 37: Effect of diffuse necking criterion (Dorn *versus* Swift) on acute necking limits in plane stress loading (a) and the localization process (b).**

## 4.5 Effect of Boundary Condition on Acute Localization

Predictions for acute necking in the presence of a compressive normal stress depicted in **Figure 38a** confirm increased necking limits, relative to plane stress, for all studied loading scenarios. Analogous to the ranking observed for diffuse necking in Section 4.2.2, the largest formability gains were found for proportional stressing followed by a constant normal load or contact pressure. For acute necking limits, the sensitivity of the boundary condition upon plastic instability is magnified since the critical subtangent is directly embedded in the major stress increment (see Eq. (42)) that governs the strain path change during quasi-stable localization. A smaller magnitude in $z$ leads to a larger major stress increment required to maintain neutral incremental stability. As a result, the localization process is accelerated due to a larger change in the strain path, $d\rho$, towards plane strain tension (see **Figure 38b**). Therefore, the markedly higher FLC for proportional stressing is the result of the combined effect of a delay in diffuse necking and a slower localization process.

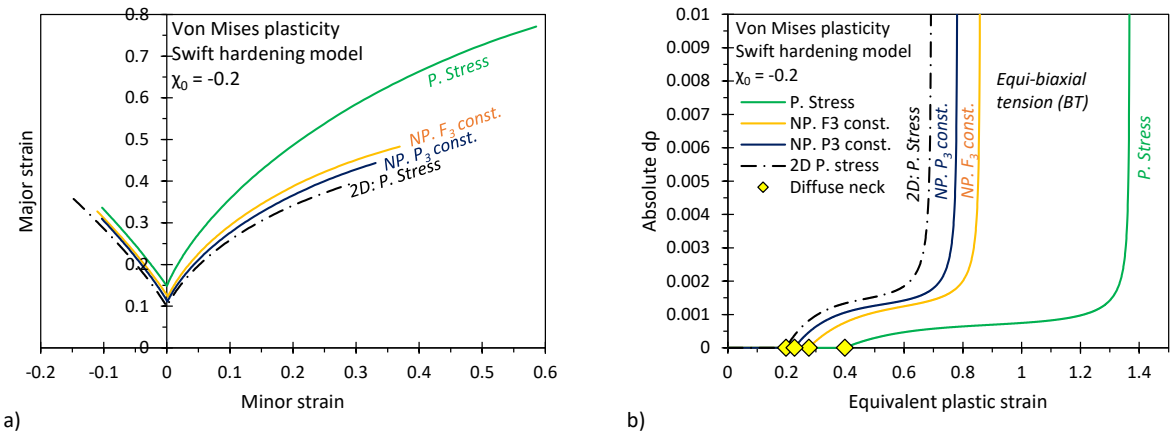


**Figure 38: Effect of boundary condition and presence of a compressive contact stress upon the acute necking limits (a) and the localization process (b)**

To quantify the difference in the predicted formability gains among the studied boundary conditions, necking limits were compared at minor strains of approximately -0.05, 0, and 0.3, representative of a strain path of UT, PST, and BT. As shown in **Figure 39**, there is a large variation in the predicted formability gains between the studied boundary conditions, particularly around the $FLC_0$ (14-51%) and on the stretch side of the FLC (8-48%). The loading scenario with a constant contact pressure results in a marginal but approximately constant offset across all tensile stress states and correlates with the observation of the 3D MK study of Zhang *et al.* (2014). Instead, the magnified formability gains for biaxial strain paths when considering a proportionally increasing contact pressure are in agreement with the reported trends of Allwood and Shouler (2009) for proportional stressing.

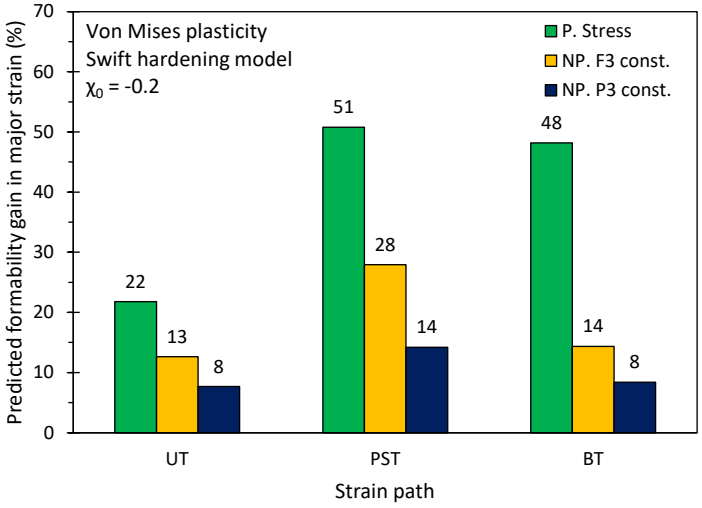


**Figure 39: Comparison of predicted formability gains for selective strain paths.**

The preceding discussion established a fundamental understanding of the importance of local boundary conditions on plastic instability that is represented in a forming limit surface (FLS), specific to the loading

condition as depicted in **Figure 40**. Overall, the biaxial limit strains are predicted to be most sensitive to the magnitude of the through-thickness stress ratio.

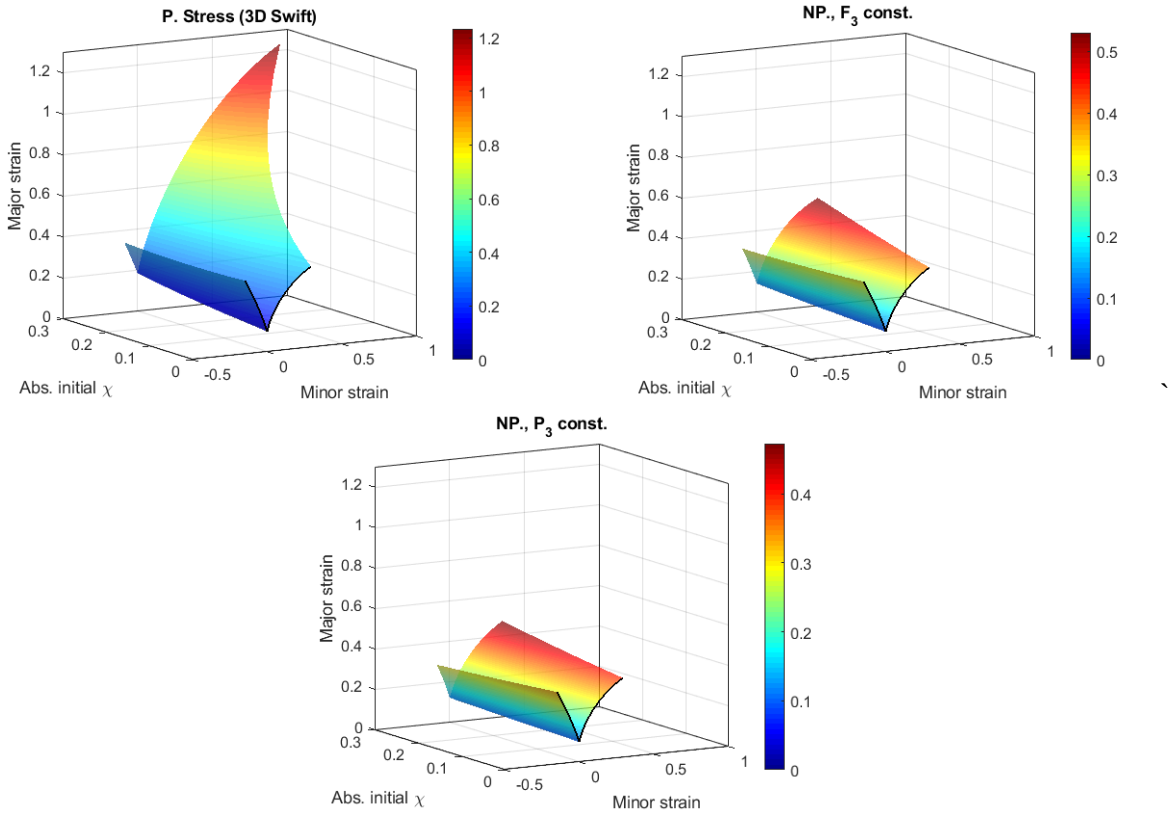


**Figure 40: Surface plots of acute necking limits to demonstrate the dependence upon the contact pressure and the boundary condition of how the normal pressure was applied.**

## 4.6 Identification of Boundary Conditions in Formability Tests

The boundary conditions in formability characterization tests (*e.g.* Marciniak or Nakazima tests) are complex since material flow is partially or fully constrained in the sheet plane and stretched out-of plane by means of a punch. To assess which of the studied boundary conditions is most applicable to common formability tests, forming limit predictions were compared to experimental data of the DP980 in Section 3.2. The flow behavior was described through the MHS hardening model with calibration parameters identified in **Table 1**.

Boundary conditions under a triaxial stress state were studied by considering Nakazima limit strains while neglecting bending effects due to the relatively large punch radius. It is noted that for comparison to the linearized Nakazima limit strains, predicted necking limits in the GISC were also linearized following the method discussed in Section 3.5. The through-thickness stress ratio of $\chi_0$ = -0.2 in **Figure 41** was selected to yield good agreement between the experimentally measured and predicted $FLC_0$ for which analytical

solutions are available in the Hillier framework (1963). Among the studied boundary conditions, the assumption of a proportionally evolving contact pressure best captures the overall trend in the limit strains for the DP980. Future work should focus on assessment of analytical contact pressure models and their evolution with deformation.

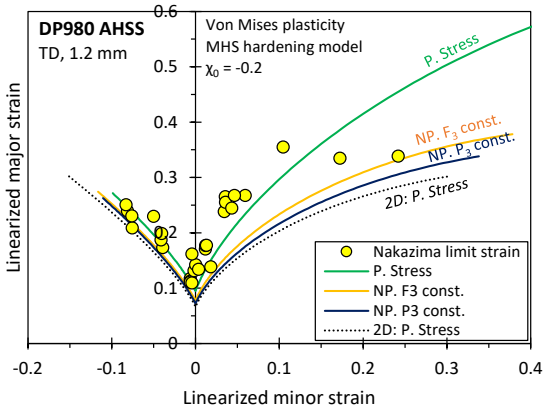


**Figure 41: Comparison of analytical FLC prediction and comparison to the linearized Nakazima necking limits in plane stress loading (a) and triaxial loading (b) of the DP980 AHSS.**

## 4.7 Discussion on the In-Plane Formability under Triaxial Stress States

This study provided fundamental insight into the effect of a compressive tool contact stress on the in-plane forming limits. Closed-form solutions, derived from the general framework of Hillier (1963) for the onset of instability, highlighted the instantaneous nature of material instability that is governed by both the boundary condition and the composition of the stress state. Overall, a compressive normal stress and shear stress are beneficial such that the magnitude of the critical subtangent is increased and thus accommodates a higher equivalent plastic strain at instability. Larger necking limits were computed for loading scenarios that have an explicit dependence of the through-thickness stress ratio embedded in the functional form of the critical subtangent, for example proportional triaxial stressing or non-proportional stressing with a constant normal load. Non-proportional stressing under a constant normal pressure still provided an increase in necking limits but the stabilization effect was reduced since the contact pressure only affected instability *via* the constitutive model. Correlations between the phenomenological mapping criteria and the analytical solutions for plane strain loading were limited to the developed work-based mapping under a constant in-plane stress ratio and non-proportional stressing under a constant contact pressure for $\chi_0$ of up to -0.25 and a hardening exponent of $n$ = 0.1. It is emphasized that this agreement is coincidental and does not hold for other hardening exponents. Drastic formability gains were projected by the stress-based mapping methods for which no analytical evidence was found; a proportionally evolving contact pressure in fact led to strong formability gains that, however, were an order of magnitude smaller. Nevertheless, the

same stress-mapping method (under a constant in-plane stress ratio) worked well in the preceding chapter when Nakazima limit strains were corrected for contact pressure effects. It is surmised that the strong sensitivity of the contact pressure magnitude upon stress mapping was balanced by the contact pressure model that was shown to be very sensitive to the assumed through-thickness distribution. The uncertainty surrounding the magnitude of the contact pressure, distribution over the sheet cross-section, and evolution with deformation should be addressed in a separate study.

An extension of the Hillier instability framework was proposed in the Generalized Incremental Stability Criterion (GISC) to account for the localization process until an acute neck has fully developed. The condition of a vanishing second order plastic work rate ($d^2W^p = 0$), which is equivalent to Drucker's postulate (1951) and Hill's incremental stability for a rigid-plastic material (1950), was employed to compute diffuse localization. The assumption of neutral incremental stability during localization was shown to either be the result of a vanishing load rate or a vanishing strain rate at the boundary of the instability band and was supported in tensile tests of a 590R and a 3rd Gen 1180 AHSS. The major stress increment for incremental neutral stability was derived from the condition of a vanishing second order plastic work rate and was provided in the form of a change in the strain path towards plane strain tension. It was revealed that the MMFC of Hora *et al.* (2013) is in fact physically motivated and just one special case of the developed GISC under the assumption of approximate proportional loading or proportional stressing with a prescribed minor load. Comparison of the GISC predictions to Nakazima limit strains of the DP980 in Section 3.2 identified the assumption of a proportionally evolving contact pressure as a good approximation of the overall trend in the formability. The extension of the GISC in the presence of combined loading of stretch-bending is addressed in Chapter 6.

# 5. Characterization of Out-of-Plane Forming Limits (Task 3 and Task 4)

Automotive structural components often feature complex geometries with a locally varying degree of stretching, bending, and tool contact. Thus, the characterization and modelling efforts in Chapters 3 and 4 are representative of the process conditions of only a small region of the part stretched in-plane. To establish an understanding of the necking limits in the presence of superimposed bending, angular stretch-bend (ASB) and V-Bend tests are conducted to characterize the out-of-plane formability that will provide guidance for the modelling efforts in Chapter 6. The main difference in the two test methods lies in the stretch-bend severity. The ASB test usually involves sufficient stretching such that necking-induced failure occurs, whereas the severe stress-strain gradients in the bending-dominated V-Bend test mostly suppress necking such that fracture occurs abruptly. Thus, the limit strains determined in the V-Bend test constitute the upper bound for materials of homogeneous microstructure whereas necking limits in the ASB tests represent intermediate forming conditions between the Nakazima and the V-Bend tests. Central to the characterization of the out-of-plane formability is the accurate detection when material instability occurs. The refined version of the LBF detection method developed in Chapter 3 is readily amenable to ASB tests but fracture detection in the V-Bend test is more controversial and is the primary focus of this chapter. A comprehensive experimental test campaign encompassing seven automotive steel grades of different strength and ductility level is conducted. The validity of the VDA 238-100 load threshold methodology is critically assessed to identify the cause of a descending punch force even in the absence of fracture. Adopting bending mechanics, a new fracture detection method is developed that accounts for sheet thinning and the cross-sectional dimension of the specimen to distinguish between material fracture and false positives. Additional concerns related to lift-off of the specimens from the punch are addressed in a strain-rate driven approach. Special attention is devoted to identification of a fracture threshold using DIC images of unpainted test samples at various thresholds.

The published and prepared manuscripts can be found in Appendix C and D, respectively, in:

**Noder, J.,** Dykeman, J., Butcher, C., (2020a). New Methodologies for Fracture Detection of Automotive Steels in Tight Radius Bending: Application to the VDA 238-100 V-Bend Test, Experimental Mechanics, https://doi.org/10.1007/s11340-020-00597-2.

**Noder, J.,** Butcher, C. On the Influence of Tool Contact Pressure on Tensile Instabilities in Plane Strain Stretching and Bending of Sheet Metals, to be submitted, May 2022.

## 5.1 Limit Strains in the Absence of Necking

First, the experimental study on V-Bend testing is discussed and the chapter will close with ASB tests.

### 5.1.1 Material Selection in the VDA 238-100 Tight Radius Bend Test

The selected steel grades for this study were grouped into three categories depending on their ductility level. The mechanical properties and engineering stress-strain response are listed in **Table 7** and depicted in **Figure 42**. The high ductility group of steel grades that have a strong risk of folding over without fracture was comprised of the 270 Mild steel and the 590R AHSS. The second group of steels of moderate ductility, which were expected to fracture at intermediate bend angles, considered the DP980 of Chapter 3 and two 3rd Gen AHSS with a nominal strength level of 980 MPa and 1180 MPa, denoted as 3rd Gen 980 and 3rd Gen 1180 V2, respectively. The last group of relatively low ductility comprised a press-hardened Al-Si coated 22MnB5 steel with an ultimate tensile strength of 1500 MPa, denoted as PHS1500, and another 3rd Gen AHSS with a nominal ultimate tensile strength of 1180 MPa (3rd Gen 1180 V1).

**Table 7: Tensile mechanical properties of the studied steel grades. The PHS1500 data was obtained by digitizing the work of ten Kortenaar (2016), thus no standard deviation is provided. Note that the total elongation is based on a virtual extensometer length of 50 mm except for the PHS1500 that utilized a 12.5 mm extensometer.**

| | Yield Stress (0.2% offset) (MPa) | Ultimate Tensile Stress (MPa) | Uniform Elongation UE (%) | Total Elongation TE (%) |
|---|---|---|---|---|
| **270 Mild steel, 1.6 mm, TD** | 256 (±1) | 311 (±2) | 31.1 (±2.8) | 43.2 (±1.0) |
| **590R AHSS, 1.4 mm, TD** | 490 (±2) | 671 (±1) | 13.7(±0.1) | 23.8 (±0.4) |
| **3rd Gen 980, 1.4 mm, TD** | 681 (±8) | 1033 (±10) | 18.0 (±0.5) | 24.9 (±0.6) |
| **3rd Gen 1180 V2, 1.4 mm, TD** | 1047 (±10) | 1219 (±5) | 10.3 (±0.3) | 16.2 (±0.1) |
| **DP980, 1.2 mm, TD** | 735 (±2) | 1065 (±3) | 7.8 (±0.2) | 14.1 (±0.6) |
| **3rd Gen 1180 V1, 1.4 mm, TD** | 950 (±12) | 1251 (±8) | 8.4 (±0.2) | 13.7 (±0.5) |
| **PHS1500, 1.2 mm, TD** | 1144 | 1571 | 5.5 | 11.0 |

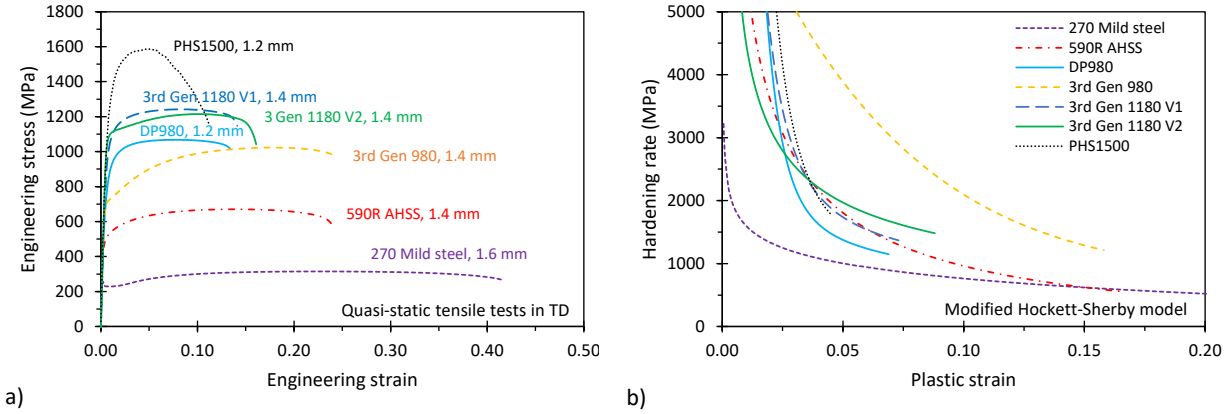


**Figure 42: Engineering stress-strain response (a) and hardening rate (b) of studied steel grades. The PHS1500 was digitized from ten Kortenaar (2016) who utilized a sub-size ASTM tensile specimen.**

### 5.1.2 Load Threshold Methodology

The VDA 238-100 tight radius bend tests were conducted on the inverted test frame developed by Cheong *et al.* (2017) that features a stationary punch and chamfered rollers to allow full-field stereoscopic DIC of the entire bend width of the sheet convex side where fracture is initiated. The VDA 238-100 recommendation was followed for selection of the punch radius and the roller gap settings, except for the

high-ductility steel grades for which the 0.4 mm nominal punch radius was replaced with the sharper 0.2 mm radius punch in light of the expected larger bend angles.

Adoption of the VDA 238-100 specification to identify fracture from a reduction in the punch force is illustrated for the 3rd Gen 980 and 270 Mild steel in **Figure 43**. Visual inspection at the VDA load threshold showed the presence of hairline cracks for the 3rd Gen 980 while no signs of material fracture were observed for the 270 Mild steel. Sectioning of the specimens and inspection under an optical microscope confirmed fracture on the convex surface for the 3rd Gen 980 but not for the 270 Mild steel despite a 75% reduction in the punch force. Relying upon the VDA 238-100 specification for fracture identification erroneously reported fracture for the 270 Mild steel.

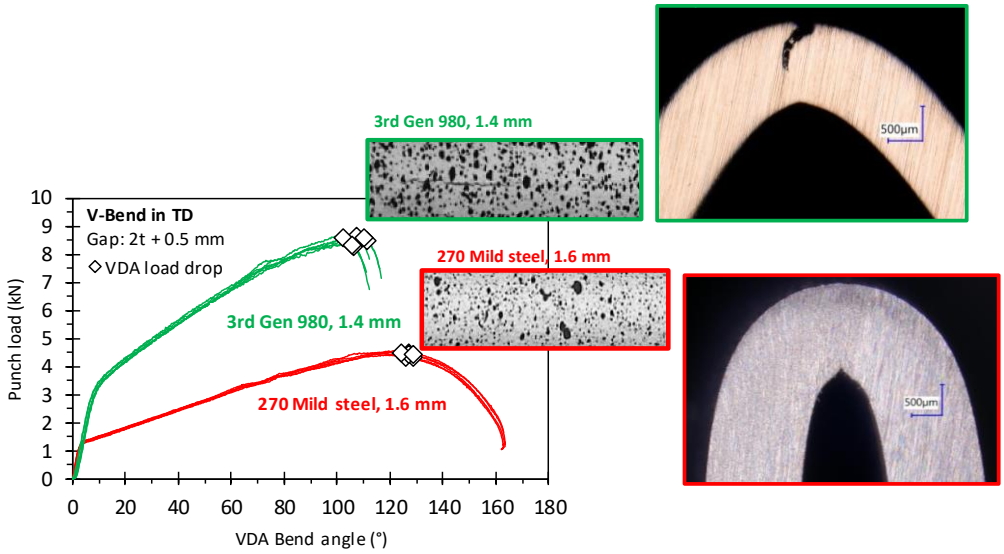


**Figure 43: Load evolution and fracture detection from a 60 N reduction of the peak punch force. The close-up view of the specimen surface and sectioned cross-section indicate fracture for the 3rd Gen 980 but not for the 270 Mild steel.**

The cause of a reduction in the punch force in the absence of material rupture was revealed to be due to the kinematic boundary condition of the test set-up as schematically illustrated in **Figure 44**. For low bend angles ($\alpha_1$) a three-point bend condition prevails and the measured punch force, $F_y$, is a good approximation for the resultant force, $F_{res}$. As bending continues ($\alpha_2$), the contact points between the specimen and the punch are gradually shifted towards the edges of the punch trip radius, representing a four-point bending scenario. The tangential contact between the roller and the specimen causes a horizontal force component, $F_x$, which rapidly increases for large bend angles ($\alpha_3$). The approximately horizontal resultant force may lead to punch lift-off when the specimen loses contact with the punch and the specimen concave radius no longer conforms to the punch tip radius. Punch lift-off is not of concern when relying on the DIC strain measurements to retrieve the fracture strain since plane strain tension prevails on the convex

layer, while the analytical bend angle approximation is no longer valid since the bend severity changes. The reduction in the punch force as a natural consequence of the mechanics in the tight radius bend test is not accounted for in the VDA 238-100 specification and may lead to significant underreporting of the material performance.

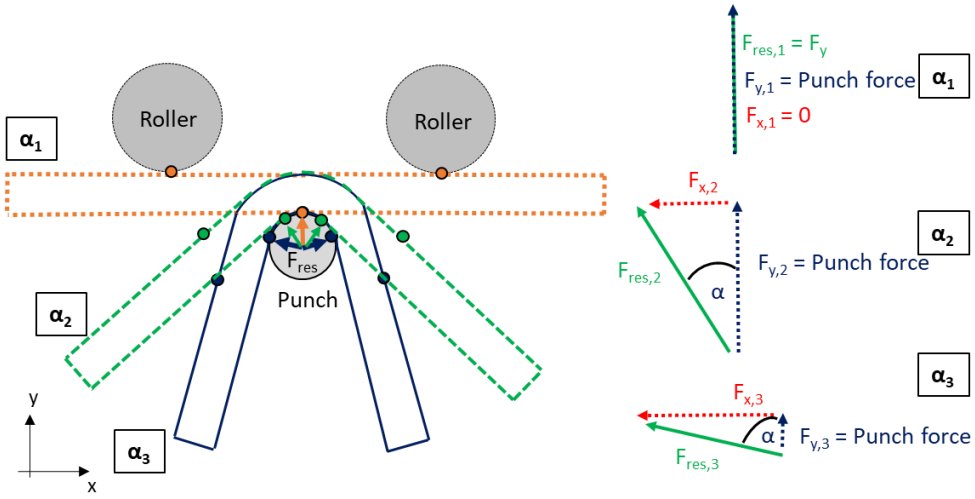


**Figure 44: Evolution of the resultant force as a function of the bend angle and the corresponding evolution of the punch force in the *y*-direction. The three different bending scenarios illustrate the phenomenon of a decrease in the punch force without material fracture due to the shift from a three-point to a four-point bending scenario.**

### 5.1.3 Bending Moment Evolution

Consideration of the bending moment naturally accounts for the evolution of the resultant force and the transition to a four-point bending scenario. Following the work of Troive (2017) and assuming the specimen flanges remain straight in the absence of punch lift-off, the cross-sectional bending moment, $M$, was derived from geometric boundary conditions

$$M = \frac{F_y}{2\cos\left(\frac{\alpha_{VDA}}{2}\right)} \frac{L_{m,x}}{\cos\left(\frac{\alpha_{VDA}}{2}\right)}, \qquad L_{m,x} \approx L_0 - \left(r_r + r_p\right)\sin\left(\frac{\alpha_{VDA}}{2}\right), \qquad L_0 = (t + 0.25) + r_r \tag{45a-c}$$

where $r_r$ correspond to the roller radius, $\alpha_{VDA}$ to the VDA bend angle, and $L_0$ to half of the width of the roller gap including the roller radius. To avoid the complexity associated with a layer-based integration of the stress-strain relations for a strain hardening material, the closed-form solution of Hill (1950) for a rigid perfectly plastic material was adopted to relate the yield stress to the bending moment of the cross-section

$$M_{RPP} = \frac{\sigma_y t^2 w}{4} = \text{constant} \tag{46}$$

where $w$ corresponds to the width of the specimen that remains constant during plane strain bending. Adopting Eq. (45a-c) and (46), dimensionless forms of the force components were obtained for a RPP material as illustrated in **Figure 45a**. The y-force, representative of the punch load, increases up to bend angles of 100° followed by a reduction as a natural consequence of the boundary conditions of the V-Bend test. **Figure 45b** highlights the dependence of the punch radius upon the critical bend angle when the punch force begins to descend. The critical metric is reached earlier for sharper punch radii.

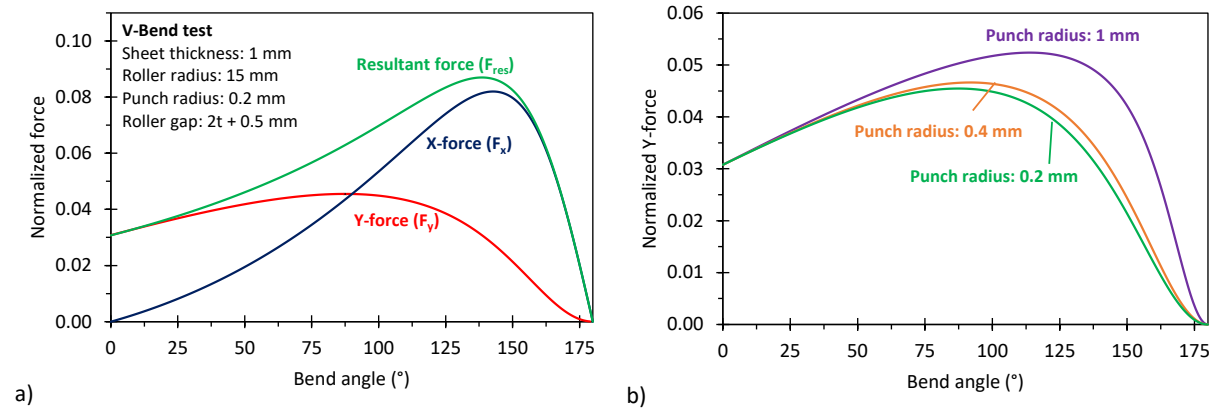


**Figure 45: Effect of a descending punch force (y-force) as a consequence of the kinematic boundary conditions in the V-Bend test (a) and the dependence upon the punch radii (b).**

The bending moment evolution for a strain-hardenable alloy is depicted for the 3rd Gen 980 in **Figure 46a** and correlates well with the punch force evolution. For the 270 Mild steel in **Figure 46b**, failure is still erroneously detected when relying on the bending moment evolution but it represents a considerable improvement over the punch force since material failure was only reported for bend angles greater than 160° instead of 127°.

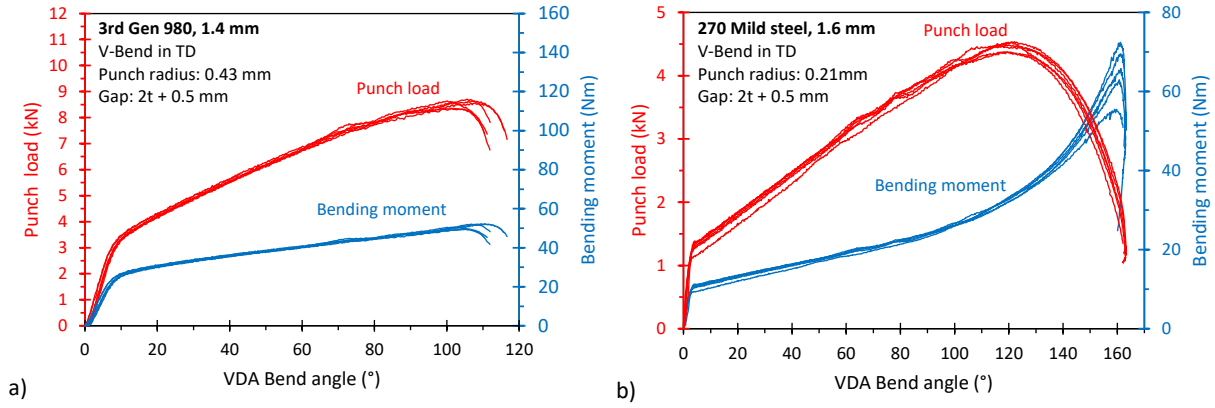


**Figure 46: Comparison of the evolution of the bending moment with the punch load for the 3rd Gen 980 (a) and the 270 Mild steel (b)**

Nevertheless, complications arise for materials with a low hardening rate as shown in **Figure 47a**. The derivative of the bending moment with respect to the bend angle, computed in 0.5° increments, has noticeable fluctuations about zero (**Figure 47b**) that makes identification of a robust failure threshold challenging. Adoption of the bending moment technique may be feasible with a robust implementation and potential signal processing.

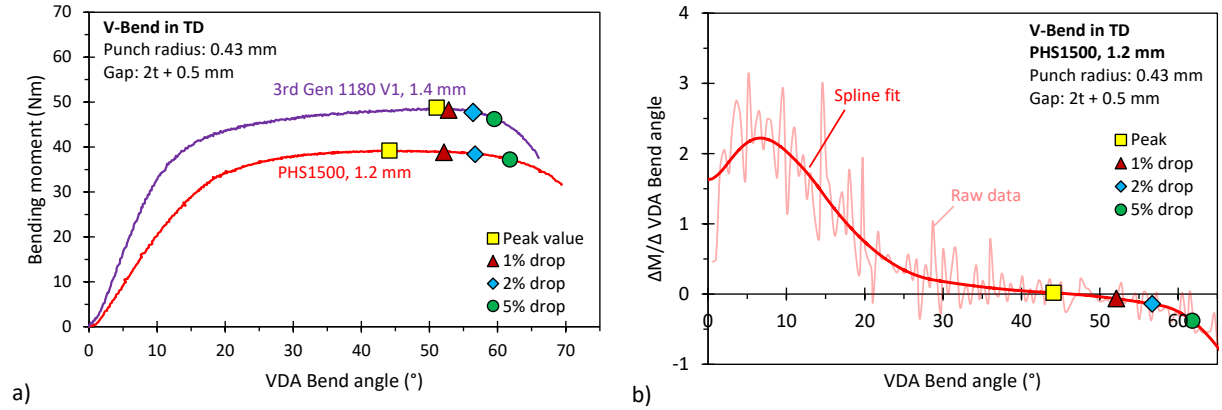


**Figure 47: Complications with identification of a robust failure threshold for materials with a low hardening rate (a) for which the change in the bending moment can remain approximately constant (b).**

### 5.1.4 Development of the Stress Metric

To avoid issues surrounding a nearly constant bending moment for materials with a saturation-type hardening behavior and the ambiguity of using force-based thresholds that do not account for the specimen dimension, a stress-driven fracture detection method was developed. The closed-form solution of the bending moment for a RPP material in Eq. (46) was adopted to define the stress metric, $\Sigma$

$$\Sigma = \frac{4}{t^2 w} M(F_y, \alpha_{VDA}), \qquad t = t_0(1-e_3), \qquad e_3 = 0.211 - 0.211\exp\left[-0.0012\left(\alpha_{VDA}\right)^{1.4636}\right] \tag{47a-c}$$

where the specimen width is obtained from measurements prior to testing. It is emphasized that Eq. (47a) can only be interpreted as a stress metric for fracture detection and cannot be adopted for constitutive characterization of a hardening material that would require a layer-based analysis. To increase the resolution of the stress metric over the bending moment, the instantaneous thickness is utilized that can either be measured from the out-of-plane displacement with the aid of DIC and a stationary punch or from the empirical relation in Eq. (47b,c). Post-mortem thickness measurements of tested V-Bend samples, as done in the study of Larour *et al.* (2013), for one representative material of each studied ductility group confirmed good correlation between thinning obtained from DIC and physical measurements in **Figure 48a**. Consideration of thinning of the cross-section during bending in **Figure 48b** induces an increase in the stress metric evolution for the PHS1500 that enables clear identification of the failure threshold. While the

magnitude of the stress metric for the PHS1500 is somewhat different when using the instantaneous instead of the empirical thinning, the trend is similar such that the bend angle at the onset of fracture is in excellent agreement. Among the studied steel grades, largest deviations of 0.01 major strain and 1° bend angle were observed for the PHS1500 and the DP980.

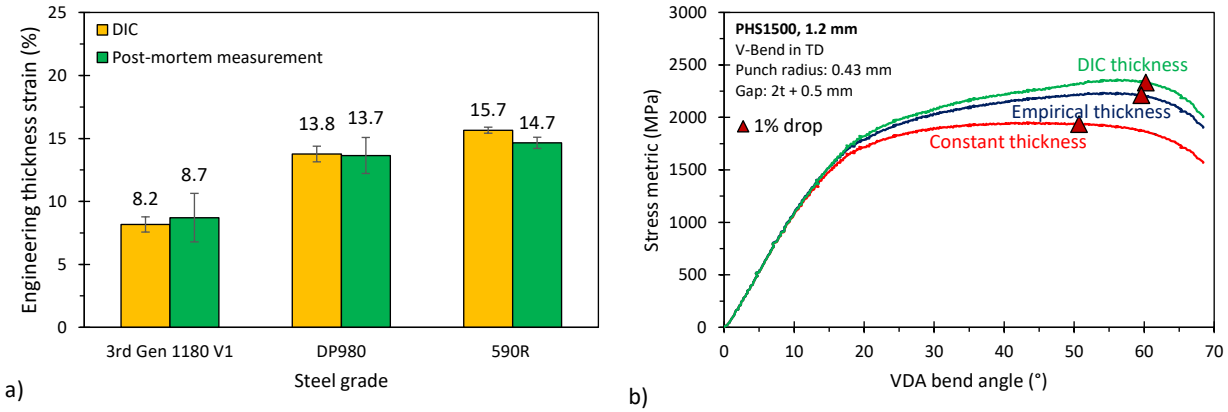


**Figure 48: Comparison of thinning of the cross-section during the V-Bend tests obtained from DIC measurements and post-mortem thickness measurements (a) and their effect on the evolution of the stress metric (b).**

### 5.1.5 Strain-based Detection Method

While the stress metric eliminates issues surrounding failure identification of materials with a low hardening rate, in analogy to the bending moment, failure is erroneously reported at bend angles greater than 160° as depicted in **Figure 49a**. Consideration of the strain rate on the convex surface of the bend is independent of the punch force evolution and thus not affected by false positives. Since through-thickness necking is suppressed in the V-Bend test, an acceleration of the strain as shown for the 3rd Gen 980 in **Figure 49b** correlates with strain localization on the tensile surface of the bend prior to cracking. By contrast, a decrease of the strain rate indicates absence of material rupture when the specimen folds over as shown for the 270 Mild steel.

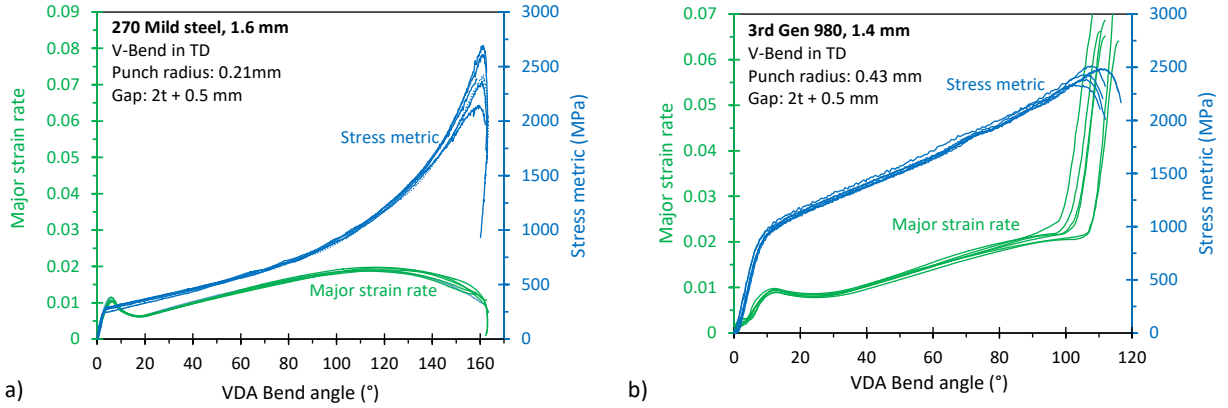


**Figure 49: Major strain rate evolution of the convex side of the specimen surface for the 270 Mild steel that folds over in the absence of fracture (a) and the 3rd Gen 980 with clear fracture (b).**

To detect an abrupt change in the major strain rate, the Linear Best Fit (LBF) methodology of Volk and Hora (2011) was refined for small radius bending. The criteria for the fitting window of the stable line fit, discussed in Section 3.2, was modified such that the beginning of the fitting window is approximated from the maximum tensile strain on the convex surface when yielding of the neutral layer is initiated (Yu and Zhang, 1996). The relative curvature at the onset of yielding, $\kappa_y$, and the maximum elastic strain, $\varepsilon_{el}^{y}$, are approximated from Hooke's law and the von Mises yield function to arrive at

$$\varepsilon_1(r_y) \approx \ln\left(\frac{r_y}{r_m}\right) = \ln\left(1+\frac{\kappa_y}{2}\right),\ \kappa_y = \frac{t}{r_m} = 2\sqrt{1-\exp\left(-2\varepsilon_{el}^{y}\right)},\ \varepsilon_{el}^{y} = \frac{1-\nu^2}{\sqrt{1-\nu+\nu^2}}\frac{\sigma_y}{E} \quad \text{(48a-c)}$$

where $\nu$ corresponds to Possion's ratio. Details on the derivation of Eq. (48a-c) are provided in Appendix E1. Compared to the large bending approximation in Section 3.2, Eq. (48a-c) now account for the shift in the neutral layer relevant for tight-radius bending. Since diffuse necking is suppressed in the tight radius bend test, the end of the stable line fit is determined from the strain rate corresponding to a 2% offset of the peak punch force instead of the approximation for diffuse necking.

### 5.1.6 Comparison of Fracture Detection Methods in the V-Bend Test

The preceding discussion demonstrated that adoption of the stress metric and the strain-rate detection method remedied the shortcomings in the VDA 238-100 failure detection method associated with occasional inconclusive results. The second concern in the V-Bend test is attributed to punch lift-off and can be addressed by tracking the out-of-plane displacement from DIC. **Figure 50a** demonstrates that thinning of the 270 Mild steel occurs up to bend angles of approximately 144° (±2) when the reverse out-of-plane displacement indicates punch lift-off. Interestingly, the punch force decreases much earlier at bend angles of about 127° (±2) and thus indicates that the false positive in the punch force occurred prior to punch lift-off. For the 3rd Gen 980 (**Figure 50b**), the reduction in the punch force correlates with the out-of-plane displacement to indicate fracture. Therefore, the stress metric needs to be limited to the maximum bend angle when punch lift-off occurs – the same applies to the thinning equation in Eq. (47b,c).

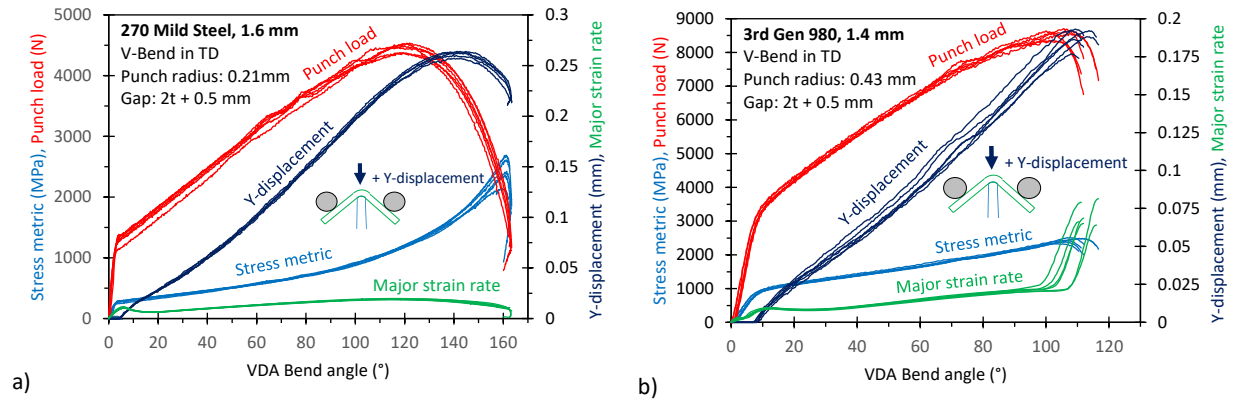


**Figure 50: Comparison of different fracture detection methods in the V-Bend tests demonstrated for the 270 Mild steel (a) and the 3rd Gen 980 (b). Note that the positive sign convention is adopted for thinning of the cross-section.**

For comparison of the failure strain among the various detection methods, the failure threshold needs to be determined. To this end, bend tests for the 3rd Gen 980 were performed with unpainted specimens such that the recorded DIC images in **Figure 51** provided a direct view of the surface evolution. In general, selection of a suitable failure threshold should be considered as material- and application-dependent. In the present study, the 3rd Gen 980 only exhibited hairline cracks at a 1% reduction in the stress metric and bending moment and might be more suitable for forming operations. Appreciable cracking, representative of crash applications, was not observed until much larger reductions in the punch force by approximately 48%.

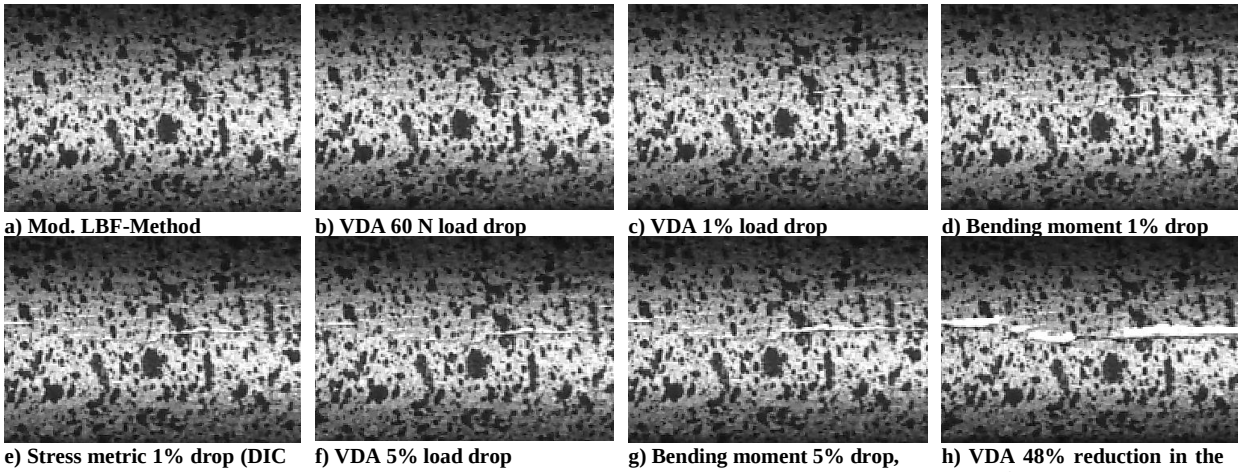


**Figure 51: Surface inspection of the 3rd Gen 980 V-Bend specimen at different thresholds for various failure detection methods. Note that DIC was performed in the absence of white background paint to provide a direct view on the material surface.**

Failure strains for a 1% threshold are depicted for the discussed failure detection methods in **Figure 52**. For materials with high ductility or during bending at low bend severity, adoption of the punch force as unique failure metric is insufficient and can lead to a marked underreporting of the material fracture strain, *e.g.* by

0.17 and 0.21 major strain for the 270 Mild steel and the 590R, respectively. Adoption of the bending moment works best for materials with appreciable hardening such as the 3rd Gen 980 and the 3rd Gen 1180 V2. In contrast, for the PHS1500 with a low hardening rate, the approximately constant bending moment makes failure detection sensitive to noise in the measurement. The stress metric is suitable for arbitrary hardening rates and also accounts for the specimen dimensions and thinning during bending through either DIC or an empirical thinning equation. Consideration of the major strain rate evolution in the Mod. LBF-Method occasionally performs too conservatively but can identify folding over of the specimen in the absence of fracture. To differentiate the performance of alloys of the same nominal strength, the plastic work of the cross-section until fracture can be employed to provide further insight since the hardening rate is embedded.

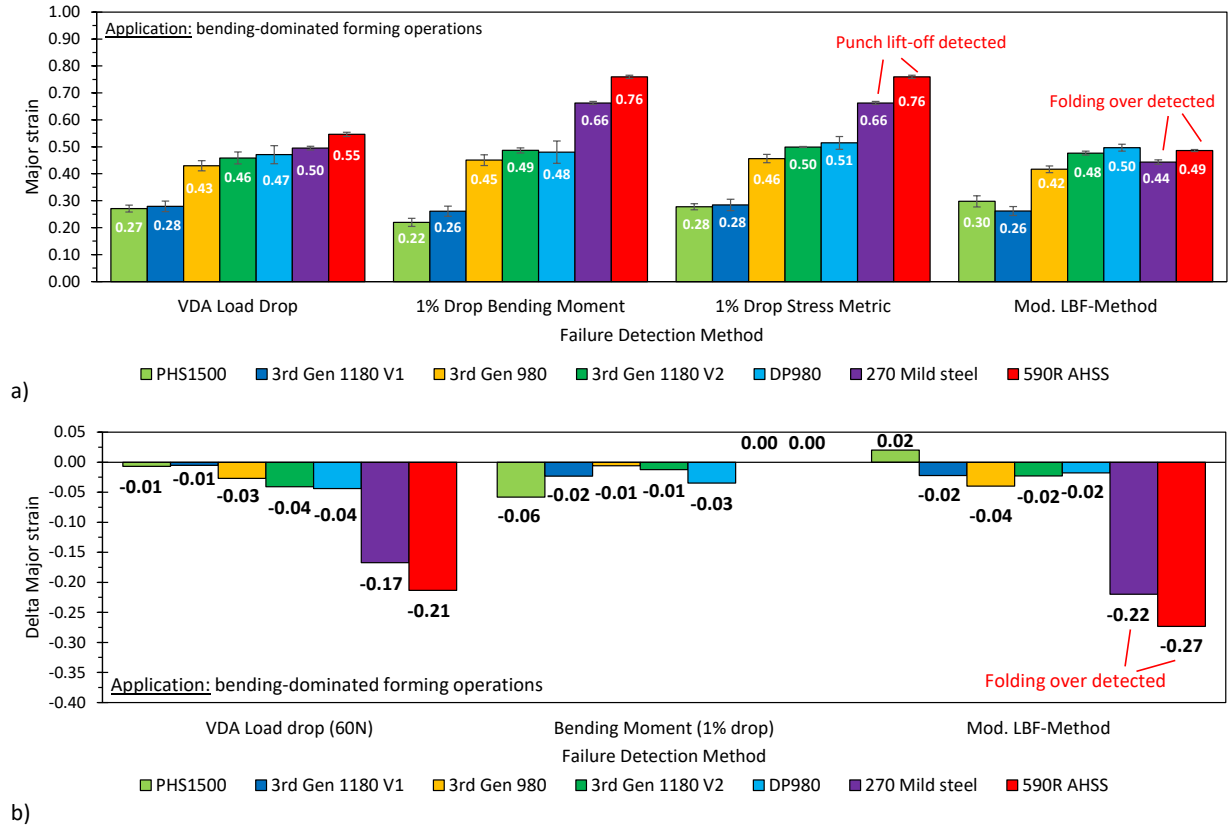


**Figure 52: Comparison of the major strain at fracture (a) and the difference in the major strain (b) reported by the VDA 238-100 specification, bending moment technique, and the Mod. LBF-Method relative to the stress metric adopting a 1% threshold and instantaneous thinning from DIC.**

## 5.2 Limit Strains in Combined Loading

The plane strain fracture strain of the 3rd Gen 980 AHSS is similar to the DP980 (0.51 *versus* 0.46 in the stress metric), but the performance of the 3rd Gen 1180 V2 with a major failure strain of 0.50 is particularly remarkable, which makes it an ideal candidate for the developed methodology in this thesis.

The in-plane forming limit of the 3rd Gen 1180 V2 discussed in Chapter 3 is moderate (plane strain limit strain of approximately 0.1) whereas the fracture limit in the presence of appreciable bending is drastically increased by a factor of about five. The strong sensitivity of the limit strains on the process conditions of bend severity and tool contact pressure can be exploited in the design of automotive lightweight components when considering the instantaneous necking limits. Therefore, the 3rd Gen 1180 V2 is focused upon and stretch-bend tests were conducted to complement the current set of experimental limit strains with necking limits under moderate bend severities.

### 5.2.1 Angular Stretch-bend Tests

A custom-made die set (see **Figure 19c**) with a 30 mm gap width and a single-curvature punch of 2 mm radius was installed in the same MTS formability press described in Chapter 3. Die and binder surfaces were knurled to mitigate material draw-in during stretch-bending. Both the specimen geometry and the punch speed of 0.25 mm/s utilized in the Marciniak and Nakazima tests were adopted in this study as well. A width of 76.3 mm was selected for the dogbone specimen in **Figure 15c** to yield a strain path of approximately plane strain tension. Ample Vaseline was utilized between the punch and the sheet to promote uniform deformation and localization at the specimen apex. The strain evolution on the convex surface was recorded utilizing full-field stereoscopic strain measurements from DIC with a VSGL of approximately unity. The resulting strain distribution at acute necking is depicted in **Figure 53** and highlights the different localization behavior in the conducted formability tests. The formation of an acute neck in the stretching-dominated tests (Marciniak and Nakazima) proceeds globally and is in stark contrast to the narrow localization band observed in the bending-dominated tests (ASB and V-Bend). Limit strains were determined from the refined LBF Method developed in Section 3.2 but the bending approximation for the stable strain rate was replaced with the relation for tight radius bending employed in the V-Bend tests in Eq. (48a-c).

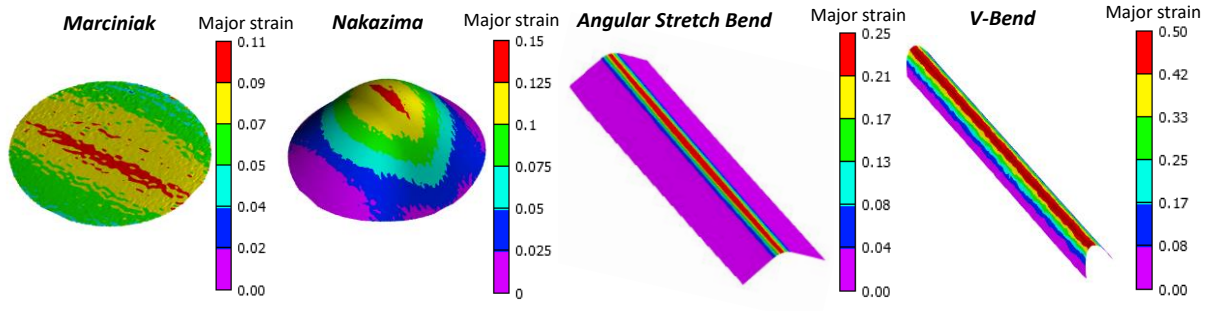


**Figure 53: Strain distribution at the necking limit for the studied formability tests. Since necking was suppressed in the V-Bend test, the fracture limit was determined from a 1% reduction in the stress metric.**

As shown in **Figure 54a,** the strain paths are fairly linear with the exception of the Nakazima test due to the hemispherical punch geometry that required linearization of the limit strains in **Figure 54b**. It is noted that the Marciniak limit strains for the 3rd Gen 1180 V2 and the fracture strains for remaining stress states, obtained from Noder *et al.* (2021a), were included in **Figure 54b** for completeness**.** The linearized Nakazima limit strains, slightly shifted to negative minor strains, only provide a marginal formability gain relative to in-plane limits of the Marciniak test. The small increase in limit strains is to be expected since the induced stress-strain gradients due to bending effects were shown to be small (Min *et al.*, 2016; Chen and Fang, 2018). Thus, the delay in plastic instability is mostly attributed to contact pressure effects. In contrast, plastic instability was markedly delayed in the stretch-bend tests that led to a stark formability gain from approximately 0.1 to 0.26 major strain. The necking limits in the ASB tests are well below the limits in the bend test of about 0.5 major strain but nevertheless represent a noticeable increase in the forming window by about 160% that can greatly relax constraints in the product design stage when properly accounted for.

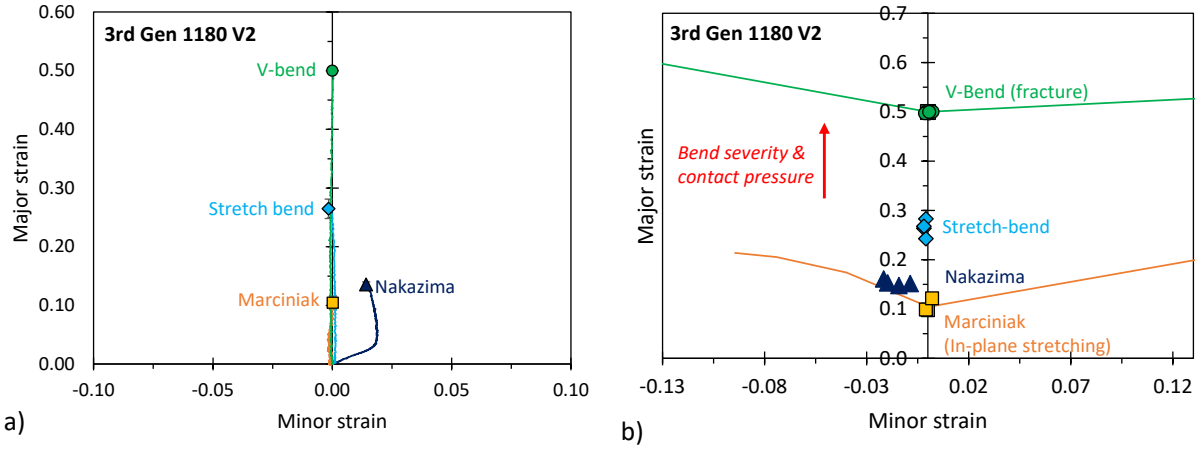


**Figure 54: One representative strain path extracted from a circular inspector tool of 0.5 mm radius for the Marciniak, Nakazima, and ASB tests and 0.25 mm radius in the V-Bend tests (a). Effect of bend severity on the limit strains (b). Note that the Nakazima limit stains in (b) were linearized.**

### 5.2.2 Analysis of Stretch-bend Severity

To provide more insight into the material behavior in combined loading, the deformation history was decoupled into contributions from bending and stretching. The instantaneous sheet curvature was approximated from a circle fit through the instantaneous node coordinates that were extracted from a line slice (length corresponds to the punch radius), positioned perpendicular to the principal loading direction in DIC (see **Figure 55a**). As shown in **Figure 55b**, the sheet in the Nakazima test gradually wraps around the punch and the average radius of the convex sheet (52.7 mm ± 0.8 mm) approximately corresponds to the punch radius plus initial sheet thickness when instability occurs. Contrary, in the ASB tests, the sheet initially wraps around the punch, reflected in a rapid decrease in the convex radius, and saturates at a radius

of approximately 10 mm halfway through the test. Interestingly, even at necking, the sheet does not conform to the punch radius and the sheet convex layer of 7.8 mm ± 0.5 mm is larger than the nominal value of 3.4 mm (initial sheet thickness plus nominal punch radius of 2 mm). Therefore, the common assumption of the two-stage deformation models that the sheet fully wraps around the punch is not justified for the tests in the present study and would lead to an overprediction of the bending effects. In contrast, in the V-Bend test, the material rapidly conforms to the punch radius in the first half of the test.

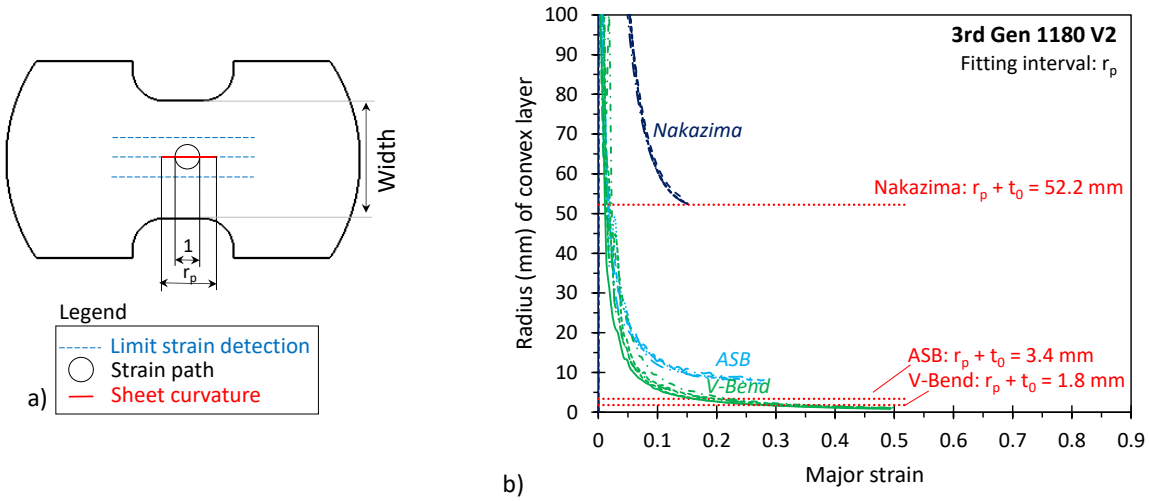


**Figure 55: Schematic of inspector tools utilized for data analysis in the Nakazima and ASB tests (a) and evolution of the sheet radius on the convex surface (b). Note that units are in mm.**

Since the convex sheet radius and strain history on the convex layer can be determined from DIC, simple bending mechanics (Hill, 1950) and volume conservation of a curved element (Aydemir, 2022) were employed to approximate the bending and membrane strain in stretch-bending. It is noted that both the shift in the neutral layer and sheet thinning were neglected in the bending analysis. The approximated strain components are depicted in **Figure 56a** and visualized in terms of the stretch-bend severity – ratio of the increment in the major bending strain to the membrane strain – in **Figure 56b**. The stretch-bend ratio is an indicator for the deformation mode, *e.g.* $\lambda > 1$ implies that the deformation is governed by bending whereas $\lambda < 1$ indicates that stretching is dominant. For ASB tests, the stretch-bend ratio is process-dependent and governed by the geometry of the tool set. The combined effect of punch radius and die gap affects how much the material is bent *versus* stretched. Since bending effects are mostly negligible in the Nakazima tests, the average stretch-bend ratio is rather low ($\lambda \sim 0.13$) and approximately constant throughout the test. In contrast, the deformation mode in the ASB tests is initially bending-dominated until a major strain of about 0.13 when the deformation transitions into a stretching mode that has direct implications upon the model strategy in Chapter 6.

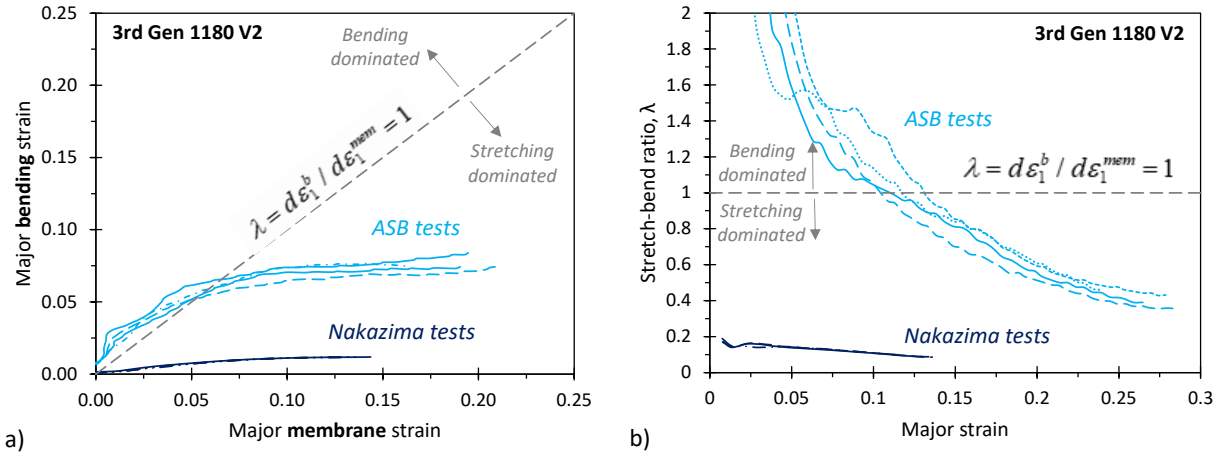


**Figure 56: Decoupled major strain components from the measured major strain in stretch-bending on the convex surface (a) and evolution of the stretch-bend ratio (b) in the Nakazima and ASB tests.**

## 5.3 Discussion on the Out-of-Plane Formability

This study provided a comprehensive experimental test campaign to characterize limit strains under process conditions of a varying degree of bending and contact pressure. The limiting case of abrupt fracture without a preceding neck in the presence of severe stress-strain gradients was studied in the V-Bend test. The controversy surrounding inconclusive results was revealed to be a natural consequence of the kinematic boundary conditions of the bend test and may lead to significant underreporting of the material performance. These complications are avoided in the novel stress metric that accounts for the specimen dimension and sheet thinning of the cross-section by means of the empirical thinning equation or direct DIC measurement. The developed methodology is readily applicable to a conventional V-Bend apparatus without a DIC system. Consideration of the major strain rate evolution on the convex sheet surface provides insight into the local fracture response and can identify folding over of the sheet specimen reflected in a decrease in the major strain rate.

Overall, the plane strain fracture performance of the two 3rd Gen 1180 variants was quite different (major failure strain of 0.28 for V1 *versus* 0.50 for V2) even though the in-plane forming limits were similar (major strain of approximately 0.1). Therefore, the 3rd Gen 1180 V2 is particularly suitable for the developed framework in this thesis due to the strong sensitivity of the process conditions on necking limits. The large window of the limit strains between in-plane loading and necking suppression can be exploited in the product design if properly accounted for.

Angular stretch-bend tests were conducted for the 3rd Gen 1180 V2 to obtain limit strains for a lower bend severity that induces sufficient stretching to trigger necking-based failure. Necking limits, identified from an extension of the Mod. LBF Method in Section 3.2 to accommodate tight radius bending, were

markedly lower than the V-Bend limits but still provided a significant increase relative to the Marciniak tests (major strain of approximately 0.26 *versus* 0.1). Further analysis of the deformation mode revealed that straining is primarily stretching-dominated in the Nakazima test for which the assumption of a constant stretch-bend ratio seems reasonable whereas deformation in the ASB tests is first bending-dominated and then transitions to a stretching mode. In addition, the sheet was found to not fully wrap around the punch in the present ASB tests, as commonly adopted in the two-stage models, and would lead to an overprediction of the stress-strain gradients over the cross-section. These experimental observations provided valuable insight into the process conditions in the formability test and serve the model development in Chapter 6.

# 6. Prediction of Forming Limits in Combined Bending and Stretching (Task 4 continued)

The experimental test campaigns documented in Chapters 3 and 5 confirmed an increase in the acute necking limits in the presence of bending and tool contact stresses – a formability gain that can be exploited when instantaneous forming limits are properly considered. The seemingly infinite combinations of process conditions render an experimental approach infeasible from a time and monetary perspective. A predictive tool is required but the complexity associated with the mechanics of plastic instability, non-monotonic straining, and complex stress states that are manifested in the form of gradients over the cross-section represent major obstacles. The GISC developed in Chapter 4 predicts acute necking limits under triaxial stress states and also accounts for the local boundary condition of how the load and tractions are applied to deform the material. It is the focus of this chapter to demonstrate how the GISC can be utilized to predict plastic instability in plane strain stretch-bending with superimposed tool contact pressures. Special attention is devoted to how the deformation history is prescribed. Although the two-stage modelling approach appeared to work well in the studies of Vallellano *et al.* (2010), Morales-Palma *et al.* (2013, 2017), and He *et al.* (2013c) it is problematic from a material standpoint since de-coupling of stretch-bending affects the neck formation (De Kruijf *et al.*, 2009). The study of Morales-Palma *et al.*, (2017) accounted for bending normal stresses but neglected the bending process; the lower cross-section could not undergo compressive loading that greatly alters the deformation mode and differs from the deformation history of the stretch-bend tests discussed in the preceding chapter. Simultaneously accounting for contributions from stretching and bending while incorporating bending normal stresses is particularly challenging since it requires knowledge of the instantaneous location of the neutral layer and adds complexity to the through-thickness stress integration. The effect of how superimposed tool contact pressure to the bending normal stresses affects the mechanics of stretch-bending adds another layer of complexity and constitutes the major novelty of this chapter.

First, the resulting stress state of the cross-section is established on continuum level and serves to develop a control algorithm to resolve the through-thickness stress-strain gradients during plane strain stretch-bending in a simplified total strain formulation and a general incremental framework. This subroutine is then coupled with the GISC of Chapter 4 to identify acute necking. A parametric study is conducted to provide insight into the mechanisms that lead to a delay in plastic instability in combined loading under complex stress states. Finally, the instability framework is applied to the experimental test campaign of the 3rd Gen 1180 V2 of Chapter 5.

The prepared manuscript can be found in Appendix D:

**Noder, J.,** Butcher, C. On the Influence of Tool Contact Pressure on Tensile Instabilities in Plane Strain Stretching and Bending of Sheet Metals, to be submitted, May 2022.

## 6.1 Mechanics of Stretch-bending

The material exhibits orthotropy with the coordinate axes in the plane defined through the direction *1*, *2*, and *3* as depicted in **Figure 57**. Loading is constrained to principal triaxial space in the absence of shear deformation. Quantities denoted with subscript *1* and *2* are attributed to the primary and secondary loading direction and are referred to as major and minor quantity, respectively. Quantities should be treated as unordered principal values since the order of the principal quantities may change due to compressive loading and also depend on the magnitude of the through-thickness stress in the out-of-plane direction *3*.

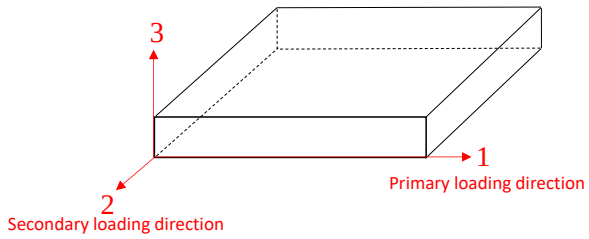


**Figure 57: Schematic of terminology used to define the stress-strain state.**

The effect of the compressive tool contact stress ($\sigma_c$) on the overall stress state during stretch-bending was derived on continuum level and is composed of plane strain bending with superimposed plane strain tensile stretching ($\sigma_{sb}$) (i) and tool contact pressures that induce uniaxial compression (ii), defined as

$$\sigma = \sigma_{sb} + \sigma_c, \qquad \sigma_{sb} = \sigma_1 \begin{bmatrix} 1 & 0 & 0 \\ 0 & \alpha & 0 \\ 0 & 0 & \chi_b \end{bmatrix}, \qquad \sigma_c = \sigma_1 \begin{bmatrix} 0 & 0 & 0 \\ 0 & 0 & 0 \\ 0 & 0 & \chi_c \end{bmatrix} \tag{49a-c}$$

where the through-thickness stress ratio can be decomposed into contributions from normal bending stresses, $\chi_b$, and tool contact pressures, $\chi_c$, defined as

$$\chi = \chi_b + \chi_c, \qquad \chi_b = \frac{\sigma_b}{\sigma_1}, \qquad \chi_c = \frac{\sigma_c}{\sigma_1}, \qquad \alpha = \frac{1+\chi_b}{2} \tag{50a-d}$$

The in-plane stress ratio for plane strain loading in Eq. (50d) is determined from the condition of a vanishing second principal deviatoric stress ($s_2 = 0$), which also corresponds to a vanishing third deviatoric stress invariant ($J_3 = 0$), discussed in Butcher and Abedini (2019b). Computation of the deviatoric stress components of the resultant stress state yields

$$s_1 = \frac{1}{6}\sigma_1\left(3-\chi_c-2\chi\right), \qquad s_2 = -\frac{1}{3}\sigma_1\chi_c, \qquad s_3 = \frac{1}{6}\sigma_1\left(-3+\chi_c+3\chi\right) \tag{51a-c}$$

which indicates a shift of the stress state towards biaxial tension. To better visualize this effect on the strain path, the evolution of the principal in-plane strain ratio for a von Mises plasticity model is depicted in **Figure 58**. The convex surface is a free surface and remains in a state of plane strain-plane stress whereas material layers within the cross-section are subjected to a shift in the strain path to positive minor strains. The magnitude of the strain path shift is governed by the magnitude of both the contact stress ratio and the through-thickness stress ratio that has the bending effects embedded. Therefore, a compressive tool contact stress effectively induces a non-linear strain path such that each material layer will experience a different deformation history that has direct implications on the modelling strategy.

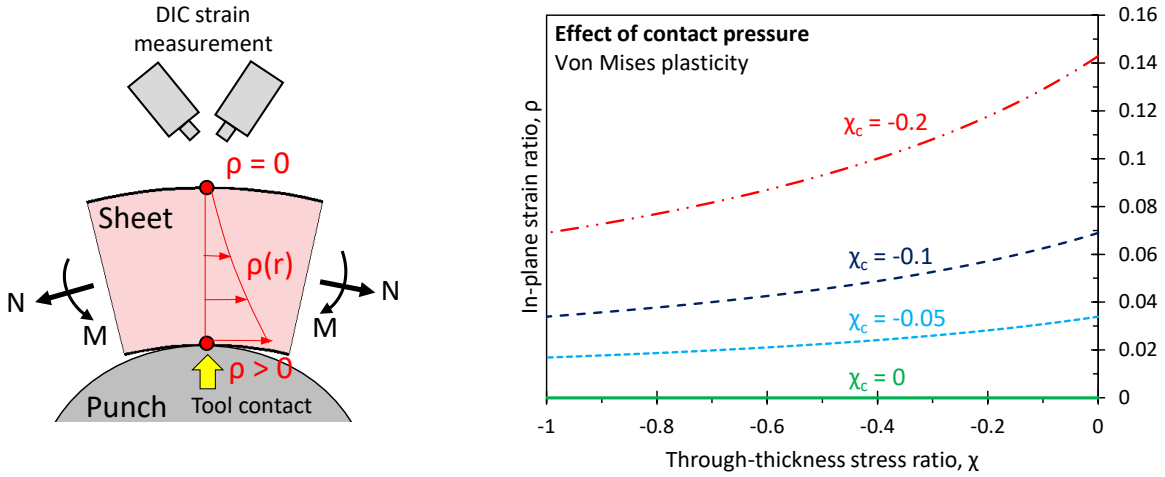


**Figure 58: Effect of a compressive tool contact stress on the strain path that is shifted to positive minor strains.**

## 6.2 Model Development

The induced shift in the strain path as a consequence of the compressive contact stress adds considerable complexity to the model development since proportional straining only prevails on the convex layer. To model the mechanics during stretch-bending with a superimposed tool contact pressure, four different modelling strategies were considered. In analogy to the strain path on the convex layer, the simplified modelling technique enforces plane strain tension (PST) of the cross-section, referred to as the PST Model. The more advanced approach accounts for the shift in the strain path towards biaxial tension (BT) and is referred to as the BT Model. Both models are implemented in a simplified total strain formulation (TL) for which closed-form solutions are derived and in a generalized multi-layer incremental framework (IL) that requires numerical methods. The different scenarios are summarized as TL-PST, IL-PST, TL-BT, and IL-BT.

It is noted that the total strain formulations, commonly used in bending mechanics, are not as rigorous since stressing is assumed proportional, but warrant consideration as a simpler alternative to the incremental multi-layer model. The following assumptions were employed in the development of the modelling strategies:

(i) The material is homogeneous without voids, damage, or softening. The flow stress is equal to the equivalent stress $\bar{\sigma}(\varepsilon_{eq}^{p}) = \sigma_{eq}$.

(ii) The material is treated as rigid-plastic such that elasticity is neglected.

(iii) The focus is on stretching-dominated loading such that reverse loading effects are neglected.

(iv) Radial sections remain plane during bending (Bernoulli theorem).

(v) A compressive normal stress is uniformly applied on the concave layer and assumed to evolve proportionally with the major in-plane stress to mimic tool contact pressure.

(vi) Sheet thinning and contact pressure effects are neglected during bending but accounted for during membrane stretching. Therefore, deformation is constrained to mild-to-moderate stretch-bending where bending effects play a secondary role and instability governs the process rather than fracture on the convex surface.

(vii) Membrane deformation in the form of tensile stretching is prescribed through a constant in-plane major strain increment, $d\varepsilon_1^{mem}$.

(viii) The deformation history of stretch-bending is modelled in a semi-coupled approach. Bending and stretching are considered simultaneously through the stretch-bend ratio, $\lambda$, that can be constant or evolve with deformation.

Instead of a two-stage deformation process, the contribution of stretching and bending is considered simultaneously, expressed through the stretch-bend ratio, $\lambda$

$$\lambda = \frac{d\varepsilon_1^b(r_y)}{d\varepsilon_1^{mem}(r_y)}, \quad \varepsilon_{1,(n+1)}^{mem}(r_y) = \varepsilon_{1,(n)}^{mem}(r_y) + d\varepsilon_1^{mem}(r_y), \quad \varepsilon_{1,(n+1)}^{b}(r_y) = \varepsilon_{1,(n)}^{b}(r_y) + \lambda d\varepsilon_1^{mem}(r_y) \quad \text{(52a-c)}$$

where the subscripts *(n+1)* and *(n)* refer to the variable in the current and previous step and are omitted in the subsequent discussion. The major strain increment in membrane stretching, $d\varepsilon_1^{mem}$, serves as a control variable and is prescribed to the convex surface in fixed increments of $5\text{x}10^{-4}$. Using Eq. (52b-c), the total major strain and its increment on the convex layer are assembled to

$$\varepsilon_1(r_y) = \varepsilon_1^{mem}(r_y) + \varepsilon_1^{b}(r_y), \quad d\varepsilon_1(r_y) = d\varepsilon_1^{mem}(r_y) + d\varepsilon_1^{b}(r_y) \quad \text{(53a,b)}$$

Computation of the strain for arbitrary material layers within the cross-section is specific to the assumption of a total or incremental strain formulation and is discussed separately in Section 6.2.1 and 6.2.2, respectively.

To account for the strain path shift as a consequence of the tool contact pressure, the stretch-bend equilibrium equation was derived from the fundamentals of bending mechanics for general loading. The deformation is prescribed through a constant major strain increment on the convex layer and was selected over adoption of tension per unit width (Hill, 1950; Hudgins *et al.*, 2010, Alexandrov *et al.*, 2011) for experimental correlation. From a practical consideration, tension per unit width appears less intuitive and may not be readily available unless using finite-element simulations. In contrast, the strain increment can be retrieved from DIC and the severity of stretch-bending is expressed in a practical manner. The strain boundary conditions applied to a differential volume element are depicted in **Figure 59a** and give rise to the stress state in **Figure 59b.** Note that the stress components denoted with an asterisk represent the resultant of the applied strain increment to mimic stretch-bending and, for convenience, are omitted in the subsequent analysis. Force equilibrium in the through-thickness direction, assuming $\sin\left(d\theta/2\right) \approx d\theta/2$, and neglecting second order terms yields

$$r\left(d\sigma_b + d\sigma_c - \sigma_b\frac{dw}{w} - \sigma_c\frac{dw}{w}\right) = \left(\sigma_1 - \sigma_b - \sigma_c\right)dr \tag{54}$$

where the term $dw/w$ is attributed to the change in the sheet width as a consequence of the compressive tool contact stress that induces a shift of the strain path towards biaxial tension. Eq. (54) reverts back to the well-known bending equilibrium equation proposed by Hill (1950) for plane-strain bending ($dw/w = 0$) in the absence of tool contact pressure ($\sigma_c = 0$).

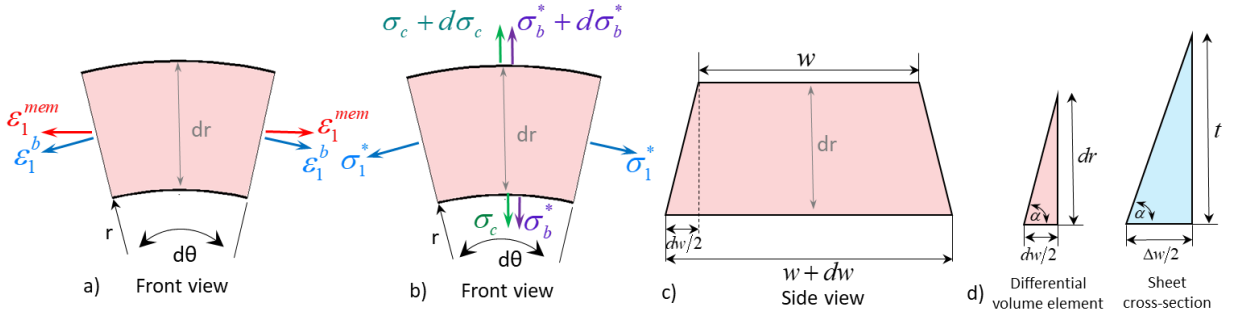


**Figure 59: Differential volume element of the prescribed strain boundary condition (a) that gives rise to the stress state (b). The side view of the differential volume element (c) schematically illustrates the change in the sheet width as a consequence of the compressive tool contact stress that is exploited in the concept of similar triangles (d) for the development of the modelling strategy in the total strain formulation.**

Solving for the unknown bending stress in Eq. (54) depends on assumptions upon the linearity of the deformation history and is discussed in the following.

### 6.2.1 Total Strain Formulation (TL)

The major strain for arbitrary locations within the sheet thickness was derived from volume conservation

$$\varepsilon_1 = \ln\left(\frac{r}{r_m}\right) - \frac{1}{(1+\bar{\rho})}\ln\left(\frac{t}{t_0}\right), \qquad r_m = r_i + \frac{t}{2}, \qquad \bar{\rho}(\alpha,\chi) = \frac{1}{t}\int_{r_i}^{r_y} \rho(\alpha,\chi)\, dr \tag{55a-c}$$

where $\bar{\rho}$ corresponds to the average change in the in-plane strain ratio of the cross-section and vanishes for proportional plane strain tension, *e.g.* in the absence of contact pressure. Neglecting sheet thinning during bending, the bending strain increment is

$$\varepsilon_1^b = \ln\left(\frac{r}{r_m^b}\right), \qquad r_m^b = r_y^b - \frac{t_0}{2}, \qquad r_y = r_y^b + t - t_0 \tag{56a-c}$$

where supercript *b* is utilized to highlight variables attributed to bending. Utilizing the strain prescribed on the convex layer and Eq. (55a), the convex layer radius due to bending is obtained and utilized with Eq. (56c) to numerically solve for the unknown sheet thickness, $t$

$$f(t) = \varepsilon_1(r_y) - \ln\left(\frac{r_y^b + t - t_0}{r_y^b - t_0 + t/2}\right) + \frac{1}{(1+\bar{\rho})}\ln\left(\frac{t}{t_0}\right) = 0, \qquad r_y^b = \frac{t_0 \exp\left[\varepsilon_1^b(r_y)\right]}{2\left\{\exp\left[\varepsilon_1^b(r_y)\right] - 1\right\}} \tag{57a,b}$$

The equivalent plastic strain is obtained from the incremental plastic work balance and volume constancy

$$\varepsilon_{eq}^p = \int d\varepsilon_{eq}^p, \quad d\varepsilon_{eq}^p = C(\alpha,\chi)\, d\varepsilon_1, \quad C = k(\alpha,\chi)\left\{1 + \alpha\rho(\alpha,\chi) - \chi\left[1 + \rho(\alpha,\chi)\right]\right\} \tag{58a-c}$$

where the strain increments are replaced with total strains in the special case of *monotonic proportional stressing*. The functional forms of $C(\alpha,\chi)$ and $k(\alpha,\chi)$ have an explicit dependence upon the stress state and are governed by the modelling assumptions. For plane-strain loading and von Mises plasticity, the stress state dependence for $C$ vanishes and reduces to the scalar value of $2/\sqrt{3}$ but is not applicable to general loading.

To solve the ordinary differential equation (ODE) in Eq. (54), the concept of similar triangles, visualized in **Figure 59d** was employed to maintain the geometry and to establish a relationship between the infinitesimal width change, $dw$, and the total width change of the sheet cross-section, $\Delta w$, such that

$$dw = \frac{\Delta w}{t} dr, \qquad \frac{dw}{w} = \frac{1}{t}\frac{\Delta w}{w} dr = \bar{\rho}(\alpha,\chi)\bar{\varepsilon}_1^{mem}, \qquad \bar{\varepsilon}_1^{mem} = -\frac{1}{(1+\bar{\rho})}\ln\left(\frac{t}{t_0}\right) \tag{59a-c}$$

where $\bar{\varepsilon}_1^{mem}$ represents the average membrane strain of the cross-section. Substitution of Eq. (59b) into Eq. (54) and adoption of the dimensionless stress ratios defined in Eq. (8c), (9b), and (50b,c) leads to

$$d\left[k(\alpha,\chi)\bar{\sigma}\left(\varepsilon_{eq}^{p}\right)\chi\right] = \frac{1}{r}k(\alpha,\chi)\bar{\sigma}\left(\varepsilon_{eq}^{p}\right)(1-\chi_b-\chi_c)dr + \bar{\rho}(\alpha,\chi)\bar{\varepsilon}_1^{mem}k(\alpha,\chi)\bar{\sigma}\left(\varepsilon_{eq}^{p}\right)\chi \qquad \chi_c(r) = \chi_{c0}\frac{(r_y - r)}{t} \tag{60a,b}$$

where $\chi_b$ is the only unknown variable. It is noted that a linear through-thickness evolution of the contact pressure, defined in Eq. (60b) is employed where $\chi_{c0}$ corresponds to the prescribed contact pressure on the concave layer. The contact stress ratio is maintained constant to mimic a proportionally evolving contact pressure with the major stress.

For simple yield functions and constitutive models, Eq. (60a) can be integrated analytically for material zones that undergo the same (monotonic) deformation history. In the present study, a two-zone model was proposed that divides the cross-section into a tensile and compressive zone for material layers located above and below the neutral layer, respectively. For simplicity, reverse loading was neglected in the total strain formulation and the neutral layer was assumed to coincide with the unstretched layer, derived from volume conservation of the cross-section

$$r_u = r_m \frac{t}{t_0}\frac{w}{w_0} = r_m \exp(-\bar{\varepsilon}_1^{mem}) \tag{61}$$

Closed-form solutions of Eq. (60a) were derived for von Mises plasticity and the Swift hardening model of Eq. (19) by making assumptions upon the stress-strain state of the cross-section. It is noted that since the boundary conditions in the stretch-bend model are only known on the convex layer, integration is performed unidirectional, starting from the convex layer where plane strain-plane stress prevails. Details on the stress integration are provided in Appendix E5.

Closed-form solutions for the bending stress ratio were derived for the TL-PST model that enforces plane strain tension of the cross-section. The in-plane strain and stress ratios are

$$\rho = 0, \qquad \alpha = \frac{1+\chi_b+\chi_c}{2} \tag{62a,b}$$

and the bending stress ratios in the respective zones are

Zone I (tension): $r \geq r_n$

$$\chi_b = \frac{Y_1^{n+1} - Y_2^{n+1}}{-\frac{2}{\sqrt{3}} Y_2^{\,n}(n+1) + Y_1^{n+1} - Y_2^{n+1}} - \chi_c, \qquad Y_1 = \varepsilon_0 + \frac{2}{\sqrt{3}} \ln\left(\frac{r_y}{r_u}\right), \quad Y_2 = \varepsilon_0 + \frac{2}{\sqrt{3}} \ln\left(\frac{r}{r_u}\right) \tag{63a-c}$$

Zone II (compression): $r < r_n$

$$\chi_b = \frac{Y_1^{n+1} - Y_3^{n+1}}{Y_1^{n+1} - Y_3^{n+1} + \frac{2}{\sqrt{3}} Y_3^{\,n}(n+1)} - \chi_c, \qquad Y_3 = \varepsilon_0 - \frac{2}{\sqrt{3}} \ln\left(\frac{r}{r_u}\right) \tag{63d,e}$$

Close inspection of Eq. (63a,d) and the in-plane stress ratio in Eq. (62b) reveals that the effect of $\chi_c$ is essentially cancelled out. As a result, the contact pressure appears to have no effect on the necking limits in the PST model and will be further discussed in Section 6.3.2.

An iterative procedure is required for the TL-BT model to account for the shift of the strain path towards positive minor strains in the presence of tool contact pressure. The stress ratios are obtained numerically, adopting the non-linear root finding function *fzero* in Matlab®. A new estimate in $\bar{\rho}$ of Eq. (55c) and the sheet thickness in Eq. (57a) is then computed until a prescribed tolerance of the change in the average strain path of $1\times10^{-3}$ is met. The in-plane strain and stress ratios are

$$\rho^{VM} = \frac{-2\chi_c}{3-3\chi+\chi_c} \geq 0, \qquad \alpha = \frac{1+\chi_b}{2} \tag{64a,b}$$

and the condition for the bending stress ratio is

Zone I (tension): $r \geq r_n,\ x_n = 1$

$$\begin{aligned} f(\chi_b) = {} & \chi k(\alpha,\chi,x_n) K Y_4^{\,n} - \frac{K}{n+1}\left[-Y_1^{n+1} + (1-\chi_b-\chi_c)\frac{k(\alpha,\chi,x_n)}{C(\alpha,\chi,x_n)} Y_4^{\,n+1}\right] \\ & + \bar{\rho}(\alpha,\chi)\bar{\varepsilon}_1^{mem}\chi k(\alpha,\chi,x_n) K Y_4^{\,n} = 0 \end{aligned} \tag{65a}$$

Zone II (compression): $r < r_n,\ x_n = -1$

$$f\left(\chi_b\right) = \chi K k\left(\alpha,\chi,x_n\right) Y_5^{\,n} - \frac{K}{n+1}\left\{-\left(1-\chi_{b,r_n}-\chi_{c,r_n}\right)\frac{k\left(\alpha_{r_n},\chi_{r_n},x_n\right)}{C\left(\alpha_{r_n},\chi_{r_n},x_n\right)}\varepsilon_0^{\,n+1} + \left(1-\chi_b-\chi_c\right)\frac{k\left(\alpha,\chi,x_n\right)}{C\left(\alpha,\chi,x_n\right)}Y_5^{\,n+1}\right\} + \bar{\rho}\left(\alpha,\chi\right)\bar{\varepsilon}_1^{mem}\chi k\left(\alpha,\chi,x_n\right)KY_5^{\,n} - k\left(\alpha_{r_n},\chi_{r_n},x_n\right)\chi_{r_n}K\varepsilon_0^{\,n} = 0 \tag{65b}$$

where

$$Y_4 = \varepsilon_0 + \frac{2\left(4\chi_c^{\,2}-6\chi_c+3\chi_b^{\,2}-6\chi_b+6\chi_b\chi_c+3\right)^{\frac{1}{2}}}{3-3\chi_b-2\chi_c}\ln\left(\frac{r}{r_u}\right),$$

$$Y_5 = \varepsilon_0 - \frac{2\left(4\chi_c^{\,2}-6\chi_c+3\chi_b^{\,2}-6\chi_b+6\chi_b\chi_c+3\right)^{\frac{1}{2}}}{3-3\chi_b-2\chi_c}\ln\left(\frac{r}{r_u}\right) \tag{65c,d}$$

It is noted that the stress ratios denoted with a subscript $r_n$ in Eq. (65b) are computed from Eq. (65a) for $r = r_n$ and are related to the continuity condition of the normal stress in Zones I and II. At the neutral layer $\sigma_3^I\left(r_n\right) = \sigma_3^{II}\left(r_n\right)$ that is analogous to $\chi^I\left(r_n\right) = -\chi^{II}\left(r_n\right)$ but requires inversion of the sign since the stress ratio is defined with respect to the in-plane stress, which is positive and negative in Zones I and II, respectively. Relative to the TL-PST model for which $\chi_b$ could be solved analytically, computing $\chi_b$ in the TL-BT model in Eq. (65a,b) is more complex and requires numerical methods due to the explicit dependence of $C\left(\alpha,\chi\right)$ and $k\left(\alpha,\chi\right)$ upon the stress state

$$k = x_n 2\left(3\chi_b^{\,2}-6\chi+6\chi_b\chi_c+4\chi_c^{\,2}+3\right)^{-\frac{1}{2}} \tag{66a}$$

$$C = x_n\frac{2\left(4\chi_c^{\,2}-6\chi_c+3\chi_b^{\,2}-6\chi_b+6\chi_b\chi_c+3\right)^{\frac{1}{2}}}{3-3\chi_b-2\chi_c} \tag{66b}$$

where $x_n$ is introduced to account for the compressive stress in the primary loading direction if the material layer is located below the neutral layer.

### 6.2.2 Incremental Strain Formulation (IL)

The equivalent plastic strain was integrated in a multi-layer model to trace out the deformation history of each material layer. The sheet thickness was divided into layers defined through the dimensionless

parameter $\xi$ ranging from 0 (convex layer) to -1 (concave layer), where the current radius is expressed through the convex layer radius and the sheet thickness. The major strain increment is derived by taking partial derivatives of the total strain formulation in Eq. (55a) to arrive at

$$r = r_y + \xi t, \qquad d\varepsilon_1 = \left(\frac{r_m - r}{r_m}\right)\frac{dr_y}{r} + \left[\frac{t}{r}\xi + \frac{t}{2r_m} - \frac{1}{\left(1+\bar{\rho}\right)}\right]\frac{dt}{t} + \frac{1}{\left(1+\bar{\rho}\right)^2}\ln\left(\frac{t}{t_0}\right)d\bar{\rho} \tag{67a,b}$$

where $d\bar{\rho}$ corresponds to the incremental change in the average strain path between steps (see Eq. (55c)). The incremental change in the sheet thickness, $dt$, is computed from Eq. (67b) by utilizing the strain increment prescribed on the convex layer in Eq. (53b) and establishing relations for the yet unknown quantities

$$f(dt) = d\varepsilon_1(r_y) - \left(\frac{r_m - r_y}{r_m}\right)\frac{dr_y}{r_y} - \left[\frac{t}{2r_m} - \frac{1}{\left(1+\bar{\rho}\right)}\right]\frac{dt}{t} - \frac{1}{\left(1+\bar{\rho}\right)^2}\ln\left(\frac{t}{t_0}\right)d\bar{\rho} = 0 \tag{68a}$$

where the change in the convex layer radius, $dr_y$, is computed from the bending strain increment

$$dr_y = dr_y^b + dt, \qquad d\varepsilon_1^b = \left(1 - \frac{r_y^b}{r_m^b}\right)\frac{dr_y^b}{r_y^b}, \qquad dr_y^b = \frac{d\varepsilon_1^b(r_y)r_y^b}{\left(1 - \dfrac{r_y^b}{r_m^b}\right)} \tag{68b-d}$$

$$t_{(n+1)} = t_{(n)} + dt, \qquad r_y = r_y^b + \left(t_{(n+1)} - t_0\right), \qquad r_m = r_y^b + \left(t_{(n+1)} - t_0\right)/2 \tag{68e-g}$$

and the current sheet thickness, $t_{(n+1)}$, is expressed in terms of the sheet thickness of the previous step, $t_{(n)}$, and current sheet thinning. Thus, the only unknown quantity in Eq. (68a) is $dt$ that is solved for numerically utilizing the *fzero* function in Matlab®. Adopting Eq. (67b), the instantaneous location of the neutral layer is readily determined from the condition of a vanishing major strain increment ($d\varepsilon_1 = 0$)

$$r_n = \frac{dr_y - r_y dt/t}{\left[-\left(1 + \dfrac{t}{2r_m} - \dfrac{1}{\left(1+\bar{\rho}\right)}\right)\dfrac{dt}{t} - \dfrac{1}{\left(1+\bar{\rho}\right)^2}\ln\left(\dfrac{t}{t_0}\right)d\bar{\rho} + \dfrac{dr_y}{r_m}\right]} \tag{69}$$

which is utilized to determine the sign of $x_n$ for integration of the equivalent plastic strain. To better demonstrate how the location of the neutral layer is embedded in the plasticity equations, the ratio of the

major stress to the equivalent stress in Eq. (8b), required to compute $C$ in Eq. (58c), is generalized for arbitrary yield functions

$$\varepsilon^{p}_{eq,(n+1)} = \varepsilon^{p}_{eq,(n)} + C\left(\alpha,\chi,x_n\right)d\varepsilon_1, \qquad k = \frac{x_n\left|\sigma_1\right|}{\sigma_{eq}\left(\alpha,\chi\right)}\begin{cases} r \geq r_n : x_n = 1 \\ r_n < r : x_n = -1 \end{cases} \tag{70a,b}$$

In light of the functional form of the major strain increment in Eq. (67b), derivation of closed-form solutions is no longer practical. The stretch-bend equilibrium equation in Eq. (54) is re-arranged and expressed in terms of the dimensionless stress ratios while noting that for small strain increments $d\varepsilon_2 = dw/w = \rho\left(\alpha,\chi\right)d\varepsilon_1^{mem}$, such that

$$\frac{d\sigma_3(\alpha,\chi)}{dr} = \frac{1}{r}\left[k\left(\alpha,\chi,x_n\right)\bar{\sigma}\left(\varepsilon^{p}_{eq}\right) - \sigma_3(\alpha,\chi)\right] + \frac{d\varepsilon_1^{mem}}{dr}\rho\left(\alpha,\chi\right)\sigma_3(\alpha,\chi) \tag{71}$$

where the change of the major membrane strain over the sheet radius is computed from the discrete increments of the radial change of Eq. (67a) and by noting that $d\varepsilon_1^{mem}(r) = d\varepsilon_1(r) - d\varepsilon_1^{b}(r)$. The algorithm utilized to solve the ordinary differential equation (ODE) in Eq. (71) is schematically illustrated in **Figure 60** and comprises a combination of Runge-Kutta and the non-linear root finding function *fzero* in the software Matlab®. In analogy to finite-element analysis, the layers of the cross-section are further discretized with integration points where Eq. (71) is evaluated. A total of 200 layers and 4 integration points over the layer were adopted. Integration is initiated from the convex layer where boundary conditions are known and the result of the last integration point of the respective layer serves as the boundary condition for solving the ODE of the subsequent layer. Details on the code implementation are provided in Appendix E4.

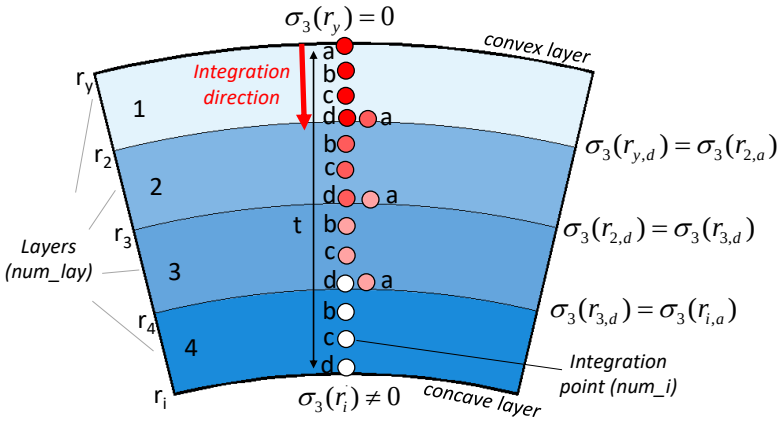


**Figure 60: Schematic of algorithm utilized to solve the ODE in the incremental multi-layer modeling approach. The sheet cross-section is divided into layers (*num_lay*) and integration points (*num_i*).**

Stress integration is repeated with an updated estimate for the sheet thickness until convergence of $\bar{\rho}$ is obtained. Necking is evaluated from the CSR of Tharrett and Stoughton (2003) but based upon the triaxial instability limits that are governed by the boundary conditions (see Eq. (29a) for proportional stressing), referred to as the instantaneous concave side rule (iCSR). In the absence of necking, the equivalent plastic strain on the convex layer is assessed for potential fracture without a preceding neck by comparison to the user-defined equivalent fracture strain. The above procedure is repeated for the next strain increment until instability occurs.

## 6.3 Limit Strain Prediction

The choice of the modelling strategy upon predicted limit strains was studied for von Mises plasticity and the Swift hardening model of Eq. (19) utilizing the same parameters as in Chapter 3 ($K$ = 500 MPa, $n$ = 0.1, and $\varepsilon_0$ = 0.002). It is noted that reverse loading effects that may activate complex hardening behavior are beyond the scope of the present study. Nevertheless, all plasticity-related quantities required for computation of the back-stress tensor and softening terms are available in the proposed modelling strategy and are readily amenable to a kinematic hardening model for future studies.

### 6.3.1 Neglecting Tool Contact Pressure

Model predictions were first compared to the special case of *plane stress* loading ($\lambda$ =1×10$^{-10}$, $\chi_c$ = 0) in plane strain tension, representative of Marciniak tests, where closed-form solutions are available. The major strain evolution in **Figure 61a** confirms the vanishing strain gradient over the cross-section and the stress and strain ratios depicted in **Figure 61b** highlight proportional plane stress-plane strain tension over the entire cross-section. Therefore, as expected, the acute necking limits for all models are identical.

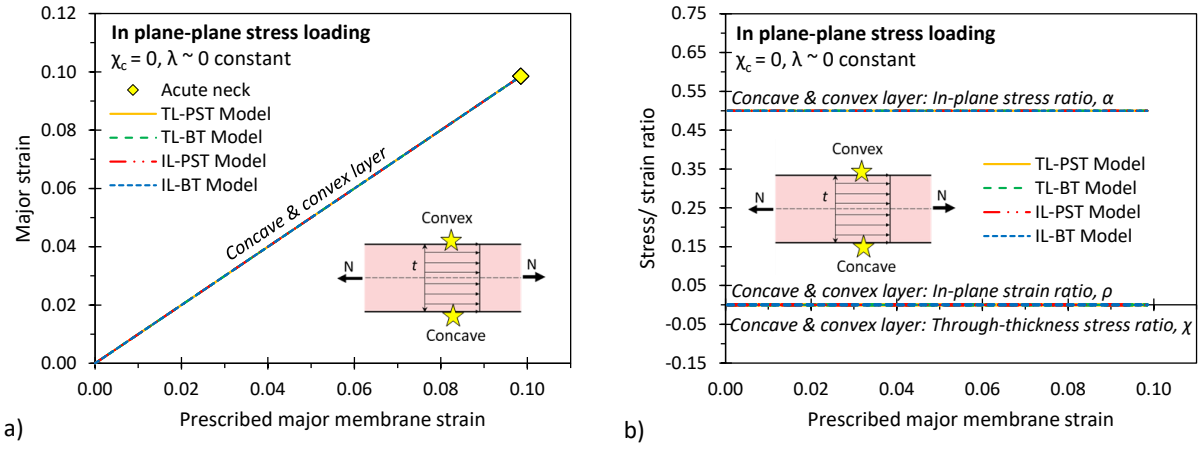


**Figure 61: Comparison of model predictions for plane stress loading in plane strain tension considering the major strain evolution (a) and the stress and strain ratios on the concave and convex layer (b).**

First, contact pressures were neglected and similar to the work of Morales-Palma *et al.* (2017), evolving normal stresses were only due to bending. The convex layer remains in a state of plane strain-plane stress (**Figure 62a**) whereas a triaxial stress state evolves for material layers within the sheet thickness, as depicted for the concave layer in **Figure 62b**. The increase in the through-thickness stress ratio with ongoing deformation is a consequence of the developing normal stresses in bending and is balanced by the in-plane stress ratio to maintain proportional plane-strain stressing, reflected in a vanishing in-plane strain ratio. Due to monotonic stretching of the cross-section ($\lambda$ = 0.2, constant), all model predictions are in good agreement.

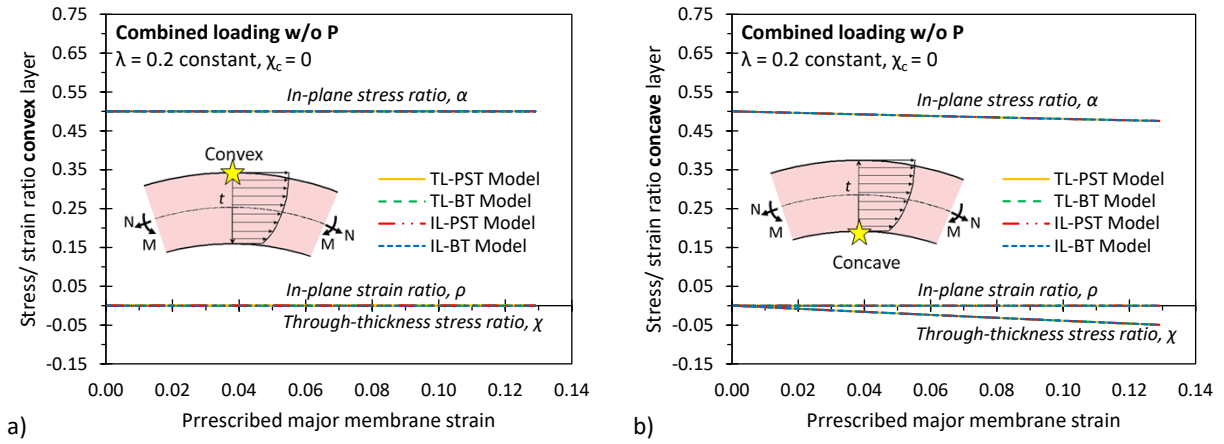


**Figure 62: Comparison of model prediction of the stress-strain state on the convex (a) and concave layer (b) for combined loading in the absence of contact pressure.**

The assumption of monotonic stressing is crucial to the adoption of the total strain formulation, but differs from the deformation history encountered in forming operations with appreciable bending when the sheet initially wraps around the punch. The two scenarios for the evolution of the stretch-bend ratio, visualized in **Figure 63a**, were studied. Consideration of an evolving stretch-bend ratio provides a realistic description of the deformation process in a forming operation, but requires a multi-zone model to accommodate sequential loading of the cross-section. The constant stretch-bend ratio of 0.4 was approximated from the average value of $\lambda\left(\varepsilon_1^{mem}\right)$. **Figure 63c-d** depict the major and equivalent plastic strain evolution of the concave layer for both loading scenarios and highlight complications surrounding the adoption of the total strain formulation since the equivalent plastic strain is not cumulative. As a result, the consumed hardening rate in the compressive stage is not reflected in the instability calculation as shown in **Figure 63b.** A delay in plastic instability is erroneously predicted from a major strain of 26% in the incremental formulation to 30% in the total strain framework. Necking limits between the constant and evolving stretch-bend ratio are

similar ( $\varepsilon_1$ = 27% *versus* 26% major strain), but are expected to show a larger deviation for materials with a higher hardening rate. Therefore, an incremental approach is required for non-monotonic stressing.

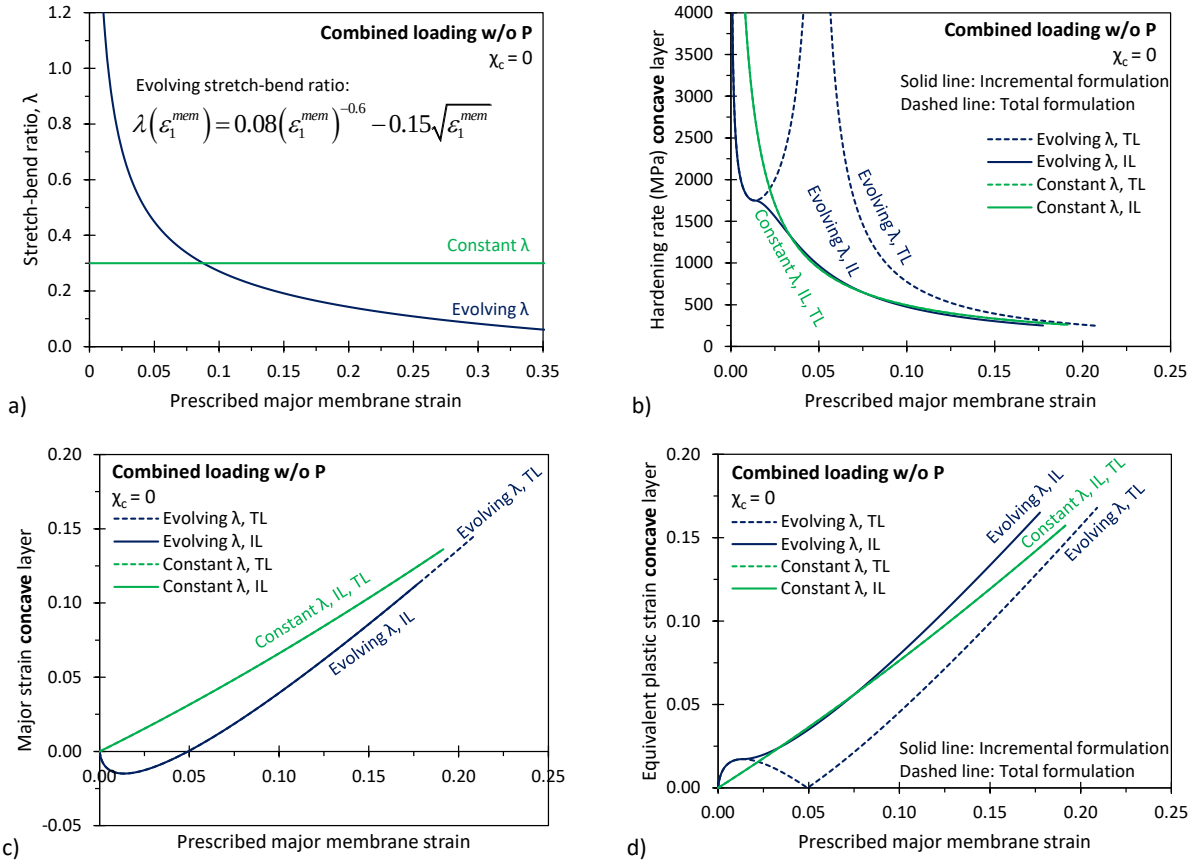


**Figure 63: Effect of assumption upon the evolution of the stretch-bend ratio (a) on the hardening rate (b) and both the major strain (c) and equivalent plastic strain (d).**

The influence of the stretch-bend severity was studied for the IL-BT model in **Figure 64**. Overall, the superposition of bending delays strain accumulation for material layers within the cross-section. A larger value of $\lambda$ induces more bending and thus results in a larger strain gradient through the sheet thickness (**Figure 64a**). Since the formation of an acute neck is assumed to be controlled by the strain evolution on the concave layer, the higher stretch-bend ratio directly translates to an increase in the necking limit. Consideration of the instantaneous forming limit in the iCSR acts as a secondary factor that delays plastic instability. Through-thickness bending stresses evolve with the stretch-bend severity (**Figure 64b**) and lead to a larger magnitude of the critical subtangent that yields larger in-plane forming limits.

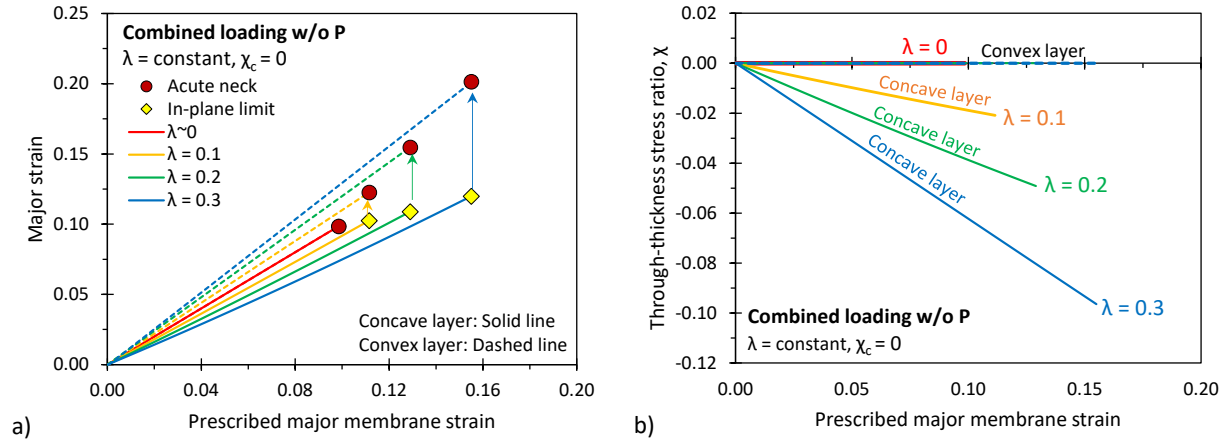


**Figure 64: Effect of stretch-bend ratio on the major strain accumulation on the concave and convex layer (a) and implications on the resulting through-thickness stress ratio (b).**

For $\lambda = 0.3$, the in-plane necking limit increased from 0.098 to 0.120 that has direct implications on the strain on the convex layer but is not considered in the traditional CSR, which neglects the local boundary conditions. The necking limits on the convex layer, identified from the iCSR, are visualized for the IL-BT model in **Figure 65**. Note that in analogy to the study of Neuhauser *et al.* (2016), a constant formability gain was assumed for remaining stress states such that a constant offset – determined from plane strain loading – is employed upon the in-plane forming limit curve. Even when neglecting contact pressure effects, superposition of bending to in-plane stretching has a strong effect on plastic instability with a predicted formability gain of 26%, 58%, and 106% for stretch-bend ratios of $\lambda$ = 0.1, 0.2, and 0.3, respectively.

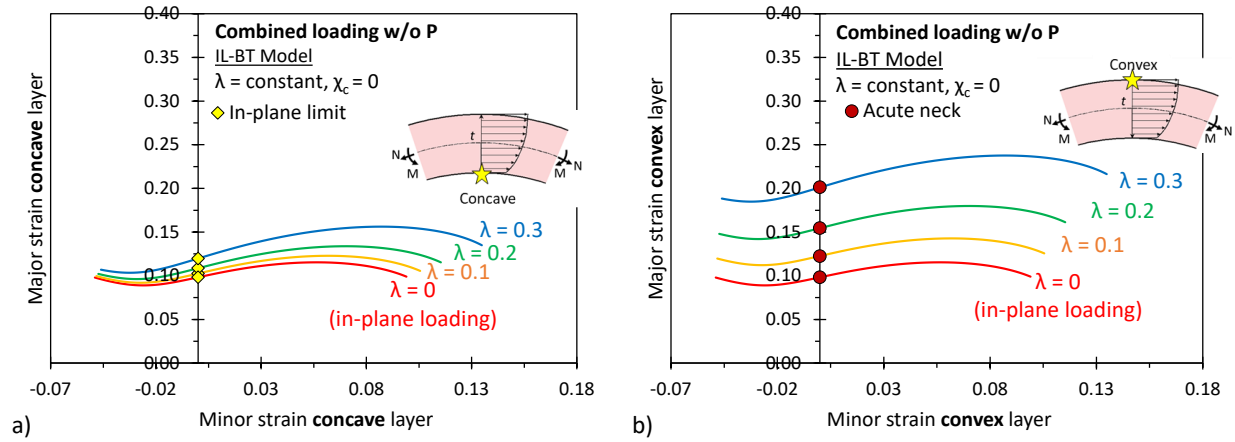


**Figure 65: Effect of stretch-bend ratio on the in-plane forming limit (a) that is utilized to identify the formation of an acute neck on the convex layer employing the iCSR (b).**

### 6.3.2 Accounting for Tool Contact Pressure

In the absence of contact pressure, the PST and BT models were in good agreement since the cross-section was subjected to plane-strain tension. However, differences in the modelling strategy are visible in

**Figure 66** when a compressive tool contact stress is superimposed. It is noted that the through-thickness stress ratio, $\chi$, now represents the resultant ratio with two contributions arising from bending and compressive contact stresses. For a constant stretch-bend ratio of $\lambda$ = 0.2 and a contact stress ratio of $\chi_c$ = -0.1, the convex layer remains in plane strain tension, but the stress-strain state on the concave layer varies among the modelling strategies. The PST model remains in plane strain tension, but the BT model captures the shift away from plane strain tension to biaxial stretching reflected in $\rho > 0$ and $\alpha > 0.5$.

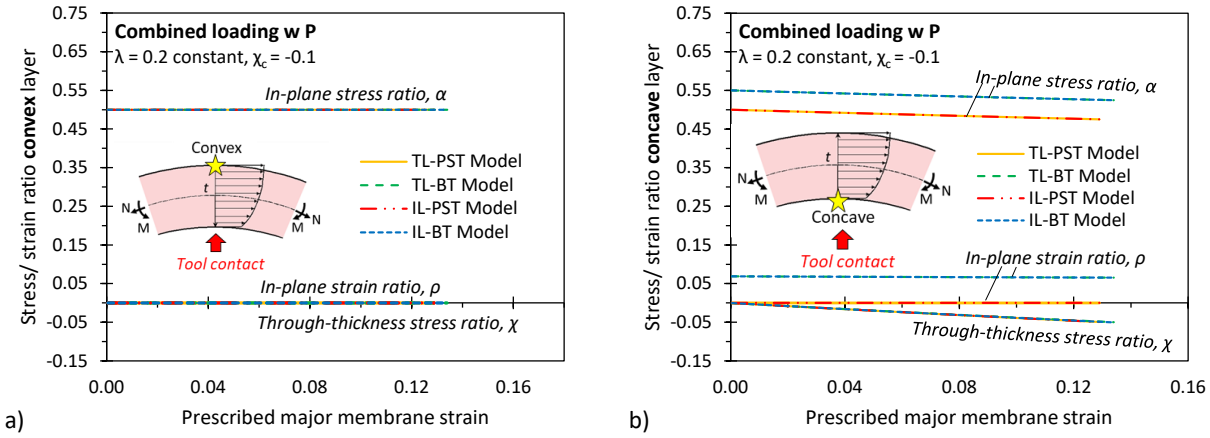


**Figure 66: Comparison of model prediction of the stress-strain state on the concave (a) and convex layer (b) for combined loading in the presence of contact pressure.**

Thus, even for monotonic straining, the presence of a compressive normal stress induces a non-proportional deformation history and, from an academic perspective, requires an incremental analysis. Nevertheless, the evolution of the in-plane strain ratio on the concave layer indicates that $\rho$ remains approximately constant (initial value of 0.069 and final value of 0.066), which explains why the total strain formulation (TL-BT) is in agreement with the incremental model (IL-BT) for the selected conditions. This observation is inherent to low values for $\chi$ that was shown in **Figure 58** to result in negligible or small changes in $\rho$. The effect of the magnitude of the contact pressure upon necking limits was studied for the incremental strain formulation and a constant stretch-bend ratio of 0.2. It was found that the contact pressure only affects the strain distribution in the IL-BT model, but has no effect in the IL-PST as depicted in **Figure 67a-b**. The major in-plane strain limit in the IL-BT model is increased for larger contact stresses, but the strain is not accumulated slower as observed for higher stretch-bend severities (refer to **Figure 64a**). The increase in the in-plane forming limits are tied to the resulting through-thickness stress ratio and the shift in the strain path. In the IL-PST model (**Figure 68a**), the resultant through-thickness stress ratio on the concave layer is constant regardless of the applied contact pressure, whereas the IL-BT model (**Figure 68b**) predicts an increase in $\chi$ for larger contact pressures that delays instability.

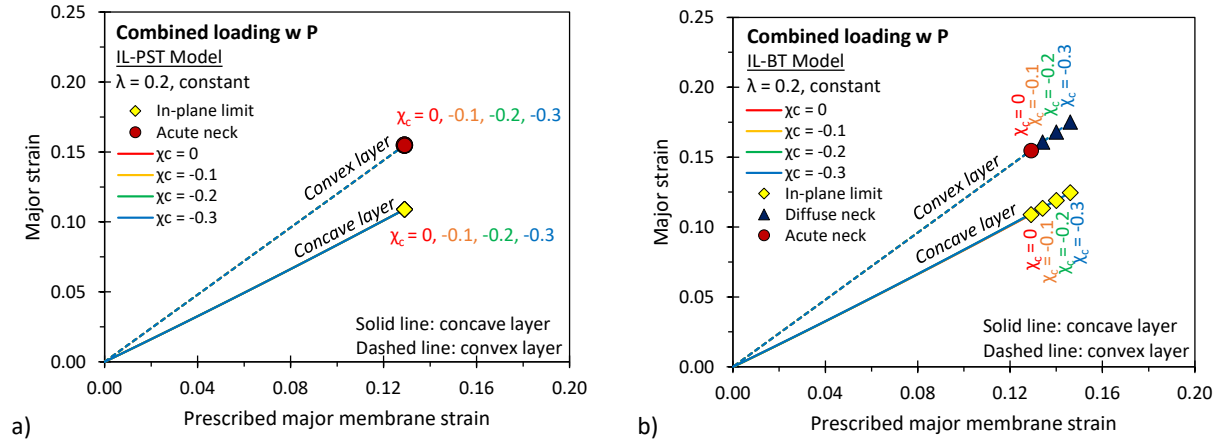


**Figure 67: Comparison of predicted major strain evolution for the IL-PST model (a) and the IL-BT model (b).**

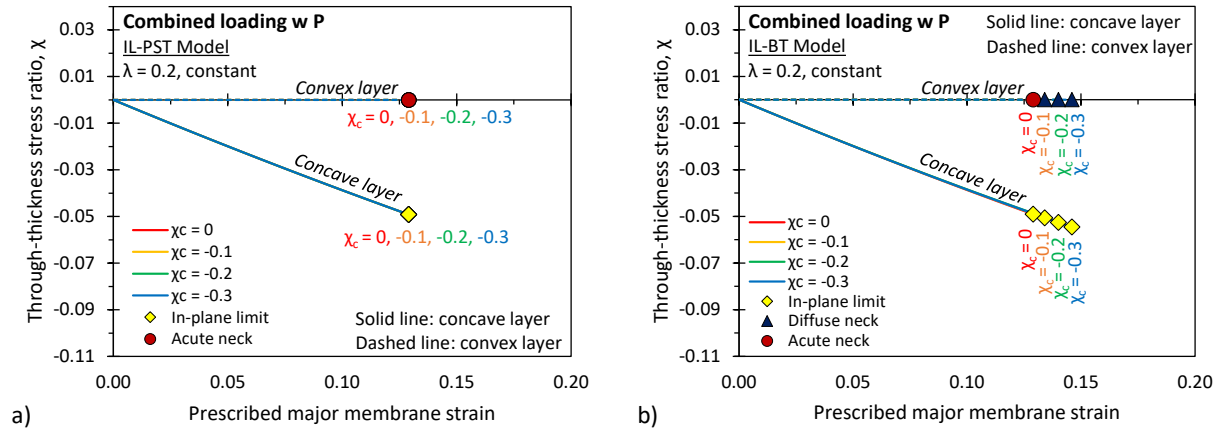


**Figure 68: Comparison of resultant through-thickness stress ratio for the IL-PST model (a) and the IL-BT model (b).**

Nevertheless, the change in the through-thickness stress ratio from $\chi$ = -0.049 to $\chi$ = -0.051, -0.053, and -0.055 for a contact stress ratio of $\chi_c$ = -0.1, -0.2, and -0.3, respectively would only lead to a marginal increase in the plane strain limit strains. In fact, it is the shift in the strain path from plane strain tension to positive minor strains that is the driving factor to delay plastic instability for compressive contact stresses in the BT model. Since the magnitude of the strain path shift is governed by the magnitude of the contact stress ratio, a larger contact pressure induces a greater shift of the strain path (see **Figure 69b**), which is associated with a stronger delay in plastic instability. The PST model fails to capture this effect (see **Figure 69a**), such that the predicted acute necking limits are not affected by the contact pressure.

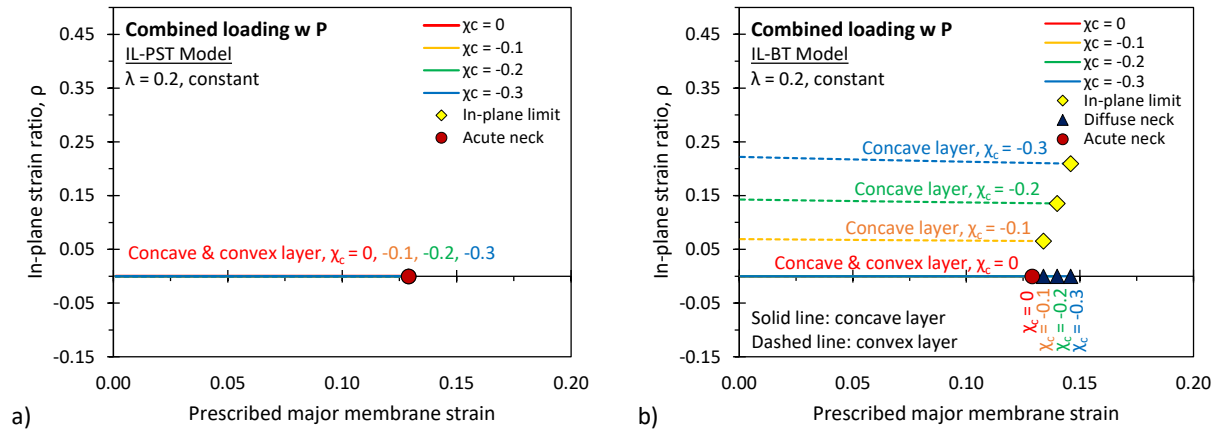


**Figure 69: Comparison of predicted in-plane strain ratio in the IL-PST model (a) and the IL-BT model (b).**

The increase in the in-plane forming limit as a consequence of the shift in the strain path is governed by the shape of the forming limit curve for stress states beyond plane strain tension. The S-shape in the 3D Swift model (proportional stressing) as depicted in **Figure 70a** is particularly favorable since the diffuse necking limits are larger for biaxial strain paths but depend upon boundary conditions of the deformation process. Adoption of the Dorn model (Dorn and Thomsen, 1947) for proportional stressing with a prescribed minor load results in an approximately straight line across stress states from uniaxial tension to biaxial stretching. In this case, the in-plane forming limits do not benefit from the induced shift in the strain path. Nevertheless, there is a secondary effect associated with the strain path related to the localization process. Only for plane strain loading, diffuse and acute necking limits are identical for a strain-rate independent material whereas for remaining strain paths, forming limits associated with an acute neck are usually higher. Therefore, the necking limits in the IL-BT model were distinguished between forming limits associated with an acute neck when the concave layer is subjected to plane-strain tension and with a diffuse neck for remaining strain paths. Acute necking limits on the concave layer, computed from the GISC for proportional stressing, are overlaid with the strain evolution on the concave layer in **Figure 70a**. For identification of the acute necking limits on the convex layer in **Figure 70b**, it was assumed that the strain gradient over the sheet thickness at the onset of diffuse necking remains constant during localization. For small contact pressure values, diffuse and acute necking limits are similar and the complexity added through modelling of the localization process may not be warranted. In this case, diffuse necking limits may serve as a first order approximation of the acute limit strains.

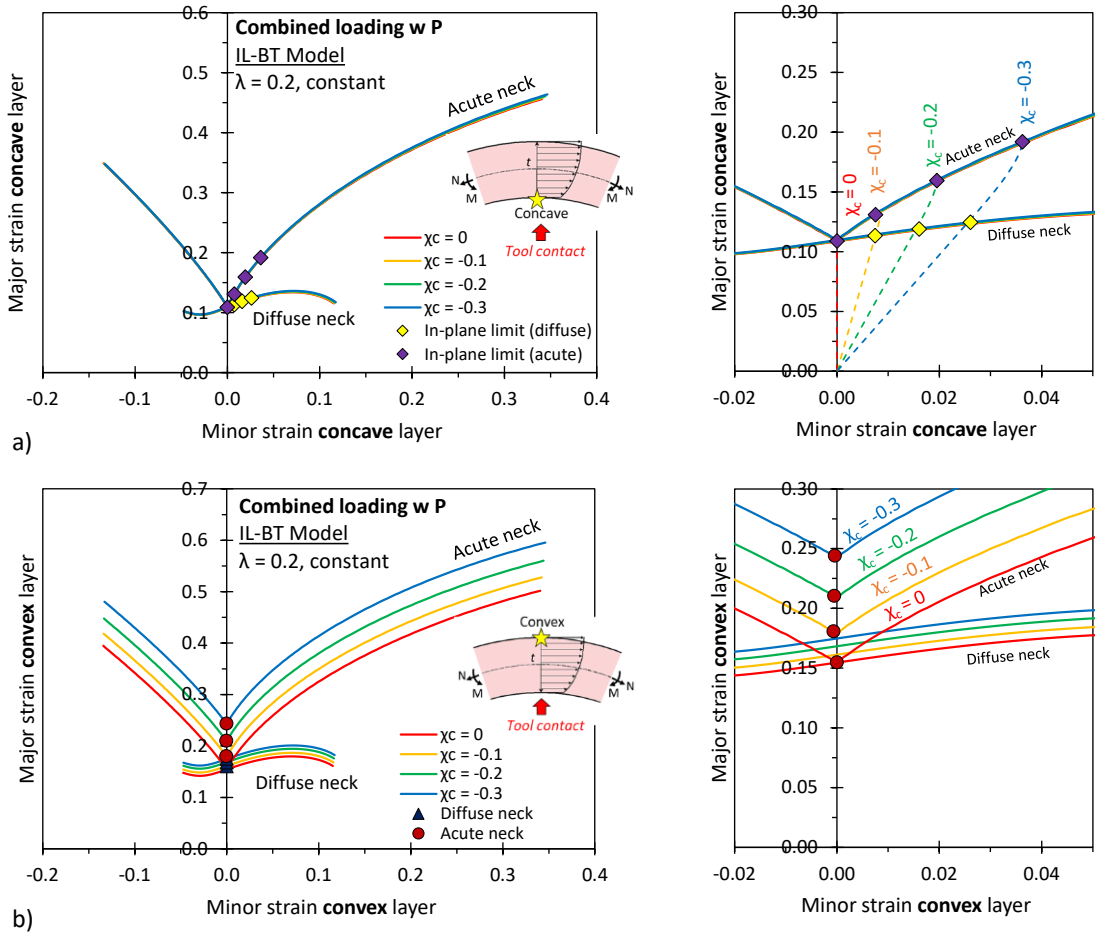


**Figure 70: Effect of the induced shift in the strain path as a consequence of compressive tool contact stresses upon acute necking limits on the concave layer (a) and convex layer (b).**

## 6.4 Application to the 3rd Gen 1180

To demonstrate applicability of the developed instability framework to AHSS for automotive lightweighting, necking limits of the IL-BT model were contrasted with the characterized forming limits of the 3rd Gen 1180 V2 in Chapter 5. It is noted that a direct comparison between predictions and experiments is not intended at this point, which would require a contact pressure model and a kinematic hardening model to account for reverse loading effects.

Model predictions are depicted in **Figure 71**. Constant stretch-bend ratios of $\lambda$ = 0.09 and $\lambda$ = 0.4 were adopted for the Nakazima and the ASB test, respectively, which corresponds to the approximate stretch-bend ratios when necking was detected in the experiments (see **Figure 56b**).The contact pressure of $\chi_{c0}$ = -0.15, linearly distributed through the sheet thickness, was selected to yield good agreement with the plane strain necking limit and was maintained constant for the predictions in both the Nakazima and the ASB tests. It is noted that the process conditions in the Nakazima test were simplified to single-curvature

bending. Consistent with the linearized necking limits in the Nakazima tests, the predicted FLC for in-plane loading was linearized following the methodology discussed in Section 3.5. Overall, the IL-BT model could successfully capture the overall trend in how plastic instability is delayed for higher bend severities and contact pressures.

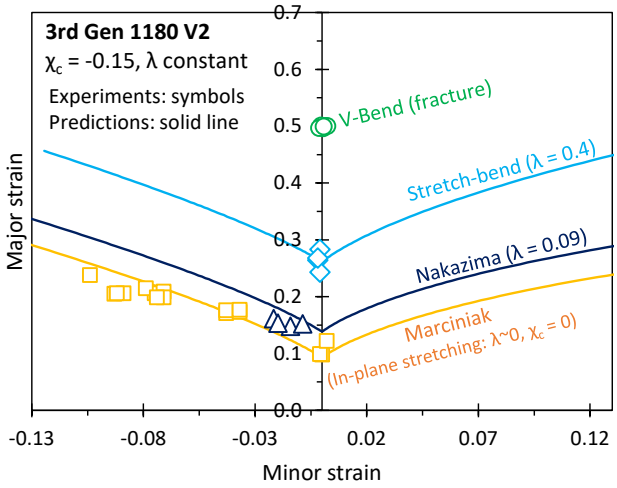


**Figure 71: Predicted forming limits for different stretch-bend severities and comparison to conducted formability tests for the 3rd Gen 1180 V2 AHSS.**

## 6.5 Discussion on the Formability in Combined Loading

The present study provided a control algorithm to resolve stress-strain gradients in plane strain stretch-bending that was coupled with the GISC of Chapter 4 to mechanistically predict acute necking limits while accounting for both bending normal stresses and compressive tool contact stresses. The effect of a superimposed contact pressure to the stress state in plane strain stretch-bending was derived on continuum level and shown to effectively induce a shift of the strain path to positive minor strains. Plasticity-related equations were derived from general bending mechanics considering a simplified total strain formulation and a general incremental multi-layer approach. Among the developed modelling strategies, only the incremental multi-layer model, which accounts for the strain path shift (IL-BT), could capture the dependence of the contact pressure upon necking limits and account for compressive loading of the concave layer. It was found that plastic instability in plane strain stretch-bending in the presence of a compressive tool contact stress is caused by four factors:

(i) The through-thickness strain gradient causes a delay in the accumulated strain on the concave layer such that the in-plane necking limit is reached later.

(ii) Compressive normal stresses as a consequence of bending mechanics lead to a larger critical subtangent that yields higher in-plane limit strains that is accounted for in the iCSR.

(iii) The shift in the strain path to positive minor strains that may be associated with higher in-plane necking limits.

(iv) The localization process from a diffuse to an acute neck that is associated with higher limit strains.

It is noted that the contribution of each factor is dependent on the process condition (*e.g.* the magnitude of the contact pressure and the stretch-bend severity) and the local boundary condition of the deformation process, *e.g.* how the load and tractions are applied, which affects the instability condition.

The simplified modelling approach of enforcing plane strain tension upon the entire cross-section (TL-PST and IL-PST) could capture the increase in necking limits in combined loading, but failed to predict a secondary delay in plastic instability due to tool contact pressure. The total strain formulation, while attractive due to its simple implementation, is problematic when contributions of stretching and bending are considered simultaneously since the equivalent plastic strain is not cumulative, which limits the deformation to monotonic tension.

Application of the developed instability framework to the experimental test campaign of the 3rd Gen 1180 V2 in Chapter 5 demonstrated the capability of the IL-BT model to capture the overall trend in the formability for a constant stretch-bend ratio and a contact stress ratio of -0.15. The instability framework in its current form can be utilized to generate acute necking limits for different bend severities for input into commercial FE software, *e.g.* AutoForm. The contact pressure, its evolution, and through-thickness distribution present large factors of uncertainty, but can be approximated from simulations for the respective forming operation and input into the theoretical model.

# 7. Conclusions

The presented research has provided insights into the effect of tool contact pressure and the importance of both process and local boundary conditions on plastic instability in sheet metal forming. Forming limits were experimentally characterized over a range of different conditions from in plane-plane stress loading in the Marciniak tests to out-of-plane loading in the Nakazima and angular stretch-bend tests. The limiting case of abrupt fracture without a preceding neck was studied in the tight-radius bend test where failure was determined from a novel fracture detection method. Considering the strong dependence of the process conditions (stretch-bend severity and contact pressure) on the necking limits of the studied 3rd Gen 1180 V2, modelling strategies were developed to account for the instantaneous nature of the forming limits. The physically-derived Generalized Incremental Stability Criterion (GISC) was developed from the work of Hillier (1963) to compute the diffuse localization process from the concept of neutral incremental stability for a continuous transition of the stress state. The boundary conditions of the deformation process are embedded in the critical subtangent of the GISC. A control algorithm was developed to resolve evolving through-thickness stress-strain gradients during plane strain stretch-bending from the fundamentals of bending mechanics and was coupled with the GISC. The main outcome of this research is the development of an instability framework to predict acute necking limits in combined plane-strain loading while accounting for the local boundary conditions of the deformation process under complex stress states. This framework will play an important role in the product design stage of automotive lightweight components to leverage formability gains by assessment of both process and local boundary conditions.

The following conclusions can be drawn from this research:

- The calibration technique of the constitutive model may have a significant effect on the accuracy of forming limit predictions and phenomenological mapping criteria. The plastic uniform elongation, identified in a tensile test, is to be enforced in the calibration of the hardening model to avoid artefacts of a shift of the $FLC_0$. The material hardening behavior should be experimentally characterized to strain levels associated with biaxial limit strains, *e.g.* in shear or bulge tests.

- Marciniak limit strains should be utilized to assess correlations with analytical plane stress models, consistent with the physics of the framework of in plane-plane stress loading. Instead, adoption of Nakazima limit strains may lead to incorrect conclusions unless limit strains are corrected for apparent process effects associated with out-of-plane triaxial loading. Identification of the limit strains plays a vital role in the non-linear strain path corrections.

- The phenomenological stress-based mapping criteria to account for the contact stress feature a direct dependence of the mapped limit strains upon the material hardening rate. Stark formability

gains are predicted for low-hardening alloys with a saturation-type hardening behavior even for infinitesimally non-zero normal pressures. Analytical solutions derived from the Hillier instability framework support appreciable formability gains for proportional triaxial stressing but the increase in limit strains is an order of magnitude smaller than predicted by the stress-based mapping methods. The proposed work-based mapping under a constant in-plane stress ratio provides some correlation with the analytical solution for non-proportional stressing under a constant contact pressure but is limited to a hardening exponent of $n = 0.1$.

- The presence of a compressive normal stress generally leads to a delay in plastic instability. The magnitude of the formability gain is governed by the magnitude of the contact pressure and the underlying boundary conditions, *e.g.* how the normal pressure is applied. The assumption that the contact pressure proportionally increases with the major stress – equivalent to a 3D Swift model – provides the largest formability gain among the studied conditions. Non-proportional stressing under a constant contact pressure constitutes the lower bound of the formability increase since the contact pressure only provides stability *via* the constitutive model.

- The limitation of the Hillier framework to diffuse necking is overcome in the Generalized Incremental Stability Criterion (GISC). The concept of neutral incremental stability is adopted to compute the quasi-stable localization process associated with a transition of the stress-strain state to plane strain tension. It is demonstrated that the 2D MMFC of Hora *et al.* (2013) is just one special case of the general framework under the assumption of proportional stressing with a prescribed minor load or approximate proportional loading.

- Characterization of the plane strain fracture strain is crucial in the presence of appreciable bending that may lead to the suppression of tensile instabilities and abrupt fracture without a preceding neck. For ductile alloys or thin materials, reliance upon the punch force for fracture identification in the VDA 238-100 tight radius bend test may lead to inconclusive results. A reduction in the punch force is a natural consequence of the kinematic boundary condition of the test frame even in the absence of material fracture. The current VDA 238-100 specification does not account for these limiting cases.

- The developed stress-based failure metric remedies the shortcomings of inconclusive results without introducing new parameters. Thinning of the cross-section is accounted for – either through DIC or a phenomenological equation – to avoid complications surrounding a constant bending moment for low-hardening materials. Consideration of the major strain rate evolution sheds light into potential folding over of the specimen associated with a reduction in the strain rate relative to an acceleration of the major strain in the case of material fracture.

- The effect of a superimposed contact pressure to plane strain stretch-bending essentially causes a shift of the strain path away from plane strain tension to positive minor strains. The magnitude of the strain path shift is governed by the magnitude of the contact pressure and the resultant through-thickness stress, which has the bending effects embedded.

- Accounting for the strain path shift in the ASB modelling technique (BT model) is crucial to capture the secondary delay in plastic instability when contact pressure is superimposed to the stress state in plane strain stretch-bending. The simplified modelling strategy that enforces plane strain tension over the cross-section (PST model) only captures the primary formability gain due to the superposition of bending effects. Necking limits in the PST model are not affected by the contact pressure.

- Adoption of the total strain formulation (TL) to describe stretch-bending is problematic in non-monotonic straining, *e.g.* when the sheet (partially) wraps around the punch, since the equivalent plastic strain is not cumulative. In this case, the incremental (IL) multi-layer model, which accounts for non-proportional non-monotonic stressing, is required.

- The following factors were identified to contribute to a formability gain in combined plane strain stretch-bending with superimposed tool contact pressure:
    (i) Delayed strain accumulation on the concave layer due to bending effects
    (ii) Increase in the in-plane forming limit due to compressive normal stresses
    (iii) Strain path shift to positive minor strains that is associated with higher limit strains for proportional stressing
    (iv) Localization process to form an acute neck that is attributed to higher limit strains

- Forming limits should be treated as an instantaneous metric that are a consequence of the process and boundary conditions, which constitute a forming limit surface (FLS) instead of a forming limit curve (FLC).

- The 3rd Gen 1180 V2 AHSS exemplifies the potential of the 3rd Gen steels for automotive lightweighting. The traditional forming window of about 0.1 major strain when relying on the in-plane forming limit is extended by a factor of approximately 2.6 when exploiting the delay in plastic instability due to bending effects and tool contact pressure. The IL-BT model is able to predict the general trend of the increased forming limits for the 3rd Gen 1180 V2.

# 8. Future Work

The following suggestions should be considered to expand on the research that was initiated as part of this thesis:

- To avoid uncertainty surrounding the limit strain detection, a curvature-based method should be considered and compared to the reported limit strains. Of particular interest are the limit strains of the AA5182 aluminum alloy that were challenging to identify in the ISO 12004-2 method in light of PLC (Portevin-Le Chatelier) effects and asymmetric strain distribution.
- The empirical thinning equation in the stress metric developed for fracture identification in the VDA 238-100 tight radius bend test should be extended to account for bend severity. To validate the evolution of the evolving tangential load in the V-Bend test, in addition to the currently installed load cell in the punch, a second load cell should be installed in the rollers to record the evolution of the tangential force.
- The current limitation of the Generalized Incremental Stability Criterion (GISC) to principal loading should be extended to arbitrary stress states to shed light into the effect of shear stresses, *e.g.* caused by frictional effects, on acute localization under complex stress states. Similarly, the stretch-bend model should be generalized to arbitrary stress states. To mitigate the limitation of the GISC to rate-insensitive materials, the current methodology of the GISC should be extended to account for the delay in plastic instability due to rate sensitivity.
- A finite-element study of different stretch-bend conditions should be conducted with a twofold purpose to (i) critically assess the validity of adopted contact pressure models in literature and (ii) assess model correlations of the predicted strain path shift and stress-strain gradients.
- To properly account for reverse loading effects in non-monotonic deformation, the isotropic hardening model should be replaced with a mixed kinematic hardening model. Particularly for the 3rd Gen 1180 V2 AHSS, a potential stress-state dependence of the complex hardening should be experimentally studied and incorporated in a modelling framework.
- The assumption in the control algorithm that contact pressure effects and sheet thinning are only due to membrane stretching should be extended, *e.g.* by analyzing bending effects and sheet thinning in a separate subroutine that is then coupled with membrane stretching.

# References


Alexandrov, S., Manabe, K., Furushima, T., (2011). A general analytic solution for plane strain bending under tension for strain-hardening material at large strains, Archive of Applied Mechanics, 81:1935-1952, https://doi.org/10.1007/s00419-011-0529-9.

Allwood, J.M., Shouler, D.R. (2009). Generalized forming limit diagrams showing increased forming limits with non-planar stress states, International Journal of Plasticity, 25, 1207-1230, https://doi.org/10.1016/j.ijplas.2008.11.001.

Arcelor Mittal, (2020). TRIP (Transformation Induced Plasticity) steels, https://automotive.arcelormittal.com/products/flat/first_gen_AHSS/TRIP, accessed: 08/06/2020.

Arrieux, R., Bedrin, C., Boivin, M., (1982). Determination of an intrinsic forming limit stress diagram for isotropic metal sheets, Proceedings of the 12th Biennial Congress of the IDDRG, 61-71.

Assempour A., Nejadkhaki, H.K., Hashemi, R., (2010). Forming limit diagrams with the existence of through-thickness normal stress, Computational Materials Science, 48, 504-508, https://doi.org/10.1016/j.commatsci.2010.02.013.

Atzema, E.H., Fictorie, E., van den Boogard, A.H., Droog, J.M.M., (2010), The influence of curvature on FLC's of mild steel, (A)HSS and aluminum, IDDRG conference proceedings, Graz, Austria.

Aydemir, N., (2022). MASc Thesis, University of Waterloo, Canada.

Azrin, M., Backofen, W.A. (1970). The deformation and failure of a biaxially stretched sheet, Metallurgical Transactions, 1, 2857-2861, https://doi.org/10.1007/BF03037824.

Barlo, A., Sigvant, M., Endelt, B., (2019). On the Failure Prediction of Dual-Phase Steel and Aluminum Alloys Exposed to Combined Tension and Bending, IOP Conference Series: Materials Science and Engineering, 651.

Bauschinger, J., (1886). On the change of the elastic limit and the strength of iron and steel, by drawing out, by heating and cooling, and by repetition of loading (summary). In: Minutes of Proceedings of the Institution of Civil Engineers with Other Selected and Abstracted Papers LXXXVII: 463.

Bertolo, V., Jiang, Q., Scholl, S., Petrov, R.H., Hangen, U., Walters, C., Sietsma, J., Popovich, V., (2022). A comprehensive quantitative characterisation of the multiphase microstructure of a thick-section high strength steel, Journal of Materials Science, 57, 7101-7126, https://doi.org/10.1007/s10853-022-07121-y.

Bettaieb, M.B., Abed-Meraim, F., (2017). Theoretical and numerical investigation of the impact of out-of-plane compressive stress on sheet metal formability, International Journal of Mechanical Sciences, 130, 244-257, https://doi.org/10.1016/j.ijmecsci.2017.05.046.

Billur, E., Altan, T., (2014a). Three generations of advanced high-strength steels for automotive applications, Part I, Stamping Journal, 12-13.

Billur, E., Altan, T., (2014b). Three generations of advanced high-strength steels for automotive applications, Part II, Stamping Journal, 12-13.

Billur, E., Altan, T., (2014c). Three generations of advanced high-strength steels for automotive applications, Part III, Stamping Journal, 12-13.

Boul, I., Lang, M., Mees, G., Sponem, F., Sturel, T., Garat, X., (2007). Bending test and bendability of ultra high strength steels, Proceedings of the IDDRG Conference, Hungary.

Bragard, A., Baret, J.C., Bonnarens, H., (1972). A simplified technique to determine FLC at the onset of necking, Rapport du Centre de Recherchers mettallurgiques, 33.

Bressan, J., D., Williams, J.A., (1983). The use of a shear instability criterion to predict local necking in sheet metal deformation, International Journal of Mechanical Sciences, 25, 3, 155-168, https://doi.org/10.1016/0020-7403(83)90089-9.

Butcher, C., Khameneh, F., Abedini, A., Connolly, D., Kurukuri, S., (2021). On the Experimental Characterization of Sheet Metal Formability and the Consistent Calibration of the MK Model for Biaxial Stretching in Plane Stress, Journal of Materials Processing Technology, https://doi.org/10.1016/j.jmatprotec.2020.116887.

Butcher, C., Abedini, A., (2019a). On Phenomenological Failure Loci of Metals under Constant Stress States of Combined Tension and Shear: Issues of Coaxiality and Non-Uniqueness, metals, 9(10), https://doi.org/10.3390/met9101052.

Butcher, C., Abedini, A., (2019b). On anisotropic plasticity models using linear transformations on the deviatoric stress: Physical constraints on plastic flow in generalized plane strain, International Journal of Mechanical Sciences, 161-162, 105044, https://doi.org/10.1016/j.ijmecsci.2019.105044.

Centeno, G., Bagudanch, I., Martinez-Donaire, A.J., Garcia-Romeu, M.L., Vallellano, C., (2014). Critical analysis of necking and fracture limit strains and forming forces in single-point incremental forming, Materials and Design, 63, 20-29, https://doi.org/10.1016/j.matdes.2014.05.066.

Charpentier, P.L., (1975). Influence of punch curvature on the stretching limits of sheet steel, Metallurgical Transactions A, 1665, https://doi.org/10.1007/BF02641986.

Chen, Z., Fang, G., (2018). Determination of forming limit for aluminum alloy sheet eliminating the interferences of through-thickness stress and non-linear strain path, IOP Conference Series: Materials Science and Engineering, 418.

Cheong, K., (2018). On the Influence of the Through-Thickness Strain Gradients for Characterization of Formability and Fracture of Sheet Metal Alloys, MASc Thesis, University of Waterloo, Canada.

Cheong, K., Butcher, C., Dykeman, J., (2018). The Influence of the Through-Thickness Strain Gradients on the Fracture Characterization of Advanced High-Strength Steels, SAE International Journal of Materials and Manufacturing, SAE Technical Paper 2018-01-0627, https://doi.org/10.4271/2018-01-0627.

Cheong, K., Omer, K., Butcher, C., George, R., Dykeman, J., (2017). Evaluation of the VDA 238-100 Tight Radius Bending Test using Digital Image Correlation Strain Measurements, IOP Conference Series: Journal of Physics.

Christodoulou, N., Woo, O.T., MacEwen, S.R., (1986). Effect of stress reversals on the work hardening behaviour of polycrystalline copper, Acta Metallurgica, 34(8), 1553-1562, https://doi.org/10.1016/0001-6160(86)90100-8.

Chung, K., Wagoner, R.H., (1986). Effect of stress-strain-law transients on formability, Metallurgical transactions A, 17, 1001-1009, https://doi.org/10.1007/BF02661266.

Considère, A., (1885). Memoire sur l'emploi du fer et de l'acier dans les constructions. Annales des Ponts et Chaussées, 9, 574-775.

Crafoord, R., (1970). Plastic sheet bending, PhD thesis, University of Gothenburg.

Dadras, P., Majlessi, S.A., (1982). Plastic bending of work hardening materials, ASME Journal of Engineering for Industry, 104, 224-230, https://doi.org/10.1115/1.3185823.

Demeri, M.Y., (1981). The stretch-bend forming of sheet metal, Journal of Applied Metalworking, 2, 3-10.

De Kruijf, N.E., Peerlings, R.H.J., Geers, M.G.D., (2009). An analysis of sheet necking under combined stretching and bending, International Journal of Material Forming, 2, 845.

DiCecco, S., Butcher, C., Worswick, M., Boettcher, E., Chu, E., Shi, C., (2016). Determination of Forming Limit Diagrams of AA6013-T6 Aluminum Alloy Sheet using a Time and Position Dependent Localized Necking Criterion, IOP Conference Series: Materials Science and Engineering, 159.

Dorn, J.E., Thomsen, E.G., (1947). The ductility of metals under general conditions of stress and strain, Transactions of American Society for Metals, 39, 741-772.

Drucker, D.C., (1951). A more fundamental approach to plastic stress-strain relations, Proceedings of the First US National Congress of Applied Mechanics, ASME, New York, 487-491.

Dunand, M., Mohr, D., (2010). Hybrid experimental-numerical analysis of basic ductile fracture experiments for sheet metals, International Journal of Solids and Structures, 47, 1130-1143, https://doi.org/10.1016/j.ijsolstr.2009.12.011.

Erfanian, M., Hashemi, R., (2018). A comparative study of the extended forming limit diagrams considering strain path, through-thickness normal and shear stress, International Journal of Mechanical Sciences, 148, 316-326, https://doi.org/10.1016/j.ijmecsci.2018.09.005.

Fast-Irvine, C., (2021). Private communication, University of Waterloo, Canada.

Geoffroy, J.L., Goncalves, J., Lemoine, X., (2007). Adequately use FLC's for simulation, Forming the Future – Innovations in Sheet Metal Forming IDDRG Conference.

Ghosh, A.K., Hecker, S.S., (1974). Stretching limits in sheet metals: In-plane versus out-of-plane deformation, Metallurgical Transactions 5, 2161-2164, https://doi.org/10.1007/BF02643929.

Goodwin, G.M., (1968). Application of strain analysis to sheet metal forming in the press shop, SAE paper No. 680093, https://doi.org/10.4271/680093.

Gotoh, M., Chung, T.H., Iwata, N., (1995). Effect of out-of-plane stress on the forming limit of sheet metals, JSME International Journal, Series A, 38(1), 123-132, https://doi.org/10.1299/jsmea1993.38.1_123.

Govindasamy, G.N., (2015). Bending Characteristics and Stretch Bendability of Monolithic and Laminated Sheet Materials, PhD Thesis, McMaster University, Canada.

Graf, A., Hosford, W., (1994). The influence of strain-path changes on forming limit diagrams of Al 6111 T4, International Journal of Mechanical Sciences, 36, 10, 897-910, https://doi.org/10.1007/BF02646529.

Graf, A., Hosford, W.F., (1993). Effect of changing strain paths on forming limit diagrams of aluminum 2008-T4, Metallurgical Transaction A24, 2503-2512.

Grolleau, V., Roth, C.C., Lafile, V., Galpin, B., Mohr, D., (2019). Loading of mini-Nakazima specimens with a dihedral punch: Determining the strain to fracture for plane strain tension through stretch-bending, International Journal of Mechanical Sciences, 152, 329-345, https://doi.org/10.1016/j.ijmecsci.2019.01.005.

Gutierrez, J.E., Noder, J., Parker, N., Bowman, J., Zhumagulov, A., Dykeman, J., Malcolm, S., Ezzat, H., Butcher, C., (2021). Formability Characterization of 3rd Generation Advanced High-Strength Steel and Application to Forming a B-Pillar, SAE Technical Paper 2021-01-0267, https://doi.org/10.4271/2021-01-0267.

Gutierrez, J.E., Noder, J., Butcher, C., (2020). Experimental Characterization and Deterministic Prediction of In-Plane Formability of 3rd Generation Advanced High Strength Steels, metals, 10(7), https://doi.org/10.3390/met10070902.

Hance, B., (2016). Advanced High Strength Steel: Deciphering Local and Global Formability, International Automotive Body Congress (IABC 2016), Dearborn, Michigan.

Hasegawa, T., Yakou, T., (1975). Deformation Behaviour and Dislocation Structures upon Stress Reversal in Polycrystalline Aluminum, Materials Science and Engineering, 20, 267-276, https://doi.org/10.1016/0025-5416(75)90159-7.

Hashemi, R., Abrinia, K., (2014). Analysis of the extended stress-based forming limit curve considering the effects of strain path and through-thickness normal stress, Materials and Design, 54, 670-677, https://doi.org/10.1016/j.matdes.2013.08.023.

He, J., Xia, Z.C., Li, S., Zeng, D., (2013a). M-K Analysis of Forming Limit Diagram Under Stretch-Bending, Journal of Manufacturing Science and Engineering ASME, 135, https://doi.org/10.1115/MSEC2012-7401.

He, J., Xia, Z.C., Zhu, X., Zeng, D., Li, S., (2013b). Sheet metal forming limits under stretch-bending with anisotropic hardening, International Journal of Mechanical Sciences, 75, 244-256, https://doi.org/10.1016/j.ijmecsci.2013.07.007.

He, J., Xia, Z.C., Zhu, X., Zeng, D., Li, S., (2013c). Forming Limits of a Sheet Metal After Continuous-Bending-Under-Tension Loading, Journal of Engineering Materials and Technology, 135(3), https://doi.org/10.1115/1.4023676.

Hendrick, A., (2017). Die Science: Handling production splitting problems, Part I, STAMPING Journal, https://www.thefabricator.com/stampingjournal/article/stamping/die-science-handling-production-splitting-problems-part-i, accessed: 07/10/2020.

Hertz, H., (1881). Über die Berührung fester elastischer Körper, Journal für die reine und angewandte Mathematik, 92, 156-171.

Hill, R. (1952). On discontinuous plastic states, with special reference to localized necking in thin sheets, Journal of the Mechanics and Physics of Solids, 1, 19-30, https://doi.org/10.1016/0022-5096(52)90003-3.

Hill, R., (1950). The Mathematical Theory of Plasticity, Oxford Press.

Hillier, M.J., (1966). Instability Strains in Plane Sheet Under Biaxial Stress, Journal of Applied Mechanics, 33(2). 282-288., https://doi.org/10.1115/1.3625039.

Hillier, M.J., (1964). The effect of pressure on the ductility of thin sheet subjected to some simple forming processes, International Journal of Production Research, 3:4, 341-352, https://doi.org/10.1080/00207546408943067.

Hillier, M.J., (1963). Tensile plastic instability under complex stress, International Journal of Mechanical Sciences, 5, 57-67, https://doi.org/10.1016/0020-7403(63)90039-0.

Hockett, J.E., Sherby, O.D., (1975). Large strain deformation of polycrystalline metals of low homologous temperatures. Journal of the Mechanics and Physics of Solids, 23(2), 87-98, https://doi.org/10.1016/0022-5096(75)90018-6.

Hollomon, J.H., (1945). Tensile deformation, Transactions of the Metallurgical Society of AIME, 162, 268-290.

Hora, P., Tong, L., Berisha, B., (2013). Modified maximum force criterion, a model for the theoretical prediction of forming limit curves, International Journal of Material Forming, 6(2), 267-279, https://doi.org/10.1007/s12289-011-1084-1.

Huang, G., Sriram, S., Yan, B., (2008). Digital image correlation technique and its application in forming limit curve

determination, Proceedings of the IDDRG 2008, 153-62.

Hudgins, A.W., Matlock, D.K., Speer, J.G., Van Tyne, C.J., (2010). Predicting instability at die radii in advanced high strength steels, Journal of Materials Processing Technology, 210, 741-750, https://doi.org/10.1016/j.jmatprotec.2009.12.012.

Hutchinson, J.W., Neale, K.W. (1977a). Sheet Necking-II. Time-independent behaviour, Mechanics of Sheet Metal Forming, 127-153, https://doi.org/10.1007/978-1-4613-2880-3_6.

Hutchinson, J.W., Neale, K.W. (1977b). Sheet Necking-III. Strain-rate effects, Mechanics of Sheet Metal Forming, 269-283.

International Organization for Standardization (2008). ISO/DIC 12004-2:2008. Metallic materials sheet and strip – Determination of forming limit curves – Part 2: determination of forming limit curves in the laboratory.

Ishigaki, H., (1977). Deformation Analysis of Large Sized Panels in the Press Shop, Mechanics of Sheet Metal Forming, 315-339, https://doi.org/10.1007/978-1-4613-2880-3_13.

Keeler, S.P., Backhofen, W.A., (1963). Plastic instability and fracture in sheet stretched over rigid punches, ASM Transactions Quarterly, 56(11), 25-48.

Kitting, D., Ofenheimer, A., Pauli, H., Till, E.T., (2010). A Phenomenological Concept to Predict Formability in Stretch-Bending Forming Operations, International Journal of Material Forming, 3, 1, 1163-1166, https://doi.org/10.1007/s12289-010-0979-6.

Kitting, D., Koplenig, M., Ofenheimer, A., Pauli, H., Till, E.T., (2009). Application of a "concave-side rule" approach for assessing formability of stretch-bend steel sheets, International Journal of Material Forming, 2, 427, https://doi.org/10.1007/s12289-009-0483-z.

Kleemola, H.J., Pelkkikangas M.T., (1977). Effect of Predeformation and Strain Path on the Forming Limits of Steel, Copper and Brass, Sheet Metal Industries, 63, 591-599.

Kuwabara, T., Ikeda, S., Kuroda, K., (1998). Measurement and analysis of differential work hardening in cold-rolled steel sheet under biaxial tension, Journal of Materials Processing Technology 80-81, 517-523, https://doi.org/10.1016/S0924-0136(98)00155-1.

Labudde, T., Bleck, W., (2011). Characterisation of Ductility of Ultra-High Strength Steels, Proceedings of the 10th International Conference on Technology of Plasticity, 25-30.

Lang, L., Cai, G., Liu, K., Alexandrov, S., Du, P., Zheng, H., (2015). Investigation on the effect of through thickness normal stress on forming limit at elevated temperature by using modified M-K model, International Journal of Material Forming, 8, 211-228, https://doi.org/10.1007/s12289-014-1161-3.

Larour, P., Hackl, B., Leomann, F., (2013). Sensitivity analysis on the calculated bending angle in the instrumented bending test, IDDRG Conference Proceedings, Zurich, Switzerland.

Lian, J., Barlat, F., Baudelet, B., (1989). Plastic behaviour and stretchability of sheet metals. Part II: Effect of yield surface shape on sheet forming limit, International Journal of Plasticity, 5, 131-147, https://doi.org/10.1016/0749-6419(89)90026-0.

Lopez, A.M., van den Boogard, A.H., (2011). Formability Limit Curves under Stretch-Bending, IDDRG Conference Proceedings, Bilbao, Spain.

Lubahn, J., Sachs, G., (1950). Bending of an ideal plastic metal, Transactions ASME, 72, 201-208.

Ludwik, P., (1903). Technologische Studie über Blechbiegung – Ein Beitrag zur Mechanik der Formänderungen. Technische Blätter, 133-159.

Ma, B.L., Wan, M., Zhang, H., Gong, X.L., Wu, X.D., (2018). Evaluation of the forming limit curve of medium steel plate based on non-constant through-thickness normal stress, Journal of Manufacturing Processes, 33, 175-183, https://doi.org/10.1016/j.jmapro.2018.05.012.

Ma, B., Diao, K., Wu, X., Li, X., Wan, M., Cai, Z., (2016). The effect of the through-thickness normal stress on sheet formability, Journal of Manufacturing Processes, 21, 124-140, https://doi.org/10.1016/j.jmapro.2015.12.006.

Manopulo, N., Hora, P., Peters, P., Gorji, M., Barlat, F., (2015). An extended Modified Maximum Force Criterion for the prediction of localized necking under non-proportional loading, International Journal of Plasticity, 75, 189-203, https://doi.org/10.1016/j.ijplas.2015.02.003.

Marciniak, Z., Duncan, J.L., Hu, S.J., (2002). Mechanics of Sheet Metal Forming, Material Behavior and Deformation Analysis, Springer, Boston, MA.

Marciniak, Z., Kuczynski, K., Pokora, T. (1973). Influence of the plastic properties of a material on the forming limit diagram for sheet metals in tension, International Journal of Mechanical Sciences, 15, 789-805, https://doi.org/10.1016/0020-7403(73)90068-4.

Marciniak, Z., Kuczynski, K., (1967). Limit Strains in the Process of Stretch-Forming Sheet Metal, International Journal of Mechanical Sciences, 9, 609-620, https://doi.org/10.1016/0020-7403(67)90066-5.

Martinez-Donaire, A.J., Garcia-Lomas, F.J., Vallellano, C., (2014). New Approaches to detect the onset of localised necking in sheets under through-thickness strain gradients, Materials and Design, 57, 135-145, https://doi.org/10.1016/j.matdes.2014.01.012.

Matin, P.H., Smith, L.M., (2005). Practical limitations to the influence of through-thickness normal stress on sheet metal formability, International Journal of Plasticity, 21, 671-690, https://doi.org/10.1016/j.ijplas.2004.05.002.

Mellor, P.B., (1962). An interpretation of the tensile test, Bulletin Mechanical Engineering Education, 1, 115.

Merklein, M., Kuppert, A., Geiger, M., (2010). Time dependent determination of forming limit diagrams, CIRP Annals – Manufacturing Technology, 59, 295-298, https://doi.org/10.1016/j.cirp.2010.03.001.

Meya, R., Löbbe, C., Tekkaya, A.E., (2019). Stress State Analysis of Radial Stress Superposed Bending, International Journal of Precision Engineering and Manufacturing, 20, 53-66, https://doi.org/10.1007/s12541-019-00040-0.

Min, J., Stoughton, T.B., Carsley, J.E., Lin, J., (2017a). A method of Detecting the Onset of Localized Necking Based on Surface Geometry Measurements, Experimental Mechanics, 57(4), 521-535.

Min, J., Stoughton, T.B., Carsley, J.E., Lin, J., (2017b) An improved curvature method to detecting the onset of localized necking in Marciniak tests and its extension to Nakazima tests, 123, 238-252, https://doi.org/10.1016/j.ijmecsci.2017.02.011.

Min, J., Stoughton, T.B., Carsley, J.E., Lin, J., (2016). Compensation for process-dependent effects in the determination of localized necking limits, International Journal of Mechanical Sciences, 117, 115-134, https://doi.org/10.1016/j.ijmecsci.2016.08.008.

Mirfalah-Nasiri, S.M., Basti, A., Hashemi, R., (2016). Forming limit curves analysis of aluminum alloy considering the through-thickness normal stress, anisotropic yield functions and strain rate, International Journal of Mechanical Sciences, 117, 93-101, https://doi.org/10.1016/j.ijmecsci.2016.08.011.

Mohr, D., Henn, S., (2007). Calibration of Stress-triaxiality Dependent Crack Formation Criteria: A New Hybrid

Experimental-Numerical Method, Journal of Experimental Mechanics, 47, 805-820, https://doi.org/10.1007/s11340-007-9039-7.

Montalvão, D., Wren, A., (2017). Redesigning axial-axial (biaxial) cruciform specimens for very high cycle fatigue ultrasonic testing machines, Heliyon, 3(11), https://doi.org/10.1016/j.heliyon.2017.e00466.

Morales-Palma, D., Martinez-Donaire, A.J., Vallellano, C., (2017). On the Use of Maximum Force Criteria to Predict Localised Necking in Metal Sheets under Stretch-Bending, metals, 7, 469.

Morales-Palma, D., Vallellano, C. Garcia-Lomas, F., (2013). Assessment of the effect of the through-thickness strain/stress gradient on the formability of stretch-bend metal sheets, Materials and Design, 50, 798-809, https://doi.org/10.3390/met7110469.

Müscheborn, W., Sonne, H.-M., (1975). Influence of the Strain Path on the Forming Limits of Sheet Metal, Arch. Eisenhüttenwesen, 46(9), 597-602.

Nakazima, N., Kikuma, T., (1967). Forming limits under biaxial stretching of sheet metals, Tetsu to Hagane, 53, 455-458.

Nanda, T., Singh, V., Sing, V. Chakraborty, A., Sharma, S., (2019). Third generation of advanced high-strength steels: Processing routes and properties, Journal of Materials: Design and Applications, 233(2), 209-238, https://doi.org/10.1177/1464420716664198.

Neuhauser, F.M., Terrazas, O., Manopulo, N., Hora, P., Van Tyne C., (2018). The bending dependency of forming limit diagrams, International Journal of Material Forming, https://doi.org/10.1007/s12289-018-1452-1.

Neuhauser, F.M., Terrazas, O. R., Manopulo, N., Hora, P., Van Tyne, C.J., (2016). Stretch bending – the plane within the sheet where strains reach the forming limit curve, IOP Conference Series: Materials Science and Engineering, 159.

Noder, J., Gutierrez, J.E., Zhumagulov, A., Dykeman, J., Ezzat, H., Butcher, C., (2021a). A Comparative Evaluation of Third-Generation Advanced High-Strength Steels for Automotive Forming and Crash Applications, Materials, 14, 4970, https://doi.org/10.3390/ma14174970.

Noder, J., Gutierrez, J.E., Zhumagulov, A., Khameneh, F., Ezzat, H., Dykeman, J., Butcher, C., (2021b). Constitutive, Formability, and Fracture Characterization of 3rd Gen AHSS with an Ultimate Tensile Strength of 1180 MPa, SAE International Journal of Advances and Current Practices in Mobility, 3(3): 1395-1407, https://doi.org/10.4271/2021-01-0308.

Noder, J., Abedini A., Butcher, C., (2020b). Evaluation of the VDA 238-100 Tight Radius Bend Test for Plane Strain Fracture Characterization of Automotive Sheet Metals, International Journal of Experimental Mechanics, 60, 787-800, https://doi.org/10.1007/s11340-020-00597-2.

Nurcheshmeh, M., Green, D.E., (2012). Influence of out-of-plane compression stress on limit strains in sheet metals, International Journal of Material Forming, 5, 213-226, https://doi.org/10.1007/s12289-011-1044-9.

Paraianu, L., Dragos, G., Bichis, I., Comsa, D.S., Banabic, D. (2010). A new formulation of the modified maximum force criterion (MMFC), International Journal of Material Forming, 3(1), 243-246, https://doi.org/10.1007/s12289-010-0752-x.

Peirs, J., Verleysen, P., Degrieck, J., (2012). Novel Technique for Static and Dynamic Shear Testing of Ti6Al4V Sheet, Experimental Mechanics, 52, 729-741, https://doi.org/10.1007/s11340-011-9541-9.

Pham, Q-T., Lee, B-H., Park, K-C., Kim, Y-S., (2018). Influence of the post-necking prediction of hardening law on the theoretical forming limit curve of aluminum sheets, International Journal of Mechanical Sciences, 140, 521-

536., https://doi.org/10.1016/j.ijmecsci.2018.02.040.

Portevin, A., Le Chatelier, F., (1923). Sur un phénomène observé lors de l'essai de traction d'alliages en cours de transformation, Comptes rendus hebdomadaires des séances de l'Académie des sciences, 176, 507-510.

Proksa, F., (1959). Plastisches Biegen von Blechen, Stahlbau, 28, 29-36.

Proksa, F., (1958). Zur Theorie des plastischen Blechbiegens, PhD Thesis, TH Hannover.

Pugh, H. , Le, D., (1964). The mechanical properties and deformation characteristics of metals and alloys under pressure, first international conference on Materials, Philadelphia, ASTM.

Rahmaan, T., Abedini, A., Butcher, C., Pathak, N., Worswick, M.J., (2017). Investigation into the shear stress, localization, and fracture behaviour of DP600 and AA5182-O sheet metal alloys under elevated strain rates, International Journal of Impact Engineering, 108, 303-321, https://doi.org/10.1016/j.ijimpeng.2017.04.006.

Rahmaan, T., (2015). Low to High Strain Rate Characterization of DP600, TRIP780, AA5182-O, Master Thesis at the University of Waterloo, Canada.

Ratchev, P., Van Houtte, P., Verlinden, B., De Smet, P., Neutjens, P., Baartman, R., Drent, P., (1994). Prediction of forming limit diagrams of al-mg rolled sheets taking texture into account, Textures and Microstructures, 22, 219-231, https://doi.org/10.1155/TSM.22.219.

Roth, C., Mohr, D., (2016). Ductile fracture experiments with locally proportional loading histories, International Journal of Plasticity, 79, 328-354, https://doi.org/10.1016/j.ijplas.2015.08.004/.

Schaeffler, D.J., (2017). The importance of local formability when working with AHSS, the Fabricator, https://www.thefabricator.com/thefabricator/article/stamping/the-importance-of-local-formability-when-working-with-ahss, accessed: 10/05/2020.

Shen, F., Lian, J., Münstermann, S., (2018). A Comparative Study on the Forming Limit Diagram Prediction between Marciniak-Kuczynski Model and Modified Maximum Force Criterion by Using the Evolving Non-associated Hill48 Plasticity Model, AIP Conference Proceedings 1960, 150013, https://doi.org/10.1063/1.5035020.

Shi, M.F., Gerdeen, J.C., (1991). Effect of Strain Gradient and Curvature on Forming Limit Diagrams for Anisotropic Sheets, Journal of Material Shaping Technologies, 9, 253-268.

Situ, Q., Jain, M.K., Metzger, D.R., (2011). Determination of forming limit diagrams of sheet materials with a hybrid experimental-numerical approach, International Journal of Mechanical Sciences, 53, 707-719, https://doi.org/10.1016/j.ijmecsci.2011.06.003.

Situ, Q., Mukesh, K., Bruhis, M., (2006). A Suitable Criterion for Precise Determination of Incipient Necking in Sheet Materials, Materials Science Forum 2006, Aluminum Alloys 2006 – ICAA10, 111-116, https://doi.org/10.4028/www.scientific.net/MSF.519-521.111.

Simha C.H.M., Grantab, R., Worswick, M.J., (2008). Application of an Extended Stress-Based Forming Limit curve to Predict Necking in Stretch Flange Forming, International Journal of Manufacturing Science and Engineering, 130(5), https://doi.org/10.1115/1.2844593.

Simha C.H.M., Gholipour, J., Bardelcik, A., Worswick, M.J., (2007). Prediction of Necking in Tubular Hydroforming Using an Extended Stress-Based Forming Limit Curve, Journal of Engineering Materials and Technology, 129(1), 36-47, https://doi.org/10.1115/1.2400269.

Smith, L.M., Averill, R.C., Lucas, J.P., Stoughton, T.B., Matin, P.H., (2003). Influence of transverse normal stress on sheet metal formability, International Journal of Plasticity, 19, 1567-1583, https://doi.org/10.1016/S0749-

6419(02)00035-9.

Speer, J.G., Matlock, D.K., De Cooman, B.C., Schroth, J.G., (2003). Carbon partitioning into austenite after martensite transformation, Acta Materialia, 51, 2611-2622, https://doi.org/10.1016/S1359-6454(03)00059-4.

Sriram, S., Wong, C., Huang, M., Yan, B., (2003). Stretch Bendability of Advanced High Strength Steels, SAE Technical Paper, 2003-01-1151. https://doi.org/10.4271/2003-01-1151.

Stoughton, T.B., Yoon, J.W., (2012). Path independent forming limits in strain and stress spaces, International Journal of Solids and Structures, 49, 3616-3625, https://doi.org/10.1016/j.ijsolstr.2012.08.004.

Stoughton, T.B., Yoon, J.W., (2011). A new approach for failure criterion for sheet metals, International Journal of Plasticity, 27, 440-459, https://doi.org/10.1016/j.ijplas.2010.07.004.

Stoughton, T.B., Zhu, X., (2004). Review of theoretical models of the strain-based FLD and their relevance to the stress-based FLD, International Journal of Plasticity, 20, 1463-1486., https://doi.org/10.1016/j.ijplas.2003.11.004.

Stoughton, T.B., (2000). A general forming limit criterion for sheet metal forming, International Journal of Mechanical Sciences, 42, 1-27, https://doi.org/10.1016/S0020-7403(98)00113-1.

Swift, H.W. (1952). Plastic Instability under plane stress. Journal of the Mechanics and Physics of Solids, 1, 1-18, https://doi.org/10.1016/0022-5096(52)90002-1.

Tadros, A.K., Mellor, P.B., (1978). An experimental study of the in-plane stretching of sheet metal, International Journal of Mechanical Sciences, 20, 121-134, https://doi.org/10.1016/0020-7403(78)90073-5.

Tan, Z., Perrson, B., Magnusson, C., (1995). Plastic bending of anisotropic sheet metals, International Journal of Mechanical Sciences, 405-421, https://doi.org/10.1016/0020-7403(94)00069-V.

ten Kortenaar, (2016). Failure Characterization of Hot Formed Boron Steels with Tailored Mechanical Properties, MSc Thesis, University of Waterloo, Canada.

Tharrett, M.R., Stoughton, T.B., (2003). Stretch-Bend Forming Limits of 1008 AK Steel, SAE Technical Paper. 2003-01-1157, https://doi.org/10.4271/2003-01-1157.

Tian, H., Brownell, B., Baral, M., Korkolis, Y.P., (2017). Earing in cup-drawing of anisotropy Al-6022-T4 sheets, International Journal of Material Forming, 10, 329-343.

Till, E.T., Berger, E., Larour, P., (2008). On an exceptional forming behaviour aspect of AHSS sheets, International Deep Drawing Research Group, Sweden.

Troive, L., (2017). New method for evaluation of bendability based on three-point-bending and the evolution of the cross-section moment, IOP Conference Series: Journal of Physics: Conference Series 896.

Vallellano, C., Morales, D., Martinez, A.J., Garcia-Lomas, F.J., (2010). On the Use of Concave-Side Rule and Critical-Distance Methods to Predict the Influence of Bending on Sheet-Metal Formability, International Journal of Material Forming, 3, 1167-1170, https://doi/10.1007/s12289-010-0980-0.

VDA 238-100, (2017). Test Specification: Plate Bending Test for Metallic Materials.

VDA 238-100, (2010). Test Specification: Plate Bending Test for Metallic Materials.

Vegter, H., van den Boogaard, A.H., (2006). A plane stress yield function for anisotropic sheet material by interpolation of biaxial stress states, International Journal of Plasticity, 22, 557-580,

https://doi.org/10.1016/j.ijplas.2005.04.009.

Volk, W., Hoffmann, H., Suh, J., Kim, J., (2012). Failure prediction for nonlinear strain paths in sheet metal forming, CIRP Annals – Manufacturing Technology, 61, 259-262, https://doi.org/10.1016/j.cirp.2012.03.111.

Volk, W., Hora, P., (2011). New algorithm for a robust user-independent evaluation of beginning instability for the experimental FLC determination, International Journal of Material Forming, 4, 339-346, https://doi.org/10.1007/s12289-010-1012-9.

Wagoner, R.H., (1980). Measurement and Analysis of Plane-Strain Work Hardening, Metallurgical and Materials Transactions A, 11, 165-175, https://doi.org/10.1007/BF02700453.

Wang, Y., Zhang, C., Yang, Y., Wang, Y., Zhao, G., Chen, L., (2020). The identification of improved Johnson-Cook constitutive model in a wide range of temperature and its application in predicting FLCs of Al-Mg-Li sheet, Journal of Materials Research and Technology, 9(3), 3782-3795, https://doi.org/10.1016/j.jmrt.2020.02.005.

Wang, Y., Zhang, C., Yang, Y., Fan, S., Wang, G., Zhao, G., Chen, L., (2019). The integration of through-thickness normal stress and friction stress in the M-K model to improve the accuracy of predicted FLCs, International Journal of Plasticity, 120, 147-163, https://doi.org/10.1016/j.ijplas.2019.04.017.

Wang K., Carsley, J.E., He, B., Li, J., Zhang, L., (2014). Measuring forming limit strains with digital image correlation analysis, Journal of Materials Processing Technology, 2014, 1120-1130, https://doi.org/10.1016/j.jmatprotec.2014.01.001.

Wollter, K., (1950). Bildsames Biegen von Blechen um gerade Kanten, PhD Thesis, TH Hannover.

Xia, Z.C., Zeng, D., (2008). Sheet metal forming limit under stretch-bending, Proceedings of the 2008 International Manufacturing Science and Engineering Conference, Illinois, USA.

Yoshida, K., Kuwabara, T., (2007). Effect of strain hardening behavior on forming limit stresses of steel tube subjected to nonproportional loading paths, International Journal of Plasticity, 23(7), 1260-1284, https://doi.org/10.1016/j.ijplas.2006.11.008.

Yu, T.X., Zhang, L.C., (1996). Plastic Bending: Theory and Applications, 2, 72-119.

Zadpoor, A.A., Campoli, G., Sinke, J., Benedictus, R., (2011). Fracture in bending – The straining limits of monolithic sheets and machined tailor-made blanks, Materials and Design, 32, 1229-1241.

Zang, S.-L., Lee, M.-G., Sun, L., Kim, J.H., (2014). Measurement of the Bauschinger behavior of sheet metals by three-point bending springback test with pre-strained strips, International Journal of Plasticity, 59, 84-107, https://doi.org/10.1016/j.ijplas.2014.03.015.

Zener, C., Hollomon, J. H. (1944). Effect of strain rate upon plastic flow of steel, Journal of Applied Physics, 15(1), 22-32, https://doi.org/10.1063/1.1707363.

Zhang, F., Chen, J., Chen, J., (2014). Effect of through-thickness normal stress on forming limits under Yld2003 yield criterion and M-K model, International Journal of Mechanical Sciences, 89, 92-100, https://doi.org/10.1016/j.ijmecsci.2014.08.024.

Zhao, L., Sowerby, R., Sklad, M.P., (1996). A theoretical and experimental investigation of limit strains in sheet metal forming, International Journal of Mechanical Sciences, 38(12), 1307-1317, https://doi.org/10.1016/0020-7403(96)00014-8.

Zuldema, B.K., (2013). On the Role of Body-In-White Weight Reduction in the Attainment of the 2012-2025 US EPA/NHTSA Fuel Economy Mandate, GDIS.

# Appendix A: Journal Publication #1

**Noder, J.,** Butcher, C., (2019a). A comparative investigation into the influence of the constitutive model on the prediction of in-plane formability for Nakazima and Marciniak tests, International Journal of Mechanical Sciences, 163, 105138, https://doi.org/10.1016/j.ijmecsci.2019.105138.

**"Accessible through the link below as well as the University of Waterloo's Institutional Repository (UW Space)"**

https://www.sciencedirect.com/science/article/abs/pii/S0020740319305788

## Appendix B: Journal Publication #2

**Noder, J.,** Butcher, C. A General Instability Framework for Ductile Metals in Complex Stress States from Diffuse to Acute Localization, to be submitted, May 2022.

**"Accessible through the University of Waterloo's Institutional Repository (UW Space)"**

# Appendix C: Journal Publication #3

**Noder, J.,** Dykeman, J., Butcher, C., (2020a). New Methodologies for Fracture Detection of Automotive Steels in Tight Radius Bending: Application to the VDA 238-100 V-Bend Test, Experimental Mechanics, https://doi.org/10.1007/s11340-020-00597-2.

**"Accessible through the link below as well as the University of Waterloo's Institutional Repository (UW Space)"**

https://link.springer.com/article/10.1007/s11340-020-00627-z

# Appendix D: Journal Publication #4

**Noder, J.,** Butcher, C. On the Influence of Tool Contact Pressure on Tensile Instabilities in Plane Strain Stretching and Bending of Sheet Metals, to be submitted, May 2022.

**"Accessible through the University of Waterloo's Institutional Repository (UW Space)"**

# Appendix E: Derivations of Mathematical Relations

### E1: Bending Approximation in the Mod. LBF-Method

For bending scenarios that involve large punch radii, such as in the Nakazima tests ($r_p$ = 50.8 mm), the engineering theory of plastic bending can be adopted. Both sheet thinning and the shift in the neutral layer are neglected (Yu and Zhang, 1996) such that the radius of the unstretched layer is approximated from the location of the mid-layer, $r_m$. The major strain on the convex layer is

$$\varepsilon_1 = \ln\left(\frac{r_y}{r_m}\right) = \ln\left(\frac{r_p + t}{r_p}\right) = \ln\left(1 + \frac{t}{r_p}\right) \tag{E1}$$

where $r_y$ is the radius of the convex sheet layer. Note that due to the large punch radius relative to the sheet thickness, $t$, the mid-layer is approximated from the punch radius, $r_p$.

For forming operations that involve appreciable bending, such as in the angular stretch-bend tests or the V-Bend test, the bending approximation in Eq. (E1) is replaced with the maximum tensile strain at the onset of yielding of the neutral layer

$$\varepsilon_1(r_n) = \ln\left(\frac{r_n}{r_u}\right) \approx \ln\left(\frac{r_n}{r_m}\right) \tag{E2}$$

where $r_n$ and $r_u$ are the radii of the neutral and unelongated layer, respectively. For simplicity, the material is treated as rigid perfectly plastic (RPP) such that the unelongated layer coincides with the mid-layer (Hill, 1950). Following the work of Yu and Zhang (1996), the relative curvature, $\kappa$, can be expressed in terms of the sheet thickness, *t*, and the mid-layer radius to derive expressions for the radius of the concave and convex sheet layer

$$\kappa = \frac{t}{r_m}, \qquad r_i = r_m - \frac{t}{2} = t\left(\frac{1}{\kappa} - \frac{1}{2}\right), \qquad r_y = r_m + \frac{t}{2} = t\left(\frac{1}{\kappa} + \frac{1}{2}\right) \tag{E3a-c}$$

Hill (1950) showed that for a RPP material, the location of the neutral layer is determined through $r_n = \sqrt{r_i r_y}$, which can be rewritten using Eq. (E3b,c) and substituted into Eq. (E2) to arrive at

$$r_n = \sqrt{r_i r_y} = \frac{t}{\kappa}\sqrt{1 - \frac{\kappa^2}{4}}, \qquad \varepsilon_1(r_n) \approx \frac{1}{2}\ln\left(1 - \frac{\kappa^2}{4}\right) \tag{E4a,b}$$

Rearranging Eq. (E4b) and adoption of Hooke's law and von Mises plasticity to approximate the maximum elastic strain, $\varepsilon_{el}^{y}$, leads to the critical relative curvature when yielding of the neutral layer occurs

$$\kappa_y = 2\sqrt{1-\exp\left(-2\varepsilon_{el}^{y}\right)}, \quad \varepsilon_{el}^{y} = \frac{1-\nu^2}{\sqrt{1-\nu+\nu^2}}\frac{\sigma_y}{E} \approx 0.002, \quad \varepsilon_1(r_y) \approx \ln\left(\frac{r_y}{r_m}\right) = \ln\left(1+\frac{\kappa_y}{2}\right) \quad \text{(E5a-c)}$$

where $\nu$ represents the Poisson's ratio, $E$ the Young's modulus, and $\sigma_y$ the yield stress. The critical relative curvature at the onset of yielding of the neutral layer, $\kappa_y$, is then adopted to compute the major strain on the convex layer in Eq. (E4b).

**E2: Phenomenological Stress Mapping for Power Law Hardening Model**

Following the work of Smith *et al.* (2003), limit strains are mapped between plane stress and triaxial stress states under (i) a constant principal in-plane stress ratio and (ii) a constant major principal stress. It is noted that in the process correction methods of Min *et al.* (2016), reverse mapping was adopted to map limit strains from the current (triaxial stress space) into plane stress space. Assuming that no softening or damage occurs, the equivalent stress is equal to the flow stress $\sigma_{eq} = \bar{\sigma}\left(\varepsilon_{eq}^{p}\right)$ and is expressed in terms of

$$\bar{\sigma}\left(\varepsilon_{eq}^{p,2D}\right) = \sigma_{eq}^{2D} = \frac{\sigma_1}{k^{2D}} = \bar{\sigma}\left(\varepsilon_{eq}^{3D}\right)\frac{k^{3D}}{k^{2D}}, \quad k^{3D} = \frac{\sigma_1}{\sigma_{eq}^{3D}}, \quad k^{2D} = \frac{\sigma_1}{\sigma_{eq}^{2D}} \quad \text{(E6a-c)}$$

where superscripts *3D* and *2D* indicate a triaxial and plane stress state, respectively. For power law hardening $\bar{\sigma} = K\left(\varepsilon_{eq}^{p}\right)^n$, Eq. (E6a) simplifies to

$$\left(\varepsilon_{eq}^{p,2D}\right)^n = \left(\varepsilon_{eq}^{p,3D}\right)^n \frac{k^{3D}}{k^{2D}} \rightarrow \varepsilon_{eq}^{p,2D} = \varepsilon_{eq}^{p,3D}\left(\frac{k^{3D}}{k^{2D}}\right)^{\frac{1}{n}} \quad \text{(E7)}$$

which involves inversion of the hardening model. Adoption of the incremental plastic work balance yields

$$\varepsilon_{eq}^{p} = \int d\varepsilon_{eq}^{p} = \frac{\sigma_i : \varepsilon_i}{\bar{\sigma}} = k(\alpha,\chi)\left[1+\alpha\rho-(1+\rho)\chi\right]\varepsilon_1, \quad \rho = \frac{d\varepsilon_2}{d\varepsilon_1} = \frac{N_2}{N_1} \quad \text{(E8a,b)}$$

where $\varepsilon_1$ represents the major strain under proportional coaxial straining, $k$ the ratio of the major stress with respect to the equivalent stress, $\alpha$ the principal in-plane stress ratio, $\chi$ the principal through-thickness

stress ratio and $\rho$ the principal in-plane strain ratio that is computed from the normal vectors, $N_i$. Eq. (E8a) is then utilized to express the equivalent plastic strain in Eq. (E7) through

$$k^{2D}\left[1+\alpha\rho^{2D}\right]\varepsilon_1^{2D} = k^{3D}\left[1+\alpha\rho^{3D}-(1+\rho^{3D})\chi\right]\varepsilon_1^{3D}\left(\frac{k^{3D}}{k^{2D}}\right)^{\frac{1}{n}} \tag{E9}$$

Rearranging of Eq. (E9) leads to the ratio of the major strains in plane stress and 3D stress space

$$\frac{\varepsilon_1^{2D}}{\varepsilon_1^{3D}} = \frac{\left[1+\alpha\rho^{3D}-(1+\rho^{3D})\chi\right]}{\left[1+\alpha\rho^{2D}\right]}\left(\frac{k^{3D}}{k^{2D}}\right)^{\frac{1+n}{n}} \tag{E10}$$

**E3: Derivation of the Dorn Instability Model**

The critical subtangent of the Dorn model (Dorn and Thomsen, 1947) is derived from the general Hillier framework. First, the original form for instability is re-casted in terms of the Hillier critical subtangent. Assuming that there is no softening or damage, $\sigma_{eq} = \bar{\sigma}\left(\varepsilon_{eq}^p\right)$. Instability in the Dorn model is reached when the major hardening rate is equal to the major stress, such that

$$\frac{\partial\sigma_1}{\partial\varepsilon_1} = \frac{\partial\sigma_1}{\partial\sigma_{eq}}\frac{\partial\sigma_{eq}}{\partial\bar{\sigma}}\frac{\partial\bar{\sigma}}{\partial\varepsilon_{eq}^p}\frac{\partial\varepsilon_{eq}^p}{\partial\varepsilon_1} = k\frac{\partial\bar{\sigma}}{\partial\varepsilon_{eq}^p}\frac{\partial\varepsilon_{eq}^p}{\partial\varepsilon_1} = \sigma_1, \qquad k = \frac{\sigma_1}{\sigma_{eq}} \tag{E11a,b}$$

Adoption of the associative flow rule $\frac{\partial\varepsilon_i}{\partial\varepsilon_{eq}^p} = \frac{\partial\sigma_{eq}}{\partial\sigma_i} = N_i$ and using Eq. (E11b) leads to

$$\sigma_{eq} = \frac{\partial\bar{\sigma}}{\partial\varepsilon_{eq}^p}\frac{\partial\varepsilon_{eq}^p}{\partial\varepsilon_1} = \frac{\partial\bar{\sigma}}{\partial\varepsilon_{eq}^p}\frac{1}{N_1} \tag{E12}$$

Rearranging of Eq. (E12) yields

$$\frac{1}{\sigma_{eq}}\frac{d\bar{\sigma}}{d\varepsilon_{eq}^p} = N_1(\alpha) = \frac{1}{z^{Dorn}}, \qquad \alpha = \frac{\sigma_2}{\sigma_1} = \text{constant} \tag{E13a,b}$$

Assuming *proportional loading*, a relation between the major and minor load rate is established. The partial derivative of the applied traction with respect to the equivalent plastic strain for proportional loading is

$$\frac{\partial\Sigma_\delta}{\partial\varepsilon_{eq}^p} = \frac{1}{A_\delta}\frac{\partial F_\delta}{\partial\varepsilon_m}\frac{d\varepsilon_m}{d\varepsilon_{eq}^p} + \Sigma_\delta N_\delta \tag{E14}$$

Rearranging of Eq. (E14), the major and minor load rates are

$$\frac{1}{A_1}\frac{\partial F_1}{\partial \varepsilon_m}\frac{d\varepsilon_m}{d\varepsilon_{eq}^p}=\frac{\partial \Sigma_1}{\partial \varepsilon_{eq}^p}-\Sigma_1 N_1, \qquad \frac{1}{A_2}\frac{\partial F_2}{\partial \varepsilon_m}\frac{d\varepsilon_m}{d\varepsilon_{eq}^p}=\frac{\partial \Sigma_2}{\partial \varepsilon_{eq}^p}-\Sigma_2 N_2=\tilde{\alpha}\frac{\partial \Sigma_1}{\partial \varepsilon_{eq}^p}-\Sigma_2 N_2, \quad \tilde{\alpha}=\frac{\sigma_2}{\sigma_1} \tag{E15a-c}$$

where $\tilde{\alpha}$ is not constant and will evolve with deformation to maintain proportionality of the applied loads. Noting that the partial derivative $\partial \Sigma_1 / \partial \varepsilon_{eq}^p$ in Eq. (E15a) is known from Eq. (E14) and replacing the traction, $\Sigma_1$, with the material stress, $\sigma_1$, the critical subtangent of the Hillier framework yields

$$\frac{1}{z}=\frac{1}{\sigma_{eq}}\left[N_1\left(\frac{1}{A_1}\frac{\partial F_1}{\partial \varepsilon_m}\frac{d\varepsilon_m}{d\varepsilon_{eq}^p}+\sigma_1 N_1\right)+\tilde{\alpha}N_2\left(\frac{1}{A_1}\frac{\partial F_1}{\partial \varepsilon_m}\frac{d\varepsilon_m}{d\varepsilon_{eq}^p}+\sigma_1 N_1\right)\right] \tag{E16}$$

Assuming that at the instant of instability, the major load rate vanishes, Eq. (E16) simplifies to

$$\frac{1}{z}=kN_1\left[N_1+\tilde{\alpha}N_2\right] \tag{E17}$$

Adopting the incremental plastic work balance for plane stress loading, it is shown that

$$dw^p=\sigma_{eq}d\varepsilon_{eq}=\sigma_i d\varepsilon_i=\sigma_1 d\varepsilon_1+\sigma_2 d\varepsilon_2 \rightarrow kN_1\left(1+\tilde{\alpha}\rho\right)=1, \qquad \rho=\frac{N_2}{N_1} \tag{E18a,b}$$

such that the critical subtangent reduces to $z^{-1}=N_1(\tilde{\alpha})$ that appears similar to the Dorn solution in Eq. (E13a) but differs by the in-plane stress ratio, which is taken as constant by Dorn and Thomsen (1947) but evolves in proportional loading.

Instead, the boundary conditions required to obtain the Dorn solution with a constant stress ratio are identified under *proportional stressing* when the major load reaches a maximum. The critical subtangent yields

$$\frac{1}{z}=\frac{1}{\sigma_{eq}}\left[\sigma_1(N_1)^2+N_2\left(\frac{1}{A_2}\frac{\partial F_2}{\partial \varepsilon_m}\frac{d\varepsilon_m}{d\varepsilon_{eq}^p}+\alpha\sigma_1 N_2\right)\right] \tag{E19}$$

Setting Eq. (E19) equal to the critical subtangent of Dorn in Eq. (E13a), it is apparent that there must be a non-zero load rate in the minor loading direction of the following form

$$\frac{1}{A_2}\frac{\partial F_2}{\partial \varepsilon_m}\frac{d\varepsilon_m}{d\varepsilon_{eq}^p}=\frac{\sigma_{eq}N_1\left(1-kN_1\right)}{N_2}-\alpha k\sigma_{eq}N_2 \tag{E20}$$

**E4: Details on Code Implementation**

A schematic of the code structure for implementation of the Generalized Incremental Stability Criterion (GISC) is depicted in **Figure E1**.

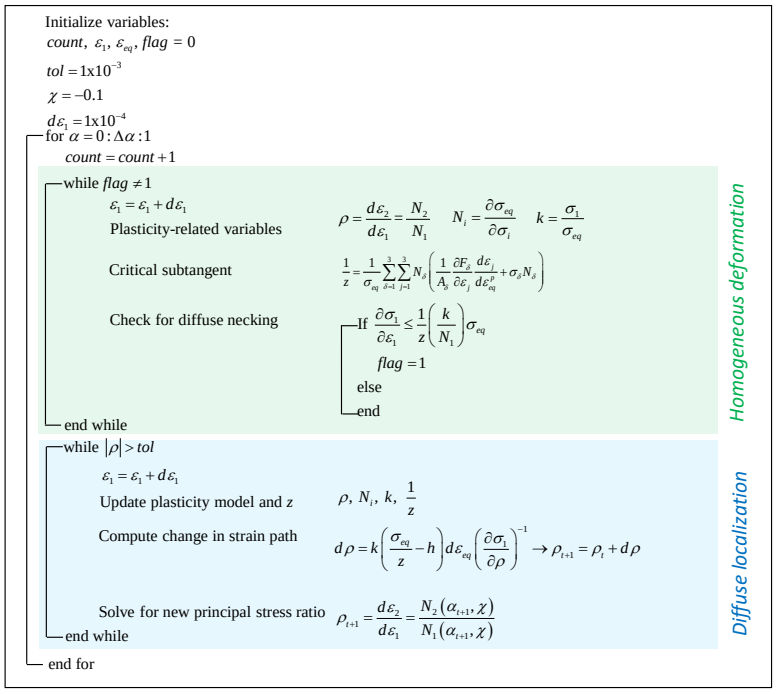


**Figure E1: Schematic of code structure for implementation of the GISC.**

A schematic of the code structure for implementation of the control algorithm to resolve evolving stress-strain gradients in plane strain stretch-bending is shown in **Figure E2**. The Fourth-Order Runge-Kutta method was employed to perform the through-thickness stress integration of

$$\frac{d\sigma_3(\alpha,\chi)}{dr}=\frac{1}{r}\left[k\left(\alpha,\chi,x_n\right)\bar{\sigma}\left(\varepsilon_{eq}^p\right)-\sigma_3(\alpha,\chi)\right]+\frac{d\varepsilon_1^{mem}}{dr}\rho\left(\alpha,\chi\right)\sigma_3(\alpha,\chi) \tag{E21a}$$

where

$$\sigma_3=\chi k\left(\alpha,\chi,x_n\right)\bar{\sigma}\left(\varepsilon_{eq}^p\right),\qquad \chi=\chi_b+\chi_c \tag{E21b}$$

The right-hand side of Eq. (E21a) is defined through $f$

$$f(r,\sigma_3)=\frac{1}{r}\left[k\left(\alpha,\chi,x_n\right)\bar{\sigma}\left(\varepsilon_{eq}^p\right)-\sigma_3(\alpha,\chi)\right]+\frac{d\varepsilon_1^{mem}}{dr}\rho\left(\alpha,\chi\right)\sigma_3(\alpha,\chi) \tag{E22}$$

Integration is initiated from the convex layer, $r_y = r_0$, where plane stress-plane strain prevails, $\sigma_3(r_0) = \sigma_{3,0} = 0$. Thus, the first Runge-Kutta step, $\Gamma^{(I)}$, is known and the bending stress ratio is $\chi_b^{(I)} = 0$ such that

$$\Gamma^{(I)} = jf(r_0, \sigma_{3,0}), \qquad \sigma_3^{(I)}(r_0) = \left(\chi_b^{(I)} + \chi_c^{(I)}\right) k\left(\alpha, \chi, x_n\right)^{(I)} \bar{\sigma}\left(\varepsilon_{eq}^p\right)^{(I)} = \sigma_{3,0} = 0 \tag{E23a,b}$$

where $j$ represents the step size – radial distance – between two integration points. The result of Eq. (E23b) is then utilized to solve for the second Runge-Kutta step, $\Gamma^{(II)}$. First, the unknown bending stress ratio, $\chi_b^{(II)}$, is solved for by noting that

$$\sigma_3^{(II)}\left(r_0 + \frac{j}{2}\right) = \left(\chi_b^{(II)} + \chi_c^{(II)}\right) k\left(\alpha, \chi, x_n\right)^{(II)} \bar{\sigma}\left(\varepsilon_{eq}^p\right)^{(II)} = \sigma_{3,0} + \frac{\Gamma^{(I)}}{2} \tag{E24a}$$

Adopting numerical methods, *e.g.* the non-linear root finding function *fzero* in Matlab®, $\chi_b^{(II)}$ is obtained from

$$g\left(\chi_b^{(II)}\right) = \left(\chi_b^{(II)} + \chi_c^{(II)}\right) k\left(\alpha, \chi, x_n\right)^{(II)} \bar{\sigma}\left(\varepsilon_{eq}^p\right)^{(II)} - \sigma_{3,0} - \frac{\Gamma^{(I)}}{2} = 0 \tag{E24b}$$

and the second Runge Kutta step can be computed utilizing Eq. (E23a)

$$\Gamma^{(II)} = jf\left(r_0 + \frac{j}{2}, \sigma_{3,0} + \frac{\Gamma^{(I)}}{2}\right) \tag{E24c}$$

Similarly for the third Runge-Kutta step

$$g\left(\chi_b^{(III)}\right) = \left(\chi_b^{(III)} + \chi_c^{(III)}\right) k\left(\alpha, \chi, x_n\right)^{(III)} \bar{\sigma}\left(\varepsilon_{eq}^p\right)^{(III)} - \sigma_{3,0} - \frac{\Gamma^{(II)}}{2} = 0 \tag{E25a}$$

$$\Gamma^{(III)} = jf\left(r_0 + \frac{j}{2}, \sigma_{3,0} + \frac{\Gamma^{(II)}}{2}\right) \tag{E25b}$$

and the fourth Runge-Kutta step

$$g\left(\chi_b^{(IV)}\right) = \left(\chi_b^{(IV)} + \chi_c^{(IV)}\right) k\left(\alpha, \chi, x_n\right)^{(IV)} \bar{\sigma}\left(\varepsilon_{eq}^p\right)^{(IV)} - \sigma_{3,0} - \Gamma^{(III)} = 0 \tag{E26a}$$

$$\Gamma^{(IV)} = jf\left(r_0 + j, \sigma_{3,0} + \Gamma^{(III)}\right) \tag{E26b}$$

Compiling the results, the evolution of the resultant through-thickness stress at the first integration point is

$$\sigma_3^{(1)} = \sigma_{3,0} + \frac{1}{6}\left(\Gamma^{(I)} + 2\Gamma^{(II)} + 2\Gamma^{(III)} + \Gamma^{(IV)}\right) \tag{E27}$$

For computation of the subsequent integration point, $\sigma_3^{(1)}$ is prescribed as the new boundary condition and the above steps are repeated.

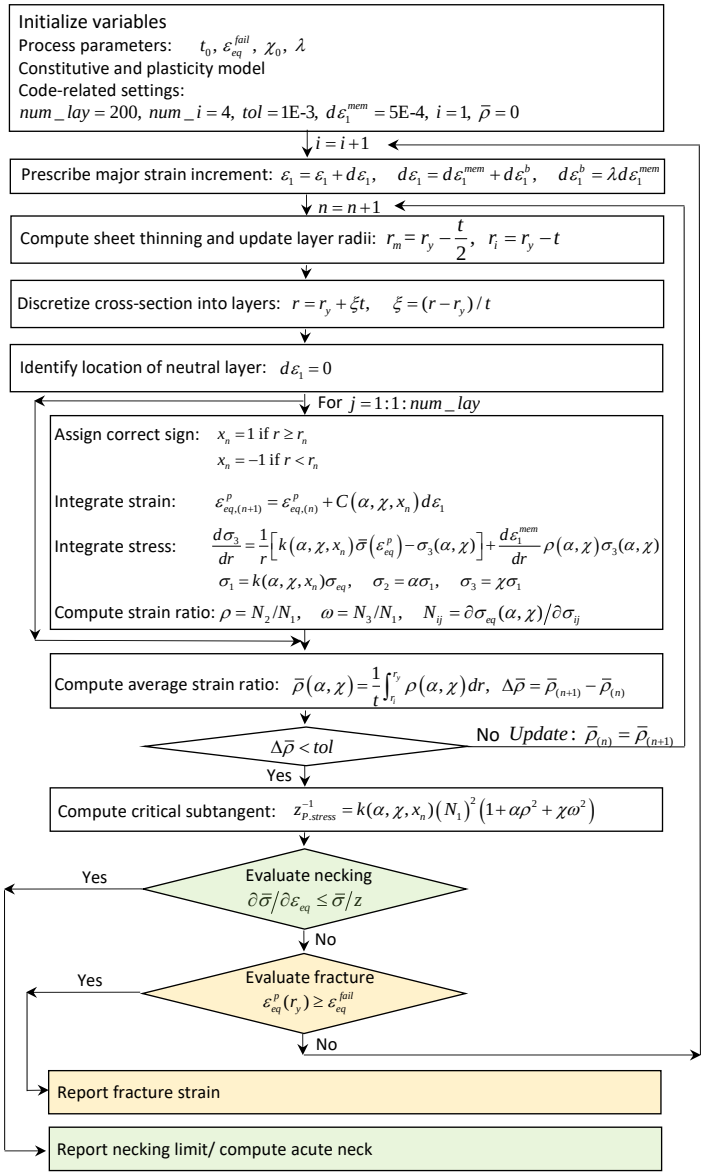


**Figure E2: Schematic of code structure for implementation of the incremental multi-layer model to predict plastic instability in combined loading.**

**E5: Through-thickness Stress Integration in the Two-Zone Stretch-bend Models**

This section provides details on how the stretch-bend equilibrium equation (Eq. (54)) was integrated in the total strain formulation adopting von Mises (vM) plasticity and the Swift hardening model. The flow stress and hardening rate, *h*, are described through

$$\bar{\sigma} = K\left(\varepsilon_0 + \varepsilon_{eq}^p\right)^n, \qquad h = \frac{d\bar{\sigma}}{d\varepsilon_{eq}^p} = \frac{n\bar{\sigma}}{\left(\varepsilon_{eq}^p + \varepsilon_0\right)} \tag{E28a,b}$$

where *K*, $\varepsilon_0$, and *n* are calibration parameters corresponding to the strength coefficient, pre-strain, and hardening exponent, respectively. It is noted that quantities specific to the von Mises yield function are denoted with a superscript *vM*.

Total Formulation – Plane Strain Tension Model (TL-PST)

The in-plane strain and stress ratios are define as

$$\rho = 0, \qquad \alpha = \frac{1+\chi}{2}, \qquad k^{VM} = \frac{x_n\left|\sigma_1\right|}{\sigma_{eq}^{VM}} = \frac{x_n 2}{\sqrt{3}\left|1-\chi\right|} \qquad \text{where } \left|1-\chi\right| \neq 0 \tag{E29a-c}$$

where the variable $x_n$ is introduced to account for the compressive stress in the major loading direction if the material layer is located below the neutral layer. The major and equivalent plastic strain are computed from

$$\varepsilon_1 = \ln\left(\frac{r}{r_m}\right) - \ln\left(\frac{t}{t_0}\right) \tag{E30}$$

$$C^{VM} = k\left(\alpha, \chi, x_n\right)\left(1-\chi\right) = x_n\frac{2}{\sqrt{3}}, \qquad \varepsilon_{eq}^p = C^{VM}\varepsilon_1 = x_n\frac{2}{\sqrt{3}}\varepsilon_1 \tag{E31)-(E32}$$

The stretch-bend equilibrium equation in Eq. (54) for $\bar{\rho} = 0$ reduces to

$$d\sigma_3 = d\sigma_b + d\sigma_c = \frac{1}{r}\left(\sigma_1 - \sigma_b - \sigma_c\right)dr \tag{E33}$$

In the two-zone stretch-bend model, the cross-section is divided into tensile and compressive loading for material layers located above and below the neutral layer, respectively. For simplicity, reverse loading effects are neglected such that the neutral layer, $r_n$, coincides with the unstretched layer, $r_u$, which was derived from volume conservation of the cross-section

$$r_u = r_m \exp(-\bar{\varepsilon}_1^{mem}), \qquad \bar{\varepsilon}_1^{mem} = -\frac{1}{(1+\bar{\rho})}\ln\left(\frac{t}{t_0}\right), \qquad \bar{\rho}(\alpha,\chi) = \frac{1}{t}\int_{r_i}^{r_y} \rho(\alpha,\chi)\, dr \tag{E34a-c}$$

where $\bar{\varepsilon}_1^{mem}$ and $\bar{\rho}$ correspond to the average major membrane strain and the average in-plane strain ratio of the cross-section, respectively. Employing the integration limits for the tensile zone and expressing the right-hand side of Eq. (E33) through dimensionless stress ratios of

$$\chi = \chi_b + \chi_c, \qquad \chi = \frac{\sigma_3}{\sigma_1}, \qquad \chi_b = \frac{\sigma_b}{\sigma_1}, \qquad \chi_c = \frac{\sigma_c}{\sigma_1}, \qquad \alpha = \frac{1+\chi_b}{2}, \qquad k = \frac{x_n|\sigma_1|}{\sigma_{eq}} \tag{E35a-f}$$

yields

$$\int_{\sigma_3(r)}^{\sigma_3(r_y)} d\sigma_3 = \int_r^{r_y} \frac{1}{r}\left[k(\alpha,\chi,x_n)\bar{\sigma}\left(\varepsilon_{eq}^p\right)(1-\chi_b-\chi_c)\right] dr \tag{E36}$$

where $x_n = 1$. Substitution of the Swift hardening model in Eq. (E28) and integration leads to

$$\sigma_3\Big|_r^{r_y} = \left\{(1-\chi_b-\chi_c)\frac{k(\alpha,\chi,x_n)}{C(\alpha,\chi,x_n)}\frac{K}{n+1}\left[\varepsilon_0 + C(\alpha,\chi,x_n)\ln\left(\frac{r}{r_u}\right)\right]^{n+1}\right\}\Bigg|_r^{r_y} \tag{E37}$$

Enforcing plane strain-plane stress on the convex layer ($\sigma_3(r_y) = 0,\ \chi(r_y) = \chi_b(r_y) = \chi_c(r_y) = 0$) and noting that for plane stress loading $k(\alpha) = C(\alpha) = 2/\sqrt{3}$ yields

$$\sigma_3(r) = -\frac{K}{n+1}\left(Y_1^{n+1} - Y_2^{n+1}\right), \qquad Y_1 = \varepsilon_0 + \frac{2}{\sqrt{3}}\ln\left(\frac{r_y}{r_u}\right), \qquad Y_2 = \varepsilon_0 + \frac{2}{\sqrt{3}}\ln\left(\frac{r}{r_u}\right) \tag{E38a-c}$$

Expanding the left-hand side of Eq. (E38a) to $\sigma_3(r) = \frac{2}{\sqrt{3}}\frac{\chi}{|1-\chi|}KY_2^{\,n}$ and rearranging yields

$$\chi_b = \frac{Y_1^{n+1} - Y_2^{n+1}}{-\frac{2}{\sqrt{3}}Y_2^{\,n}(n+1) + Y_1^{n+1} - Y_2^{n+1}} - \chi_c \tag{E39}$$

The closed-form solution for $\chi_b$ in Eq. (E39) is only feasible since the stress-dependence of $C$ vanishes for the PST model such that the term $\left(1-\chi_b-\chi_c\right)\dfrac{k\left(\alpha,\chi,x_n\right)}{C\left(\alpha,\chi,x_n\right)}$ effectively reduces to unity for $\chi \le 0$. Similarly, Eq. (E33) is integrated for the compressive zone ( $x_n=-1$)

$$\sigma_3\Big|_r^{r_n}=\left\{\left(1-\chi_b-\chi_c\right)\frac{k\left(\alpha,\chi,x_n\right)}{C\left(\alpha,\chi,x_n\right)}\frac{K}{n+1}\left[\varepsilon_0+C\left(\alpha,\chi,x_n\right)\ln\left(\frac{r}{r_u}\right)\right]^{n+1}\right\}\Bigg|_r^{r_n} \tag{E40}$$

where both $k$ and $C$ take on negative values. Recalling that $r_n=r_u$ in the two-zone model, Eq. (E40) yields

$$\sigma_3(r)=\sigma_3(r_n)-\frac{K}{n+1}\left(\varepsilon_0{}^{n+1}-Y_3{}^{n+1}\right),\qquad Y_3=\varepsilon_0-\frac{2}{\sqrt{3}}\ln\left(\frac{r}{r_u}\right) \tag{E41a,b}$$

Expanding the left-hand side of Eq. (E41a) and rearranging yields

$$\chi_b=\frac{\sigma_3(r_n)-\dfrac{K}{n+1}\left(\varepsilon_0{}^{n+1}-Y_3{}^{n+1}\right)}{\sigma_3(r_n)-\dfrac{K}{n+1}\left(\varepsilon_0{}^{n+1}-Y_3{}^{n+1}\right)-\dfrac{2}{\sqrt{3}}KY_3{}^{n}}-\chi_c \tag{E42}$$

where $\sigma_3(r_n)$ is computed from the condition that the normal stress over the cross-section is to be continuous. Substitution of $r=r_n$ into Eq. (E38a) and noting that $r_n=r_u$ in Eq. (E38c) yields

$$\sigma_3(r_n)=-\frac{K}{n+1}\left(Y_1{}^{n+1}-\varepsilon_0{}^{n+1}\right) \tag{E43a}$$

Substitute Eq. (E43a) back into Eq. (E42) leads to

$$\chi_b=\frac{Y_1{}^{n+1}-Y_3{}^{n+1}}{Y_1{}^{n+1}-Y_3{}^{n+1}+\dfrac{2}{\sqrt{3}}(n+1)Y_3{}^{n}}-\chi_c \tag{E43b}$$

Total Formulation – Biaxial Tension Model (TL-BT)

The in-plane strain and stress ratios are

$$\rho^{VM} = \frac{-2\chi_c}{3-3\chi+\chi_c}, \qquad \alpha = \frac{1+\chi_b}{2} \tag{E44a,b}$$

and the quantities required for the strain computation are

$$k^{VM} = \frac{x_n|\sigma_1|}{\sigma_{eq}^{VM}} = x_n 2\left(3\chi_b{}^2 - 6\chi_b - 6\chi_c + 6\chi_b\chi_c + 4\chi_c{}^2 + 3\right)^{-\frac{1}{2}} \tag{E45}$$

$$C^{VM} = \frac{x_n 2\left(4\chi_c{}^2 - 6\chi_c + 3\chi_b{}^2 - 6\chi_b + 6\chi_b\chi_c + 3\right)^{\frac{1}{2}}}{3-3\chi_b-2\chi_c} \tag{E46}$$

where the explicit dependence of $C(\alpha,\chi)$ upon the stress state is embedded. The major and equivalent strain are computed in an iterative procedure since the average in-plane strain ratio over the cross-section, $\bar{\rho}$, is initially unknown

$$\varepsilon_1 = \ln\left(\frac{r}{r_m}\right) - \frac{1}{(1+\bar{\rho})}\ln\left(\frac{t}{t_0}\right), \qquad \varepsilon_{eq}^{p} = C^{VM}\varepsilon_1 \tag{E47a,b}$$

The stretch-bend equilibrium equation of Eq. (54) is

$$d\sigma_3 = d\sigma_b + d\sigma_c = \frac{1}{r}(\sigma_1 - \sigma_b - \sigma_c)\,dr + \bar{\rho}(\alpha,\chi)\,\bar{\varepsilon}_1^{mem}(\sigma_b + \sigma_c) \tag{E48}$$

Substitution of the Swift hardening model in Eq. (E28), expressing the right-hand side of Eq. (E48) through dimensionless stress ratios in Eq. (E35a-f), and integration leads to

$$\begin{aligned}\sigma_3\Big|_r^{r_y} = &\left\{(1-\chi_b-\chi_c)\frac{k(\alpha,\chi,x_n)}{C(\alpha,\chi,x_n)}\frac{K}{n+1}\left[\varepsilon_0 + C(\alpha,\chi,x_n)\ln\left(\frac{r}{r_u}\right)\right]^{n+1}\right\}\Bigg|_r^{r_y} \\ &+ \bar{\rho}(\alpha,\chi)\,\bar{\varepsilon}_1^{mem}\chi k(\alpha,\chi,x_n)K\left[\varepsilon_0 + C(\alpha,\chi,x_n)\ln\left(\frac{r}{r_u}\right)\right]^{n}\end{aligned} \tag{E49}$$

Enforcing the boundary condition of plane strain-plane stress on the convex layer $(\sigma_3(r_y)=0,\ \chi(r_y)=\chi_b(r_y)=\chi_c(r_y)=0)$ and noting that for plane stress loading $k(\alpha)=C(\alpha)=2/\sqrt{3}$ yields

$$\sigma_3(r) = -\frac{K}{n+1}\left[ Y_1^{n+1} - (1-\chi_b-\chi_c)\frac{k(\alpha,\chi,x_n)}{C(\alpha,\chi,x_n)} Y_4^{n+1} \right] - \bar{\rho}(\alpha,\chi)\bar{\varepsilon}_1^{mem}\chi k(\alpha,\chi,x_n) K Y_4^{n},$$
$$Y_4 = \varepsilon_0 + \frac{2\left(4\chi_c^{\,2} - 6\chi_c + 3\chi_b^{\,2} - 6\chi_b + 6\chi_b\chi_c + 3\right)^{\frac{1}{2}}}{3-3\chi_b-2\chi_c}\ln\left(\frac{r}{r_u}\right) \qquad \text{(E50a,b)}$$

where $x_n = 1$. Expanding the left-hand side of Eq. (E50a) and rearranging finally yields

$$f(\chi_b) = \chi k(\alpha,\chi,x_n) K Y_4^{\,n} - \frac{K}{n+1}\left[ -Y_1^{n+1} + (1-\chi_b-\chi_c)\frac{k(\alpha,\chi,x_n)}{C(\alpha,\chi,x_n)} Y_4^{n+1} \right] + \bar{\rho}(\alpha,\chi)\bar{\varepsilon}_1^{mem}\chi k(\alpha,\chi,x_n) K Y_4^{\,n} = 0 \qquad \text{(E51)}$$

Recalling that $\chi = \chi_b + \chi_c$, the only unknown variable in Eq. (E51) is $\chi_b$ but due to the explicit dependence of both $k(\alpha,\chi)$ and $C(\alpha,\chi)$ on $\chi_b$, Eq. (E51) needs to be solved for numerically, *e.g.* using Newton-Raphson or the non-linear root finding function *fzero* in Matlab®.

Similarly, Eq. (E48) is integrated for the compressive zone. Substitution of the Swift hardening model and integration yields

$$\sigma_3\Big|_r^{r_n} = \left\{ (1-\chi_b-\chi_c)\frac{k(\alpha,\chi,x_n)}{C(\alpha,\chi,x_n)}\frac{K}{n+1}\left[ \varepsilon_0 + C(\alpha,\chi,x_n)\ln\left(\frac{r}{r_u}\right)\right]^{n+1} \right\}\Bigg|_r^{r_n} + \bar{\rho}(\alpha,\chi)\bar{\varepsilon}_1^{mem}\chi k(\alpha,\chi,x_n) K\left[ \varepsilon_0 + C(\alpha,\chi,x_n)\ln\left(\frac{r}{r_u}\right)\right]^{n} \qquad \text{(E52)}$$

where $x_n = -1$ and thus leads to negative values for both $k(\alpha,\chi)$ and $C(\alpha,\chi)$. Recalling that $r_n = r_u$ in the two-zone model, Eq. (E52) simplifies to

$$f(\chi_b) = \chi k(\alpha,\chi,x_n) K Y_5^{\,n} - \frac{K}{n+1}\left\{ -(1-\chi_{b,r_n}-\chi_{c,r_n})\frac{k(\alpha_{r_n},\chi_{r_n},x_n)}{C(\alpha_{r_n},\chi_{r_n},x_n)}\varepsilon_0^{\,n+1} + (1-\chi_b-\chi_c)\frac{k(\alpha,\chi,x_n)}{C(\alpha,\chi,x_n)} Y_5^{n+1} \right\} + \bar{\rho}(\alpha,\chi)\bar{\varepsilon}_1^{mem}\chi k(\alpha,\chi,x_n) K Y_5^{\,n} - \sigma_3(r_n) = 0 \qquad \text{(E53a)}$$

where

$$Y_5 = \varepsilon_0 - \frac{2\left(4\chi_c{}^2 - 6\chi_c + 3\chi_b{}^2 - 6\chi_b + 6\chi_b\chi_c + 3\right)^{\frac{1}{2}}}{3 - 3\chi_b - 2\chi_c} \ln\left(\frac{r}{r_u}\right) \tag{E53b}$$

The stress ratios with a subscript $r_n$ need to be computed from Eq. (51) noting that due to the continuity condition of the normal stress, $\sigma_3$ in both zones is identical at the neutral layer such that $\sigma_3^I\left(r_n\right) = \sigma_3^{II}\left(r_n\right) = k\left(\alpha_{r_n}, \chi_{r_n}, x_n\right)\chi_{r_n} K\varepsilon_0{}^n$. The latter is analogous to $\chi^I\left(r_n\right) = -\chi^{II}\left(r_n\right)$ but the sign needs to be inverted since the stress ratio is defined with respect to the in-plane stress that is positive and negative in Zone I and II, respectively. Substitution into Eq. (E53a) finally yields

$$\begin{aligned} f\left(\chi_b\right) = {} & \chi k\left(\alpha, \chi, x_n\right) K Y_5{}^n \\ & - \frac{K}{n+1}\left\{-\left(1 - \chi_{b,r_n} - \chi_{c,r_n}\right)\frac{k\left(\alpha_{r_n}, \chi_{r_n}, x_n\right)}{C\left(\alpha_{r_n}, \chi_{r_n}, x_n\right)}\varepsilon_0{}^{n+1} + \left(1 - \chi_b - \chi_c\right)\frac{k\left(\alpha, \chi, x_n\right)}{C\left(\alpha, \chi, x_n\right)} Y_5{}^{n+1}\right\} \\ & + \bar{\rho}\left(\alpha, \chi\right)\bar{\varepsilon}_1^{mem}\chi k\left(\alpha, \chi, x_n\right) K Y_5{}^n - k\left(\alpha_{r_n}, \chi_{r_n}, x_n\right)\chi_{r_n} K\varepsilon_0{}^n = 0 \end{aligned} \tag{E54}$$

which is numerically solved for $\chi_b$.